2024
NCREE Research

Programs and Accomplishments

NCREE

使用聲明

任何閱覽本報告的使用者(以下簡稱使用者),即代表已確認及接納須就本報告的使用自行承擔一切風險。

本報告之所有內容為財團法人國家實驗研究院國家地震工程研究中心(以下簡稱國震中心)享有著作權及所有權，嚴禁抄襲與改作。非經國震中心同意，使用者不得將本報告之全部或一部以任何形式或方式進行轉載、重製、摘錄、引用、公開傳輸、公開播送、散布或發行，亦不得於任何未經國震中心同意之管道刊登或披露(如以超連結等方式內嵌於任何網頁或網站)。若有符合合理使用之情形，應正確引註以表彰權利人之權益。

本報告僅供學術、教育、研究或公益等非營利用途之參考，使用者不得將本報告使用於銷售商品或服務之宣傳或行銷，不得在商業推廣時(如廣告、產品或投資說明等)使用本報告之內容或數據,且不得擅自使用或利用國科會、國研院、國震中心及其所屬單位、員工之名稱、院徽、商標或以任何方式使用國科會、國研院或國震中心之名義。

因使用、閱覽或無法使用本報告而產生的直接、間接、附帶、特別、衍生性或懲罰性等所受損害或所失利益，包含但不限於利潤、營業、客戶、機會、商譽、使用、資料損失等純粹經濟上損失或其他無形損失，使用者應自負其責，概與國震中心無關。因使用本報告而引致任何誹謗、侵犯著作權或智慧財產權等情事，亦同。

國震中心對於本報告之內容或數據，概不為任何明示或默示之保證或聲明，亦不對資料之準確性、完整性或正確性作出任何陳述或保證，亦不會承擔任何賠償責任。同時，本報告所有內容可隨時停止公開或變更而毋須事前通知使用者。

Any user who accesses this report (hereinafter referred to as the "User") represents and acknowledges that they must assume all risks associated with their use of this report.

The content of this report is copyrighted and owned by the National Center for Research on Earthquake Engineering (hereinafter referred to as the "NCREE"), which is a foundation established under the laws of Taiwan. Any copying or modification of this report is strictly prohibited. Unless authorized by the NCREE, the User is not permitted to reproduce, duplicate, extract, quote, publicly transmit, publicly broadcast, distribute, or publish the whole or any part of this report in any form or manner, nor are they allowed to post or disclose any part of this report through any unauthorized

channels (such as embedding in any web page or website using a hyperlink). If there are circumstances that qualify as fair use, the User should properly cite the report to acknowledge the interests of the rights holder.

This report is provided for reference purposes only and is intended for non-profit uses such as academic, educational, research, or public welfare. The User is not allowed to use this report for promoting or marketing goods or services, nor to use the content or data of this report in commercial promotions (such as advertisements, product or investment instructions, etc.), and is not allowed to use or exploit the names, emblems, trademarks, or any other aspect of the name of the National Science and Technology Council, the National Institutes of Applied Research, the NCREE, or its affiliated units or employees in any way.

The User assumes full responsibility for any direct, indirect, incidental, special, derivative, or punitive damages or loss of benefits resulting from the use, browsing, or inability to use this report, including but not limited to pure economic losses such as profits, business, customers, opportunities, reputation, use, data loss, or other intangible losses. The same applies to any defamation, infringement of copyright or intellectual property rights, or any other consequences resulting from the use of this report.

The NCREE does not provide any express or implied warranties or representations regarding the content or data of this report. The NCREE also makes no statements or warranties regarding the accuracy, completeness, or correctness of the data, and does not assume any liability for any compensation. At the same time, the NCREE reserves the right to stop the publication or modify the contents of this report at any time without prior notice to the User.

Contents

Key Revisions to the Requirements for the Allowable Inter-story Relative Lateral Displacement Angles of Buildings Subjected to Small-to-medium Intensity Earthquakes

Yuan-Tao Weng[1], Gee-Jin Yu[2], and Te-Kuang Chow[2]

翁元滔[1]、於積瑨[2]、周德光[2]

Abstract

Disaster investigations of major earthquakes that have occurred in Taiwan in recent years have revealed that non-structural walls and other non-structural elements of buildings are susceptible to significant damage. However, lateral deformation of the building structure affects some structural components of the lateral force resistance system and components not designed for lateral resistance. Therefore, the current seismic design code for buildings in Taiwan stipulates that the relative lateral displacement angle between floors shall not exceed 0.005 when subjected to low- and medium-intensity earthquakes. However, the test results for related non-structural wall components indicate that when the lateral displacement angle value is approximately 0.004, the non-structural wall is susceptible to obvious damage, which can easily affect the use function of the building and increase repair costs. This study compiles relevant domestic and international regulations and experimental data on the relative lateral displacement angle between floors, reviews the current regulations, and formulates relevant revision plans to effectively control the seismic performance of buildings and reduce the cost of seismic repair.

Keywords: drift ratio, non-structural walls, seismic codes

Introduction

In seismic design, lateral deformation and inter-story relative lateral displacement angles affect both components of the lateral force-resisting system and components that are not part of it. In a lateral force resisting system, when lateral forces act on a structure, the structure responds, causing it to move. Therefore, a relationship exists between the lateral force-resisting system and the structural response under lateral loading. This relationship can generally be calculated manually or analyzed using computer simulations. The analysis results indicate whether design requirements, such as the rotation angle of eccentric brace frame joints or special moment frame beam-column joints, are satisfied. Pushover analysis can also reveal the effects on structural components that are not part of the lateral force-resisting system, such as beams and columns within the load-bearing system. Design specifications often require that moment-resisting frames and eccentric braced frames must ensure the structural performance under nonlinear rotation angles generated by specific lateral cyclic deformation. If the structure lacks appropriate design considerations for the preset lateral movement, its lateral force resisting system is susceptible to premature failure and reduction of strength. If the lateral displacement of the structure is exceedingly large, the resulting P- effect may cause structural instability and collapse.

The current building seismic code [3] stipulates the allowable relative lateral displacement angle between floors as follows:

2.16.1 Allowable inter-story relative lateral displacement angle

Under the action of seismic force $V = \frac{IF_u}{4.2}\left(\frac{S_{aD}}{F_u}\right)_m W$ *, the relative lateral displacement between adjacent upper and lower floors divided by the story height is referred to as the inter-story relative lateral displacement angle, which shall be limited and shall not exceed 0.005 radians per floor.*

[1] Associate Researcher, National Center for Research on Earthquake Engineering
[2] Associate Technologist, National Center for Research on Earthquake Engineering

When calculating displacement, translational and torsional displacements must be taken into account.

If it can be demonstrated that non-structural members can withstand large inter-story displacements without causing damage that compromises occupant safety, the above limitations may be appropriately relaxed.

For the applied design seismic force when determining the displacement, if the fundamental vibration period is computed based on structural mechanics, the resulting T value does not need to be less than 1.4 times the period calculated using the empirical formula. Additionally, S_{aD} does not need to be less than 0.4 S_{DS}. In addition, for buildings with an importance factor greater than 1.0, displacements may also be calculated using a seismic force with I = 1.0.

The primary consideration of the above provisions is that when the earthquake is not serious, the relative lateral displacement angle between layers should also be limited to avoid non-structural components being damaged when the earthquake is not serious, thereby affecting the usability and occupant safety.

Building Codes

At present, the estimation methods and restriction requirements for inter-story displacement in the United States Uniform Building Code (UBC 1997) [1], American Society of Civil Engineers (ASCE 7-22) [2], and European Union standards [4] are as follows:

Code	Design force	Drift	Modified drif	Limitation of interstorey drift
ASCE 7-22	$\frac{S_a}{R} \cdot I \cdot W$	δ_e	$\frac{C_d \cdot \delta_e}{I} = \delta_{DE}$	$0.7\sim2.5\% \cdot h_{sx}$
UBC 1997	$\frac{C_v \cdot I}{R \cdot T} \cdot W$	Δ_s	$\Delta_s \cdot R \cdot 0.7 = \Delta_M$	$2\sim2.5\% \cdot h_{sx}$
EuroCode 8	$a_g \cdot S \cdot \frac{2.5}{q} \cdot \eta \cdot m$ (平台段)	d_e	$d_e \cdot q_d = d_s$	$\frac{0.5\sim1\% \cdot h_{sx}}{v}$

where C_d, q_d are deflection amplification factor and displacement behavior factor, R, q are response modification coefficient and behavior factor, I is importance factor, C_v is seismic coefficient (according to the ground type and the seismic zone), and v is reduction factor taking into account the lower return period of the seismic action. Eurocode 8 specifies that an earthquake with a 10% probability of exceedance in 10 years (95-year mean return period) may be considered a frequent seismic event.

In addition, the New Zealand Standard (NZS 1170.5) [5] stipulates that the load setting for the serviceability limit states (SLS) (return period of 25 years, which is 1/4 of the ULS return period of 500 years) aims to prevent damage or the need for repairs to structural or non-structural elements under such events (Section 2.1.4). Inter-story displacements should be limited so as not to adversely affect the required properties of other structural elements (Section 7.5.2). In past moderate and minor earthquakes in New Zealand, the cost of restoring buildings was considerable. After cost-benefit analysis, SLS loads should adopt a 50-year return period and limit inter-story displacement to 0.25% to significantly reduce non-structural damage and service interruptions. Eurocode 8 sets a 0.5% limit on inter-story displacement for brittle non-structural elements connected to the structure [6].

Performance of Non-structural Wall Components

The results of the non-structural wall frame test conducted by Yu-Chen Ou et al., using a frame with an opening and a non-structural wall thickness of 10 cm as an example, are shown in Figure 1(a). When the lateral displacement angle reached 0.37% radian, the non-structural wall exhibited many oblique cracks, and when the lateral displacement angle reached 0.62% radian as shown in Figure 1(b), the non-structural wall exhibited more oblique cracks and concrete peeling.

(a) Drift angle reaches 0.37%

(b) Drift angle reaches 0.62%

Fig. 1. Experimental observation of shear walls with openings

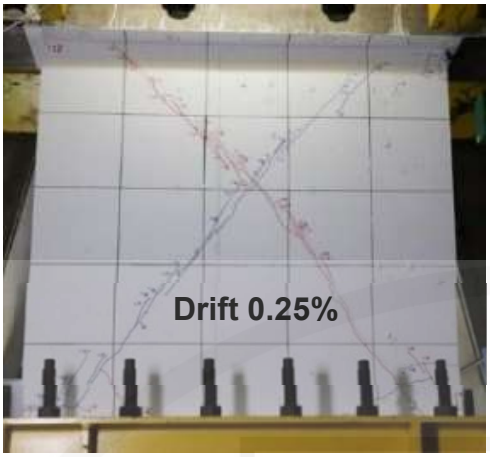

(a) Drift angle reaches 0.25%

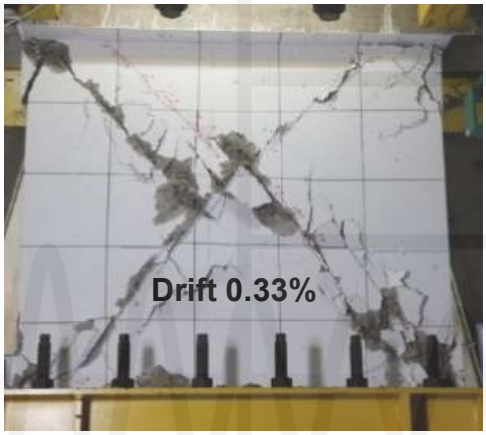

(b) Drift angle reaches 0.33%

Fig. 2. Experimental observation of shear walls without openings

An experimental study on shear failure of reinforced concrete walls was performed by Fang-Yu Lin et al. [7]. They demonstrated that when the axial compression ratio is 20%, the oblique cracks and damage states of the shear wall without openings are as shown in Figure 2(a) and 2(b), when the lateral displacement angle reaches 0.25% and 0.33%, respectively.

From the experimental observations shown in Figure 2, when the axial compression ratio is 20% and the lateral displacement angle is approximately 0.33%, the shear cracks of the wall without openings are intensified and there is obvious concrete spalling.

The oblique cracks and damage states of the open shear wall when the axial compression ratio is 20% and the lateral displacement angle reaches 0.375% and 0.5% are shown in Figure 3(a) and 3(b), respectively.

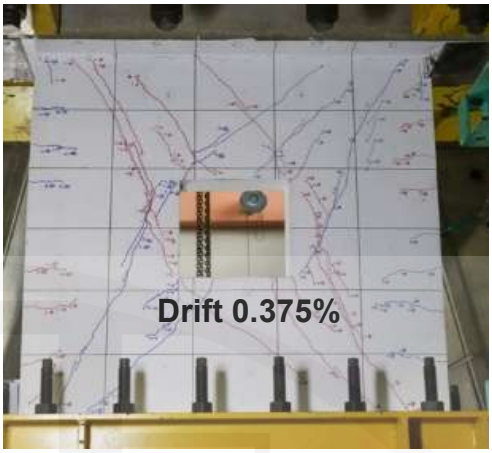

(a) Drift angle reaches 0.375%

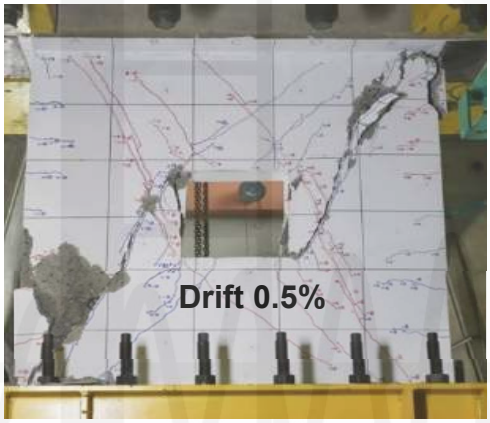

(b) Drift angle reaches 0.5%

Fig. 3. Experimental observation of shear walls with openings

From the observations in Figure 3, when the axial compression ratio is 20% and the lateral displacement angle reaches approximately 0.5%, the shear cracks of the wall with open shear force intensify and concrete peeling occurs.

Discussion on the requirements for lateral displacement angle limitation

There are two primary requirements for limiting the lateral displacement angle between floors of buildings in various national standards: (1) similar to ASCE 7-22, the nonlinear lateral displacement angle must be checked within an earthquake return period of 475 years, and (2) the lateral displacement angle must be assessed under small to moderate earthquake levels or at the serviceability limit state. Taiwan's current building seismic code stipulates that, under small to medium-intensity seismic forces, the relative lateral displacement of each floor from its upper and lower adjacent floors divided by the floor height, namely the inter-story relative lateral displacement angle, must be limited and must not exceed 0.005. However, based on the aforementioned non-structural wall tests,

significant damage may occur when vertical components of mid- to high-rise buildings are subjected to a large axial pressure when the floor lateral displacement angle reaches approximately 0.5%, thereby affecting the building's functionality and increasing the cost of repair.

Conclusions

The seismic design principle set out in the building seismic code states that, under the action of low- to medium-intensity earthquakes, the structure should remain elastic and functional. However, when designing building structures in Taiwan, the basic vibration period of the structure often fails to account for the stiffness contribution of non-structural walls. As a result, the structural period is overestimated, leading to an underestimation of the seismic force demand and inter-story displacement under small- to moderate-intensity earthquakes. Consequently, the damage to non-structural components is also underestimated [8].

Experimental results on non-structural walls indicate that when the lateral displacement angle reaches 0.3%, a small number of oblique cracks are likely to occur. When the lateral displacement angle reaches 0.5%, a considerable number of oblique cracks are likely to occur and concrete is likely to begin to peel away. Therefore, the restriction requirement that the lateral displacement angle should not exceed 0.5% under low- and medium-intensity earthquakes warrants further study and revision.

The rigor of seismic provisions reflects the level of societal commitment to earthquake safety and the degree of economic development of the country. By formulating earthquake-resistant design codes, buildings can be constructed to satisfy certain earthquake-resistant standards, ensuring a safe environment and reducing public fear of earthquake hazards, which is one of the factors for social stability and development. Revising the provisions of the earthquake-resistant design code to reflect the earthquake-resistant requirements of buildings, reduces construction costs prevents waste under the premise of safety requirements; it also improves the level of earthquake-resistant design.

References

ICBO (1997). 1997 Uniform Building Code. International Conference of Building Officials, Whittier, CA.

ASCE/SEI 7, 2022. Minimum Design Loads and Associated Criteria for Buildings and Other Structures, ASCE STANDARD: ASCE/SEI 7-22.

Architecture Buildings Research Institute (ABRI), 2022. *Recommended Provisions for Building Seismic Regulations*, Taipei (in Chinese).

Eurocode 8: Design of structures for earthquake resistance – Part 1: General rules, seismic actions and rules for buildings, EN 1998-3:20050.

NZS 1170.5: 2004 Structural Design Actions Structural Design Actions (2004).

Thomas A. Moore (2018). “Repairing SLS anomalies in NZ seismic code to reduce earthquake losses”, Bulletin of the New Zealand Society for Earthquake Engineering.

Fang-Yu Lin, Pu-Wen Weng and Shyh-Jiann Hwang (2022).「Experimental study on shear failure of reinforced concrete walls」, the 16th National Conference on Structural Engineering and the 6th National Conference on Earthquake Engineering. (in Chinese)

R. Ditommaso, etc (2018). “Prediction of the fundamental period of infilled RC framed structures considering the maximum inter-story drift at different design limit states”, Structures.I. (2009). Updated seismic design guidelines for buildings of a model code of Mexico. Earthquake Spectra, 25 (4): 869-898, November, doi: 10.1193/1.3240413.

Seabed Liquefaction Potential Under Different Limit States in OWF Design

Shang-Yi Hsu[1], Yu-Wen Chang[2], Yuan-Chang Deng[3], Jiun-Shiang Wang[4], and Juin-Fu Chai[5]

許尚逸[1]、張毓文[2]、鄧源昌[3]、王俊翔[4]、柴駿甫[5]

Abstract

The seabed soil of Offshore Wind Farms (OWFs) in western Taiwan exhibits a soft composition with a significant potential for soil liquefaction. Therefore, it is necessary to consider the impact of seismic forces on soil liquefaction when designing support structures for offshore wind turbines. Simplified soil liquefaction assessment methods typically concentrate on soil layers at depths of up to 20 m. However, in various locations along the west coast of Taiwan, the soil depth typically exceeds 20 m. The consideration of liquefaction potential in deeper strata remains a topic requiring further investigation. Therefore, the objectives of this study are to compare and evaluate soil liquefaction conditions using both the effective-stress site response analysis (E-SRA) and the cone penetration test (CPT) simplified liquefaction assessment method. The comparative results indicate that the liquefaction potential within the upper 20 m of soil layers is consistent between both methods, suggesting that the simplified assessment method provides reliable results within this depth range. By contrast, E-SRA may serve as a valuable reference for assessing liquefaction potential in soil conditions that extend beyond the 20-m threshold. As the seabed depths along the western coast of Taiwan frequently exceed 20 m, the findings of this study underscore the importance of employing E-SRA in the initial assessment phase of offshore wind farm design.

Keywords: limit state for OWF design, soil liquefaction, effective-stress site response analysis

Introduction

According to Appendix I of the national standard CNS15176-1 issued by the Bureau of Standards, Metrology, and Inspection (MOEA), as well as the "Technical Guidelines for Site Investigation and Design of Offshore Wind Turbines," it is essential to evaluate the liquefaction potential at each wind turbine and substation location within a site. However, the foundation depths of wind turbines in the western offshore regions of Taiwan may exceed 20 m. Therefore, the suitability of employing simplified liquefaction assessment methods for wind turbine support structures with foundation depths greater than 20 m requires further investigation.

The effective stress site response analysis considers the accumulation or dissipation of pore water pressure induced by seismic excitation, thereby influencing the seismic dynamic behavior of soil layers. The DEEPSOIL program provides a pore water pressure (PWP) model to simulate the generation and dissipation of excess pore water pressure, the variation in soil effective stress, and the nonlinear stress–strain characteristics of soils under effective stress conditions. Currently, this approach is widely used in the seismic design of offshore wind farms in Taiwan.

This study adopts the second-phase offshore wind farm of the Taiwan Power Company (TPC), referred to as TPC Phase II OWF, as a case study. The liquefaction potential evaluation results from effective-stress site response analysis (E-SRA) and the simplified liquefaction assessment method based on cone penetration test (CPT) data are compared under design earthquake return periods: the ultimate limit

[1] Associate Researcher, National Center for Research on Earthquake Engineering
[2] Research Fellow, National Center for Research on Earthquake Engineering
[3] Assistant Researcher, National Center for Research on Earthquake Engineering
[4] Researcher Assistant, National Center for Research on Earthquake Engineering
[5] Deputy Director, National Center for Research on Earthquake Engineering

state (ULS) with a 475-year seismic return period and the serviceability limit state (SLS) with a 95-year return period. Recommendations for soil liquefaction assessment methodologies tailored to seabed depths greater than 20 m are proposed accordingly.

Target Site Overview

The feasibility report for TPC Phase II OWF details the completion of five CPT boreholes in the seabed west of Lukang Township in Changhua County, adjacent to the Changhua Coastal Industrial Park. Each borehole reached a depth of 100 meters, as shown in Figure 1. Since borehole BH04 is the closest to the planned wind turbine location, this study selected CPT data from BH04 as the basis for the case study.

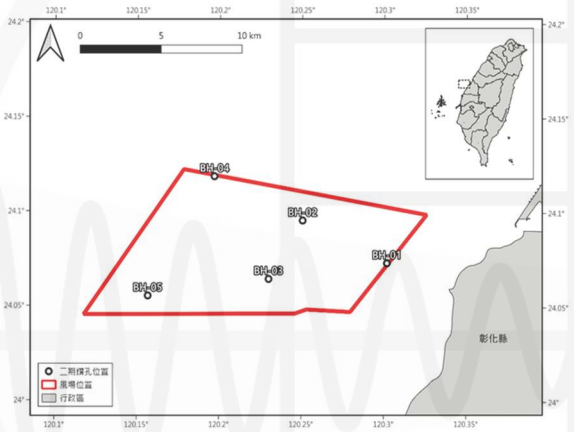

Fig. 1. CPT boreholes from the feasibility report of TPC Phase II OWF

Geotechnical Parameters of Target site

Subsurface geotechnical investigations at the offshore wind farm primarily used CPT to obtain corrected cone resistance q_t, sleeve friction f_s, and pore pressure u_2 to characterize the CPT material index (I_c) and derive geotechnical parameters such as unit weight (γ_t) and shear wave velocity (V_s) at various depths. Figure 2 illustrates the soil profile at borehole BH04 based on CPT-derived parameters.

The site-specific shear wave velocity $(V_s)_{30}$ for BH04 was 136 m/s. Below the depth of 88.2 m, the shear wave velocity of strata exceeded 360 m/s, designating this location as the reference base depth. The design-level ground motion, determined from the seismic hazard analysis of this wind farm site, was applied at this reference base for subsequent effective stress site response analyses.

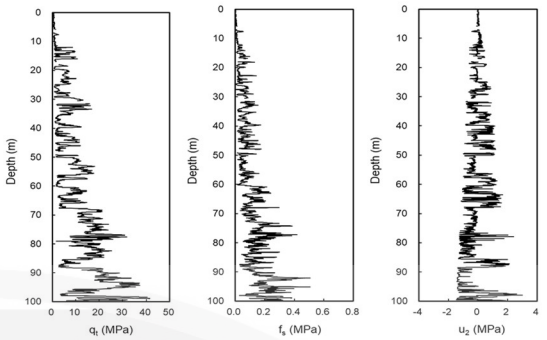

(a) CPT data

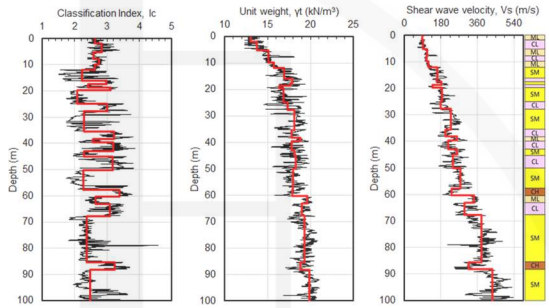

(b) Geotechnical parameters and profile

Fig. 2. CPT data and geotechnical parameters of BH04 profile

UHRS of Reference Base at Target Site

The geological conditions of the reference bedrock surface for the TPC Phase II offshore wind farm were set in accordance with the standard requirements, where $(V_s)_{30}$ is specified as 360 m/s. Based on seismic hazard analysis, seismic hazard curves for various periods were derived, enabling the determination of uniform hazard response spectra (UHRS) for the reference bedrock outcropping at seismic return periods of 30, 95, 475, and 2,500 years (Figure 3). In this study, the spectral acceleration S_A value at a period of 1 s was adopted as the reference for conditional mean spectra. Through the selection of seismic sources, eight events were identified as seeds. The response spectra of artificial earthquakes corresponding to the UHRS for the 95-year and 475-year return periods were then matched (as shown in Figure 4). The outcropping motions at the reference bedrock level were subsequently used as input for E-SRA.

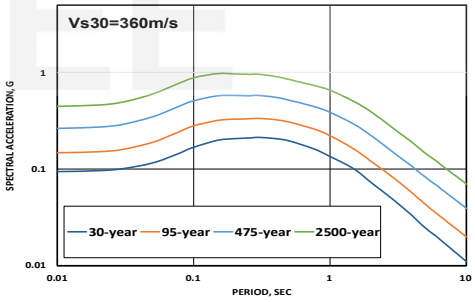

Fig. 3. UHRS under different return periods

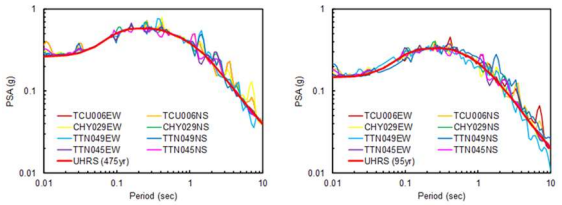

(a) ULS level (b) SLS level

Fig. 4. Response spectra of 8 input motions for E-SRA

Effective-stress Site Response Analysis

Non-linear Curves for Layers

For the various soil strata at this site, including silty sands (SM) and low-plasticity silts (ML), the dynamic properties curves for cohesionless soils recommended by the Electric Power Research Institute (EPRI) were applied. For low-plasticity clays (CL) and high-plasticity clays (CH), the dynamic property curves proposed by Vucetic and Dobry (1991) with plasticity indices (PIs) of 15 and 50, respectively, were adopted. E-SRA were conducted for borehole BH04.

PWP models for E-SRA

This research used the P&A model available in the DEEPSOIL program to simulate non-cohesive soils, including SM and ML. The threshold value of the cyclic resistance ratio, CSR_t, corresponding to 200 cycles of cyclic loading, was used as an indicator for evaluating the liquefaction resistance of sandy soils at this site. Parameters such as fines content, F_C, and relative density, D_r, specific to each layer were calibrated to meet the requirements of the P&A model.

For the saturated cohesive soil in BH04, the study used the C-M model recommended by DEEPSOIL. The PIs for the CL and CH strata were 15 and 50, respectively. All clay layers were assumed to be normally consolidated. Based on these assumptions, the relevant parameters were derived to facilitate subsequent E-SRA.

Results of E-SRA

Figure 5(a) presents the profiles of the maximum shear strain, γ_{max}, and the maximum pore water pressure ratio, R_u, obtained from the analysis of eight sets of input motions under the ULS level (475-year return period). The results indicate that at the ULS level, the seabed strata at depths exceeding 20 m, particularly within the 20–40 m range of SM and ML soil layers, exhibited significant excess pore water pressure generation. This results in the occurrence of liquefaction in some cases within strata deeper than 20 m (with the allowable maximum pore water pressure ratio (i.e. max PWP ratio), $(R_u)_{max}$ for sandy soils set to 0.95 in the DEEPSOIL program).

Figure 5(b) illustrates the analysis results under the SLS level (95-year return period). The results show that the shallow strata (L1-ML and L3-ML) generally reach the threshold condition of $(R_u)_{max} = 0.95$. The most significant excess pore pressure excitation occurs in strata shallower than 20 m. For strata deeper than 20 m, the R_u values of all cases remain below 0.7.

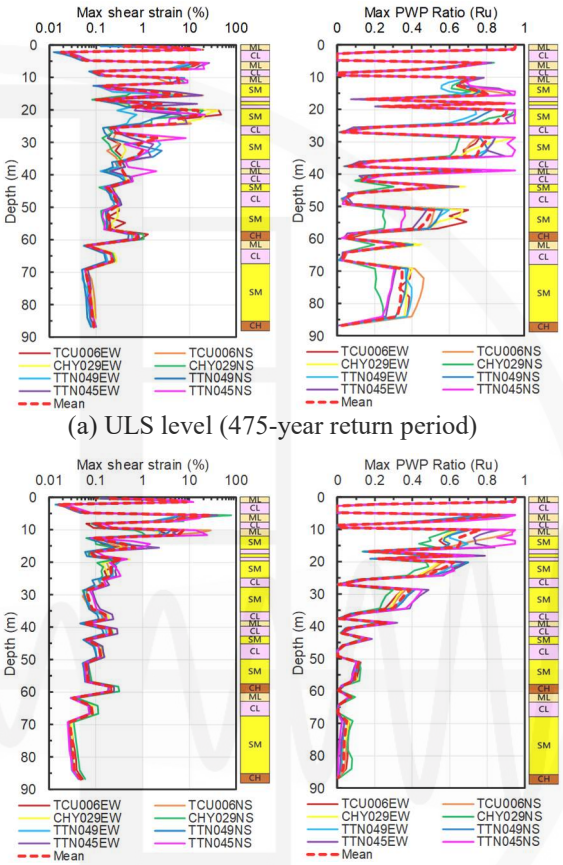

(a) ULS level (475-year return period)

(b) SLS level (95-year return period)

Fig. 5. E-SRA results for BH04 site

Soil Liquefaction Potential Assessment

From a physical perspective, soil liquefaction occurs when R_u equals 1, implying that the excess pore pressure is equivalent to the vertical effective stress. To assess liquefaction potential using E-SRA, R_u was considered alongside additional criteria, such as the maximum shear strain, γ_{max}, and the limiting shear strain (γ_{limit}), where γ_{limit} corresponds to the shear strain under full liquefaction conditions and is related to the relative density (D_r) of cohesionless soils. Following established criteria from prior studies, this research defines three liquefaction states: (a) Non-liquefaction: $R_u < 0.8$, then liquefaction state index = 2; (b) Marginal liquefaction: $0.8 \leq R_u < 0.9$ and $\gamma_{max} < \gamma_{limit}$, then liquefaction state index = 1; (c) Full liquefaction: if $0.8 \leq R_u < 0.9$ and $\gamma_{max} > \gamma_{limit}$, or $R_u > 0.9$, then liquefaction state index = 0.

Figure 6 presents a comparative analysis of the liquefaction potential evaluation results for seabed strata within a depth of 20 m under design earthquake

levels of ULS and SLS, derived using the simplified CPT-based liquefaction evaluation method (HBF method) and the defined liquefaction state scores based on the average results of eight E-SRA conducted in this study. The results reveal that under ULS conditions, if the stratification and types of strata with liquefaction potential within a depth of 20 m are accurately characterized, the evaluation outcomes of the two methodologies demonstrate substantial consistency. Under SLS conditions, the simplified evaluation method continues to identify significant liquefaction potential, consistent with trends observed under ULS. By contrast, the E-SRA suggests that significant liquefaction potential is confined to shallow strata, with liquefaction occurring in only a limited number of seismic scenarios within the SM layer at depths below 10 m.

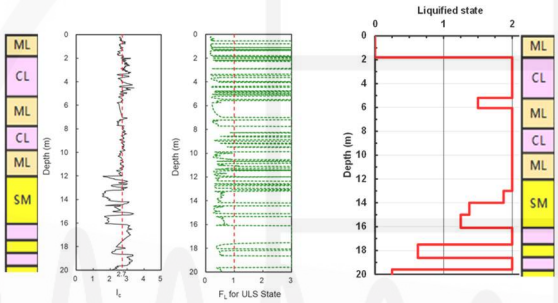

(a) ULS level

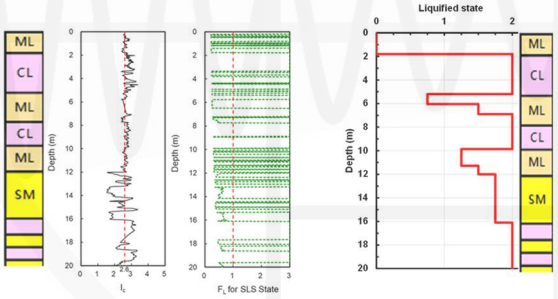

(b) SLS level

Fig. 6. Comparison of liquefaction assessment results for BH04 within a depth of 20 m (left: HBF method; right: E-SRA results)

Figure 7 presents the results of the liquefaction assessment for the entire seabed strata at BH04 under ULS and SLS conditions, utilizing E-SRA. The findings indicate that the SM strata at a depth of 24.2 m continue to demonstrate complete liquefaction, with several seismic scenarios indicating that liquefaction may extend to the SM strata at a depth of 34.5 m. These observations highlight the necessity of careful consideration in the subsequent foundation design of offshore wind turbine support structures, as well as in the performance evaluation of turbine substructures. Appropriate soil reduction factors should be applied to account for the influences of soil liquefaction or stiffness degradation within the strata.

Discussion and Recommendations

The comparison between CPT-based simplified liquefaction evaluation results and E-SRA results conducted within a depth of 20 m, demonstrates that the E-SRA results possess a significant degree of reliability and feasibility for assessing the liquefaction potential of soil strata. However, the E-SRA model incorporates numerous parameters, including nonlinear soil constitutive laws, pore pressure generation models, and various empirical formulations. To ensure its applicability for design purposes and validation, it is essential to corroborate the analysis with reliable laboratory dynamic test results.

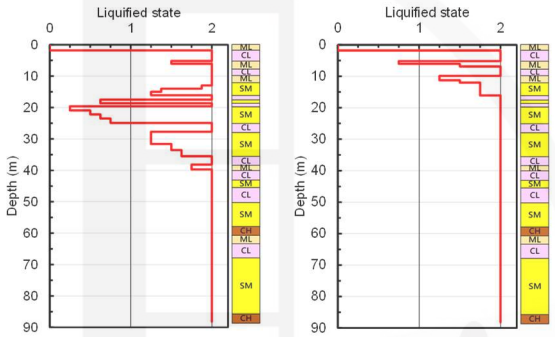

(a) ULS level (b) SLS level

Fig. 7. Liquefaction assessment results for BH04

References

Bureau of Standards, Metrology, and Inspection (MOEA), (2018), ″Wind turbines – Part 1: Design requirements,″ CNS15176-1. (in Chinese)

Bureau of Standards, Metrology, and Inspection (MOEA), (2023), “Technical Guidelines for Site Investigation and Design of Offshore Wind Turbines”. (in Chinese)

Taiwan Power Company (TPC), (2018), “Feasibility report of TPC Phase II Offshore Wind Farm”. (in Chinese)

Hsu-Po Wang, (2021), “Development and Application of Conditional Mean Spectra in Taiwan,” Master's thesis, Department of Construction Engineering, National Taiwan University of Science and Technology. (in Chinese)

Shang-Yi Hsu, Yuan-Chang Deng, Yu-Wen Chang, Jiun-Shiang Wang, Juin-Fu Chai, (2024), “A Study on Evaluation of Seabed Liquefaction Potential：Using Effective Stress Site Response Analysis And CPT Liquefaction Assessment,” Journal of the Chinese Institute of Civil and Hydraulic Engineering, Vol. 36, No. 1, pp. 085–099. (in Chinese)

Hwang, J. H., Lu, C. C., and Wang, J. S., (2023), “Characterized model uncertainties of CPT-based simplified procedures for assessing soil liquefaction and its application to Taiwan offshore wind farms,” Applied Ocean Research, Vol. 138.

Development and Application of a Generalized Building Model

Jui-Liang Lin[1], Ming-Chieh Chuang[1], Passakorn Kamolamnuaykit[2], and Keh-Chyuan Tsai[2]

林瑞良[1]、莊明介[1]、Passakorn Kamolamnuaykit[2]、蔡克銓[2]

Abstract

The generalized building model (GBM) has been satisfactorily verified to be an effective surrogate model for seismic analyses of buildings. The GBM, which consists of a pure shear stick, a pure flexural stick, and *N* lumped masses, can reflect the flexural–shear coupled deformation of buildings with arbitrarily distributed story mass and story stiffness. The present study further extends the applications of the GBM to base-isolated buildings with inelastic superstructures. The effectiveness of this extended application is verified by comparing the seismic responses of a base-isolated nine-story steel building estimated using the base-isolated GBM with those obtained from the corresponding finite-element model. Moreover, the GBM is extended to incorporate viscous damper properties, thus offering a versatile and efficient numerical model for elastic buildings with viscous dampers. The aforementioned nine-story building but with fixed base and added viscous dampers is used to verify the proposed approach of determining the non-proportional damping properties of the GBM.

Keywords: numerical model, seismic analysis, generalized building model, base-isolated buildings, non-proportional damping, viscous dampers.

Introduction

Simplified seismic analyses of base-isolated buildings can be achieved through either simplified numerical methods or simplified numerical modeling. For instance, the 1997 Uniform Building Code (UBC 1997) introduced a statically equivalent method for preliminary design. Kilar and Koren (2010) proposed an inelastic static analysis method for base-isolated buildings. Regarding simplified numerical modeling, superstructures are commonly idealized as either rigid bodies or linear elastic single-degree-of-freedom (SDOF) structures (Fig. 1(a)). However, these approaches overlook superstructure flexibility and higher-mode effects. Therefore, simplified numerical modeling of superstructures as multi-degree-of-freedom (MDOF) structures is preferable. Ramirez and Miranda (2007) employed a continuous beam model for simplified seismic analysis of base-isolated buildings with elastic superstructures (Fig. 1b). By optimizing few parameter values, this model can effectively simulate the elastic seismic responses of mid-rise to high-rise buildings with regularly distributed story masses and story stiffness along the building height. Notably, the continuous beam model captures the flexural–shear coupled deformation of buildings, a feature typically absent in stick models with multiple lumped masses.

Although a new base-isolated building is typically designed to maintain the superstructure within the linear elastic range, the response of an older, weaker building retrofitted with base isolators or a new base-isolated building subjected to extreme earthquakes may deviate from this ideal behavior. Moreover, near-fault pulse-like ground motions, which often impose high seismic demands on long-period structures, may put base-isolated buildings at a disadvantage. Recently, Tsiavos *et al*. (2024) conducted a large-scale experimental investigation of the seismic vulnerability and variability in the inelastic response of base-isolated structures subjected to ground motions of varying seismic intensity levels.

This research proposes a simplified method for assessing the seismic performance of base-isolated buildings while accounting for higher-mode effects and superstructure inelasticity. To achieve this, the

[1] National Center for Research on Earthquake Engineering, Taiwan, R.O.C.

[2] Department of Civil Engineering, National Taiwan University, Taiwan, R.O.C

present study develops a surrogate model for base-isolated buildings, designated as the base-isolated generalized building model (GBM) (Fig. 1(c)). The base-isolated GBM is a variation of the fixed-base GBM, which has been shown to be suitable for simplified seismic analyses of both elastic and inelastic fixed-base buildings (Lin 2019; Lin and Chuang 2023).

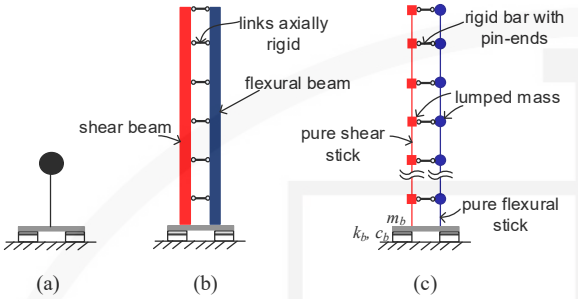

Fig. 1. Simplified numerical modeling for base-isolated buildings: (a) base-isolated SDOF model, (b) base-isolated continuous beam model, and (c) base-isolated GBM.

Equation of Motion for Base-isolated GBM

In order to represent a fixed-base N-story building with rigid diaphragms, the lateral stiffness matrix of a GBM (denoted as $\mathbf{K}$), which is an $N \times N$ full matrix, is equal to the sum of the lateral stiffness matrices of the pure flexural stick and the pure shear stick (denoted as $\mathbf{K}_b$ and $\mathbf{K}_s$, respectively). Moreover, a non-dimensional parameter α, with values ranging from 0 to 1, is used to adjust the deformation type of the GBM. When α is 0, the GBM exhibits pure flexural deformation, whereas when α is 1, it deforms in a pure shear type. The inelastic properties of each segment of the two sticks in a GBM are calibrated by replicating the hysteretic loop of the corresponding story of the building, which is obtained by cyclically pushing the finite-element model (FEM) of the structure (Lin and Chuang 2023). The mass matrix of a GBM (denoted as $\mathbf{M}$), an $N \times N$ diagonal matrix, is directly obtained from the FEM. Rayleigh damping is assumed for constructing the damping matrix of a GBM (denoted as $\mathbf{C}$). The base isolation system illustrated in Fig. 1 is simplified as a lumped mass, m_b, connected to a spring–dashpot system with stiffness k_b and c_b. The equation of motion of a base-isolated GBM representing a base-isolated N-story building is as follows:

$$\begin{bmatrix} \mathbf{M} & \mathbf{M1} \\ \mathbf{1}^T\mathbf{M} & \mathbf{1}^T\mathbf{M1}+m_b \end{bmatrix}\begin{bmatrix} \ddot{\mathbf{v}}_s \\ \ddot{u}_b \end{bmatrix}+\begin{bmatrix} \mathbf{C} & \mathbf{0} \\ \mathbf{0}^T & c_b \end{bmatrix}\begin{bmatrix} \dot{\mathbf{v}}_s \\ \dot{u}_b \end{bmatrix} + \begin{bmatrix} \mathbf{K} & \mathbf{0} \\ \mathbf{0}^T & k_b \end{bmatrix}\begin{bmatrix} \mathbf{v}_s \\ u_b \end{bmatrix} = -\begin{bmatrix} \mathbf{M} & \mathbf{M1} \\ \mathbf{1}^T\mathbf{M} & \mathbf{1}^T\mathbf{M1}+m_b \end{bmatrix}\begin{bmatrix} \mathbf{0} \\ 1 \end{bmatrix}\ddot{u}_g \quad (1)$$

where $\mathbf{1}$ is an $N \times 1$ vector of ones, $\mathbf{0}$ is an $N \times 1$ vector of zeros, $\ddot{u}_g$ is ground acceleration, u_b is the lateral displacement of mass m_b relative to the ground, $\mathbf{v}_s$ is the $N \times 1$ lateral displacement vector of the superstructure relative to its base (*i.e.*, relative to the motion of mass m_b).

Non-proportionally Damped GBM

The unit impulse method (Lin *et al.*, 2014) is employed to determine the equivalent damping coefficient, C_{eq}, for each floor in the GBM. When applying an impulse to excite a specific story with lower stories fixed, responses from both FEM and GBM are compared. The damping coefficient and damping exponent are then optimized to ensure the GBM's displacement history best mimics that obtained from the FEM. This optimization process is conducted sequentially from the top story to the bottom story, considering the influence of added dampers on each level. The proposed approach effectively determines the optimal damper parameters for the GBM to reflect the seismic responses of multistory buildings with viscous dampers.

Numerical Validation

The nine-story steel building was a prototype from the SAC research project, representing typical mid-rise office buildings in Los Angeles (FEMA-355C 2000) (Fig. 2). The SAC research project was a joint venture of the Structural Engineers Association of California (SEAOC), the Applied Technology Council (ATC), and the California Universities for Research in Earthquake Engineering (CUREe) (hence, SAC). An effective period (T_e) of 3.0 s was prescribed for the building with added base isolators. According to FEMA-355C (2000), the design spectral acceleration at a 1-s period (S_{D1}) for buildings in Los Angeles is 0.68 g. Thus, the design spectral acceleration (S_{aD}) for buildings with a fundamental period of 3.0 s is 0.227 g (calculated as 0.68/3). Accordingly, the design displacement, D, is 50.7 cm (calculated as $S_{aD}/(2\pi/T_e)^2$). The mass m_b and damping c_b were assumed to be twice the mass of the first story (*i.e.*, 20.16 kN×s^2/cm) and 0, respectively. A bilinear isolator system with a yield force of 10% of the total weight (*i.e.*, $\mathbf{1}^T\mathbf{M1}+ m_b$) and a post-yielding stiffness of 10% of the elastic stiffness was assumed.

In order to induce inelastic excursions in the superstructures of the building, two near-fault pulse-like ground motions (denoted as HWA019 and Antakya3123), characterized by long-period energy, were selected for numerical verification. Both ground motions were applied in the x-direction of the example building. HWA019 is the EW component of the ground motion recorded at station HWA019 during the magnitude M_L 6.26 earthquake on February 6, 2018,

in Hualien, Taiwan. Antakya3123 is the NS component of the ground motion recorded at station 3123 in Antakya City during the magnitude M_w 7.8 earthquake on February 6, 2023, in Turkey.

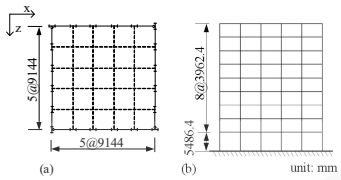

(c)

Floor	Columns		Girder
	at corners	elsewhere	
1	W14×370	W14×500	W36×150
2	W14×370	W14×500	W36×150
3	W14×370	W14×455	W33×141
4	W14×370	W14×455	W33×141
5	W14×283	W14×370	W33×141
6	W14×283	W14×370	W33×130
7	W14×257	W14×283	W27×102
8	W14×257	W14×283	W27×94
9	W14×233	W14×257	W24×62

Fig. 2. (a) Typical floor plan, (b) elevation, and (c) member sizes of the nine-story building.

Figures 3(a) and (b) show the displacement and acceleration of the ninth story (*i.e.*, the roof) relative to the base isolators (denoted as v_{9F} and $\ddot{v}_{9F}$, respectively) when the nine-story building was subjected to unscaled HWA019 (*i.e.*, SF = 1.0). Figures 3(c) and (d) present the corresponding base-isolator displacement and acceleration relative to the ground (denoted as u_b and $\ddot{u}_b$, respectively). Figures 3(e) to (h) are the counterparts of Figs. 3(a) to (d) but for the unscaled Antakya3123 (*i.e.*, SF = 1.0). Figures 3(i) and (j) show the hysteretic loops of the base isolators for the nine-story building subjected to unscaled HWA019 and unscaled Antakya3123, respectively. Overall, Fig. 3 indicates that the proposed method, which employed a simplified numerical model instead of a complete FEM, effectively estimated the seismic responses of the roof and isolators in the nine-story building. Moreover, the analysis time for the base-isolated nine-story building subjected to Antakya3123 using the simplified numerical model and the complete FEM was approximately 46.5 s and 443.2 s, respectively. This result demonstrates that the computational efficiency of the simplified model was significantly superior, with an improvement of approximately tenfold.

Figures 4(a) to (c) show the variations in the peak values of story accelerations, story displacements, and IDRs along the height of the nine-story building subjected to unscaled HWA019, respectively. Figures 4(d) to (f) present the corresponding results for the building subjected to unscaled Antakya3123. Overall, the proposed method effectively estimated the peak acceleration and displacement values for all stories. Accordingly, Figs. 3 and 4 together demonstrate that the base-isolated GBM serves as an effective alternative to the complete FEM of the nine-story building for estimating not only peak values but also the phases of acceleration and displacement responses.

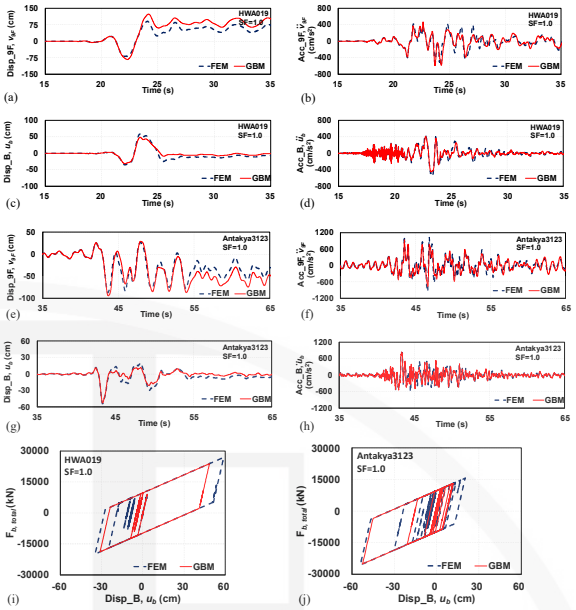

Fig. 3. (a) Displacement and (b) acceleration of the ninth story relative to the base isolators, (c) base-isolator displacement, and (d) base-isolator acceleration relative to the ground for the nine-story building subjected to HWA019 with SF = 1.0. (e) to (h) correspond to (a) to (d) but for the building subjected to Antakya3123 with SF = 1.0. (i) and (j) show the hysteretic loops of the base isolators subjected to HWA019 and Antakya3123, respectively, both with SF = 1.0.

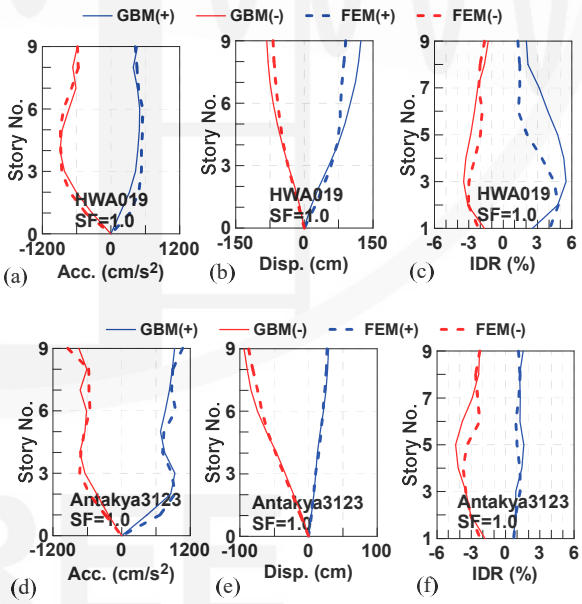

Fig. 4. (a) Peak story accelerations, (b) peak story displacements, and (c) peak IDRs of the nine-story building subjected to HWA019 with SF = 1.0. (d) to (f) correspond to (a) to (c) but for the building subjected to Antakya3123 with SF = 1.0.

Subsequently, a two-dimensional (2D) frame of the SAC nine-story building with a fixed base was used for verifying the effectiveness of the proposed

approach for determining the supplemental damping properties of a GBM (Fig. 5). The 2D frame was incorporated with linear viscous dampers placed randomly on different floors. The damping coefficient (c) is 5.52 kN·s/mm. The calibration process for determining the damping coefficient of the GBM starts from the top story with the lower floors fixed during calibration and then proceeds downward, repeating this procedure for all floors. The calibration aims to minimize the discrepancy between the seismic responses of the GBM and the FEM. The FEM and GBM with the set of equivalent damping coefficients were subjected to the LA44 ground-motion record, which was one of the ground motions used in the SAC project. Figure 6 shows that GBM can perform very well in mimicking the response of the non-proportionally damped FEM (Kamolamnuaykit *et al*. 2023).

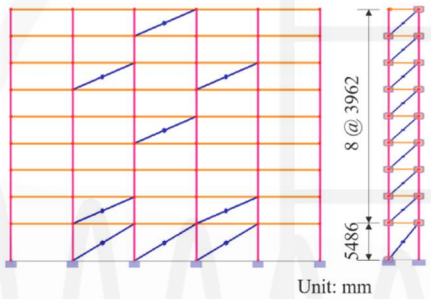

Fig. 5. FEM and GBM of the nine-story steel building with randomly distributed viscous dampers.

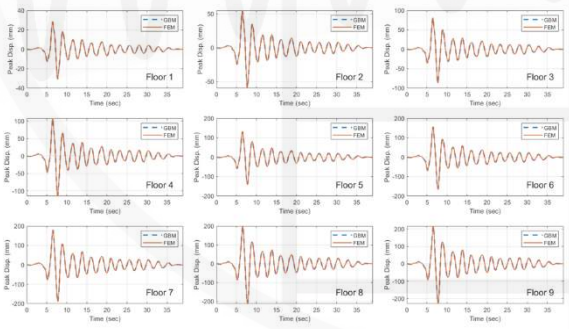

Fig. 6. Peak floor displacement of the nine-story steel building subjected to the LA44 ground motion.

Conclusions

This study proposed a base-isolated generalized building model (GBM) for the simplified seismic analysis of base-isolated buildings. The base-isolated GBM comprised a pure shear stick and a pure flexural stick, which are connected to the ground through a spring–dashpot system. This study verified the effectiveness of the base-isolated GBM in estimating the seismic responses of a base-isolated nine-story steel moment-resisting frame building subjected to two near-fault pulse-like ground motions. Not only the peak values but also the phases of the story accelerations and displacements of the building were satisfactorily estimated using the proposed simplified approach. This study also verified the effectiveness of the proposed approach that determines the optimal damping parameters of a GBM for representing a finite-element model with viscous dampers. This study marks a significant advancement in the versatile applications of the GBM to seismic analyses of buildings of various types.

References

Kamolamnuaykit, P., Lin, J.L., Chuang, M.C., and Tsai, K.C. (2023), "Simplified modelling for seismic response analysis of buildings with viscous dampers", *The 34th KKHTCNN Symposium on Civil Engineering*. November 23-24, 2023, Pattaya, Thailand.

Kilar, V., and Koren, D. (2010), "Simplified inelastic seismic analysis of base-isolated structures using the N2 method", *Earthquake Engineering and Structural Dynamics*, 39: 967–989.

Lin, J.L. (2019), "Approximate quantification of higher-mode effects on seismic demands of buildings", *International Journal of Structural Stability and Dynamics*, 19 (3), 1950023.

Lin, J.L., and Chuang, M.C. (2023), "Simplified nonlinear modeling for estimating the seismic response of buildings", *Engineering Structures*, 279, 115590.

Lin, J.L., Bui, M.T., and Tsai, K.C. (2014), "An Energy-based approach to the generalized optimal locations of viscous dampers in two-way asymmetrical buildings", *Earthquake Spectra*, 30(2):867-889.

Ramirez, C.M., and Miranda E. (2007), "Simplified analysis for preliminary design of base-isolated structures", *Structural Congress: New Horizons and Better Practices*, ASCE.

Tsiavos, A., Nunes, M.F., and Stojadinovic, B. (2024), "Does seismic isolation reduce the seismic vulnerability and the variability of the inelastic seismic response? Large-scale experimental investigation", *Bulletin of Earthquake Engineering*, 22:7359–7381.

FEMA-355C. (2000), "State of the art report on systems performance of steel moment frames subject to earthquake ground shaking", prepared by the SAC Joint Venture for the Federal Emergency Management Agency.

Development of Construction Diagrams for an *in situ* Cast-in-place Retrofitting Method Using Ultra-High-Performance Concrete in Reinforced-Concrete Walls

Yuan-Tao Weng[1], Chung-Chan Hung[2], and You-Ting Wei[3]

翁元滔[1]、洪崇展[2]、魏銷廷[3]

Abstract

In recent years, events such as the 2016 Kaohsiung Meinong earthquake and the 2018 and 2024 Hualien earthquakes have caused many buildings in Taiwan to suffer damage or even collapse. However, most of these buildings were privately owned and reinforcement works were difficult to implement. In addition to the difficulty of raising funds, the long construction period also affects the use of space in such buildings, which greatly reduces the willingness of users. Reinforced-concrete (RC) walls within RC frames can effectively improve the lateral strength and stiffness of the entire frame, preventing the RC frame from collapsing during strong earthquakes. This method utilizes a straightforward reinforcement method with ultra-high-performance concrete (UHPC) to enhance the seismic and collapse resistance of RC walls and similar wall structures. Cladding construction methods can be divided into grouting, hand troweling, shotcreting, and pre-cast slab jointing. The first three are categorized as wet construction, while the last is semi-wet construction. Hand troweling is using a trowel to directly apply and cut UHPC material on the reinforcement surface, whereas shotcreting involves transferring the mixed UHPC slurry into the pumping equipment and spraying it evenly on the construction surface.

Keywords: ultra-high-performance concrete, seismic retrofitting, construction diagrams.

Introduction

Ultra-high-performance concrete (UHPC) is produced by incorporating fine aggregates such as quartz sand and silica fume to increase the density of the slurry and reduce weak surfaces caused by coarse aggregates. Fibers are added to address the limitations of traditional concrete, namely low tensile strength and poor crack resistance. UHPC exhibits excellent crack suppression and significantly improved ductility and strength. Hence, it is applied in earthquake-resistant structures to greatly enhance the earthquake resistance of the structure, reduce the use of confinement and shear reinforcement, increase workability, and simplify the construction process. Research has demonstrated that UHPC can achieve compressive strengths of 120–140 MPa and tensile strengths exceeding 7 MPa—both values more than four times those of conventional concrete. It reduces the cross-section of components and increases construction efficiency and usable space. Owing to its dense structure, the porosity, water absorption, chloride ion permeability and other durability indicators of this material are ten to a hundred times lower than those of traditional concrete, which greatly reduces aging of the structure and extends the service life of the building.

The RC wall within an RC frame can effectively improve the lateral strength and stiffness of the entire frame, preventing the RC frame from collapsing under strong earthquakes. This study employs a simplified UHPC reinforcement method to improve the earthquake resistance and collapse resistance of RC walls or similar wall structures. The covering construction methods used in this approach include grouting, hand troweling, shotcreting, and pre-cast plate jointing. The first three methods are classified as

[1] Associate Research Fellow, National Center for Research on Earthquake Engineering
[2] Professor, Department of Civil Engineering, National Cheng Kung University,
[3] Assistant Technical Engineer, National Center for Research on Earthquake Engineering

wet construction, while the last is semi-wet construction. In the hand troweling method, a trowel is used to directly apply and cut UHPC material on the reinforcement surface. In the spraying shotcrete method, the mixed UHPC slurry is fed into pumping equipment and sprayed uniformly onto the construction surface via a spraying system. This article focuses on the construction methods involving hand troweling and shotcreting.

The application scenarios of this method are as follows:

(1) Reinforcement: To improve the shear strength of the wall structure and the deformation toughness on and beneath the surface, so as to effectively improve the earthquake resistance and collapse resistance of the wall.

(2) Reinforcement direction: Improving the lateral strength of the wall.

(3) Material properties: In order to increase the bonding strength between new and existing interfaces, appropriate bolt components must be used in accordance with the wall thickness and site conditions. For RC walls with poor surface conditions (*e.g.*, extensive cracking), the bolt installation position or method should be adjusted.

The main features of this method are as follows:

(1) The hand troweling, shotcreting, and pre-cast slab jointing methods do not require the assembly of formwork, which effectively reduces the need for temporary works.

(2) Hand troweling and shotcrete reinforcement have good construction efficiency.

(3) Construction time is reduced.

(4) Compared with conventional concrete encapsulation reinforcement, the use of UHPC can effectively reduce the thickness of the reinforcement layer.

Key Points of Retrofitting Design

1. Cladding involves adding a reinforcement layer to the wall surface. Therefore, the joints between the new and existing surfaces must be carefully evaluated and constructed to ensure effective force transfer. Prior to construction, the original structure, including steel-bar design and wall-material quality, should be investigated to inform reinforcement design and construction.

2. The wall surface must be roughened and cleaned before coating to ensure adequate bonding at the interface. In addition, among the available coating methods, the spraying technique requires more machinery and equipment, so the site dimensions, water supply, and power-supply requirements must be evaluated in detail prior to construction.

3. The overlap method for steel mesh should be used in accordance with Chapter 03220 of the Construction Engineering Specifications of the Construction and Planning Agency. When the protective layer is taken into consideration, the steel mesh may be placed on the same plane, and additional steel bars of equivalent strength (A_s, f_y) can be added for welding overlap. The recommended overlap length is at least ten times the diameter of the steel bar.

4. The relevant material test items and requirements are as follows:

   (1) According to the CNS1010 test method, the 28-day compressive strength of UHPC must be greater than 1000 kgf/cm^2.

   (2) According to the CNS1233 or ASTM C1856 and ASTM C1609 test methods, the 28-day flexural strength of UHPC must be greater than 120 kgf/cm^2.

   (3) According to the CNS14703 test method for water-soluble chloride0ion content in hardened cement mortar and concrete, the water-soluble chloride ion content of UHPC must be less than or equal to 0.15 kg/m^3.

Development of Construction Diagrams

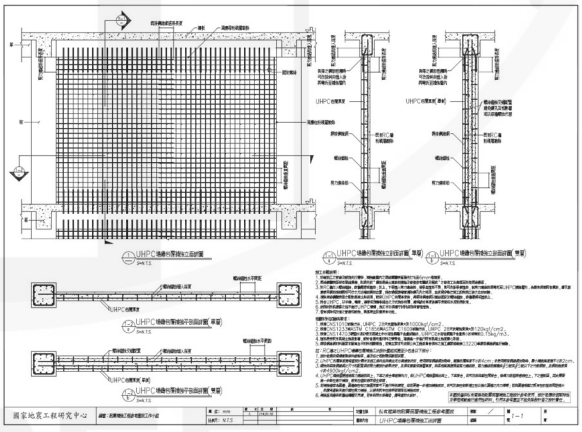

Fig. 1 Reference diagram of UHPC application in the RC wall casting reinforcement method.

The following aspects should be addressed:

1. The designer must provide detailed cross-sectional drawings showing the relationship between beams and walls based on actual site conditions.

2. The thickness of UHPC should be determined with consideration of both the design

requirements and construction conditions, following thorough communication with the project owner. When steel mesh is used for reinforcement, the recommended reinforcement thickness is not less than 4 cm. If no steel mesh is used, the minimum reinforcement thickness should be not less than 2 cm.

3. The size and configuration of bolts and steel wire mesh should be determined according to the strength design calculations, while maintaining appropriate protective layer thickness. Shear connecting bars must be included adjacent to the beam. It is recommended that these shear connecting bars be #5 or smaller bamboo-type steel bars, with a strength less than 4900 kgf/cm^2.
4. The UHPC reinforcement layer must transmit lateral forces through the connection between the shear reinforcement bars and the upper and lower beams. If the UHPC reinforcement layer cannot be connected to the upper and lower beams, then the reinforcement layer can be anchored to adjacent columns. However, in such cases, force transmission will occur through the plastic hinge regions above and below the columns. Therefore, the columns need to be further reinforced to avoid premature damage to the plastic hinges of the columns.
5. The number of shear tie bars must be calculated by the designer. Before bar installation, construction or design drawings of the existing beams should be reviewed to prevent conflicts. In addition, a bar scanning instrument can be used to confirm the actual positions of existing beam bars before installation.
6. If the reinforced wall surface includes a wing wall, and one side lacks columns, then the unbounded surface does not require special treatment. However, to enhance the reinforcement effect, new columns may be added to such wing walls to improve internal force transmission. If the spacing between the stirrups of the existing columns adjacent to the wing wall is too large, then consideration should be given to expanding the existing columns for shear reinforcement and increasing the amount of transverse reinforcement. This is to avoid premature damage to the existing columns due to the transverse forces applied to the wing wall after UHPC reinforcement.
7. A waterproof design should be considered for areas around the reinforcement surface and at the interface between new and existing structures exposed to rainwater.

Construction Steps

The construction steps for the UHPC RC wall-reinforcement field-casting cladding method are as follows:

1. Relocation of construction pipelines and facilities must be prevented.
2. The surface of the original structure within the reinforcement construction area should first be roughened to a roughness of 6 mm.
3. Crack treatment: A steel brush is used to remove debris from the cracks, and a vacuum cleaner or industrial air blower is used to remove dust and particles. For more serious cracks, a stronger repair material is used. For deeper or wider cracks, mortar, epoxy resin, or UHPC is used for repair. When troweling the surface, a spatula is used to smooth the surface, and the repaired area is flushed with the surrounding area.
4. After drilling holes in the wall, screw anchors or through-hole screws are inserted, and any dirt is cleaned out.
5. After detecting the positions of the existing steel bars of the upper and lower beams, shear connecting bars are implanted according to the design results while avoiding the original positions of the structural steel bars.
6. After setting the covering thickness, the steel mesh is fixed to the screw anchors or through-thread screws.
7. UHPC is mixed and the coating is applied.
8. The surface is smoothed or cement plaster is applied.
9. UHPC maintenance: The material manufacturer's instructions on maintenance requirements must be followed and the material must be kept moist. For larger repairs, keeping the repair area moist helps UHPC strength development. The material can be covered with a wet cloth or plastic film to maintain humidity. Material storage and management measures must be followed during construction.
10. If any pipelines or facilities have been removed or diverted, they must be restored and their original functions restored.

Review of Key Points of Retrofitting Design

1. Related material test items and requirements:

(1) According to the CNS1010 test method, the 28-day compressive strength of UHPC must be greater than 1000 kgf/cm^2.

(2) According to the CNS1233 or ASTM C1856 and ASTM C1609 test methods, the 28-day flexural strength of UHPC must be greater than 120

kgf/cm^2.

(3) According to the CNS 14703 test method for water-soluble chloride-ion content in hardened cement mortar and concrete, the water-soluble chloride-ion content of UHPC must be less than or equal to 0.15 kg/m^3.

(4) Anchor reinforcement performance depends on the strength of the existing concrete. Designers should account for material variability and are advised to conduct additional core sampling of the existing concrete to assess its strength.

(5) The steel mesh manufacturer must provide relevant material reports. If required by the owner, inspection of the welded steel wire mesh can be conducted in accordance with Chapter 03220 of the Public Works Committee.

2. The size of the steel mesh or steel bars must be selected based on the analysis results and must include an appropriate protective layer.

3. The joint opening position must be designed according to the specified screw-anchor-hole location. The number of bolts or screws must be sufficient to transmit the shear force from the UHPC reinforcement layer.

Conclusions

Ultra-high-performance concrete (UHPC) is a cement-based composite material developed in recent years both domestically and internationally. With its ultra-high strength and dense microstructure, it can address the problem of reinforcement projects often affecting the usable space as a result of excessive volume, and also provides good waterproofing performance. In terms of workability, the required slump flow can be adjusted according to the construction conditions to overcome suboptimal reinforcement construction conditions.

In order to facilitate the application of this reinforcement method in projects in practice, this study developed a reference diagram and instructional document, which outline the characteristics of the method, applicable timing, reinforcement design procedures and precautions, construction steps, design review items, *etc*., in order to allow users to smoothly carry out reinforcement design and to improve the quality of seismic-reinforcement projects.

References

Architecture Buildings Research Institute (ABRI), 2022. *Recommended Provisions for Building Seismic Regulations*, Taipei (in Chinese).

Structural Engineers Association of California (SEAOC). (1999). “Recommended Lateral Force Requirements and Commentary,” *7th Edition*, Seismology Committee, Structural Engineers Association of California, Sacramento, California.

American Society of Civil Engineers (ASCE/SEI 7-22). (2022). “Minimum Design Loads and Associated Criteria for Buildings and Other Structures.” *ASCE 7-22*, American Society of Civil Engineers, USA.

ACI (American Concrete Institute). 2019. Building code requirements for structural concrete and commentary. ACI 318-14/19, 318R-14/19. Farmington Hills, MI: ACI.

ASTM International. (2015). E519/E519M-15 Standard Test Method for Diagonal Tension (Shear) in Masonry Assemblages.

Graybeal, B.A.: Design and Construction of Field-Cast UHPC Connections, FHWA, U.S. Department of Transportation, Publication No: FHWA-HRT-19-011 (2019)

Kyriakides, M. A., & Billington, S. L. (2014). Cyclic response of nonductile reinforced concrete frames with unreinforced masonry infills retrofitted with engineered cementitious composites. Journal of Structural Engineering, 140(2), 04013046.

Lin, Y. W., Wotherspoon, L., Scott, A., & Ingham, J. M. (2014). In-plane strengthening of clay brick unreinforced masonry wallettes using ECC shotcrete. Engineering Structures, 66, 57-65.

Qiu, H., Chin, R., Ingham, J., & Dizhur, D. (2016, April). Experimental shear testing of unreinforced masonry wall panels. In 2016 New Zealand Society for Earthquake Engineering (NZSEE) Annual Technical Conference. New Zealand Society for Earthquake Engineering.

French Standardization Association. (2016). National Addition to Eurocode 2–Design of Concrete Structures: Specific Rules for Ultra-High Performance Fibre-Reinforced Concrete (UHPFRC). AFNOR, France.

Haber, Z. B., Foden, A., McDonagh, M., Ocel, J. M., Zmetra, K., & Graybeal, B. A. (2022). Design and Construction of UHPC-Based Bridge Preservation and Repair Solutions (No. FHWA-HRT-22-065). United States. Federal Highway Administration. Office of Infrastructure Research and Development.

The American Association of State Highway and Transportation .Guide Specifications for Structural Design with Ultra-High Performance Concrete, 2024

Study on Seismic Retrofitting Assessment and Experimental Verifications of Reinforced Concrete Building using Buckling Restrained Braces

Fu-Pei Hsiao[1], Pu-Wen Weng[2], Chia-Chen Lin[3], Po-Hsun Lee[4], and Chao-Hsun Huang[5]

蕭輔沛[1]、翁樸文[2]、林佳蓁[3]、李柏勳[4]、黃昭勳[5]

Abstract

This study establishes a structural model of a reinforced concrete (RC) building using the ETABS analysis software and incorporates nonlinear hinges with the assistance of the TEASDA program. The seismic performance of the building is evaluated through nonlinear dynamic analysis, and buckling-restrained braces (BRBs) are designed and applied for seismic retrofitting to enhance the building's seismic performance. To better understand the actual seismic behavior of the retrofitted building, a hybrid experimental technique is employed, combining multiple physical substructures and numerical substructures for composite simulation. The experiment involves a full-scale two-story reinforced concrete frame and a full-scale BRB element. In order to simplify the research scope, the connection problem between the BRB and RC frame is neglected. The experimental and analytical results verify that the structural model, which incorporates nonlinear hinges for reinforced concrete components using the TEASDA program and adopts the BRB nonlinear hinge settings recommended by ASCE 41-17, can reasonably simulate the seismic behavior of the building.

Keywords: reinforced concrete buildings, buckling restrained brace, seismic retrofitting, seismic assessment, hybrid simulation.

Introduction

Buckling-restrained brace (BRB) is widely adopted as effective seismic retrofitting tool to enhance the seismic performance of buildings. One of the primary advantages of BRBs is their ability to be prefabricated in manufacturing plants and subsequently assembled on-site, thereby expediting the retrofitting process while minimizing disruptions to building occupants.

To accurately assess the seismic response of a structure, full-scale shaking table tests can be conducted. However, such experiments are often constrained by significant time and financial requirements. Alternatively, numerical simulation provides an efficient means of analyzing structural behavior under seismic loading while substantially reducing costs. Nevertheless, discrepancies between numerical predictions and actual structural responses may persist due to inherent modeling assumptions and simplifications.

Hybrid experimental techniques integrate physical testing with numerical simulation, leveraging the advantages of both approaches. In this methodology, a complete structure is partitioned into physical and numerical substructures. Typically, the most complex and challenging-to-simulate components are constructed as physical substructures, while the remaining portions are modeled computationally. The integration of these components enables synchronized experimental analysis, reducing the costs and time associated with full-scale structural testing while improving the accuracy of seismic response predictions.

This study investigates the effectiveness of BRB

[1] Research Fellow, National Center for Research on Earthquake Engineering
[2] Associate Researcher, National Center for Research on Earthquake Engineering
[3] Associate Technologist, National Center for Research on Earthquake Engineering
[4] Master, National Taipei University of Technology
[5] Professor, National Taipei University of Technology

diagonal braces in enhancing the seismic performance of reinforced concrete (RC) buildings. A structural model is developed and evaluated using nonlinear dynamic time-history analysis to assess its seismic capacity and optimize the retrofitting design. Furthermore, to validate the numerical model and assess its ability to capture actual structural behavior, two physical substructure specimens are constructed. The hybrid experimental approach employed in this research aims to provide a more accurate representation of the structural response of retrofitted buildings under seismic excitation.

Seismic Retrofitting Assessment

In this study, a structural model was developed using the ETABS structural analysis software. The analyzed building is a seven-story RC structure. Detailed building information is provided in Table 1. The floor plans feature identical beam and column cross-section designs across all stories, with an RC wall located at the middle bay from the fourth to the seventh floor. The column sections are 500 mm × 500 mm, while the beam sections are 450 mm × 350 mm. High-strength reinforced concrete was used, with SD420W reinforcement for the longitudinal steel of beams and columns, and SD785 reinforcement for the stirrups. The material properties for structural analysis were based on experimental results from shaking table tests on high-strength RC frames conducted by Yang (2021). A 3D structural model was constructed in ETABS, as shown in Fig. 1. The nonlinear behavior of beam and column components was simulated using nonlinear hinges generated through the TEASDA auxiliary program (Hsiao et al., 2021).

Table 1. Building information

Building type	Mixed residential and commercial apartment
Structure type	Reinforced concrete
Dimension	18 m by 18 m
Stories	7
Height	22.05 m

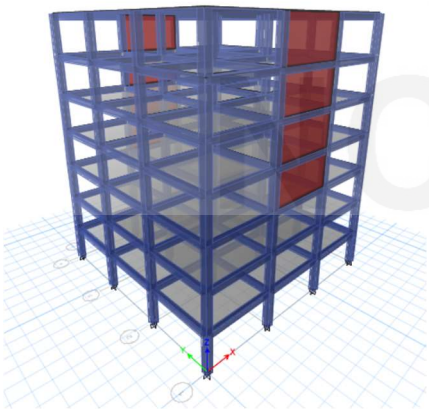

Fig. 1. Numerical model of the structure

To ensure the retrofitted RC building meets its performance requirements and is suitable for subsequent hybrid experiments, the design of the BRB follows the recommendations from full-scale two-story RC frame experiments (Yang, 2015). The simulation of the BRB behavior is based on the ASCE 41-17 standard (ASCE, 2017), where the nonlinear axial force plastic hinges for the BRB are defined. The selected BRB core material is A36 steel, with a nominal yield strength of 245 MPa and a core cross-sectional area of 20 mm × 90 mm. The nominal yield strength of the core can be calculated as follows:

$$P_y = 1800 \times 245 / 1000 = 441\ kN \quad (1)$$

The building was retrofitted with BRBs on the first through third floors, with braces positioned at the middle bay. Four BRBs were added to each floor, resulting in a total of twelve BRBs for the entire building. After retrofitting, the structural model of the building was established in the ETABS software, as shown in Fig. 2.

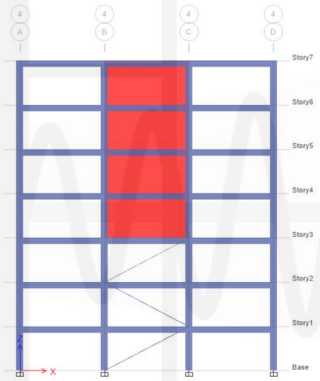

Fig. 2. Numerical model of the retrofitted structure

Seven ground motion records were selected through the Platform of Input Motion Selection for Taiwan (INMOST) (Liu et al., 2022) for nonlinear dynamic time-history analysis to assess the seismic performance of the structure. The peak interstory drift ratios in both positive and negative directions from the seven records were averaged to obtain a more representative structural response. The maximum interstory drift ratios for each floor before and after retrofitting with BRBs are presented in Fig. 3 and 4.

Before retrofitting, the average maximum interstory drift ratio from the seven records, the red line in Fig. 3, indicates that the second-floor drift ratio reached 2.79%, exceeding the performance target of 2.0% for an importance factor I = 1.25. After retrofitting, the second-floor interstory drift ratio was reduced to 1.09%, as shown in Fig. 3, demonstrating that the BRB retrofit effectively improved seismic performance and met the target performance criteria.

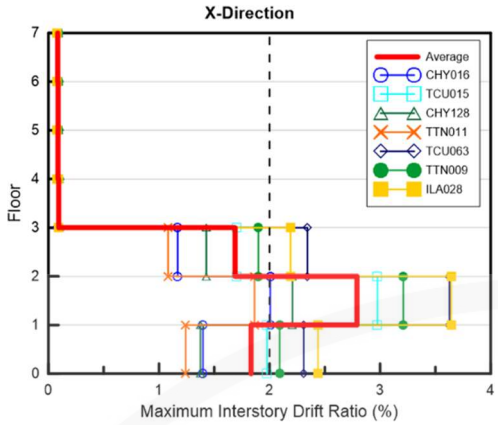

Fig. 3. Maximum story drift of the non-retrofitted structure

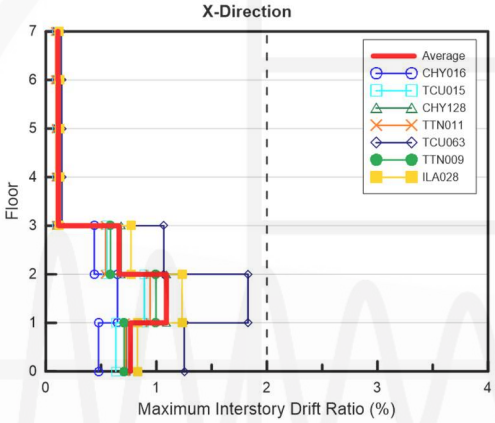

Fig. 4. Maximum story drift of the retrofitted structure

Hybrid Tests

To investigate the actual structural response of buildings retrofitted with BRBs under seismic excitation, this study was conducted in collaboration with Professor Tony Yang's research team at the University of British Columbia (UBC) and was performed at the National Center for Research on Earthquake Engineering (NCREE) Tainan laboratory. The hybrid experiment utilized a two-story, single-span RC frame specimen and a full-scale BRB specimen as physical substructures. These specimens represented the lower two stories of the retrofitted RC structure's middle bay and the retrofitted BRB, respectively. The hybrid simulation was executed using the Hardware-in-the-loop Hybrid Simulation Software (HHS) for structural analysis and the Advanced Low-level Controller (ALC) for experimental control, ensuring synchronized interaction between the numerical and physical substructures. The architecture diagram of the hybrid test is illustrated in Fig. 5.

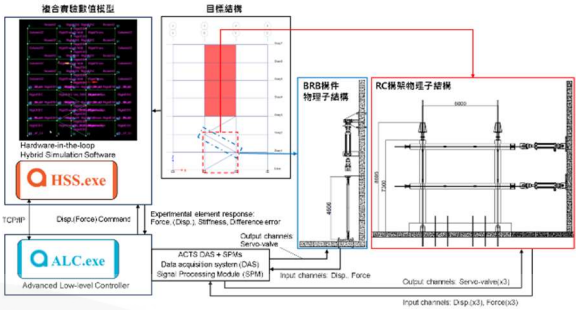

Fig. 5. Architecture diagram of the hybrid test

The experiment applied seismic ground motion to the RC frame in the horizontal direction using actuators while maintaining a constant axial force at the column tops with hydraulic jacks, as shown in Fig. 6. The BRB specimen was subjected to axial tension and compression forces through displacement-controlled loading via actuators, as illustrated in Fig. 7. The hybrid experiment was conducted without considering the influence of the connection details between the BRB and the RC frame.

Fig. 6. Test setup of the RC frame

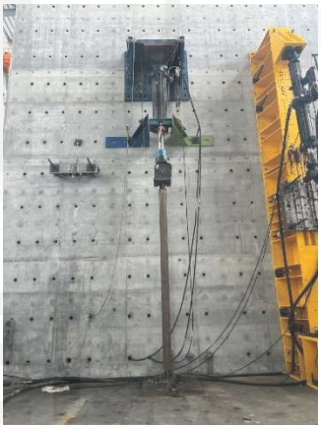

Fig. 7. Test setup of the BRB

The input ground motion for the experiment is the ground motion recorded at Station CHY063 during the February 6 2016 Meinong earthquake (Fig. 8). The experiment was conducted in three sequential phases using scaled versions of the original seismic record at 25%, 50%, and 100% intensity levels.

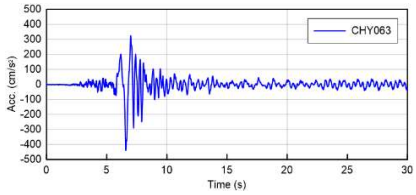

Fig. 8. Time history - CHY063

Comparison of Experimental and Analytical Results

The physical substructure test results from the CHY063-100% confirm the actual strength contribution of the BRB in the retrofitted structure as well as the relationship between interstory drift of the RC frame at the first and second floors.

A comparison between the experimental and numerical simulation results is presented in Fig. 9. The analysis indicates that the simulated axial force response of the BRB is higher than the experimental results, suggesting an overestimation of the BRB's strengthening contribution. However, the overall behavioral trends remain consistent. Additionally, the comparison of interstory drift results for the RC frame at the first and second floors shows close agreement between numerical simulations and experimental observations, demonstrating the reliability of the nonlinear numerical model.

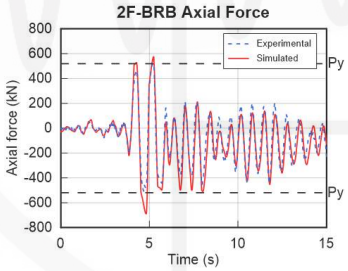

(a) BRB

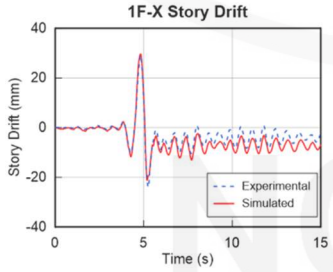

(b) Interstory drift of 1F

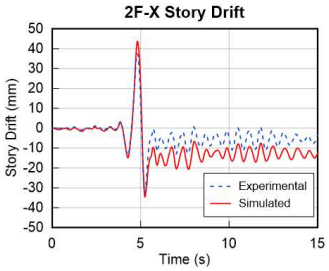

(c) Interstory drift of 2F

Fig. 9. Comparison of experimental and analytical results for the BRB and interstory drift of first and second floors (1F and 2F)

Conclusions

This study investigated the application of BRBs for the seismic retrofitting of buildings. Nonlinear dynamic analysis results indicate that BRBs effectively reduce interstory drift, demonstrating that the retrofitted structure meets seismic performance requirements. Furthermore, comparisons between hybrid experimental results and numerical simulations validate that the developed structural model accurately represents the actual structural behavior. The findings confirm that a structural model incorporating nonlinear hinges for reinforced concrete components, defined using the TEASDA auxiliary program, along with BRB nonlinear hinge properties specified in ASCE 41-17, can reliably simulate the nonlinear response of the structure.

References

Yang, Y.H., (2021). "Earthquake Response of RC Frames with High-strength Reinforcement." Master thesis, Department of civil engineering, National Taiwan University, 298 pp.

Hsiao, F.P., Tsai, R.J., Weng P.W., Shen W.C., Hsu, Y.C., Chow, T.K., Weng Y.T., Jean W.Y., Lin, C.C., Liu H.J., (2021), Taiwan Earthquake Assessment for RC Structures by Dynamic Analysis (TEASDA 1.0), National Center for Research on Earthquake Engineering Technical Report, NCREE-21-001.

Yang, H.H., (2015). "Seismic Design and Tests of a Full-scale 2-story RC Frame with Buckling Restrained Braces." Master thesis, Department of civil engineering, National Taiwan University, 202 pp.

ASCE (2017). "Seismic Evaluation and Retrofit of Existing Buildings (41-17)." American Society of Civil Engineers, ASCE/SEI 41-17, Reston, VA., 576 pp.

Liu, H.J., Lu, X.M., and Jean W.Y., (2022), Platform of Input Motion Selection for Taiwan (INMOST), 2021 NCREE Research Programs and Accomplishments, pp. 173-176.

Feasibility Study on Simulating the Hysteretic Behavior of High-Strength Reinforced-Concrete Bridge Columns Using Commercial Structural-Analysis Software

Fang-Yao Yeh[1] and Jhen-Wei Wu[2]

葉芳耀[1]、吳振維[2]

Abstract

This paper studies the feasibility of simulating the hysteretic behavior of high-strength reinforced-concrete (RC) bridge columns using commercial structural-analysis software. Both automatic and user-defined plastic hinges are used to model four types of plastic hinges: automatic plastic hinges, FEMA plastic hinges, code-suggested plastic hinges (Takeda hysteresis model), and code-suggested plastic hinges (Pivot hysteresis model). The hysteretic behavior of high-strength RC bridge columns under cyclic lateral loads is analyzed and compared with experimental results. The results show the following. (1) By using commercial structural-analysis software, setting appropriate backbone curves and selecting appropriate hysteresis models, the hysteretic behavior of high-strength RC bridge columns under cyclic lateral loads can be fully simulated. (2) A comparison of envelope curves for numerical and experimental results shows that each plastic hinge effectively captures the behavior from the elastic region to the reinforcement-yielding region. The stiffness degradation of the FEMA plastic hinge in the strain-hardening region is higher than in the experimental results. The automatic plastic hinge overestimates the maximum strength of the bridge column, whereas the other three plastic hinges slightly underestimate it. In the post-peak-strength region, the strength of the automatic plastic hinge decreases faster than the experimental results, while the strength of the other three types of plastic hinges decreases slightly slower. (3) A comparison of the analytical and the experimental results shows that the cumulative dissipated energy of the automatic plastic hinge is much higher than the experimental results, followed by the FEMA plastic hinge. The code-suggested plastic hinge (Takeda hysteresis model) dissipates less energy than the FEMA plastic hinge but still exceeds that of the experimental results. The cumulative dissipated energy of the code-suggested plastic hinge (Pivot hysteresis model) is closer to that of the experimental results.

Keywords: high-strength reinforced-concrete bridge columns, cyclic lateral loading tests, hysteretic behavior simulation

Introduction

Taiwan is located in a region that is frequently affected by natural disasters such as earthquakes and typhoons. Therefore, the use of high-strength materials for structural design and construction is a future trend. Innovative research and development of engineering technology for high-strength reinforced-concrete (RC) structural systems in Taiwan has achieved great results in building structures [1]. However, there has been relatively little research on the seismic performance of high-strength RC bridges, and research on the applicability of such bridges in earthquake-prone regions has practical value.

This study evaluates the feasibility of simulating the hysteretic behavior of high-strength RC bridge columns using commercial structural-analysis software. Both automatic and user-defined plastic hinges are used to configure the backbone curves and hysteresis models of plastic hinges. The simulated hysteretic behavior of the columns is analyzed and compared with experimental results to determine whether the software can accurately reproduce the energy dissipation behavior of bridge columns subjected to cyclic lateral loads.

[1] Research Fellow, Bridge Engineering Division, National Center for Research on Earthquake Engineering
[2] Assistant Researcher, Bridge Engineering Division, National Center for Research on Earthquake Engineering

Experiment on a High-Strength Reinforced-Concrete Bridge Column

The high-strength RC bridge column specimen, designated C550D36L, has a height of 450 cm, a cross-section of 135 × 90 cm, a nominal concrete design strength of 350 kgf/cm^2, 28 main reinforcement bars of SD550W-D36, SD420W-D16@14cm stirrups in the confining area, and SD420W-D16@18cm stirrups in the non-confining area. The design drawing is shown in Fig. 1.

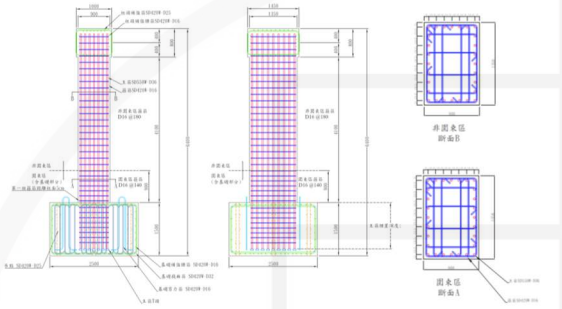

Fig. 1. Design drawing of the C550D36 column.

The cyclic lateral loading test of the bridge columns adopted displacement control with weak axis loading. The target displacement ratios were 0.25%, 0.375%, 0.5%, 0.75%, 1.0%, 1.5%, 2.0%, 3.0%, 4.0%, 5.0%, 6.0%, 7.0% and 8.0%. The experimental setup and results are shown in Fig. 2. During the experiment, flexural cracks appeared on the specimen at a displacement ratio of 0.25%, with a spacing of approximately 15 cm. When the displacement ratio was 2.0%, the protective layer in the plastic hinge zone began to spall. The maximum strength in the negative direction was 188 tf, which was observed at a displacement ratio of 4.0%, and the maximum strength in the positive direction was 180 tf, which was also observed at a displacement ratio of 4.0%. When the displacement ratio was 5.0%, the main reinforcement began to buckle. When the displacement ratio was 7.0% during the first cycle in the positive direction, all main bars buckled. When the displacement ratio was 7.0% during the second cycle in the negative direction, one main bar on the tensile side broke. When the displacement ratio was 8.0%, one of the main bars on the negative pressure side of the first cycle exhibited severe buckling.

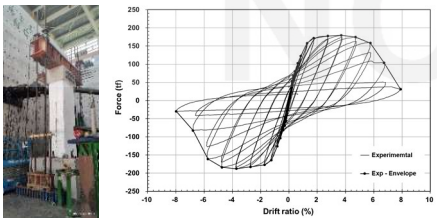

Fig. 2. Experimental setup and experimental results for the C550D36L bridge column.

Plastic Hinge Setting in Commercial Structural-Analysis Software

SAP2000, a commercial structural-analysis software [2], was used to simulate the hysteretic behavior of bridge columns under cyclic lateral loading. SAP2000 provides two options for defining plastic hinges: automatic and user-defined hinges. This study set four types of plastic hinges for comparison. The first type is the automatic hinge. For RC columns, the software uses Table 10-8 of ASCE 41-17 [3] to define the backbone curve. The relationship between the moment and the rotation of the column hinge is shown in Fig. 3. The isotropic hysteresis model is used by default for this type of hinge.

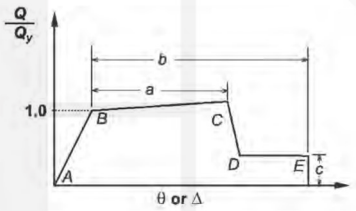

Fig. 3. Generalized moment–rotation relations for a concrete column.

The second type is the FEMA-recommended plastic hinge, which allows the user to define the backbone curve and select the hysteresis model. This configuration is based on Table 6-8 of FEMA 356 [4]. The relationship between the moment and the rotation in the column hinge is shown in Fig. 3, where $a = 0.002$, $b = 0.003$ and $c = 0.2$. The Takeda hysteresis model is selected for this type of hinge.

The third and fourth types of plastic hinges refer to the detailed evaluation of seismic capacity in Chapter 4 of the Code for Seismic Evaluation and Reinforcement Design of Highway Bridges [5], which establishes the relationship between the moment and the rotation of the backbone curve. The third type of plastic hinge uses the Takeda hysteresis model. Because the hysteretic behavior during the experiment produces a pinching effect, the Pivot hysteresis model is selected for the fourth plastic hinge. Based on the research results of Ling [6], the parameters α and β in the Pivot hysteresis model for flexural failure columns are defined by as follows:

$$\alpha = 0.15 \times \left(\frac{N}{A_g f_c'}\right)^{-2} \times \rho_l{}^{-3} \times \rho_t + 2.5 \leq 10 \quad (1)$$

$$\beta = 0.5 \times \left(\frac{N}{A_g f_c'}\right)^{0.65} \times \rho_l{}^{0.7} + 0.4 \leq 1 \quad (2)$$

Comparison of Simulation and Experimental Results for Hysteresis Behavior of a Bridge Column

The simulation results for an automatic plastic hinge are shown in Fig. 4. A comparison of the

envelope curves indicates that the automatic plastic hinge captures the behavior from the elastic region to the reinforcement-yielding region. Strain hardening is observed after the reinforcement yields, but the maximum strength of the bridge column is overestimated. In the post-peak-strength region, the simulated strength of the bridge column decreases more rapidly than the experimental value, although the maximum displacement in the simulation is close to the experimental results. A comparison of the hysteretic behavior indicates that the hysteresis loop of the automatic plastic hinge is relatively full. The unloading and reloading behavior diverges significantly from the experimental results, likely because of the characteristics of the isotropic hysteresis model.

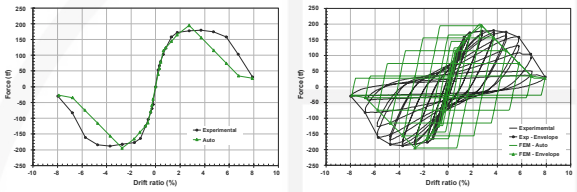

(a) Envelope (b) Hysteretic behavior

Fig. 4. Analysis results for the automatic plastic hinge.

The simulation results for the FEMA plastic hinge are shown in Fig. 5. A comparison of the envelope curves indicates that the FEMA plastic hinge captures the behavior from the elastic region to the reinforcement-yielding region. Strain hardening occurs after yielding, and stiffness degradation is greater than that observed experimentally. The maximum strength of the bridge column is slightly underestimated. In the post-peak-strength region, the simulated strength of the bridge column decreases slightly faster than the experimental value, while the maximum displacement is close to the experimental result. The hysteresis loop of the FEMA plastic hinge is slightly fuller than that observed in the experimental results. The unloading and reloading behavior shows a linear softening trend, which differs slightly from the experimental results. However, the use of the Takeda hysteresis model yields more accurate results than the isotropic hysteresis model.

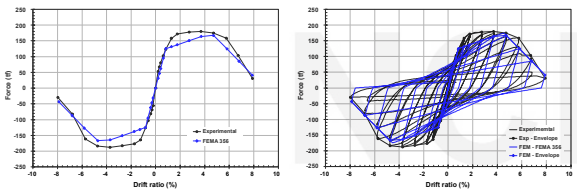

(a) Envelope (b) Hysteretic behavior

Fig. 5. Analysis results for the FEMA plastic hinge.

The simulation results for the code-suggested plastic hinge using the Takeda hysteresis model are shown in Fig. 6. A comparison of the envelope curves indicates that this model accurately captures the behavior in the elastic, reinforcement-yielding, and strain-hardening regions, although it slightly underestimates the maximum strength of the bridge column. In the post-peak-strength region, the simulated strength of the bridge column decreases slightly slower than the experimental value. The estimated residual strength is slightly higher than the experimental result, and the maximum displacement is consistent with the experiment. The hysteresis loop is slightly fuller than that in the experimental result. The unloading and reloading behavior displays a linear softening trend, which differs slightly from the experimental data. Although the model does not fully capture the pinching behavior, the Takeda hysteresis model provides more accurate results than the isotropic hysteresis model.

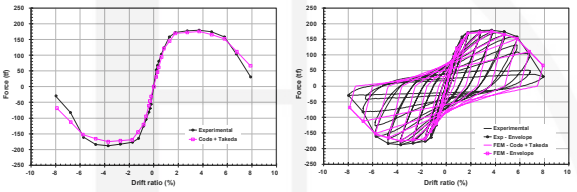

(a) Envelope (b) Hysteretic behavior

Fig. 6. Analysis results for the code-suggested plastic hinge (Takeda hysteresis model).

The simulation results for the code-suggested plastic hinge (Pivot hysteresis model) are shown in Fig. 7. A comparison of the envelope curves indicates that the code-suggested plastic hinge (Pivot hysteresis model) accurately captures the behavior in the elastic, reinforcement-yielding, and strain-hardening regions, but slightly underestimates the maximum strength of the bridge column. In the post-peak-strength region, the strength of the bridge column decreases slightly slower than the experimental value. The estimated residual strength is slightly higher than the experimental value and the simulated maximum displacement is close to the experimental result. A comparison of the hysteretic behavior indicates that the hysteresis loop of the code-suggested plastic hinge (Pivot hysteresis model) is only slightly fuller than the experimental result. The unloading behavior and the softening during reloading are well captured and the pinching behavior is better represented than for the code-suggested plastic hinge (Takeda hysteresis model).

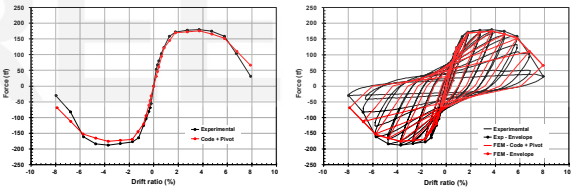

(a) Envelope (b) Hysteretic behavior

Fig. 7. Analysis results for the code-suggested plastic hinge (Pivot hysteresis model).

The configuration of plastic hinge characteristics includes the backbone curve and hysteresis model. The

backbone curve is used in nonlinear static analysis (nonlinear pushover analysis), while both the backbone curve and hysteresis model are used in nonlinear dynamic analysis (nonlinear time-history analysis) to evaluate the seismic capacity of the structure and to assess the hysteresis energy dissipation of the component after it enters the plastic range.

Figure 8 compares the envelope and cumulative dissipated energy for the four plastic hinge simulation results and experimental results. Figure 8(a) compares the envelopes; each plastic hinge captures the behavior from the elastic region to the reinforcement-yielding region. The stiffness degradation of the FEMA plastic hinge in the strain-hardening region is greater than that in the experimental results. The automatic plastic hinge overestimates the maximum strength of the bridge column, while the other three plastic hinges slightly underestimate it. In the post-peak-strength region, the strength of the automatic plastic hinge decreases faster than in the experimental results, whereas the strengths of the other three plastic hinges decreases slightly slower. The simulated maximum displacements for all plastic hinges are close to the experimental results. Figure 8(b) compares the cumulative dissipated energy; the cumulative dissipated energy of the automatic plastic hinge is much higher than the experimental result, followed by the FEMA plastic hinge. The code-suggested plastic hinge (Takeda hysteresis model) has a lower cumulative dissipated energy than the FEMA hinge but remains above the experimental result. The cumulative dissipated energy of the code-suggested plastic hinge (Pivot hysteresis model) is closest to the experimental results.

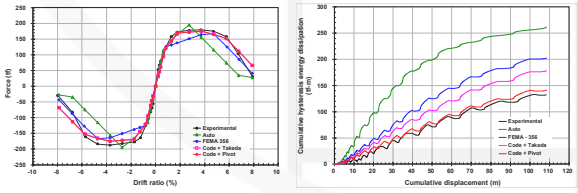

(a) Envelope (b) Cumulative dissipated energy

Fig. 8. Comparison of envelope and cumulative dissipated energy for each plastic hinge.

Conclusions

The hysteretic behavior of high-strength reinforced-concrete (RC) bridge columns under cyclic lateral loads was analyzed and compared with experimental results. The findings are as follows:

1. By using commercial structural-analysis software and setting appropriate backbone curves, and selecting appropriate hysteresis models, the hysteretic behavior of high-strength RC bridge columns under cyclic lateral loads can be accurately simulated.

2. A comparison of the envelope curves from the numerical and experimental results shows that each plastic hinge captures the behavior from the elastic region to the reinforcement-yielding region. The stiffness degradation of the FEMA plastic hinge in the strain-hardening region is higher than observed in the experimental results. The automatic plastic hinge overestimates the maximum strength of the bridge column, while the other three plastic hinges slightly underestimate the it. In the post-peak-strength region, the strength of the automatic plastic hinge decreases faster than in the experimental results, whereas the strength of the other three types of plastic hinges decreases slightly slower. The simulated maximum displacement of each plastic hinge closely matches the experimental values.

3. A comparison of cumulative dissipated energy indicates that the automatic plastic hinge exhibits significantly higher energy dissipation in the analytic results than in the experimental results, followed by the FEMA plastic hinge. The code-suggested plastic hinge (Takeda hysteresis model) dissipates less energy than the FEMA plastic hinge but still exceeds the experimental values. The cumulative dissipated energy of the code-suggested plastic hinge (Pivot hysteresis model) is closer to the experimental values.

References

1. CSSE, Design Manual of High Strength Reinforced Concrete Structures, Chinese Society of Structural Engineering, Taipei, 2022. (In Chinese)
2. CSI, SAP2000 Integrated Software for Structural Analysis and Design, Computers and Structures Inc., Berkeley, California, Version 26.1.0, 2024.
3. ASCE, Seismic Evaluation and Retrofit of Existing Buildings, American Society of Civil Engineers, ASCE/SEI 41-17, 2017.
4. FEMA, Prestandard and Commentary for Seismic Rehabilitation of Buildings, Federal Emergency Management Agency, FEMA-356, 2000.
5. MOTC, Code for Seismic Evaluation and Reinforcement Design of Highway Bridges, Ministry of Transportation and Communications, R.O.C., 2020.
6. Ling, Yu-Che, A study on Hysteresis Modeling of Reinforced Concrete Columns, Master Thesis, Department of Civil Engineering, National Taiwan University, 2019. (In Chinese)

Verification Tests for Design Specifications of Ultra-High-Performance Concrete in Bridge Engineering

Yu-Chen Ou[1], Chen-Chung Chen[2], Jhen-Wei Wu[3], and Chi-Lon Jang[4]

歐昱辰[1]、陳俊仲[2]、吳振維[3]、江奇融[4]

Abstract

Ultra-high-performance concrete (UHPC) is a new construction material that has attracted considerable attention. Its compressive strength exceeds four times that of conventional concrete, allowing it to perform exceptionally under heavy structural loads. Moreover, UHPC offers excellent tensile strength, exceeding 5 MPa. When reinforced with steel fibers, it undergoes tensile strain-hardening, and its strength exceeds 8 MPa (about four times that of conventional concrete), maintaining performance up to a strain of 2.5×10^{-3}. For this reason, it maintains structural stability under external tensile forces. Additionally, UHPC has outstanding durability because of its dense microstructure, giving it high resistance to wear, corrosion, and impact.

In bridge engineering, UHPC is emerging as an essential material in Taiwan. Given its superior strength and durability, it is widely used in bridge construction, repair, and reinforcement. As a material for bridge joints and structural elements, its high strength and lightweight nature help reduce the size and weight of components, thereby improving bridge safety and service life. Moreover, the excellent corrosion resistance and bonding properties of UHPC make it ideal for repairing damaged sections, effectively extending the lifespan of bridges. Furthermore, it is used in precast bridge components to boost production efficiency and quality while accelerating construction speed and reducing costs.

Keywords: Ultra-high-performance concrete, Tensile strength, Durability, Bridge engineering

Introduction

This project aims to localize the design proportions of ultra-high-performance concrete (UHPC) mixes for bridge engineering applications in Taiwan. Based on previous research, a suitable UHPC mix proportion is selected and applied to the planned development items, namely a UHPC U-shaped prestressed beam specimen and a UHPC bridge deck joint specimen. These tests will be conducted at NCREE's Taipei Laboratory.

UHPC U-shaped Prestressed Beam

A scaled-down U-shaped prestressed beam specimen was planned, as illustrated in Fig. 1. For the deck portion, conventional concrete (compressive strength of 35 MPa) was used, while for the U-beam region, UHPC (compressive strength exceeding 120 MPa) was used. This allowed the beam to be designed as a fully prestressed section by using post-tensioning methods. UHPC procured from the Ruentex Group was used. The specimen was cast in segments (4–6) at the Ruentex Yangmei precast plant, cured, and then transported to NCREE's Taipei Laboratory for assembly. The beam span was approximately 25 m, and the beam width was approximately 4 m. The inclusion of steel fibers in UHPC greatly enhances its tensile strength and facilitates tensile strain-hardening behavior. According to international literature, this can replace some of the shear reinforcement, which was considered in the beam web's stirrup design.

[1] Director, National Center for Research on Earthquake Engineering and Distinguished Professor, Department of Civil Engineering, National Taiwan University.

[2] Division Head and Research Fellow, Bridge Engineering Division, National Center for Research on Earthquake Engineering.

[3] Assistant Researcher, Bridge Engineering Division, National Center for Research on Earthquake Engineering.

[4] Associate Technician, Bridge Engineering Division, National Center for Research on Earthquake Engineering.

Fig.1. Planned UHPC U-shaped prestressed beam specimen (image from Dura Company, Malaysia).

Testing will be performed on the strong floor area in NCREE's Taipei Laboratory. A portal steel frame setup will be used for simply supported, unidirectional loading, as illustrated in Fig. 2. The test will be displacement-controlled, and it will be continued until flexural failure or until the equipment's limits are reached.

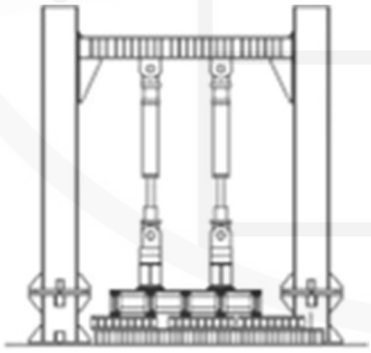

Fig. 2. Loading setup diagram for the prestressed beam specimen.

UHPC Bridge Deck Joint

According to the literature, UHPC can be used in the closure regions between precast deck panels, as illustrated in Fig. 3. It is cast on-site over non-contact lap splices to ensure structural continuity.

Fig. 3. Closure region between precast bridge deck panels.

This study includes a bridge deck joint specimen, as illustrated in Fig. 4. The precast panels use conventional concrete (35 MPa), while the closure (joint) uses UHPC. The design references FEMA's "Design and Construction of Field-Cast UHPC Connections" (2014) and other literature, adopting a shear key geometry. The non-contact lap splice lengths are designed by following local bridge design codes, FEMA 2014, and the related international literature.

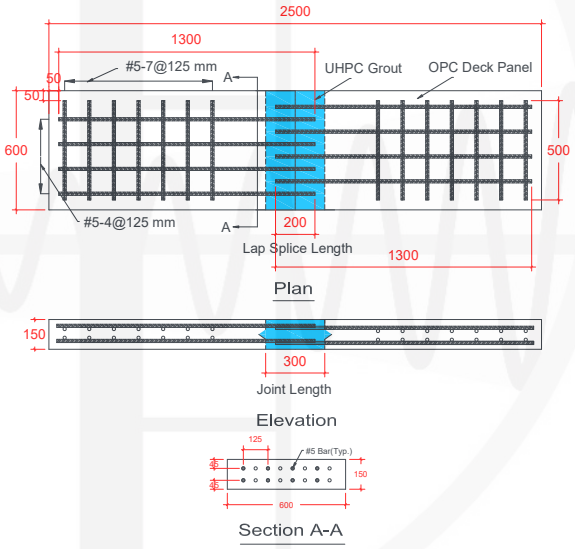

Fig. 4. Preliminary design of bridge deck joint specimen.

The testing configuration is similar to that of the prestressed beam, where a portal steel frame is used for simply supported, unidirectional loading, as depicted in Fig. 5. This test, too, will be conducted at NCREE's Taipei Laboratory.

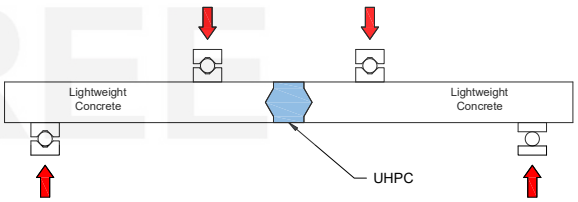

Fig. 5. Preliminary test configuration of bridge deck joint specimen.

Conclusion and Outlook

UHPC, a novel concrete material, holds great potential for use in Taiwan's construction industry. Its superior mechanical and durability properties provide more reliable and long-lasting solutions for engineering projects, thereby promoting advancement and innovation in the field.

Reference

1. AASHTO. AASHTO LRFD Bridge Design Specifications, 9th Edition. American Association of State Highway and Transportation Officials, Washington, DC, 2020.
2. AASHTO, Standard Method of Test for Uniaxial Tensile Response of Ultra-High Performance Concrete, T 397. American Association of State Highway and Transportation Officials, Washington, DC, 2024.
3. Deng, E.-F., Zhang, Z., Zhang, C.-X., Tang, Y., Wang, W., Du, Z.-J., & Gao, J.-P. (2023). Experimental study on flexural behavior of UHPC wet joint in prefabricated multi-girder bridge. Engineering Structures, 275, 115314.
4. Federal Highway Administration. (2014). Design and construction of field-cast UHPC connections (FHWA-HRT-14-084). U.S. Department of Transportation.
5. Federal Highway Administration. (2019). Design and construction of field-cast UHPC connections (FHWA-HRT-19-011). U.S. Department of Transportation.
6. Haber, Z. B., & Graybeal, B. A. (2018). Performance of grouted connections for prefabricated bridge deck elements (FHWA-HIF-19-003). Federal Highway Administration.
7. Haber, Z. B., & Graybeal, B. A. (2018). Lap-spliced rebar connections with UHPC closures. Journal of Bridge Engineering, 23(6), 04018028. https://doi.org/10.1061/(ASCE)BE.1943-5592.0001239
8. Hiew, S. Y., Teoh, K. B., Raman, S. N., Hung, C. C., Chaen, Y. X., Kong, D., & Hafezolghorani, M. (2024). A unified tensile constitutive model for mono/hybrid fibre-reinforced ultra-high performance concrete (UHPC). Engineering Structures, 292, 117002.
9. Jia, J., Ren, Z., Bai, Y., Li, J., Li, B., Sun, Y., Zhang, Z., & Zhang, J. (2023). Tensile behavior of UHPC wet joints for precast bridge deck panels. Engineering Structures, 282, 115826.
10. Jiang, H., Tu, W., Li, M., Liang, W., & Gao, X. (2024). Flexural performance of UHPC-filled narrow joints between precast concrete bridge slabs. Case Studies in Construction Materials, 20, e03108.
11. PCI. Guidelines for the Use of Ultra-High-Performance Concrete (UHPC) in Precast and Prestressed Concrete PC! Concrete Materials Technology Committee, TR-9-22. Precast/Prestressed Concrete Institute, Chicago, IL, 2022.
12. Yuan, J., & Graybeal, B. (2015). Bond of reinforcement in ultra-high-performance concrete. ACI Structural Journal, 112(6), 851–862.

NCREE

Outdoor Temperature Compensation Experiment of a FBG-Based Settlement Sensor

Zheng-Kuan Lee[1] and Hsiao-Hui Hung[2]

李政寬[1]、洪曉慧[2]

Abstract

This study investigates the effectiveness of temperature compensation of a fiber-Bragg-grating (FBG)–based differential settlement sensor through an outdoor experiment. The compensation method involves using the wavelength response of adjacent stress-free FBGs, positioned near the grating attached to the core block of the settlement sensor, so as to correct for temperature effects. The experiment is conducted on the parapet wall of a building roof. The designed sensor is exposed to direct sunlight during daytime and cooled naturally at nighttime for more than twenty days. The wavelength responses of the FBGs are analyzed to verify the effectiveness of the temperature compensation method.

Keywords: temperature compensation, bridge safety monitoring, settlement sensor, fiber Bragg grating.

Introduction

The fiber-Bragg-grating (FBG)–based differential settlement measurement sensor (FBG-DSM) is used to measure the differential settlement of civil structures. In Taiwan, this sensor was first developed by the National Center for Research on Earthquake Engineering (NCREE) for monitoring on-site bridge leveling changes. Since 2015, the sensor has been systematically improved for quick *in situ* installation. It has been applied to improvement projects for railway-track embankments and viaducts. Figures 1 and 2 show some of these project cases. Previous application cases assumed that temperature effects on these sensors in the field were consistent and that the resulting errors were negligible. Therefore, no compensation mechanism was included in the sensors. However, many studies have indicated that temperature effects on sensors must be addressed carefully to avoid misreadings. Therefore, this study investigates temperature compensation (TC) for the FBG-based differential settlement sensor and performs outdoor experimental tests for verification.

Fig. 1. Real-time monitoring of a track-embankment improvement project in Miaoli, Taiwan.

Fig. 2. Real-time monitoring of a viaduct foundation-reinforcement project in Yunlin, Taiwan.

[1] Associate Researcher, National Center for Research on Earthquake Engineering
[2] Research Fellow, National Center for Research on Earthquake Engineering

Temperature Compensation Method for FBG-DSM

Materials expand when heated and contract when cooled, so instruments are affected to varying degrees by temperature. However, whether it is necessary to design an instrument with a TC function depends on the acceptable error tolerance. The significance of temperature-induced measurement errors varies with the structure type, its function, and the surrounding environment. For example, the measurement accuracy requirements for highway bridges are relatively lower, and, thus, temperature effects may be disregarded. In contrast, the requirements for high-speed railways and oil tanks demand higher precision, necessitating careful consideration of temperature effects. For general purposes, a sensor with TC is preferable to one without, regardless of cost. However, the TC function must be experimentally validated before field application.

Figure 3 shows the internal structure of the instrument with a TC function used in this study. Assuming that the water level remains unchanged or the tension of the grating λB1S is constant, then the following equations should hold under temperature changes, indicating the validity of TC:

$$\Delta\lambda B1S \fallingdotseq \Delta\lambda B1T \text{ and} \quad (1)$$

$$(\Delta\lambda B1S - \Delta\lambda B1T) \,/\, \Delta\lambda B1S << 1. \quad (2)$$

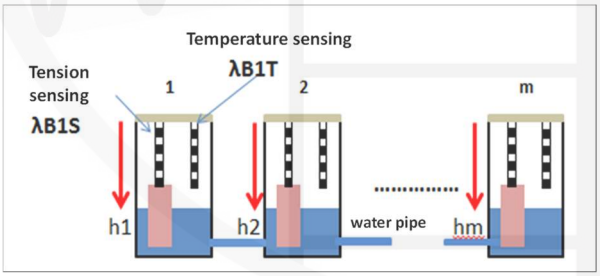

Fig. 3. FBG-DSM array and internal structure.

Temperature-Compensation Experiment

As shown in Figures 4(a)–(c), a total of eight FBGs were used to test TC. The #8 FBG was suspended with a cylindrical hanging object, and its tension is constant. FBGs #1 through #7 were stress-free with zero tension. After installing the instrument as shown in Figure 4, an acrylic container was covered with a steel box for protection, as is done in field applications.

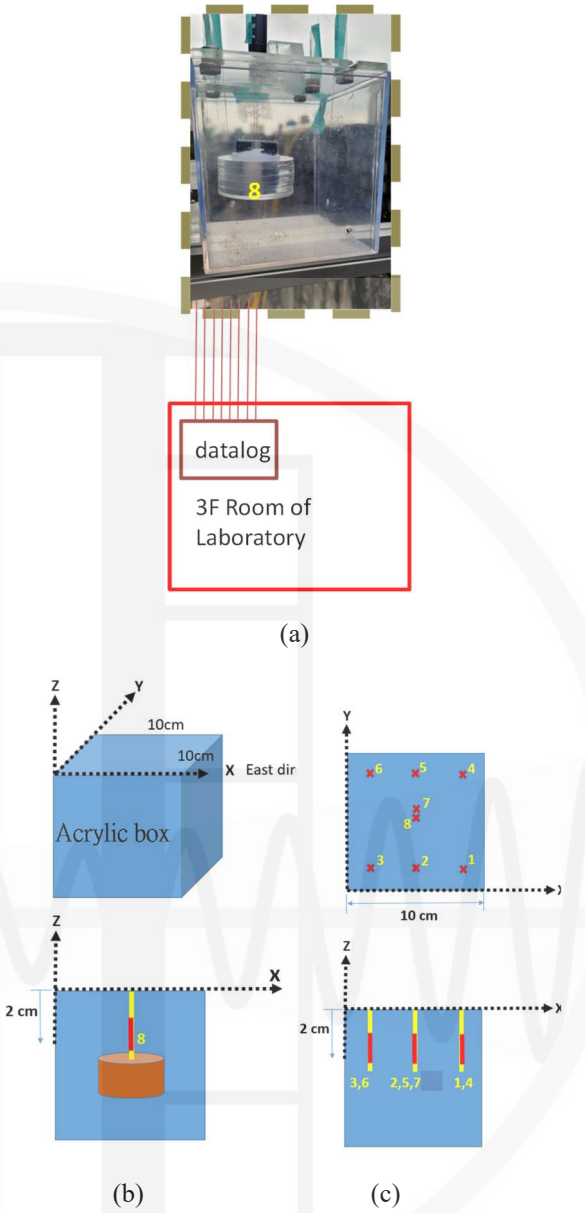

Fig. 4. (a) Steel box covering the instrument on the 4th-floor roof, with the datalogger located in a room on the 3rd floor. (b) The container dimensions. (c) Positions of all the FBGs.

The nominal wavelengths of the eight commercial FBGs were all 1557 nm ± 0.25 nm, each independently connected to the datalogger. Figure 5 shows the variation of the wavelengths. A visual comparison of the signals in Figures 5(a) and (b) reveals that they are quite similar. To examine the differences between the signals in more detail and determine which of FBGs #1 through #7 best reflects the temperature variation affecting #8, a correlation analysis is conducted in the next section.

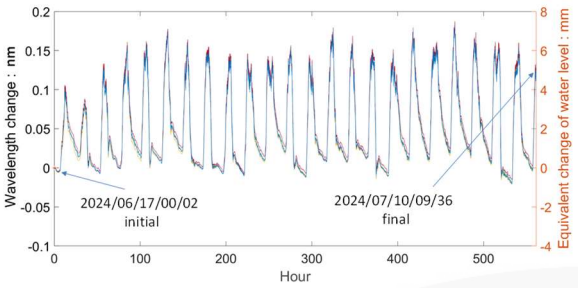

Fig. 5(a) Wavelength signals of the eight FBGs.

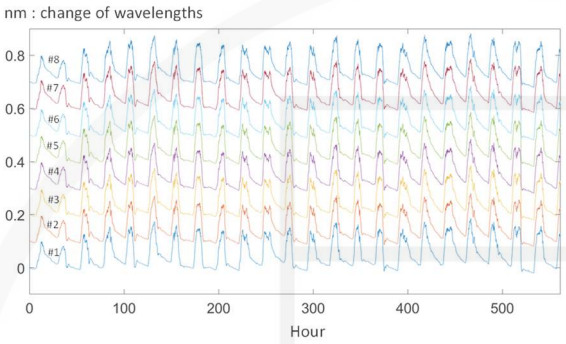

Fig. 5(b) Wavelength signals of the eight FBGs.

Correlation Analysis

The collected signals were grouped into pairs. Table 1 presents the matrix table with 28 pairs. Figure 6 shows the scatter plot of #4 and #5 for regression analysis and Figure 7 shows the scatterplot of #7 and #8. After regression analysis, Tables 2 and 3 list the correlation coefficients and the sum of squared errors (SSE), respectively.

Table 2 indicates that each of the 28 pairs has a high correlation coefficient. For any pair among #1–#6, the correlation coefficient exceeds 0.999. For #8, the correlation coefficient when paired with #7 is higher than with any of #1–#6, indicating that #7 is more suitable for TC of #8, likely because #7 is spatially closest to #8. Additionally, the SSEs for the 28 pairs are shown in Table 3. The SSE for #8 paired with #7 is the smallest. The correlation coefficients in Table 2 and the SSEs in Table 3 are plotted in Figure 8, which shows a nearly linear relationship.

Table 4 lists the regression coefficients (slopes) for the 28 datasets. The slopes are close to, but not exactly, 1. For example, in the pair of #1 and #4, the slope is 0.9588, indicating a 4.12% difference in thermal sensitivity between them. Therefore, before packaging the sensors, it is advisable to mechanically and thermally test the FBGs.

Table 1. The 28 pairs of grouped signals.

	1	2	3	4	5	6	7	8
1		1	2	3	4	5	6	7
2			8	9	10	11	12	13
3				14	15	16	17	18
4					19	20	21	22
5						23	24	25
6							26	27
7								28
8								

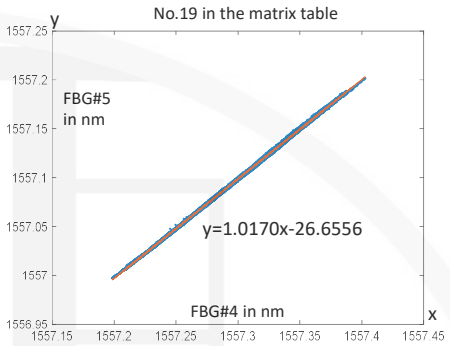

Fig. 6. Scatter plot of #4 and #5.

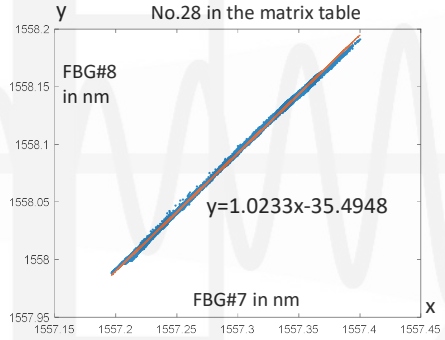

Fig. 7. Scatter plot of #7 and #8.

Table 2. Correlation coefficients for each pair.

	1	2	3	4	5	6	7	8
1		0.9995	0.9995	0.9994	0.9996	0.9997	0.9987	0.9984
2			0.9993	0.9993	0.9995	0.9993	0.9993	0.9990
3				0.9990	0.9993	0.9994	0.9983	0.9978
4					0.9998	0.9996	0.9991	0.9990
5						0.9998	0.9993	0.9991
6							0.9988	0.9985
7								0.9997
8								

0.999

0.999

Table 3. Sum of squared errors for each pair.

	1	2	3	4	5	6	7	8
1		0.0889	0.0868	0.0982	0.0641	0.0470	0.2123	0.2807
2			0.1278	0.1142	0.0796	0.1223	0.1213	0.1775
3				0.1581	0.1103	0.1017	0.2801	0.3830
4					0.0318	0.0734	0.1525	0.1775
5						0.0399	0.1116	0.1593
6							0.1968	0.2586
7								0.0603
8								

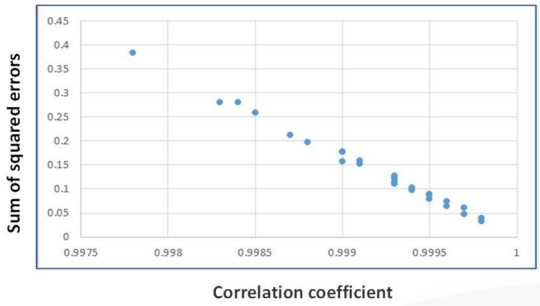

Fig. 8. Scatter plot of SSEs versus correlation coefficients.

Table 4. The regression coefficients (slope) for the 28 datasets.

	1-y	2-y	3-y	4-y	5-y	6-y	7-y	8-y
1-x		0.9619	0.9932	0.9588	0.9755	0.9692	0.9720	0.9946
2-x			1.0317	0.9962	1.0135	1.0066	1.0105	1.0341
3-x				0.9646	0.9815	0.9751	0.9778	1.0004
4-x					1.0170	1.0100	1.0135	1.0374
5-x						0.9932	0.9966	1.0199
6-x							1.0027	1.0261
7-x								1.0233
8-x								

Temperature Compensation Effectiveness

In Figure 4(a), the #8 grating is suspended with a cylindrical acrylic block with a radius of 25 mm and weighing approximately 24 g. Using the sensitivity equation from Consales *et al*. (2018):

$$\Delta\lambda B / \Delta h \approx 0.0434 r^2 \quad \text{pm/mm} \qquad (1)$$

the apparent water level error in the experiment can be calculated by:

$$[W\#8 - W\#7 - (W\#8_{ini} - W\#7_{ini})]/0.0434 r^2 \quad \text{pm/mm} \quad (2)$$

where W is the wavelength in picometers, 'ini' indicates the initial value, and r represents the radius in mm of the cylinder. The apparent water level error is shown in Figure 9.

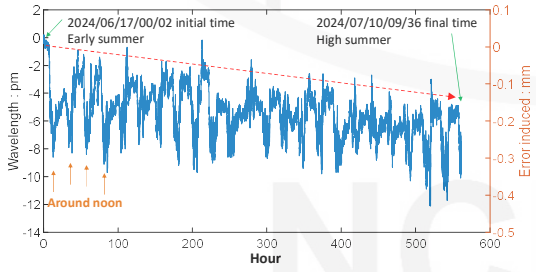

Fig. 9. Wavelength difference (#8 − #7) and its apparent water level error.

From the above study, the following observations were made. (1) The oscillation amplitude in Figure 9 is much smaller than that in Figure 5(a). (2) Temperature compensation is effective but does not completely eliminate temperature-induced errors. (3) The red slope in Figure 9 might be caused by seasonal effects through the heat conduction mechanism between #8 and the cylindrical acrylic block. (4) Based on the scale of the vertical axis on the right side of Figure 9, the effectiveness of TC is sufficient for general applications.

Reference

Marco Consales, Sofia Principe, Antonio Iele, Marco Leone, Haitham Zaraket, Ihab Jomaa, Antonello Cutolo, and Andrea Cusano (2018). "A Fiber Bragg Grating Liquid Level Sensor Based on the Archimedes' Law of Buoyancy," J. Lightwave Technol. 36, 4936–4941.

Acknowledgements

The authors would like to express their thanks to the Ministry of Transportation and Communications, Taiwan, for providing project funding for this study. They also thank Professor Yiching Lin, National Chung Hsing University, Taiwan, for his guidance regarding the temperature effects on concrete structures and sensors.

Correlation Analysis of Monitoring Data from an Extradosed Bridge

Hsiao-Hui Hung[1], Zheng-Kuan Lee[2], Chia-Chuan Hsu[2], and Kuang-Wu Chou[2]

洪曉慧[1]、李政寬[2]、許家銓[2]、周光武[2]

Abstract

Extradosed bridges combine the structural characteristics of cable-stayed and box-girder bridges, showcasing an innovative design that incorporates pylons, cables, and girders. To ensure their structural safety and provide a scientific foundation for management and maintenance, structural health monitoring systems have been widely implemented in cable-equipped extradosed bridges throughout Taiwan. This study examines the real-time structural health monitoring system of an extradosed bridge, utilizing long-term monitoring data to analyze correlations among various measured variables, specifically focusing on the effects of environmental temperature. The study examines the relationship between environmental temperature and cable vibration frequencies, girder frequencies, and the relative displacement of expansion joints based on calculated correlation coefficients.

Keywords: extradosed bridge, cable frequency, environmental temperature, correlation coefficient

Introduction

To mitigate the risk of unexpected and sudden failures of bridges, many bridges worldwide, especially those with rare and unique structural designs, have been equipped with long-term structural health monitoring systems in recent years [1]. Extradosed bridges, which use a distinct type of long-span prestressed system, commonly known as low-pylon cable-stayed bridges, consist primarily of pylons, prestressed girders, and external cables. These bridges exhibit significant differences in structural behavior compared to traditional prestressed box-girder bridges. Consequently, health monitoring systems have been installed in most newly constructed extradosed bridges in Taiwan to ensure their structural integrity. This study examines the health monitoring system of an extradosed bridge characterized by an asymmetrical span configuration. Utilizing four years of monitoring data, the study investigates the correlations among various measured variables, including cable frequency, girder frequency, expansion joint displacement, and environmental temperature at different locations.

Bridge structural health monitoring data are inherently influenced by a range of environmental and operational factors, such as traffic loads, wind forces, humidity, solar radiation, and ambient temperature. These external influences may introduce fluctuations in the measured data, potentially obscuring abnormal variations resulting from structural damage. To ensure the reliability of damage detection and early warning mechanisms, it is crucial to accurately distinguish between anomalies caused by structural damage and fluctuations stemming from environmental change. Such differentiation reduces the likelihood of false positive alarms triggered by typical variations and false negative results overlook damage-induced abnormalities, thereby enhancing the precision of structural health monitoring systems [2]. Based on this premise, this study investigates the monitoring data from an extradosed bridge to establish correlations between monitoring parameters and environmental temperature. Understanding these relationships provides valuable insights for formulating scientifically informed strategies for the seasonal maintenance of the bridge.

Bridge Description and its Monitoring System

The extradosed bridge examined in this study, depicted in Fig. 1, is an asymmetric single-pylon structure with a total length of 160 m, comprising spans of 70 m and 90 m. Its cable system includes a

[1] Research Fellow, National Center for Research on Earthquake Engineering
[2] Associate Researcher, National Center for Research on Earthquake Engineering

single row of six 43T-15.2 mm diameter cable bundles (CL1-CL6) on the shorter span and two rows of fourteen 27T-15.2 mm diameter cable bundles (CR1-CR14) on the longer span, totaling 20 cables. The superstructure consists of a prestressed concrete three-cell box girder, while the substructure is composed of rectangular reinforced concrete columns approximately 14 m in height. The supports at bridge piers P72 and P74 are pot bearings that permit unrestricted movement in the longitudinal direction, whereas the central pylon uses rigid connections.

Fig. 2 illustrates the instrumentation layout of the bridge, which incorporates a variety of sensing devices. The configuration includes 10 liquid level sensing systems, 20 cable accelerometers, 6 girder accelerometers, 2 expansion joint displacement sensors, and 6 thermometers. These instruments are employed to comprehensively monitor the structural performance of the bridge and assess the impact of environmental factors.

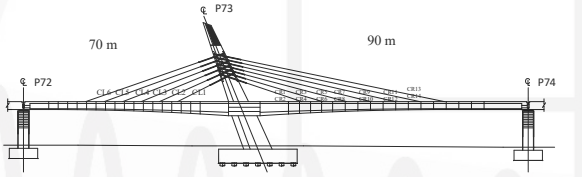

Fig. 1. Target bridge.

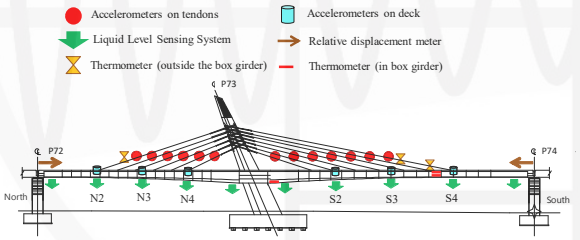

Fig. 2. Sensor locations.

Correlation Analysis of Monitoring Data

In previous monitoring projects, four years of monitoring data were accumulated for this bridge. Parameters included cable vibration frequency, girder frequency, deck deflection, relative displacement of expansion joints, and environmental temperature at various locations. By performing correlation analysis on these data, relationships among the variables can be identified. This study utilizes the Pearson correlation coefficient to quantitatively assess the correlations between different monitoring variables. The Pearson correlation coefficient is defined as the ratio of the covariance between two variables to the product of their standard deviations. This method is used to measure the linear relationship between two variables, and is calculated using the formula in Eq. (1),

$$R = \frac{\sum_{i=1}^{n}(X_i-\bar{X})(Y_i-\bar{Y})}{\sqrt{\sum_{i=0}^{n}(X_i-\bar{X})^2}\sqrt{\sum_{i=0}^{n}(Y_i-\bar{Y})^2}} \quad (1)$$

where $\bar{X}$ and $\bar{Y}$ represent the mean values of the variables X_i and Y_i, respectively, and n denotes the number of data points. The correlation coefficient R ranges from −1 to 1. A larger absolute value of R indicates a stronger covariation between the two variables, whereas a smaller absolute value suggests a weaker correlation. Generally, values within the range $0.7 < R < 1$ denote a strong positive linear correlation between the datasets, whereas those in the range $-1 < R < -0.7$ indicate a strong negative linear correlation.

By conducting correlation analyses on different sets of monitoring data, it is possible to effectively differentiate between abnormal data caused by structural damage and normal variations due to environmental fluctuations. This distinction provides critical insights for the preventative maintenance of bridges. This study primarily investigates the impact of environmental temperature on monitoring data. To clarify the distinct effects of seasonal temperature variations and day–night temperature fluctuations on monitoring variables, both long-term daily monitoring data collected over four years and short-term monitoring data capturing daily and nightly variations were analyzed. Using the temperature of the CR13 cable (designated as Temp-S1) and the main frequency of the CR11 cable (designated as CR11) as examples, Fig. 3 presents four years of monitoring records. To minimize the effect of day–night temperature fluctuations, the data were averaged across 48 time points per day, condensing them into a single data point per day. Fig. 4 illustrates one week's monitoring data, recorded at 30-minute intervals from July 1 to July 7, 2024.

In Fig. 3, the red curve represents the 30-day moving average, showing a clear trend in temperature changes across the seasons. The highest temperature, approximately 35°C, is observed in early August, whereas the lowest temperature, approximately 17°C, is recorded during winter in February. Additionally, the main frequency of the CR11 cable exhibits a notable seasonal pattern, exhibiting significantly higher levels in summer and lower levels in winter. Fig. 4 highlights the effects of day–night temperature variations, with the dashed line marking 12:00 AM each day. The temperature of the CR13 cable begins to decline daily at around 6:00 PM, reaching its lowest point around 5:00 AM the following morning, after which a rapid increase occurs. Concurrently, the main frequency of the CR11 cable peaks between midnight and 5:00 AM, coinciding with the cable's lowest temperature, and subsequently decreases during midday when the temperature is higher. Notably, the trend of day–night temperature variation contrasts with that of the seasonal temperature variation depicted in Fig. 3.

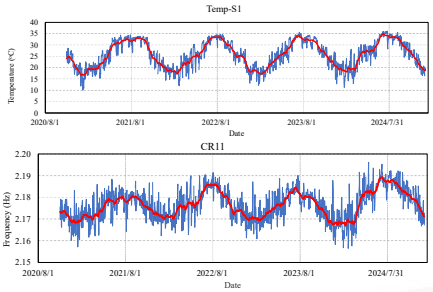

Fig. 3. Long-term monitoring data spanning four years (one data point per day)

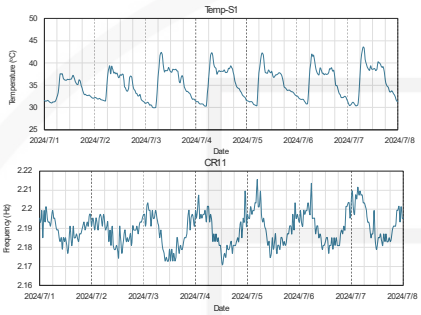

Fig. 4 Short-term monitoring data for one week (from July 1, 2024 to July 7, 2024, one data point every 30 min).

Correlation Analysis Results

This study analyzes the correlations between monitoring variables using long-term monitoring data collected over four years and short-term data from a single week, as outlined in the previous section. The scope of the analysis includes cable frequency, main girder frequency, relative displacement at expansion joints, and environmental temperature measured at various locations. The correlations between these variables have been calculated, and this section provides an excerpt of the results.

Tables 1 and 2 summarize the correlation coefficients between cable frequencies and both seasonal and day–night temperature variations, respectively. Strong correlations are highlighted in red within these tables. Temp-S1 and Temp-S2 represent the environmental temperature collected at the CR13 cable and the deck of the long span. Temp-S3, Temp-S4, and Temp-S5 correspond to the temperatures measured at the pylon surface, the web surface, and above the lower flange within the middle cell of the box girder. The results presented in Table 1 indicate a strong positive correlation between cable frequency and the internal temperature of the box girder (particularly Temp-S4) under the influence of seasonal temperature variations. Conversely, Table 2 reveals a significant negative correlation between cable frequency and the external temperature of the box girder (especially the deck temperature, Temp-S2) as affected by day–night temperature variations. These findings align with the observations presented in Figs. 3 and 4. Furthermore, the scatter plots shown in Figs. 5 and 6 clearly validate the trends described above.

Table 1 Correlation coefficient between cable frequency and long-term environmental temperature.

	CR5	CR6	CR7	CR8	CR9	CR10	CR11	CR12	CR13	CR14
Temp-S1	0.351	0.467	0.417	0.376	0.441	0.392	0.585	0.517	0.561	0.537
Temp-S2	0.316	0.413	0.346	0.311	0.380	0.323	0.583	0.442	0.445	0.456
Temp-S3	0.552	0.652	0.619	0.598	0.647	0.609	0.753	0.697	0.699	0.716
Temp-S4	0.622	0.723	0.676	0.656	0.701	0.664	0.793	0.741	0.764	0.767
Temp-S5	0.568	0.667	0.618	0.595	0.645	0.603	0.763	0.693	0.714	0.718

Table 2 Correlation coefficient between cable frequency and short-term environmental temperature

	CR5	CR6	CR7	CR8	CR9	CR10	CR11	CR12	CR13	CR14
Temp-S1	-0.668	-0.683	-0.722	-0.649	-0.652	-0.598	-0.589	-0.586	-0.497	-0.609
Temp-S2	-0.759	-0.855	-0.825	-0.818	-0.821	-0.838	-0.760	-0.850	-0.804	-0.874
Temp-S3	0.109	0.093	0.121	0.077	0.088	0.059	0.174	0.059	0.119	0.053
Temp-S4	0.261	0.270	0.291	0.256	0.257	0.240	0.333	0.241	0.314	0.240
Temp-S5	0.176	0.130	0.189	0.111	0.146	0.079	0.209	0.069	0.092	0.083

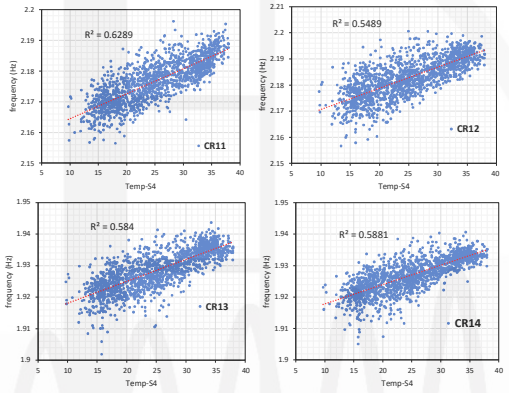

Fig. 5 Scatter plot of cable frequency versus long-term temperature change.

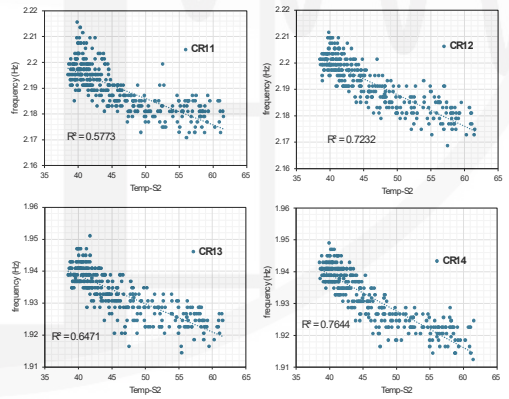

Fig. 6 Scatter plot of cable frequency versus short-term temperature change.

Tables 3 and 4 respectively display the correlation coefficients between the main girder frequency and both long-term environmental temperature and short-term temperature variations. S1 to S3 represent the fundamental frequencies of the main girder measured at various locations. The data in the tables reveals a significant negative correlation between the main girder frequency and long-term seasonal temperature variations, indicating that the main girder frequency decreases markedly with temperature. Conversely, the correlation between the main girder frequency and short-term day–night temperature variations is relatively weak, with R

values consistently below 0.2. Similar patterns are evident in the scatter plots shown in Figs. 7 and 8, where the horizontal axis represents temperatures measured at the web surface inside the box girder.

Table 3 Correlation coefficient between girder frequency and long-term environmental temperature.

	Temp-S1	Temp-S2	Temp-S3	Temp-S4	Temp-S5
ACC-S1	-0.862	-0.803	-0.753	-0.843	-0.845
ACC-S2	-0.863	-0.804	-0.754	-0.843	-0.845
ACC-S3	-0.861	-0.802	-0.750	-0.840	-0.842

Table 4 Correlation coefficient between girder frequency and short-term environmental temperature

	Temp-S1	Temp-S2	Temp-S3	Temp-S4	Temp-S5
ACC-S1	-0.152	-0.097	0.090	0.108	0.100
ACC-S2	-0.119	-0.068	0.131	0.145	0.128
ACC-S3	-0.129	-0.064	0.129	0.137	0.141

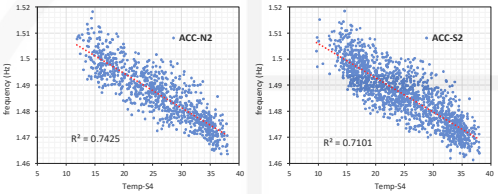

Fig. 7 Scatter plot of girder frequency versus long-term temperature change.

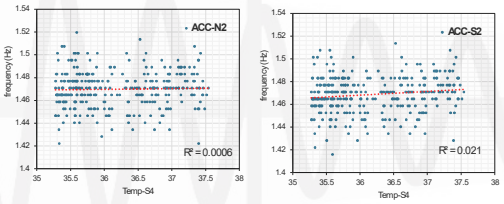

Fig. 8 Scatter plot of girder frequency versus short-term temperature change.

Table 5 Correlation coefficients between expansion joint displacement and long-term temperature.

	Temp-S1	Temp-S2	Temp-S3	Temp-S4	Temp-S5
DISP-N	-0.84926	-0.76746	-0.83673	-0.86564	-0.86746
DISP-S	-0.88855	-0.89336	-0.85386	-0.90442	-0.90795

Table 6 Correlation coefficients between expansion joint displacement and short-term temperature.

	Temp-S1	Temp-S2	Temp-S3	Temp-S4	Temp-S5
DISP-N	-0.30297	-0.67404	-0.69245	-0.52097	-0.77589
DISP-S	-0.00533	-0.38355	-0.75925	-0.62796	-0.89815

Tables 5 and 6 summarize the correlation coefficients between expansion joint displacement and both long-term and short-term environmental temperature variations. DISP-N and DISP-S denote the expansion joint displacement on the short-span and long-span, respectively. The data in Table 5 reveal a significant negative correlation between expansion joint displacement and environmental temperature under the influence of seasonal temperature variations, indicating that during summer, as temperatures rise, the thermal expansion of the main girder reduces the expansion joint gap. Table 6, which focuses on the effects of day–night temperature fluctuations, indicate a similar trend. However, the correlation associated with day–night temperature variations is relatively weak, likely due to the time lag in thermal expansion and contraction responses in prestressed concrete beams, as well as the smaller amplitude of day–night temperature fluctuations compared with those of seasonal temperature changes. These observations are further validated by the scatter plots presented in Figs. 9 and 10.

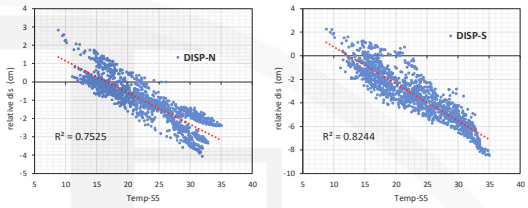

Fig. 9 Scatter plot of expansion joint displacement and long-term temperature.

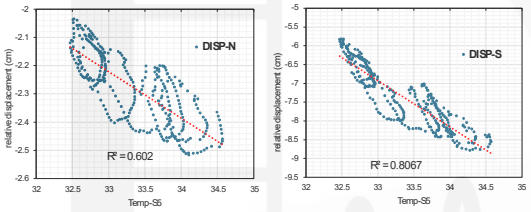

Fig. 10 Scatter plot of expansion joint displacement versus short-term temperature change.

Conclusions

This study investigated an extradosed bridge by applying correlation analysis to four years of long-term monitoring data collected from the bridge. The research examined the impacts of seasonal temperature variations and day–night temperature fluctuations on various monitored variables. The findings reveal significant differences between the impact of seasonal temperature variations and day–night temperature fluctuations on cable frequencies.

Acknowledgements

This study is a partial outcome of a project funded by the Northern Region Branch Office of the Highway Bureau, MOTC, Taiwan. Their invaluable support played a key role in facilitating the research efforts and findings presented in this paper.

References

1. Sonbul, O. S., Rashid, M. “Algorithms and Techniques for the Structural Health Monitoring of Bridges: Systematic Literature Review”, Sensors 2023, 23(9), 4230.
2. Ni, Y. Q., Hua, X. G., Fan, K. Q., and Ko, J. M., “Correlating modal properties with temperature using long-term monitoring data and support vector machine technique”, Engineering Structure, 2005, 27, 1762-1773.

Shaking Table Tests of Suspended Nonstructural Components

Wei-Chung Chen[1], Min-Chi Ko[2], Juin-Fu Chai[3], and Fan-Ru Lin[4]

陳威中[1]、柯敏琪[2]、柴駿甫[3]、林凡茹[4]

Abstract

Following the significant earthquake that struck Hualien on April 3, 2024, the National Center for Research on Earthquake Engineering (NCREE) promptly conducted investigations in the affected area. Extensive damage to suspended nonstructural components in hospitals and schools was observed, resulting in substantial financial losses and affecting the functionality of these buildings. To gain a comprehensive understanding of the seismic performance and dynamic behavior of suspended nonstructural components, as well as to enhance domestic seismic construction techniques, a series of full-scale shaking table tests on air handling units and pipeline systems were conducted at the NCREE Tainan Laboratory. This paper will present the preliminary research findings from the shaking table tests.

Keywords: suspended nonstructural components, air handling unit, pipeline systems, shaking table tests, nonstructural components

Introduction

On April 3, 2024, a powerful earthquake with a magnitude of 7.2 on the Richter scale struck the Hualien area, marking the largest seismic event in Taiwan since the 1999 Chi-Chi Earthquake. Following the earthquake, the National Center for Research on Earthquake Engineering (NCREE) promptly conducted a thorough investigation of the seismic damage to suspended nonstructural components. The investigation revealed extensive damage to suspended pipeline systems (Fig. 1) and suspended air handling units (Fig. 2) in numerous hospitals and schools. This damage resulted in water leakage within indoor spaces, significantly compromising the functionality and operational capacity of the affected buildings.

It was observed that the suspended nonstructural components that were affected by the earthquake had no seismic reinforcement measures. The primary reason for this deficiency is related to their suspension methods. For example, the suspended air handling units are fixed beneath the floor slab using spring vibration isolators, as shown in Fig. 3. The function of the spring isolators is to prevent mechanical vibrations generated by the fan motors inside the air handling units from being transmitted through the suspension rods to the upper floor slab, thereby avoiding discomfort for the occupants.

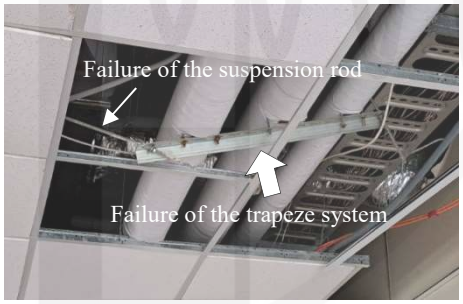

Fig. 1. Failure of the trapeze system

Fig. 2. Failure of the air handling unit

[1] Assistant Researcher, National Center for Research on Earthquake Engineering
[2] Deputy Director General, National Center for Research on Earthquake Engineering
[3] Associate Researcher, National Center for Research on Earthquake Engineering
[4] Assistant Researcher, National Center for Research on Earthquake Engineering

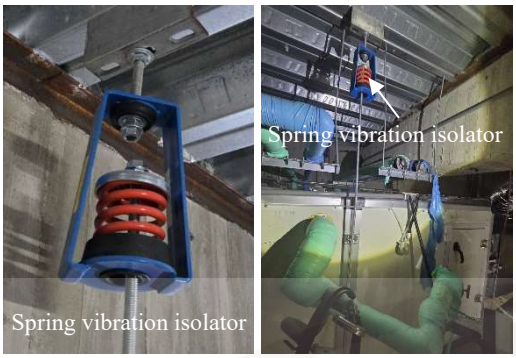

Fig. 3. Spring vibration isolators

By contrast, using traditional seismic reinforcement methods to strengthen the air handling units could result in mechanical vibrations from the units being directly transmitted to the floor slab through the reinforced components. Consequently, suspended air handling units in Taiwan often lack seismic measures, resulting in significant displacement during earthquakes and various seismic damage issues.

Test Setup

To obtain a comprehensive understanding of the seismic performance of suspended nonstructural components in Taiwan, this study conducted a series of shake table tests at the National Center for Research on Earthquake Engineering (NCREE) Tainan Laboratory. To accurately simulate real-world conditions of nonstructural components suspended within a building, a three-story steel frame structure was constructed on the shaking table as the test frame. Full-scale pipeline systems and air handling units were installed within this test frame, as shown in Fig. 4. The test frame possesses a floor plan dimension of 5 m × 5 m, with each floor having a height of 4 m, resulting in a total structural height of 12.7 m.

Fig. 4. (a) Pipeline system on the first floor; (b) Air handling unit on the second floor; (b) Air handling unit on the third floor

This experiment was conducted in two phases. The first phase involved the assessment of specimens equipped with seismic retrofitting measures, with the objective of assessing the actual effectiveness of these reinforcement measures. Conversely, the second phase did not incorporate any seismic measures, aiming instead to simulate the seismic response of suspended nonstructural components in a real-world disaster scenario. By comparing the outcomes of these two phases, this study seeks to identify critical characteristics of seismic damage and propose reasonable seismic strategies.

In this study, two suspended pipeline systems were designed for installation on the first floor, comprising a 4-inch electrical conduit (upper layer) and a 4-inch fire sprinkler system (lower layer), as shown in Fig. 5(a). The pipelines were supported with 4/8-inch fully threaded rods used as suspension elements. Fig. 5(b) depicts a dual-layer angle steel frame, which was installed prior to the divergence of the upper and lower pipelines. This angle steel frame serves as a seismic reinforcement measure, effectively restraining the two layers of pipelines.

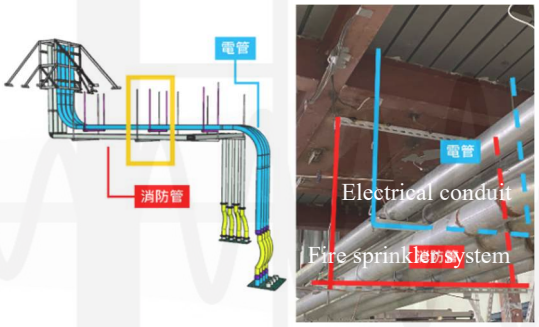

(a)

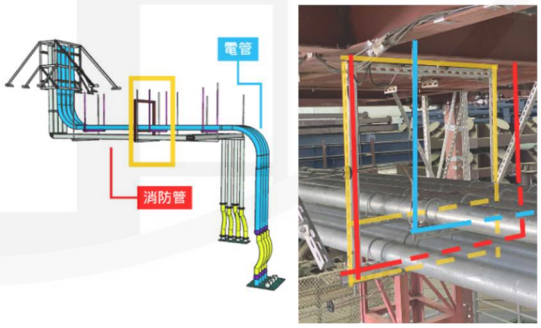

(b)

Fig. 5. (a) Two suspended pipeline systems; (b) Angle steel frame

Based on the findings from the reconnaissance survey, limiting the displacement of suspended air handling units is considered a rational approach for seismic design. In the case of the air handling unit located on the second floor, two diagonal cable wires were installed at each of the four corners, as shown in Fig. 6. The cables were arranged orthogonally and set at a 45° angle to the horizontal plane. For the air

handling unit situated on the third floor, eight stoppers were installed around the unit, as shown in Fig. 7. These stoppers were positioned with a slight gap to prevent direct contact with the unit, ensuring that mechanical vibrations generated during operation do not transmit through the stoppers to the floor above.

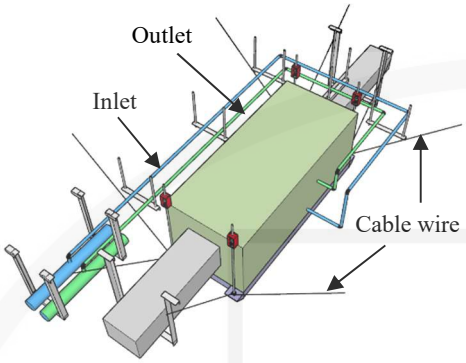

Fig. 6. Cable wires applied

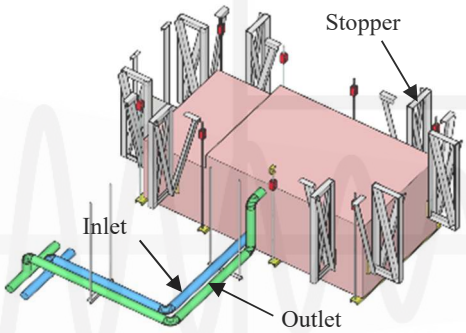

Fig. 7. Stoppers applied

Test Motions

This study selected three earthquake ground motion records from Taiwan and Japan to serve as input motions for the shaking table tests. The first input motion was derived from the time history recorded on the B2 floor of a building at Tzu Chi Hospital in Hualien during the 0403 Hualien earthquake. The experimental procedure was conducted sequentially with input motion intensities of 25%, 50%, 75%, and 100%. The second input motion was obtained from the ground time history recorded at a station near Donghua University in Hualien during the same seismic event, with input motion intensities of 33%, 66%, and 100%. The third input motion was based on the ground time history recorded by the Japan Meteorological Agency (JMA) station during the Kobe earthquake in Japan. Due to the original peak ground acceleration of this earthquake record exceeding 800 gal, the time history was scaled down to 30% of its original intensity to prevent significant structural damage to the three-story test frame during the experiment.

Test Results

The test results indicated that the air handling unit predominantly exhibited translational and rotational motion, along with the swinging characteristics akin to a simple pendulum. The substantial displacement resulted in impact reactions, which were identified as the primary cause of seismic damage. During the earthquake, the air handling unit initially contacted its suspension rods (Fig. 8), and as the displacement increased, it ultimately impacted the chilled water pipes, leading to their fracture, as illustrated in Fig. 9. Analysis of the displacement data from this test revealed that the suspended air handling unit experienced displacement vibrations exceeding 500 mm during seismic events. Therefore, limiting the displacement of suspended air handling units proved to be of particular importance to ensure structural integrity.

Fig.8. Failure of rod

Fig.9. Failure of pipeline

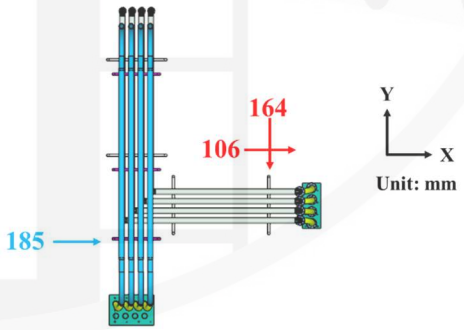

(a)

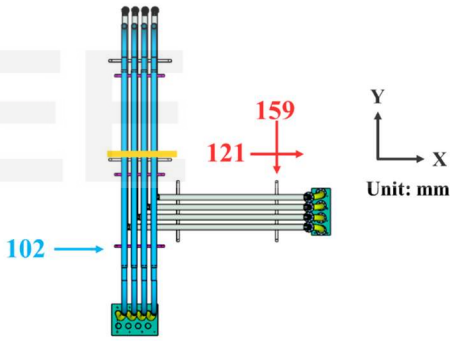

(b)

Fig. 10. (a) No reinforcement measures; (b) Angle steel frame applied

Fig. 10 shows the displacement of the pipeline system under the seismic conditions simulated by the JMA Kobe 30% earthquake scenario. The experimental results indicate that the use of an angle steel frame for reinforcement effectively reduced the lateral displacement of the upper electrical conduit. However, it resulted in an increased displacement of the lower fire sprinkler system. This phenomenon can be primarily attributed to the design of the angle steel frame used in this study, which was a portal-type structure lacking in-plane or out-of-plane bracing. This study recommends the broader application of angle steel frames as seismic reinforcement for pipeline systems in practical scenarios. Additionally, it is recommended that diagonal braces be integrated into the angle steel frames to effectively reduce the displacement of the pipeline system, thereby mitigating the risk of seismic damage.

Conclusions

The test results reveal that suspended air handling units without seismic reinforcement are susceptible to substantial displacement vibrations during seismic events, which can lead to frequent impacts with their suspension rods and chilled water pipes, resulting in severe damage. This finding is corroborated by results from post-earthquake investigations following the 0403 Hualien earthquake. The post-disaster survey indicated that a majority of suspended nonstructural components in current practice are not equipped with adequate seismic reinforcement, which contributes to significant damage to key building systems. This experiment further quantifies this phenomenon, confirming that the dynamic displacement and impact reactions of suspended nonstructural components during seismic events are major causes of seismic damage, thereby highlighting the necessity of seismic reinforcement.

Traditional methods of seismic reinforcement that aim to enhance system stiffness are unsuitable for suspended air handling units, as these measures may facilitate the direct transmission of mechanical vibrations to the floor above. This study has confirmed the effectiveness of both stoppers and cable wires as reinforcement strategies. However, the design of the stoppers must account for impact effects to ensure their proper functionality. Additionally, the cable wires should be regularly inspected, especially after significant seismic events, to prevent a reduction in effectiveness due to excessive slackening.

References

Wei-Chung Chen, Zeng-Wei Zeng, Fan-Ru Lin, Juin-Fu Chai. (2022), “Experimental study of suspended busway systems,” 8ACEE, Taipei, Taiwan.

ISAT (2002). Engineered Seismic Bracing of Suspended Utilities (2002 Ed.), USA: International Seismic Application Technology.

National Fire Protection Association (2009). NFPA13: Standard for the Installation of Sprinkler, 2013 Ed., NFPA, Massachusetts, USA.

Experimental and Numerical Studies on a Wind Turbine Nacelle

Bai-Yi Huang[1], Wei-Hung Hsu[2], Juin-Fu Chai[3], and Fan-Ru Lin[4]

黃百誼[1]、徐瑋鴻[2]、柴駿甫[3]、林凡茹[4]

Abstract

Taiwan is located between the Asian continent and the Pacific Ocean within the East Asia monsoon region. The Taiwan Strait experiences high monsoon wind speeds because of the funnel effect, making it an ideal location for offshore wind farms. However, Taiwan is also situated in the Northwestern Pacific typhoon activity zone and at the boundary between the Philippine Sea Plate and the Eurasian Plate, an area characterized by high seismic activity. Because of these locational characteristics, the country is susceptible to natural disasters. Therefore, the development of offshore wind power in Taiwan is challenging, and it is critical to ensure that wind turbines can withstand both typhoons and seismic events. The most effective approach for assessing the seismic performance of wind turbines is through shaking table tests to confirm the structural integrity of towers, nacelles, and other key components. However, the size of modern turbines exceeds the capacity of existing shaking tables, rendering direct seismic performance testing impractical and necessitating the exploration of alternative methods. This study aims to conduct seismic performance tests on a small-scale wind turbine nacelle and use the experimental results to verify and refine a corresponding numerical model. The ultimate objective is to develop a numerical approach for evaluating the seismic performance of wind turbine nacelles, which can then be applied to assess ultra-large wind turbines.

Keywords: wind turbine nacelle, shaking table test, system identification, ABAQUS analysis

Introduction

The first onshore wind farm began commercial operation twenty years ago. The development of green energy has accelerated in recent years, with the first offshore wind farm starting commercial operation in 2019. However, wind farms remain vulnerable to earthquake hazards. Both domestic and international technical guidelines and standards emphasize site investigation as well as the design of supporting structures and foundations. However, the stability of wind power systems depends not only on these structures but also on the components within wind farm assets. To ensure the resilience of the assets of wind farms, proper design and certification of these components are essential. Seismic qualification through shaking table tests, using appropriate testing parameters, represents one of the most direct and effective methods for investigating earthquake risks. However, a significant lack of monitoring data for wind turbines limits understanding of their seismic response and the interaction of their components. Moreover, as turbine capacity increases (Fig. 1), component size grows, leading to higher costs and greater complexity.

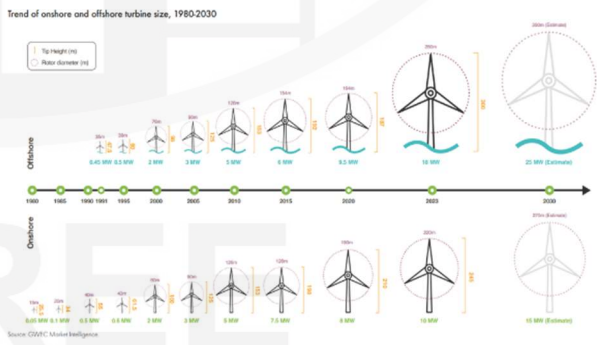

Fig. 1. Trends in wind turbine size development (Global Wind Energy Council, 2024)

[1] Assistant research, National Center for Research on Earthquake Engineering
[2] Associate research, National Center for Research on Earthquake Engineering
[3] Deputy Director General, National Center for Research on Earthquake Engineering
[4] Research Fellow, National Center for Research on Earthquake Engineering

These factors pose challenges to conducting seismic qualification tests for wind turbine components. Similarly to design documents, seismic studies on wind turbines have primarily focused on foundations and supporting structures. Most studies have employed scaled models for shaking table tests, often in combination with shear boxes or wind tunnels, to simulate composite load conditions. However, limited literature exists on the seismic performance of wind turbine components. To address this issue, shaking table tests were conducted using a decommissioned turbine nacelle (Fig. 2) at the National Center for Research on Earthquake Engineering (NCREE) Tainan laboratory. The primary objective was to observe the actual seismic response and identify the dynamic characteristics of the nacelle's components.

Fig. 2. The decommissioned onshore wind turbine

Methodology

The most effective approach for assessing the seismic performance of wind turbines is conducting shaking table tests to confirm the structural integrity of towers, nacelles, and other key components. According to the manual of the decommissioned wind turbine, the nacelle and rotor weigh approximately 27 tons (Vestas, 2000), which is within the payload capacity of the shaking table.

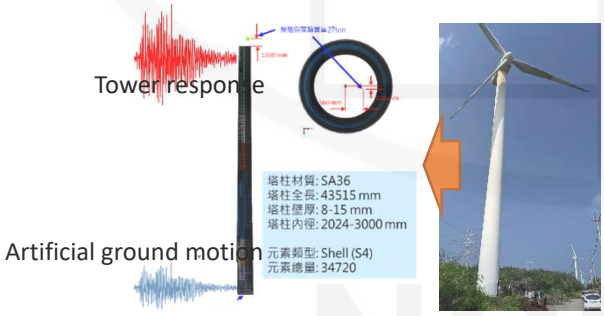

Fig. 3. The simulation of tower responses

However, the tower height and blade length exceed 40 m and 20 m, respectively, making it impractical to utilize the entire wind turbine, including the supporting structure and rotor-nacelle assembly (RNA), as a specimen. To address this limitation, this study employed a combination of numerical simulation and physical testing. Initially, a simplified numerical model of the wind turbine was developed in ABAQUS software based on the physical dimensions and material properties shown in Fig. 3. In the model, the RNA was represented as a lumped mass located at its center of mass.

Following the instructions and requirements specified in Taiwan's building code (Ministry of the Interior, 2024), artificial ground motions were synthesized based on earthquake records from strong-motion stations near the site. These motions were made compatible with the specified design spectra, as shown in Fig. 4. The synthesized ground motions were then used as input excitations for the simplified wind turbine model.

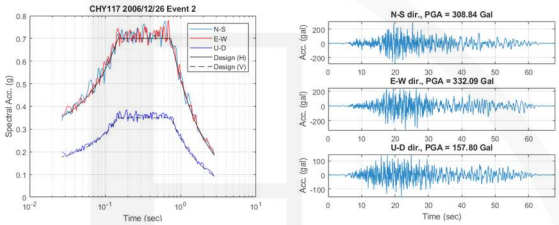

Fig. 4. An example of artificial ground motions

Using finite element analysis (FEA), the seismic responses at the top of the tower under these ground motions were simulated. These responses served as input motions for the shaking table tests. An example is presented in Fig. 5, which indicates that the horizontal responses were primarily influenced by the tower's fundamental frequencies.

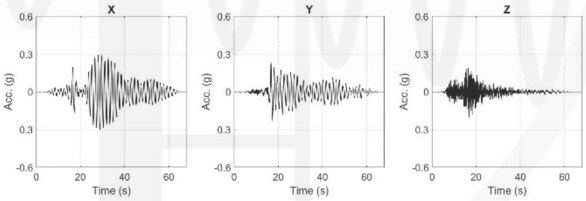

Fig. 5. An example of input motions for shaking table tests

Shaking Table Tests on the Nacelle

By replicating the simulated seismic responses at the tower top on the shaking table, the shaking tests were conducted without the tower. However, the blades were too long to be accommodated on the shaking table. Therefore, the blades and the nose cone were removed prior to testing. To compensate for the removed blade mass, three counterweights were attached to the hub to restore the inertia effect of the blades. Additionally, to perform the shaking table test without a tower or blades, the nacelle was secured to the table using steel I-beam jigs with stiffener plates. These jigs included through-holes in the upper and lower plates, aligned with the bolt holes on the yaw flange and the shaking table, respectively. The configuration of the jigs, counterweights, and nacelle is shown in Figs. 6 and 7.

Fig. 6. Jigs secured to the shaking table

Fig. 7. The fully prepared specimen

Accelerometers were installed on the nacelle's components and structures to monitor vibration responses. Analysis of white noise tests revealed the fundamental frequencies of the components. Among these, the VMP controller, supported by a cantilevered angle steel bracket, exhibited the lowest fundamental vibration frequency in the horizontal directions (Fig. 8) and showed significant vibration responses during testing. As shown in Fig. 9, the vibration response at the top of the controller was more than twice that at the anchor point of the bracket, indicating notable amplification.

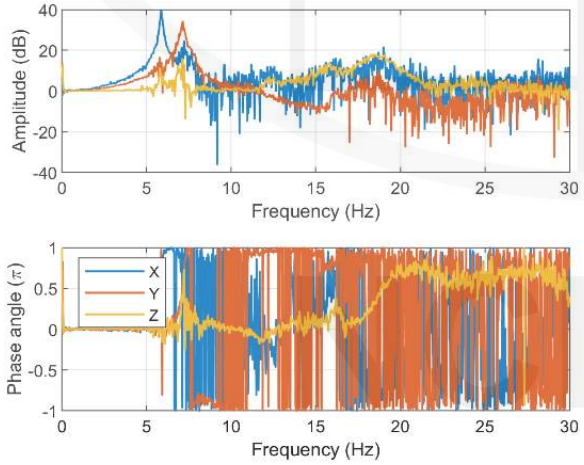

Fig. 8. Frequency response functions between the top and base of the VMP controller

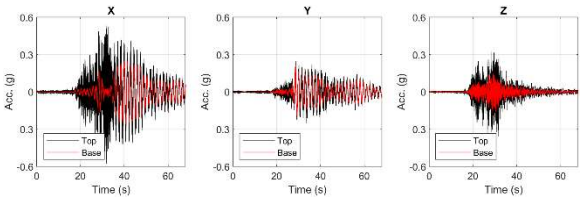

Fig. 9. Acceleration responses of the top and base of the VMP controller

Numerical Simulation of the Nacelle

Laser scanning technology and direct measurements were used to construct a finite element model of a small-scale wind turbine nacelle, as shown in Fig. 10. The model incorporates various components represented by solid and shell elements. The material properties were assumed to correspond to general structural steel, cast iron, FRP, and rubber. Adjustments were made based on the natural frequencies of each component identified through testing, as illustrated in Fig. 11.

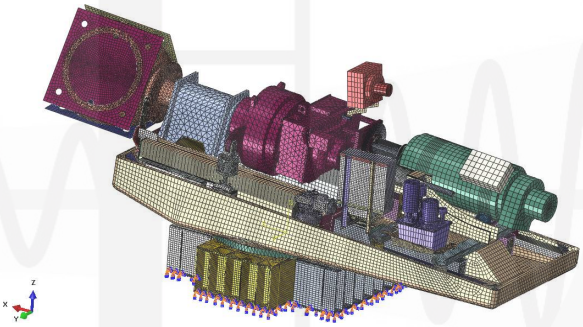

Fig. 10. Finite element model of the wind turbine nacelle

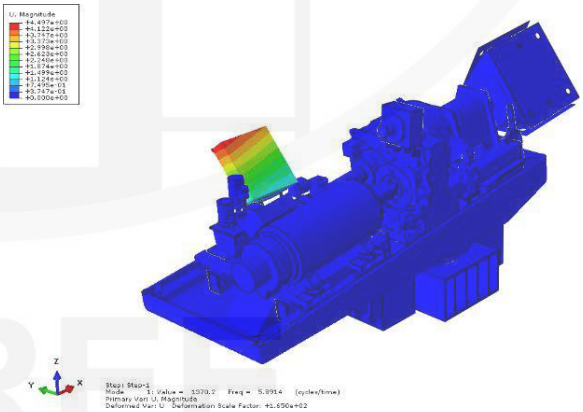

Fig. 11. Example of modal analysis

The input motions employed in this study are depicted in Fig. 12. To compare the results from experimental and numerical approaches, the simulation results were obtained at two positions depicted in Fig. 13, where the accelerometers were attached. Figs. 14 and 15 present comparisons between the experimental and numerical acceleration responses

at the VMP controller and generator anchorage points. The horizontal acceleration responses were similar. However, discrepancies were observed at the top of the equipment. These differences can be attributed to limitations in accurately modeling the rubber material beneath the equipment and the internal structure of the equipment within the numerical model.

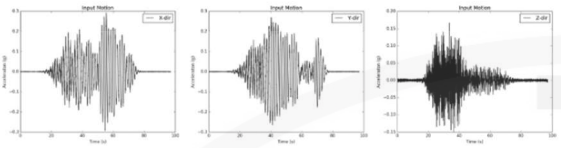

Fig. 12. Input motions for the numerical simulation

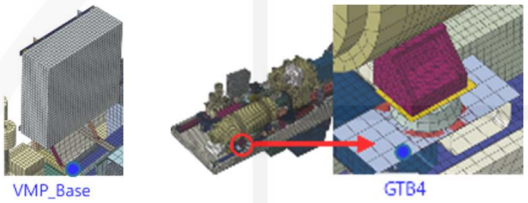

Fig. 13. Output points of VMP controller and generator anchorage points

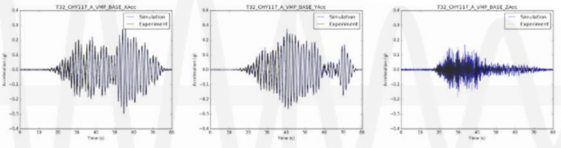

Fig. 14. Acceleration responses at the VMP controller anchorage point

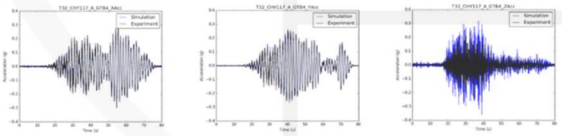

Fig. 15. Acceleration responses at generator anchorage point

Conclusions

Wind energy plays a significant role in transition to renewable energy in Taiwan. However, further research and data are required to ensure the seismic performance of wind turbines and their key components. This study is likely the first to employ a real nacelle in shaking table tests. The resulting data provide valuable insights into the dynamic characteristics and interactions of components, indicating components potentially at risk of seismic damage. Additionally, the experimental data can be used to calibrate numerical models and improve certification techniques.

Preliminary validation in this study revealed that the response at the equipment anchorage points can be reproduced using the numerical model, with results closely matching those from the shaking table tests. Therefore, for seismic performance verification of offshore wind turbines, it is recommended to first establish a numerical model to estimate the anchorage point response of each critical component. Subsequently, shaking table tests can be conducted independently for each component to confirm its functionality and structural integrity.

References

Global Wind Energy Council (n.d.), “GLOBAL WIND REPORT 2024”, https://www.gwec.net/reports/globalwindreport

Ministry of the Interior (2024), “Seismic Design Specifications and Commentary of Buildings”

Vestas wind system (2000). General Specification 660 kW Variable Slip Wind Turbines Item no.:94311R4.

Study on Seismic Behavior of Steel Shear Yielding Link Beams

Sheng-Jhih Jhuang,[1], Ker-Chun Lin,[2], Kai-Ning Chi[1], Mine-Yi Su[3], and Chui-Hsin Chen[4]

莊勝智[1]、林克強[2]、紀凱甯[1]、蘇名浥[3]、陳垂欣[4]

Abstract

This study primarily aims to replace coupling beams with steel link beams. The present goal is to develop design methods for assessing the shear deformation capacity and shear strength capacity of these link beams. Previous studies have indicated that placing vertically oriented longitudinal stiffeners in the core section of the yielding range can reduce the shear strain hardening factor and, subsequently, decrease shear demands on connections. The core segment's shear deformation and the normalized width–thickness ratio are correlated. Based on this finding, this study designed five sets of short-span shear yielding link beams with stiffeners oriented in different directions using the width–thickness ratio and the proportion of the core segment as variables. Test results demonstrate that both the core segment shear deformation capacity and shear strength capacity can be predicted using the normalized width-thickness ratio. Furthermore, the shear strain hardening factor with transverse stiffeners is greater than that with longitudinal stiffeners. These observations, combined with past test results, allow for the summarization of a design process for shear yielding link beams.

Keywords: link beams, longitudinal stiffeners, transverse stiffeners, width–thickness ratio

Introduction

The link beam in this study replaces the reinforced concrete (RC) coupling beam and the shear link of the eccentric diagonal brace frame, generating a shear plastic hinge in the web, as shown in Figure 1. The force and deformation mode of the link beam, under the assumption that the connection segment remains elastic, is the same as that of the seismic stud column (SSC) without axial force; a comparison of the force models is shown in Figure 2. If the required inter-story drift is known, the shear deformation demand of the link beam can be obtained from the structural geometric deformation.

Previous studies on SSCs have indicated that the shear deformation capacity (γ_c) of the core segment with a shear plastic hinge is negatively correlated with the short side width–thickness ratio (λ_{ssc}) of the core segment, with the ratio (δ) of the core segment length to the overall specimen length limited to 0.2–0.6. Historically, the manufacturing method for such SSC members involved removing the web from the core segment of the original member and replacing it with a steel plate of lower strength or thinner thickness for stiffening. Although this method ensures shear yielding occurs at the web of the core segment, it is cumbersome and prone to construction errors. When the core segment constitutes a large proportion of the member and the flange is thin, the absence of a web may lead to initial defects, such as lateral torsional deformation. In this study, five full-scale shear yielding link beam specimens were designed, and cyclic load tests were conducted using the multi-axial test system (MATS) in the large structural laboratory at the National Center for Research on Earthquake Engineering (NCREE). Unlike previous designs of SSCs that used two materials, these test specimens used the same material and section to demonstrate that varying the stiffening methods on the same H-shaped section can concentrate most of the shear deformation on the core segment. Therefore, the design focuses on "controlling the width–thickness ratio ($(b/t)_c/(b/t)_j$) of the core segment and the connection segment" as the main variable, providing design methods and recommendations for shear yielding link beams.

Research Methods

In this study, the seismic performance of the shear yielding link beam was mainly verified through five

[1] Assistant Researcher, National Center for Research on Earthquake Engineering
[2] Research Fellow, National Center for Research on Earthquake Engineering
[3] Master, Department of Civil Engineering, National Yang Ming Chiao Tung University
[4] Associate Professor, Department of Civil Engineering, National Yang Ming Chiao Tung University.

cyclic tests conducted on full-scale specimens (labeled CB1 to CB5). The dimensions of the five specimens, all with the same height of 2.5 m, are shown in Figure 3. The material used in this study was SN490B, and all cross-sections were BH 800 × 300 × 7 × 24. The specimens varied in their configuration of the stiffening plate, the width–thickness ratio of the core segment ($(b/t)_c$), the width–thickness ratio of the joint segment ($(b/t)_j$), and the core segment ratio (δ). The differences between the five specimens are described as follows:

(a) The core segment ratio δ of CB1 was 1.0, which is the largest among the core segment ratios of all specimens. This specimen did not include a joint segment.

(b) The core segment ratio δ of CB2 was 0.68, which is slightly larger than the previous limit of SSCs ($0.2 \leq \delta \leq 0.6$). In this specimen, the width–thickness ratio of the core segment to the joint segment was 1.3.

(c) The δ values for CB3 and CB4 were 0.53, with the difference lying in the width–thickness ratio of the core segment and the joint segment. This ratio for CB3 was 1.0, whereas that for CB4 was 1.3. CB3 and CB4 were expected to have higher shear deformation capacities than CB1 and CB2.

(d) CB5 and CB1 shared the same short-side width–thickness ratio, with the only difference being the configuration of the stiffener plates. CB1 was configured with only longitudinal stiffener plates, whereas CB5 had only transverse stiffener plates. This configuration was mainly used to verify the influence of stiffener plate configuration on the magnitude of strain hardening shear force.

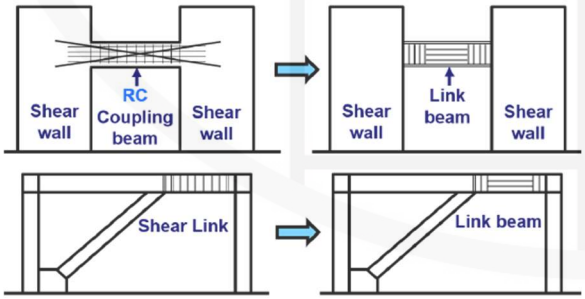

Fig. 1. Schematic diagram of an RC connecting beam and eccentric diagonal bracing shear link replaced by a connecting rod beam.

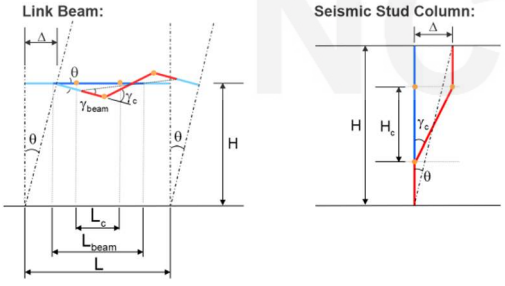

Fig. 2. Force modal and structural geometric deformation of a seismic stud column and link beam

All tests were conducted using MATS. The specimen's height, including both top and bottom fixtures, was 3,500 mm. The top and bottom ends of the specimens were fixed to the reaction frame and loading platform of MATS using an appropriate number of prestressed steel rods. 1,200 kN vertical actuators were arranged on each of the south and north sides of the specimens. In addition, two hydraulic servo actuators were arranged horizontally to apply a shear force to the specimens. One end of each actuator was connected to the loading platform, while the other end was fixed to the reaction wall. The actuators were controlled using the MATS control system, and all tests were conducted by applying interstory drift loading in accordance with the American Institute of Steel Construction (AISC) 341-16 sequence for beam-to-column moment connections at the bottom of the fixed specimens. Before this test sequence, additional interstory drifts of 0.125% and 0.25% were applied. The overall configuration of the link beam test is depicted in Figure 4. In these tests, displacement and strain measurements were taken at specific points using an optical image measurement system and strain gauges. The horizontal displacement difference between the top and bottom endpoints of the core segment was measured using a lateral displacement sensor. This displacement difference was divided by the core segment length to obtain the shear deformation angle (γ) of the core segment. During the test, the timing and process of yielding in each part of the specimen were observed, and the angle and behavior of the tension field in the core segment web under shear force were measured and recorded.

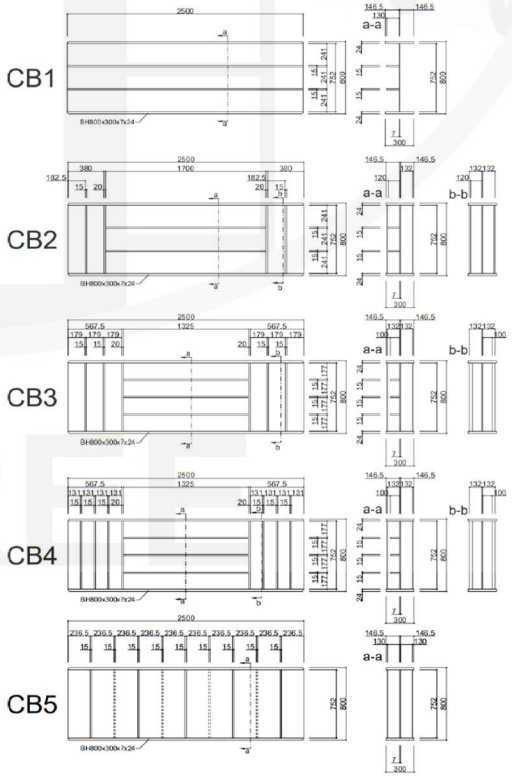

Fig. 3. Schematic diagrams of the link beam specimens.

Test Results and Discussion

The failure modes of all specimens in this study varied, except for specimen CB5, which was damaged at the weld between the flange and the fixture at the top and bottom ends. All other specimens experienced concave folds and fractures due to repeated tension and compression buckling, with ruptures occurring at the web center and edge welds of the web panel. The failure conditions and the hysteresis loops of deformation and strength for the four specimens are shown in Figures 5–9. The maximum deformation for the tests was determined as follows: (1) Throughout the entire loading process, the test strength remained above 80% of the maximum shear strength of the link beam. (2) No significant shrinkage was observed after at least one complete cycle. (3) The average of the maximum positive and negative deformation was used to determine the result. The test results indicate that the maximum overall drift angles of the link beam for specimens CB1 to CB5 were 4%, 4%, 6%, 6%, and 3% radians, respectively, while the maximum shear deformation angles of the core segments of CB2, CB3, and CB4 were 5.00%, 8.46%, and 8.74% radians, respectively.

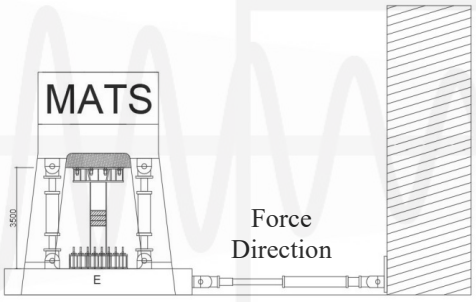

Fig. 4. Test configuration for the link beam specimens.

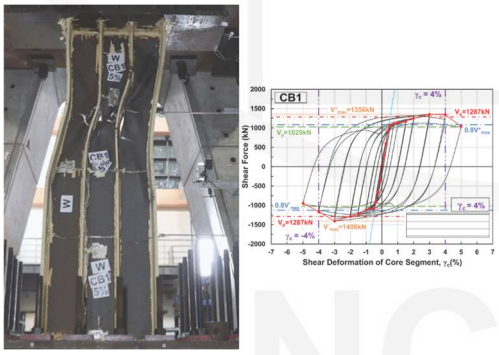

Fig. 5. Failure conditions and hysteresis loops of deformation and strength for specimen CB1.

For the five specimens in this study, the shear strain hardening factors of the web of the core segment were calculated by dividing the maximum shear strength of the test by the actual plastic shear strength of the core segment, resulting in values of 1.07, 1.19, 1.24, 1.24, and 1.17 for CB1-CB5. The core segment configurations of CB3 and CB4 were identical, with the only difference being the short-side width–thickness ratio after the joint segment was stiffened. The CB4 joint segment included more transverse stiffener plates, making it more rigid than CB3. Consequently, the development of shear deformation in the CB4 core segment should exceed that of CB3. The comprehensive test results also indicate that the width–thickness ratio affects the strain development of the cross-section. If the width–thickness ratio is too large, the cross-section buckles before the strain develops evenly, leading to a decrease in shear strength and continued strain development in that area. Therefore, to ensure uniform strain development across the same cross-section, the width–thickness ratio should not be excessively large.

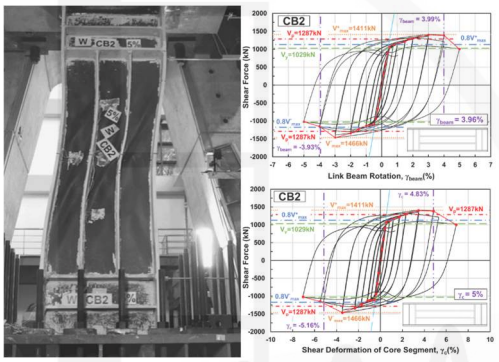

Fig. 6. Failure conditions and hysteresis loops of deformation and strength for specimen CB2.

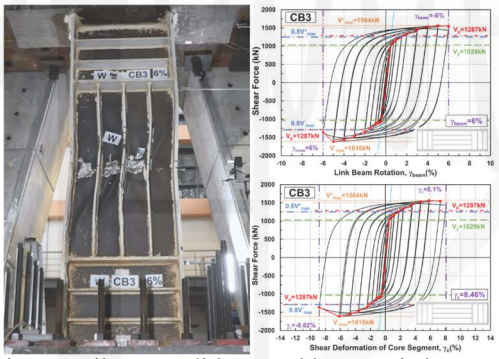

Fig. 7. Failure conditions and hysteresis loops of deformation and strength for specimen CB3.

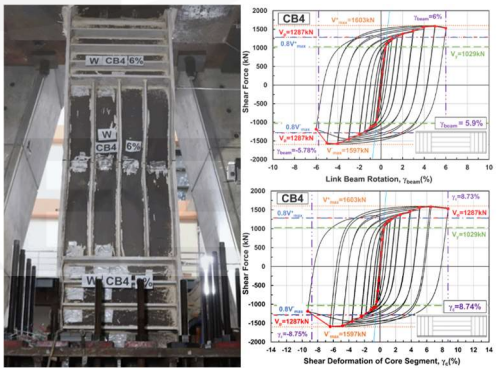

Fig. 8. Failure conditions and hysteresis loops of deformation and strength for specimen CB4.

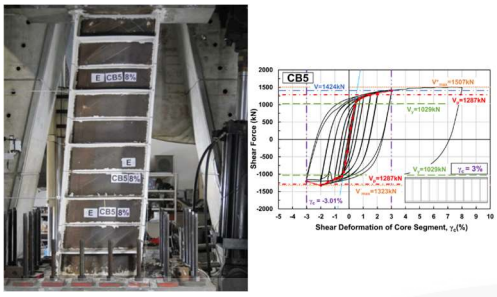

Fig. 9. Failure conditions and hysteresis loops of deformation and strength for specimen CB5.

To make this study more widely applicable, we not only discuss the five shear yielding link beam specimens but also incorporate test data from 21 SSC specimens found in the literature. Using linear regression analysis, we found an approximately linear relationship between the shear deformation capacity (γ) of the web of the core segment before the development of the tensile field and the dimensionless width–thickness ratio limit (λ_{ssc}) of the short direction of the specimen web. This relationship is illustrated in Figure 10 and expressed by the equation $\gamma = -12.471\lambda_{ssc}+23.392$. This indicates that the smaller the short-side width–thickness ratio of the core segment web, the larger the shear deformation capacity.

The shear deformation demand (γ_{dem}) of the core segment was estimated based on the relationship between the interstory drift demand (θ_{dem}) and the ratio (δ) of the length of the core segment to the net length of the specimen (calculated as $\gamma_{dem} = \theta_{dem}/\delta$). Based on the aforementioned relationship between shear deformation capacity (γ) and the dimensionless short-side width–thickness ratio (λ_{ssc}) of the core segment web, the core segment stiffener of the shear type link beam can be accurately designed to provide effective shear deformation capacity.

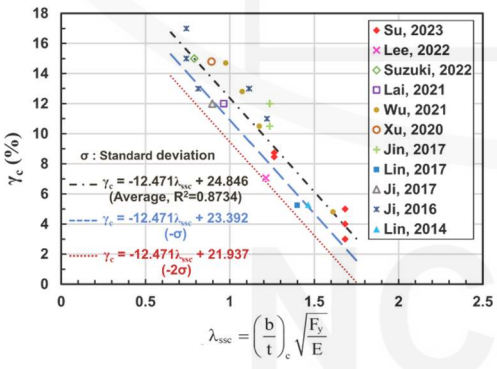

Fig. 10. Relationship between the maximum shear deformation and the width–thickness ratio of the short side of the link beam.

Conclusions and Suggestions

1. The cross-sections of the five link beam specimens in this study are similar, differing only in their stiffening methods; the λ_{ssc} of the CB3 core segment and the joint segment are the same. The test results indicate that the entire link beam section enters shear yielding, but the final shear deformation is concentrated in the core segment with longitudinal stiffener plates. This demonstrates that when λ_{ssc} is constant, the shear deformation capacity of the longitudinal stiffener plate is less than that of the transverse stiffener plate.
2. For shear yielding link beams without axial force, the core segment shear deformation capacity design formula $\gamma_c = -12.471\lambda_{ssc}+23.392$ proposed in this study can be used to determine the shear deformation capacity of the core segment. When a link beam designed using this formula reaches the expected core shear deformation, the shear strength can be maintained at 80% of the maximum shear strength.
3. The maximum ratio of the shear deformation capacity (γ_c) of the core segment to the overall shear deformation capacity (γ_{beam}) of link beam CB4 is 1.46. This indicates that the overall real drift deformation capacity of the link beam is approximately equal to $1.5\gamma_c$, and the δ value is between 0.53 and 0.68.

References

AISC (2016), Seismic Provisions for structural Steel Buildings, American Institute of Steel Construction, Chicago.

ASCE (2022), Minimum Design Loads and Associated Criteria for Buildings and Other Structures, ASCE/SEI 7-22, American Society of Civil Engineers, Reston, VA.

Construction and Planning Agency, Ministry of the Interior (2011), "Seismic Design Specifications and Commentary of Buildings".

Chang-Jui Wu (2021), "Test Behaviors of Seismic Stud Columns with Combination of Strength and Energy Dissipation", National Yang Ming Chiao Tung University, Master Thesis.

Chen-Wei Syu (2020), "A Study on Seismic Behaviors and Design Recommendations of Seismic Stud Columns with Shear Energy Dissipation", National Yang Ming Chiao Tung University, Master Thesis.

Hsu, C. H., Li, C. H., Chin, P. Y., and Tsai, K. C. (2017), "Seismic Design and Analysis of Steel Frame with Steel Panel Dampers", Structural Engineering, Volume 32, Issue 2, Pages 5~34.

Tsung-Jui Lee (2022), "Study on Axial Force Effect of Shear-Type Seismic Stud Columns", National Yang Ming Chiao Tung University, Master Thesis.

Smart Monitoring System for Structural and Non-structural Components in the NCREE Taipei Building

Meng-Huang Gu[1]

古孟晃[1]

Abstract

In order to create a seismically resistant and sustainable homeland, the National Center for Research on Earthquake Engineering (NCREE) was officially established in Taiwan in 1990. In 1997, a six-story reinforced concrete (RC) building was constructed as its headquarters in Taipei. After two decades of operation, the working space in the building gradually became insufficient. As a result, the NCREE launched a project in 2019 to vertically extend the structure into a thirteen-story building. The extended stories (from the seventh to the thirteenth) are constructed with steel, transforming the building into a composite structure of steel and RC. In this extension project, seismic retrofitting measures were implemented, including the expansion of existing shear walls, the addition of new shear walls, and the strengthening of some beams by wrapping them with fiber-reinforced polymer. In addition, advanced technologies such as buckling-restrained braces, steel panel dampers, and fluid viscous dampers were employed to enhance seismic resistance. These measures collectively make the building unique worldwide. Furthermore, to gain a deeper understanding of its seismic behavior, a smart structural monitoring system for both structural and non-structural components was installed to collect real-time seismic response data during earthquakes. This report describes the details of the smart structural monitoring system, which is expected to support future research in areas such as structural analysis and structural health monitoring.

Keywords: smart monitoring, structural components, non-structural components

I. Introduction

In order to better understand the seismic response of the new thirteen-story composite research building at the National Center for Research on Earthquake Engineering (NCREE) in Taipei, a smart structural monitoring system (SSMS) was installed in 2020 for long-term online monitoring. Sensors were installed at appropriate locations on several floors of the building to measure the response of structural and non-structural components. The measured data are continuously recorded using a data acquisition (DAQ) system. Data collected during seismic events are archived to support subsequent analysis and research. This report presents the configuration and detailed information of the sensors used in the system.

II. Hardware configuration

Table 1 lists the devices adopted in the SSMS. Sensor specifications are provided in Table 2. Figure 1 shows the data transmission flow. Figure 2 displays the DAQ system with all cables connected. The DAQ sampling rate is 200 Hz. The accuracy of the recorded data partly depends on the resolution of the analog signal input module of the DAQ system.

[1] Associate Researcher, National Center for Research on Earthquake Engineering

Table 1 Devices adopted in the SSMS

Device type	Product Name	Brand Name	Model	Quantity	Application
Sensor	Draw-wire Displacement Sensor	Fristmark	160-0803	4	Measurement SPD deformation
		Fristmark	160-0963	2	Measurement of damper stroke
	Strain Gauge	TML	FLAB-5-11	6	Measurement of SPD strain
		MFL	-	12	Measurement of damper strain
	Linear Variable Differential Transformer	RDP	DCWH4000B	2	Measurement of damper stroke
		RDP	DCTH4000C	2	Measurement of damper stroke
		RDP	DCWH15000B	2	Measurement of seismic isolator stroke
	Laser Displacement Meter	Riftek	RF603 260/1250	2	Measurement of ceiling displacement with seismic absorber
		Baumer	OT500	2	Measurement of ceiling displacement with seismic absorber
	Uni-axial Accelerometer	Tokyo Sokushin	AS-303D1W2	2	Measurement of seismic isolator acceleration
	Tri-axial Accelerometer	SDI	2460-002	7	Measurement of pipeline acceleration

Table 1 Devices adopted in the SSMS (continued)

Device type	Product Name	Brand Name	Model	Quantity	Application
DAQ Module	Data Acquisition Module	IMC	CRFX-400	1	1. Digitization of analog data from sensors 2. Data transmission
			DCB2-8	7	
			LV3-8	1	
			CS-1208-FD	1	

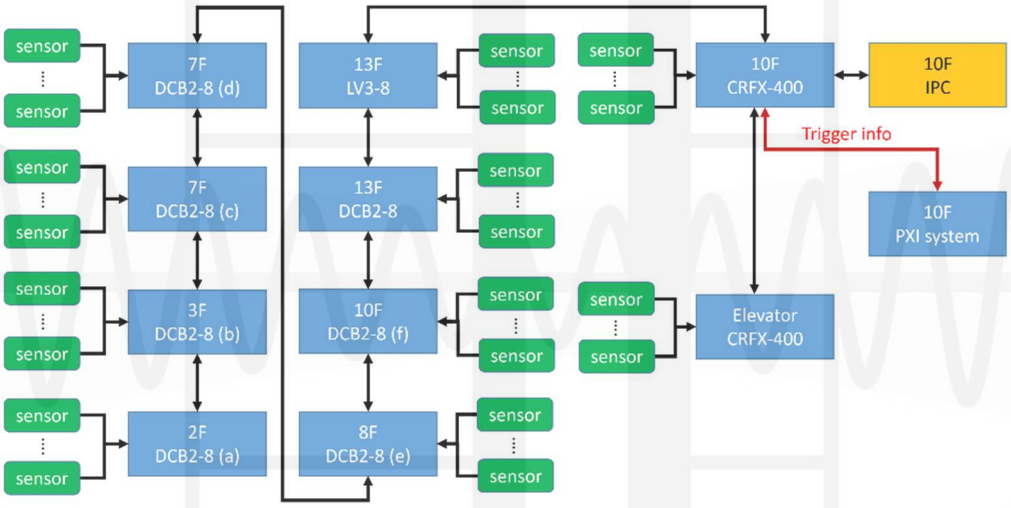

Fig. 1. Data flow diagram

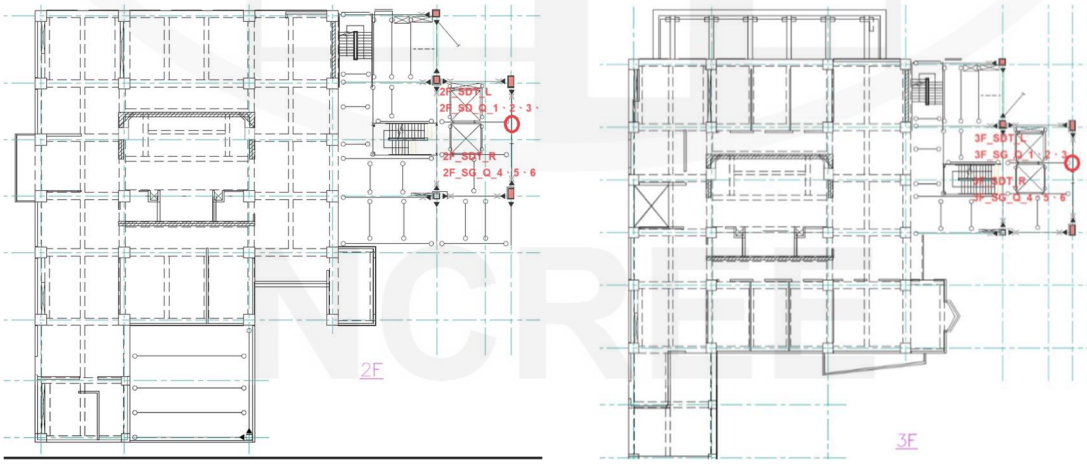

(a) 2F (b) 3F

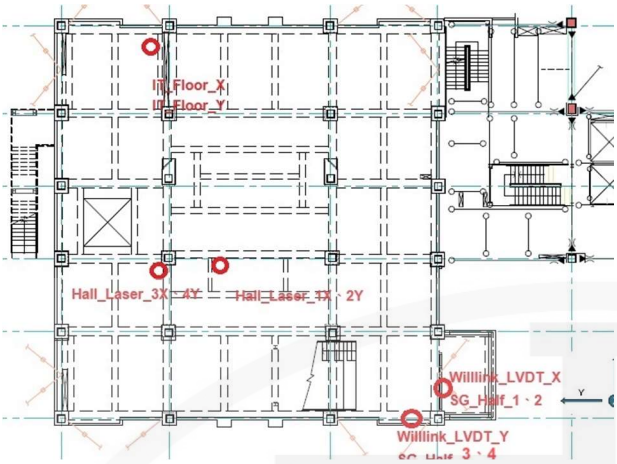

(c) 7F

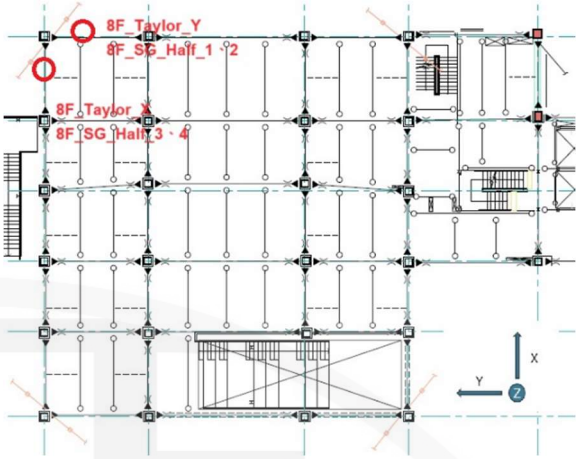

(d) 8F

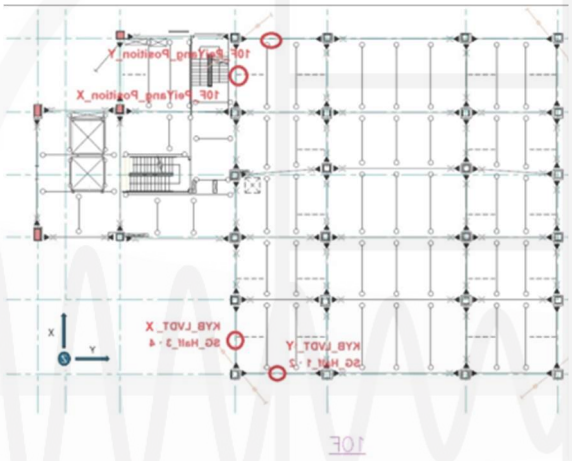

(e) 10F

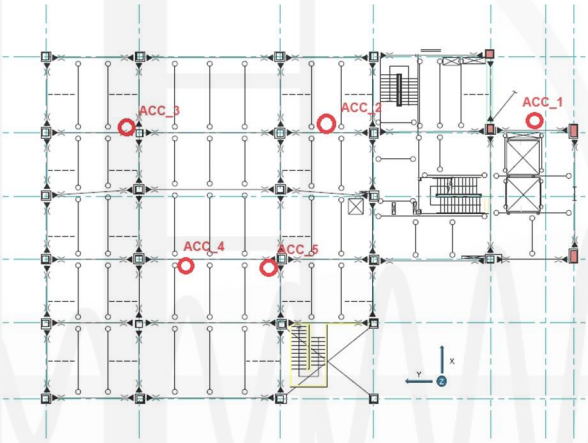

(f) 13F

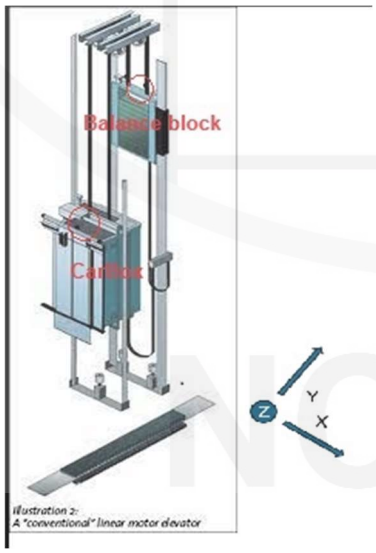

(g) Elevator

Fig. 2. Sensor configurations on (a-f) floors 2F

3F, 7F, 8F, 10F, and 13F and (g) the elevator

Ambient Vibration Study of the NLAC Building and Preliminary Study on Simplified Model

Kung-Chun Lu[1]

盧恭君 [1]

Abstract

In response to the need for refinement of structural numerical models, this study conducted ambient vibration tests, system identification, and model refinement with a focus on the National Laboratory Animal Center[2] Taipei building. This structure features a seismic isolation system, which distinguishes it from ordinary structures, and the importance of this will be discussed in the model refinement. The study also discusses a preliminary study on simplified model.

Keywords: ambient vibration tests, model refinement

Introduction

This study is part of the general building model (GBM) updating project. Using the National Laboratory Animal Center[2] (NLAC) Taipei building as the target, ambient vibration tests, system identification, and model refinement were conducted based on the principles of vibration analysis. The study also includes a preliminary study on simplified model.

Ambient Vibration Test and Identification Results

This study focuses on data obtained from ambient vibration tests of the entire building. The test plan is shown in **Fig. 1**.

The objective was to obtain the modal characteristics of the target structure. The sensor layout was based on ST16 and ST17, whose localities are shown in **Fig. 1**, each using an independent monitoring system.

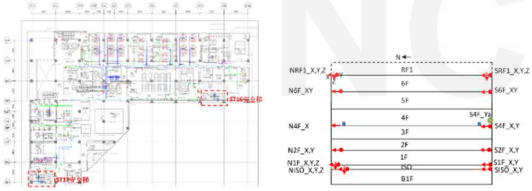

Fig. 1. The test plan of the whole building ambient test

as shown in **Fig. 1**, each utilizing an independent monitoring system. The monitored floors are indicated on the right side of **Fig. 1**. The time axes of the two sets of monitoring data was aligned during post-processing.

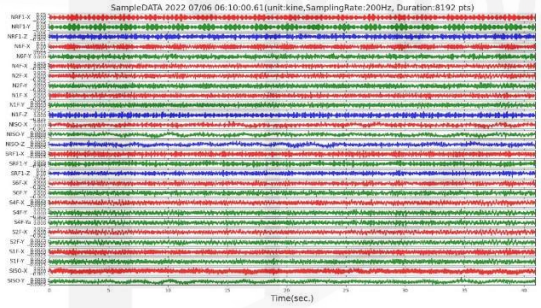

Fig. 2. Selected signal for identification

In this study, the selected signal duration contained 8,192 points. The sampling rate was 200 Hz, and the sampling duration was approximately 40 seconds. The starting time of the selected signal was 7/6 at 06:10. The selected signal is shown in **Fig. 2**. The signal was subjected to quality verification, direction confirmation, signal content inspection, and time axis alignment.

In the analysis of the signal and structural dynamic feature identification, the frequency domain decomposition (FDD) method was applied to extract

[1] Assistant Researcher, National Center for Research on Earthquake Engineering
[2] National Laboratory Animal Center (NLAC; now the National Center for Biomodels)

signal features. The resulting singular spectrum in **Fig. 3** shows that the signal contains numerous eigen-frequencies and has many close modes. For detailed inspection, some sections were enlarged to display local features, as shown in **Fig. 4**.

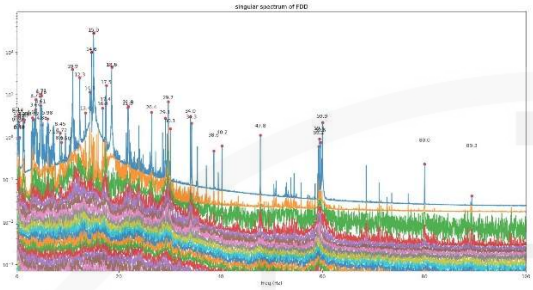

Fig. 3. Singular spectrum from the frequency domain decomposition method

Several prominent frequency values were identified from the peak frequency points in the singular spectrum (**Fig. 3 and 4**). In this case, 52 characteristic frequency values were identified, as shown in **Fig. 4**.

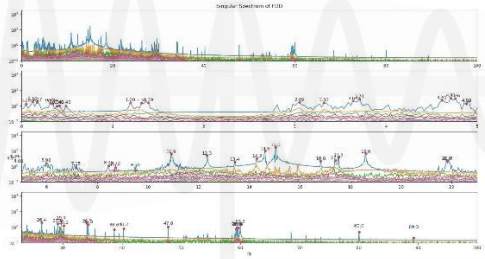

Fig. 4. Enlarged singular spectrum

The 52 eigenfrequencies listed in **Fig. 5** relate to structural dynamic characteristics, such as eigen-frequency ranges and mode shapes. Among these, the most probable eigen-frequencies were selected for further analysis. However, uncertainty remains regarding the modal shape results, and the complete characterization of structural dynamic features is not yet confirmed.

1	2	3	4	5	6	7	8	9	10
0.049	0.122	0.171	0.317	0.342	0.391	0.415	0.488	1.196	1.318
1.392	3.052	3.320	3.638	3.711	4.614	4.712	4.761	4.883	5.981
7.153	8.447	8.667	8.716	9.497	10.913	12.329	13.428	14.307	14.624
15.039	16.821	17.407	17.529	18.604	21.802	21.851	26.440	29.126	29.712
30.127	34.082	34.302	38.672	40.259	47.803	59.253	59.424	59.644	59.985
80.054	89.307								

Fig. 5. Table of selected eigenfrequencies

To verify the identification results, reference was made to the ETABS model from the design stage. The theoretical structural dynamic characteristics derived from the ETABS model are as follows.

As indicated by the comparison in **Fig. 6**, the abnormal mode shapes observed in the ambient vibration data did not offer clarification. The results show agreement in mode group characteristics, with 15 matching characteristic frequencies. The measured modal frequencies are slightly lower than those in the ETABS model, possibly because the equivalent stiffness value of the isolation used in the ETABS model is higher than that in reality. This discrepancy is most apparent at 10.93 Hz, 15.04 Hz, and 18.275 Hz, frequencies not reflected in the ETABS model. Further investigation of the actual vibration source conditions is recommended. Based on the current ambient vibration signals, only partial conclusions can be drawn from the comparison. If additional ambient vibration tests are conducted, many existing uncertainties may be resolved, resulting in clearer findings.

etabs	0.587	0.599	0.687	1.712	1.777	1.965	3.524	3.683	3.922
Test	0.391	0.415	0.488	1.196	1.318	1.396	3.32	3.638	3.711
etabs	5.436	5.605	6.015	10.68	15.51	18.28			
Test	4.712	4.761	4.883	10.93	15.04	18.6			

Fig. 6. Comparison of modal frequencies between ETABS and the ambient vibration test

Model Refinement

During the ambient vibration analysis, the ETABS model from the structural design provided by NLAC[2] was used as a reference. A qualitative comparison between the two confirmed the validity of the ambient vibration analysis. However, numerical discrepancies remain between the model and the actual structure. To refine the model further, potential sources of discrepancy between the numerical model and the real structure were examined. Parameters were adjusted based on reasonable estimates to correct the model, aligning it with the actual structure.

RB=0.1666	LRB=2.297	0.587	0.600	0.687	1.713	1.777	1.965	3.524	3.683	3.922
RB=0.1666	LRB=0.218	0.265	0.267	0.289	1.523	1.589	1.724	3.407	3.571	3.766
ambient test		0.391	0.451	0.488	1.196	1.318	1.396	3.320	3.638	3.711
RB=0.1666	LRB=2.297	5.436	5.606	6.015	10.677	15.509	18.276			
RB=0.1666	LRB=0.218	5.386	5.555	5.958	10.668	15.509	18.271			
ambient test		4.712	4.761	4.883	10.930	15.040	18.600			

Fig. 7. Comparison of modal frequencies between different parameters

According to the performance test report [1], the following characteristics were noted: the average test stiffnesses of RB and LRB are both 166.6 tonf/m, whereas the design value for both is 153.8 tonf/m. The effective stiffness estimation method presented in report [7] indicates that small displacements before yielding fall within a high-stiffness region. Based on these isolator characteristics, adjusting the equivalent stiffness value during model refinement may align it more closely with the actual structure. However, providing this value directly in the performance test

report would streamline the process.

The initial model applied the ultimate stiffness (*Ku* = 2.2979 t/mm) as the effective stiffness of the LRB. The modified model applied the equivalent stiffness (*Keff* = 0.2182 t/mm), corresponding to the shear strain under the design displacement of 365 mm (179.8%). In both models, the effective RB stiffness was set to the test value of 0.16666 tonf/mm. Simulation results indicate that neither model perfectly matches the measured data; however, the first three modes are distributed around the measured values. This suggests that the actual effective stiffness likely lies between the two values. Furthermore, comparing the relationship between parameter modulations of the isolation floor and changes in the modal frequency reveals that only the low-frequency modes are dominated by the characteristics of the isolation floor. The high-frequency modes are only marginally affected but are influenced by other factors. Therefore, deviations from the model require detailed examination and clarification of individual contributing factors. Factors that may be discussed include differences between the actual mass of the floor and the model, differences between the structural type of the model and the actual structure, and differences between the stiffness of the structural members and the actual structure. The difference in structural type between the model and reality can be determined by comparing mode shapes. The GBM provides a method for this analysis. However, the ambient vibration mode shapes must first be clarified.

Preliminary Study on Simpilied Model

This study obtained the real structural dynamic characteristics through structural ambient vibration analysis and compared and refined the finite element model from the design stage. During this process, the characteristics of the structure were observed. Next, a simplified model was established for rapid assessment after an earthquake. Important requirements for this simplified model are representation of real structural behavior and fast simulation. Considering the structural dynamic characteristics that have been identified, the structural characteristic frequency is complex and involves three-dimensional irregular geometry. Thus, the simplification process must be rigorous and checked to ensure that the true structural dynamic characteristics are fully represented. This section of the report focuses on requirement analysis and method evaluation.

Two approaches can be used to build a model based on the identification results. One approach is to use the modal characteristics obtained from the identification with state-space equations. This method is intuitive for the identification results and can include the structural dynamic characteristics obtained during the identification stage. However, it cannot represent the actual structure and therefore cannot support physical mechanics research. This is inconsistent with the goals of this study, though it was considered as a reference. The second method involves modifying and simplifying the finite element model to create an accurate simplified model. This approach focuses on the structural form, and its results highly depend on the simplification technology. Additionally, the complex dynamic characteristics of the research target in this case increase the difficulty of the simplification process. However, this approach meets the needs of this study and can be directly applied, so we attempt to identify a suitable technology to achieve this.

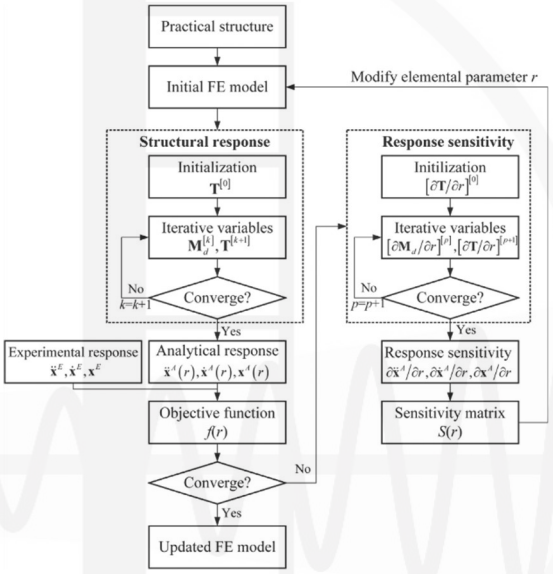

Fig. 8. Flowchart of model refinement [3]

Based on the two approaches described above, this study conducted a relevant literature review, summarized as follows. The first reference is modal decomposition of state-space models proposed by Dahle et al. [1], an online teaching module (OpenCourseWare) from Massachusetts Institute of Technology (MIT). This material clearly introduces the basic concepts of model construction, including the transfer function matrix, system poles and zeros, approximate transformations, and modal coordinates. The formulation is presented clearly.

Another related study on finite element model simplification is the dynamic condensation approach for response-based finite element model updating of large-scale structures proposed by Tian et al. [2]. This study focuses on advanced finite element model operations, including model updating based on structural response verification and the effect of concentrated degrees of freedom (DOF). It also presents demonstration examples of a steel structure and a large-scale suspension bridge. The content of this study closely matches the current needs of this research. The formulation to be addressed in this study

is outlined here. A model updating operation flow diagram is proposed (**Fig. 8)**. The arrangement of the response verification and refinement mechanisms is clearly shown in this figure. In addition, its motivation aligns with the role and importance of fast and effective simulation methods in realistic applications.

A further relevant study is computing the modal mass from the state space model in combined experimental–operational modal analysis (Cara [3]). This study focuses on solving the modal mass in the state space model, which differs slightly from the current study. However, it clearly presents the process, from obtaining experimental vibration data to establishing a state-space model. This offers a useful reference for an alternative research method to this study.

In addition, three related studies described by Lin et al. [4-6] address advanced considerations of simplified models. This proposes a new technology, the general building model, which primarily improves the gap between the old shear-type model and real buildings, making it more accurate. Reference [4] expounds on this novel concept and introduces the technology; references [5] and [6] explore related applications.

Conclusions and Future Work

This study focused on the Taipei building of the NLAC^2, using structural ambient vibration tests to obtain dynamic features. Based on the finite element model derived from the design stage and the performance test report of the isolation components, preliminary model refinement was performed. However, the limited ambient vibration test was unable to clarify abnormal mode shapes or facilitate the pre-planning of the GBM. During model refinement, the corresponding relationship between the isolation floor parameters and the overall structural mode was thoroughly discussed and revised. However, other effects need to be clarified and addressed to improve the alignment between the numerical model and the actual structure. The original plan was to directly apply the generalized building model. However, to account for the complexity of the three-dimensional structure and streamline the research focus, we re-examined the research topic, conducted a literature review, and adjusted the research direction to more clearly define the topic. The results of this discussion are based on three related papers, which provide clear examples and methodological outlines. MIT's online teaching materials also significantly supplements the theoretical background. In addition, the review of the generalized building model was presented. Through these three related papers, the core concepts and relevant application examples of the generalized building model are fully understood. This study will continue to refine and move towards establishing an accurate, rapidly simulated simplified model.

Acknowledgments: I would like to express my special thanks to the executive team of the NLAC^2 ambient vibration test, Mr. H.C. Lin, Prof. C.H. Loh, and colleagues at NLAC^2. I also thank Dr. W.C. Lin for his support in the discussion of the isolation floor.

References

1. Mohammed Dahleh, Munther A. Dahleh, George Verghese, Modal Decomposition of State-Space Models, Dynamic Systems and Control, MIT OpenCurseWare,Spring 2011
2. Wei Tian, Shun Weng, Qi Xia , Yong Xia, Dynamic condensation approach for response-based finite element model updating of large-scale structures, Journal of Sound and Vibration 506 (2021) 116176
3. JavierCara, Computing the modal mass from the state space model in combined experimental–operational modal analysis, Journal of Sound and Vibration, 370(2016)94–110
4. Jui-Liang Lina, Meng-Kwee Kek, Keh-Chyuan Tsaib, Stiffness configuration of strongbacks to mitigate inter-story drift concentration in buildings, Engineering Structures 199 (2019) 109615
5. Jui-Liang Lin, Approximate Quantification of Higher-Mode Effects on Seismic Demands of Buildings, International Journal of Structural Stability and Dynamics Vol. 19, No. 3 (2019) 1950023
6. Jui-Liang Lin, Jyun-Ying Dai, and Keh-Chyuan Tsai, Optimization Approach to Uniformly Distributed Peak Interstory Drifts along Building Heights, J. Struct. Eng., 2019, 145(5): 04019032
7. 榮工工程股份有限公司,中央研究院國家生技研究園區興建工程之 G 棟隔震器 LRB 及 RB 性能保證試驗報告(定稿本),中華民國 105 年 04 月 30 日

Seismic Responses of High-Rise Building Structures to Near-Fault Ground Motions

Wang-Chuen Lin[1], Yi-Hong Li[2] and Jenn-Shin Hwang[3]

林旺春[1]、李奕宏[2]、黃震興[3]

Abstract

Previous studies have shown that high-rise buildings suffer severe damage between one-third to one-half of their height under near-fault ground motions as a result of rapid displacement changes and large velocity pulses. This damage pattern differs from that of far-field ground motions, which typically concentrate damage at the base. Conventional displacement-based design and response spectrum analysis fail to capture such inelastic responses, highlighting the challenge of understanding high-rise building behavior under near-fault ground motions. This study designs two 35-story dual-structural-system buildings according to seismic design codes: (1) a structure with braces at each story and (2) a structure with braces and nonlinear viscous dampers at each story. Nonlinear dynamic time analysis by PISA3D is used to compare responses of high-rise buildings under near-fault and far-field ground motions and explore the inelastic behavior and failure characteristics of the structures. The research results show that both structures suffer serious damage under the whip-like behavior of near-fault earthquakes, but the installation of dampers can slightly reduce the seismic response of the structure and also cause differences in story response. This finding highlights the complexity of the destructive behavior of high-rise buildings under near-fault ground motions. Subsequent research should further analyze the causes and mechanisms underlying this destructive behavior to provide more comprehensive earthquake-resistant design recommendations.

Keywords: near-fault ground motions, responses of high-rise buildings, PISA3D, nonlinear dynamic analysis, nonlinear viscous damper

Introduction

Comparisons of past earthquake records indicate that near-fault earthquakes exhibit significantly different strong-ground-motion characteristics compared to far-field earthquakes. These characteristics include directivity effects caused by fault rupture, permanent ground displacement, early occurrence of velocity pulses, and distinct velocity increments. Such features can strongly influence structural behavior, particularly the dynamic response of high-rise buildings.

In 1978, Bertero *et al*. [1] investigated structural responses under various earthquakes, finding that near-fault ground motions may induce severe inelastic behavior in buildings and that acceleration responses cannot be accurately predicted using conventional response spectrum analysis. Later, Hall *et al*. [2] conducted analyses on a 20-story steel structure model and a 3-story base-isolated structure model. Their results revealed that near-fault ground motions could cause unexpectedly large displacement demands in base-isolated systems, while significant permanent deformations were observed in the mid-to-lower stories of the steel structure. Furthermore, Hall *et al*. emphasized that the influence of ground displacement pulses on structural behavior cannot be adequately predicted by traditional structural dynamics approaches, such as modal analysis of structures. They contended that merely elongating the structural period is insufficient to mitigate the energy input from near-fault earthquakes; instead, enhancing structural ductility is essential to effectively resist near-fault

[1] Associate Researcher, National Center for Research on Earthquake Engineering
[2] Master, National Taiwan University of Science and Technology
[3] Professor, National Taiwan University of Science and Technology

ground motions.

To further investigate the impact of near-fault ground motions on long-period structures, this study designed two 35-story high-rise buildings using steel dual structural systems, in accordance with seismic design codes. Both buildings are equipped with concentrically braced frames throughout all stories; one is additionally equipped with viscous dampers to enhance seismic performance and mitigate damage under near-fault ground motions. Representative near-fault and far-field ground motion records are selected, and nonlinear time-history analyses are conducted to examine the dynamic responses and failure characteristics of high-rise structures subjected to near-fault ground motions.

Research Methods

In this study, a steel dual-structural-system structure composed of conventional concentrically braced frames and special moment-resisting frames is adopted for the structural design. The braced frame system utilizes a diagonal brace configuration. The site is located in Wufeng District, Taichung City, in proximity to the Chelungpu Fault. The structure is designed as a 35-story building, with story heights of 4 m for the first to third stories and 3.5 m for the remaining stories, resulting in a total height of 124 m. In the *x* direction, the structure consists of six bays with a span of 6 m each; in the *y* direction, it comprises four bays with spans of 8 m each. The design dead load is 1 tf/m^2, and the live load is 0.25 tf/m^2. SN490B grade steel is used for the structural members, with member sizes detailed in Table 1.

Table 1. List of member sizes and sections.

Story	Column	Beam	Brace
1–3	□850×36	H50×350×16×30	□400×19
4–6	□800×36	H750×350×16×28	□400×19
7–9	□800×32	H750×300×14×32	□400×16
10–12	□750×32	H700×350×14×30	□400×16
13–15	□750×32	H700×300×14×32	□350×19
16–18	□700×32	H650×300×14×32	□350×19
19–21	□700×28	H650×300×14×30	□350×16
22–24	□650×28	H600×300×14×32	□350×16
25–27	□600×28	H600×300×14×30	□300×19
28–30	□600×25	H600×300×12×28	□300×19
31–33	□550×25	H550×300×12×22	□300×16
34–35	□550×22	H550×200×12×22	□300×16

Two 35-story structures are designed in this study. Model A consists of a concentrically braced frame system with braces installed at all stories. Model B is configured similarly to Model A but is additionally equipped with nonlinear viscous dampers at each story. The structural layouts of both models are illustrated in Fig. 1 and 2, where the left and right sides of each figure depict the configurations of the braced frames and special moment-resisting frames, respectively. Dynamic analyses are conducted using the structural analysis software PISA3D [3]. The fundamental periods of the structures are summarized in Table 2. Model B incorporates a diagonal-type nonlinear viscous damper system designed to achieve a total effective damping ratio of 10%. The bare frame is assumed to have an inherent damping ratio of 5%, with the viscous dampers contributing an additional 5%. To account for flexural and rotational deformation effects commonly observed in mid- to high-rise buildings, a correction formula for the equivalent damping ratio of viscous dampers is applied, as proposed in previous research [4]. Each story is equipped with four dampers in one direction. A uniform distribution method is used to assign the damping coefficients, resulting in a value of 241.53 kN-(s/m)$^{0.3}$ for each damper.

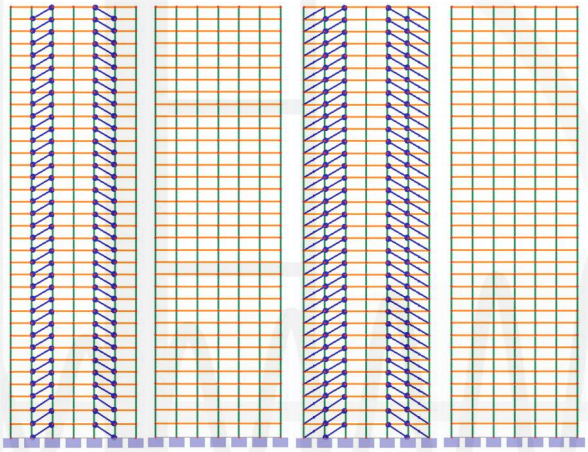

Fig. 1. Model A.

Fig. 2. Model B.

Table 2. The fundamental periods.

	1st model	2nd model
Model A	3.498 s	1.23 s
Model B	3.478 s	1.159 s

Analysis Results

In this study, the north–south component of the ground motion record from the 1940 El Centro earthquake is selected as the far-field seismic input, amplified by 250%. Additionally, the east–west ground motion record from the HWA019 station during the 2018 Hualien earthquake is selected as the near-fault seismic input. These records are used to evaluate structural response differences under varying seismic conditions.

Under the far-field earthquake, plastic hinges are developed based on Model A, as illustrated in Fig. 3(a). The results show that plastic hinges are primarily distributed in the mid-to-upper stories of the structure, without a significant concentration of plastic deformations in any specific region. At 5.3 s, the story drift ratio at the 22nd story reaches a maximum value of 1.11%, as shown in Fig. 3(b). Fig. 4 presents the absolute-displacement response of each story before and after the peak story drift ratio, indicating apparent whip-like behavior.

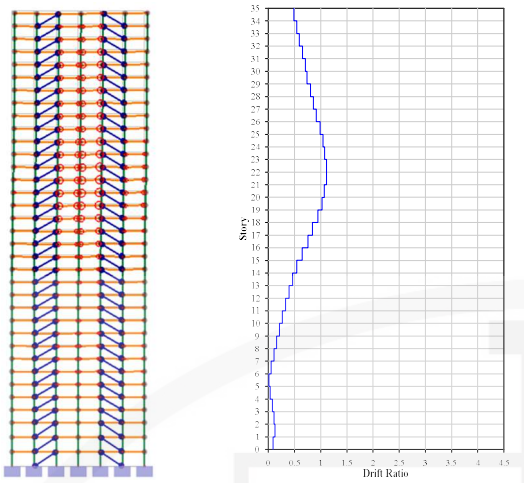

(a) Plastic hinge (b) Story drift ratio

Fig. 3. Model A structural responses (1940 El Centro).

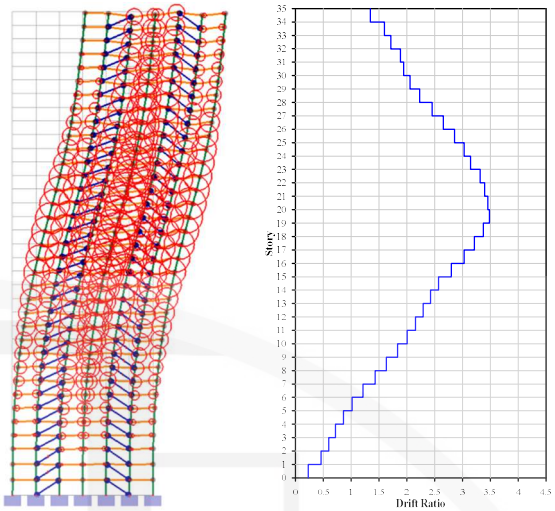

(a) Plastic hinge (b) Story drift ratio

Fig. 5. Model A structural responses (HWA019).

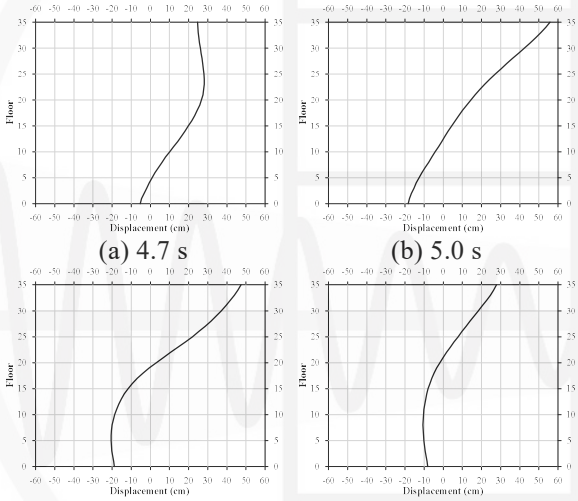

(a) 4.7 s (b) 5.0 s

(c) 5.3 s (d) 5.5 s

Fig. 4. Model A absolute-displacement responses (1940 El Centro).

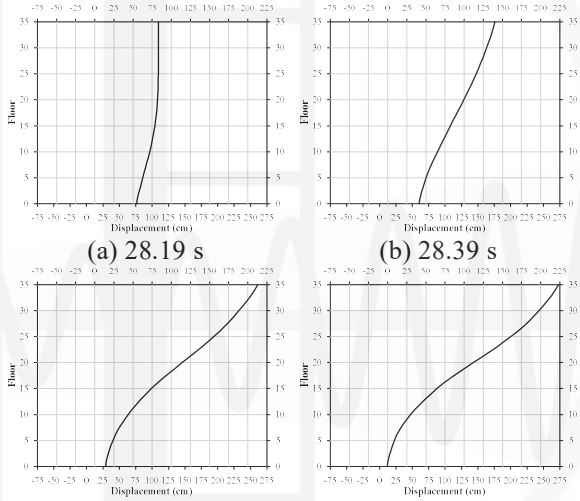

(a) 28.19 s (b) 28.39 s

(c) 28.79 s (d) 29.09 s

Fig. 6. Model A absolute-displacement responses (HWA019).

The plastic hinge development in Model A under the near-fault earthquake is depicted in Fig. 5(a), indicating widespread formation of plastic hinges throughout the entire structure. At 29.09 s, the story drift ratio at the 20th story reached 3.49%, as shown in Fig. 5(b). Unlike the damage patterns described in Hall *et al*. [2], this study finds that the location of maximum damage occurs at approximately 4/7ths of the building height, rather than the 1/3rd height position suggested in the literature. Moreover, the story drift ratio at the 11th story reaches 2%, indicating a considerable level of structural damage. As observed in Fig. 6, at 28.19 s, distinct whip-like behavior begins to emerge, with the lower stories moving to the left while the upper stories move to the right. This opposing movement reaches its peak at 29.09 s, resulting in severe damage and permanent deformation concentrated in the mid-height stories.

Under far-field excitation, Model B reached a maximum story drift ratio of 0.89% at the 28th story at 5.3 s, as shown in Fig. 7(a). The corresponding relative displacement is shown in Fig. 7(b). Comparing the structural responses of Model A and Model B, it is evident that the installation of viscous dampers reduces the maximum story drift ratio, and the location of this maximum story drift ratio shifts from the 22nd story in Model A to the 27th story in Model B. Further comparison of their relative displacements (Fig. 7(b)) reveals that the lateral deformation pattern of Model B, with dampers installed, closely resembles that of the first vibration mode. This suggests that the structure largely remains in the elastic range, with the first mode dominating the deformation. In contrast, the lateral deformation of Model A, without dampers, shows more pronounced inflection points.

Under the near-fault earthquake, Model B reaches a maximum story drift ratio of 3.2% at the 20th story at 29.09 s. Comparing the results of Model A and Model B reveals that the installation of viscous dampers

reduces the maximum story drift ratio from 3.49% to 3.2%, demonstrating the effectiveness of the dampers in mitigating structural deformation, as shown in Fig. 8(a). Although the location of the maximum story drift ratio remains at the 20th story, the overall deformation pattern exhibits some differences. Specifically, the story drift ratio below the 14th story slightly increases, whereas those between the 15th and 35th stories significantly decrease, indicating an overall reduction in structural response. As shown in Fig. 8(b), the relative displacement of the upper stories in Model B is noticeably smaller than that in Model A, confirming that the viscous dampers are effective in reducing displacement demands in the upper stories.

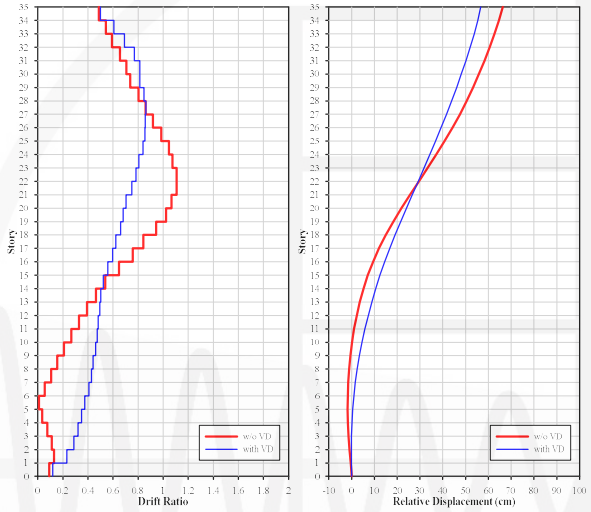

(a) Story drift ratio (b) Relative displacement

Fig. 7. Model B structural responses (1940 El Centro).

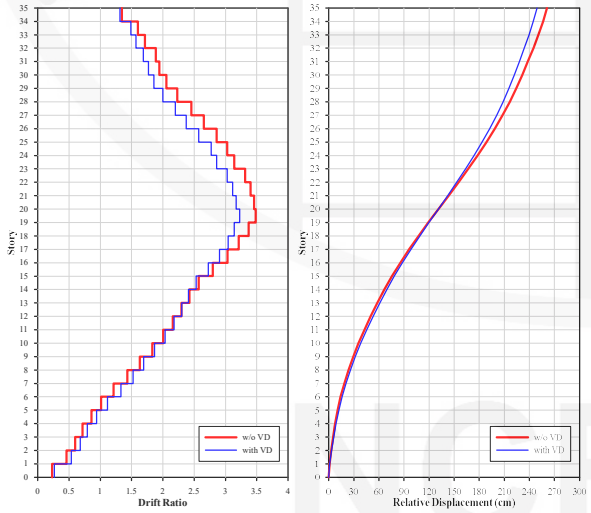

(a) Story drift ratio (b) Relative displacement

Fig. 8. Model B structural responses (HWA019).

Conclusions

This study aimed to investigate the impact of near-fault ground motions on high-rise buildings. Nonlinear analyses were conducted using PISA3D to evaluate the structural responses and failure mechanisms under different seismic conditions. Based on the analysis results, the following conclusions can be drawn:

1. Far-field earthquake effects:

For the 35-story structure with concentrically braced frames installed throughout all stories, the damage under far-field earthquakes is primarily concentrated in the upper stories, consistent with typical far-field seismic damage patterns. Additionally, the absolute-displacement time-history analysis shows no significant occurrence of whip-like behavior.

2. Near-fault earthquake effects:

Under near-fault ground motions, both absolute- and relative-displacement time-history responses reveal pronounced whip-like effects, accompanied by large-scale plastic deformations and permanent displacements. These findings highlight the substantial impact of near-fault earthquakes on high-rise structures.

3. Effects of viscous dampers:

The addition of viscous dampers to the concentrically braced frame system effectively reduces structural responses under far-field earthquakes. However, under near-fault ground motions, although the dampers provide noticeable damping effects, plastic hinges are still observed to form, indicating considerable structural damage.

Future studies should incorporate a broader set of near-fault earthquake records to further investigate relevant damage indices. Moreover, optimizing the distribution formula for the damping constants of viscous dampers may enhance the seismic performance of high-rise buildings subjected to near-fault ground motions.

References

1. Bertero, V.V., Mahin, S.A. and Herrera, R.A. (1978), “Aseismic Design Implications of Near-Fault San Fernando Earthquake Records.” Earthquake Engineering and Structural Dynamics, Vol.6, 31-42.
2. Hall, J.F., Heaton, T.H., Halling, M.W. and Wald, D.J. (1995), “Near-Source Ground Motion and Its Effects on Flexible Buildings.” Earthquake Spectra, Vol.11, No.4.
3. Lin BZ, Chuang MC, Tsai KC. Object-oriented development and application of a nonlinear structural analysis framework. Advances in Engineering Software 2009;40(1):66-82.
4. Hwang, J.S., Huang, Y.N., Yi, S.L. and Ho, S.Y., “Design Formulations for Supplemental Viscous Dampers to Building Structures,” Journal of Structural Engineering, ASCE, (special issue on design and analysis of structures with damping systems), Vol. 134, No.1, pp. 22-31,2008.

Feasibility Study on the Application of Discontinuous Inerters in Equipment Isolation

Wei-Kai Chen[1], Chia-Ming Chang[2], and Cho-Yen Yang[3]

陳威愷[1]、張家銘[2]、楊卓諺[3]

Abstract

Recently, the application of inerters in the control field has attracted considerable interest from researchers. The concept of inerters is to increase the effective mass of dynamic systems by increasing rotational inertia, and its control force is proportional to the relative acceleration at both ends of the inerter. This mechanical property is innovative and entirely different from conventional stiffness and damping mechanisms. Thus, the application of inerters in structural control has become a popular topic, and various mechanisms of inerters have been proposed to improve the performance of seismic isolation. The most basic inertial mechanism involves full-motion coupling with the dynamic system. In seismic isolation, the inertial force acts in opposition to the direction of motion, which allows a well-designed inertial mechanism to effectively reduce the displacement response of the isolation system and improve its seismic performance. However, for such full-motion coupling inerters, if the inertia of the inerter is significantly higher than that of the isolation system, energy may be transferred back to the isolation system, which may increase the acceleration response. To address this disadvantage of full-motion coupling inerters, a discontinuous switching inerter is proposed and investigated in this paper. The discontinuous switching is implemented mechanically so that the inerter works only when the isolation displacement is within a specific effective range to mitigate the isolation displacement. Conversely, the inerter and isolation systems are independent in motion when the isolation displacement exceeds the effective range, which prevents the increase in acceleration response.

Keywords: seismic isolation, discontinuous inerter, friction pendulum bearing, shaking table, harmonic balance method

Introduction

Due to their unique mechanical characteristics, inerters have attracted considerable attention from scholars, leading to numerous studies on their feasibility for structural control applications. The development of the inerter can be traced back to the flywheel in the mechanical field. As early as 2000, Kuroda et al. (2000) employed a ball screw mechanism to convert the originally simple linear relative motion of a mass into rotational motion. Subsequently, Smith (2002) developed a similar device using a different mechanism, which enhanced the overall mass contribution and effectively improved the control performance of mass dampers, particularly in automotive suspension systems. In structural control, Zhang et al. (2020) investigated the potential application of inerters in seismic isolation of buildings. They integrated inerters with nonlinear isolation systems and demonstrated that such systems exhibit excellent isolation performance within specific frequency ranges, effectively suppressing the transmission of energy to the main structure. Building on this research, the present study proposes a novel

[1] Graduate Student, National Taiwan University

[2] Professor, National Taiwan University and Adjunct Research Fellow, National Center for Research on Earthquake Engineering

[3] Associate Researcher, National Center for Research on Earthquake Engineering

nonlinear isolation system that combines a self-resetting pendulum-friction bearing with a discontinuous inerter. The discontinuous inerter adopts a segmented design: within the effective length, defined as the coupling displacement range, the inerter fully engages with the isolation system. This engagement enables the inerter to utilize its properties to reduce displacement responses. When the displacement of the isolation system exceeds the coupling range, the inerter disengages to avoid its adverse effects on post-isolation acceleration, achieving a certain degree of multi-objective performance. Thus, the engagement of the inerter is a function of displacement. For this dynamically nonlinear system, a probabilistic statistical approach is proposed for design, allowing for the incorporation of uncertainties in both the system and external forces. These uncertainties are modeled as random variables described by probability density functions and analyzed within a stochastic process framework, which provides better insight into the behavior of nonlinear systems under seismic action (Jensen and Sepulveda, 2000). Di Paola and Navarra (2009) applied statistical linearization techniques together with the response spectrum method to determine the equivalent damping ratio under steady-state structural vibration. In control system design, stochastic vibration theory can be combined with the corresponding frequency response spectra as seismic input. By minimizing the root-mean-square error, a statistical linearization model can be constructed, enabling the direct design of control system parameters through a linear model. This approach addresses the complexity and uncertainty of nonlinear systems and facilitates the design of parameters that meet design criteria under various seismic forces.

Mathematic Model

The schematic diagram of the proposed isolation system with a discontinuous inerter is shown in Fig. 1. The mechanism consists of an isolation platform, roller, flywheel, rolling surface, frictional plate, and driven roller. The inerter is driven by the friction force between the frictional plate and the driven roller when the isolation system is in motion. The curvature of the rolling surface is R, and the radius of the driven roller and flywheel are r_{d1} and r_{d2}, respectively. δ is the effective length.

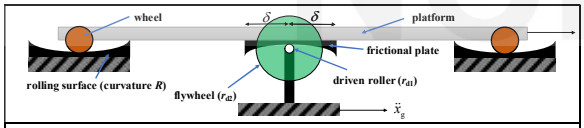

Fig. 1 Schematic diagram of the isolation system with a discontinuous inerter.

According to the mechanical concept of the system illustrated in Fig. 1, the equation of motion (Eq. 1) could be derived and obtained by the energy method, where m is the mass of the platform, c is the damping coefficient representing the lightly damping effect in motion. $\beta = \frac{1}{2}\frac{m_d}{m}\frac{r_{d2}^2}{r_{d1}^2}$ is a mass ratio that represents the increment of mass for the system due to the inerter.

$$\begin{cases} x + \frac{c}{m}x + \frac{g}{R}x = -x_g, if|x| > \delta \\ (1+\beta)x + \frac{c}{m}x + \frac{g}{R}x = -x_g, if|x| \le \delta \end{cases} \quad (1)$$

Eq. (1) indicates that the system is a normal friction pendulum system when the isolation displacement exceeds the effective length δ. On the contrary, the additional inertia would join and affect the dynamic behavior through the mass ratio β.

Numerical Simulation

In conventional analysis of a linear system, the Laplace transform can be implemented to obtain the frequency response of the system. However, this method is not feasible for a nonlinear system. Thus, the harmonic balance method can be implemented to indirectly obtain the frequency response of the system. To derive the frequency response, the ground motion is assumed to be a sinusoidal excitation as $\ddot{x}_g = B\sin\omega t$, and the response is assumed as $x = Asin(\omega t + \phi)$. Based on the harmonic balance method, the frequency of displacement and acceleration can be represented as follows:

$$B^2 = \left(-\frac{Awc}{m}\right)^2 + \left(-Aw^2 + \frac{gA}{R} - Aw^2\beta\left(\frac{z_1}{\pi}\right)\right)^2 \quad (2)$$

$$||\ddot{u}_{abs}|| = \sqrt{B^2 + \omega^4A^2 - 2B\omega^2Acos\phi}$$

$$cos\phi = -\frac{Aw^2}{B} + \frac{gA}{RB} - \frac{Aw^2\beta}{B}\left(\frac{z_1}{\pi}\right) \quad (3)$$

where $z_1 = 2\phi_0 - 2sin\phi_0$ and $\phi_0 = \sin^{-1}(\frac{\delta}{A})$. Substituting the design parameters of the system, that is, the amplitude and frequency of the excitation, into Eqs. (2) and (3), the amplitude in the frequency response can be obtained. Similarly, this method can be used to derive the frequency response for the case with a full-motion coupling inerter and that without an inerter. However, due to the length limitation, only the result of the isolation systems with a discontinuous inerter is introduced.

Based on the frequency response functions derived using the harmonic balance method, the

displacement and acceleration responses for the three isolation cases subjected to 0.1 g sinusoidal excitation are illustrated in Figs. 2 and 3. Fig. 2 clearly shows that the displacement frequency response of the discontinuous case matches that of the case with the full-motion coupling inerter (i.e., the continuous inerter) when the isolation displacement is within the effective length, which demonstrates the effectiveness in mitigating the displacement response. A similar result can be observed in Fig. 3, where the acceleration response is effectively mitigated for an excitation frequency of 0.8–1.2 Hz. However, the acceleration response increases with increasing excitation frequency and is even higher than the case without an inerter in the high-frequency region. For the isolation system with a discontinuous inerter, the fundamental frequency of the system may lie between the fundamental frequencies of the system with a continuous inerter and that without an inerter.

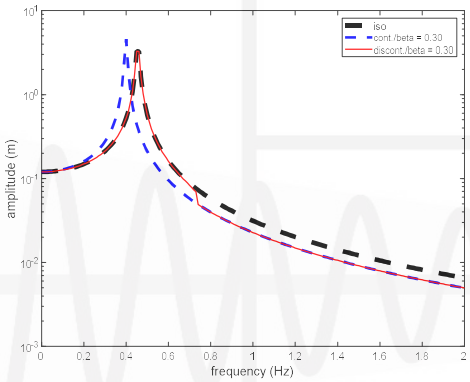

Fig. 2 Comparison of frequency response to displacement.

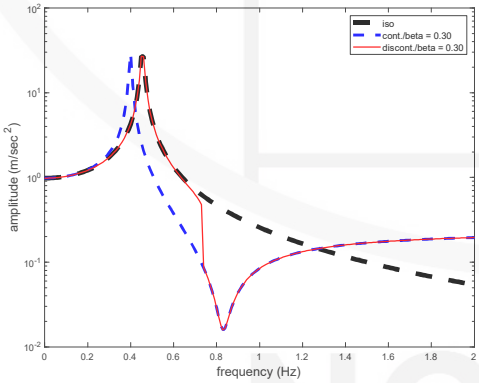

Fig. 3 Comparison of frequency response to acceleration.

To further investigate the influence of mass ratio on the frequency response, six cases with mass ratios varying from 0.05 to 0.5 are simulated and compared in Figs. 4 and 5. In Fig. 4, in the high-frequency region, a higher mass ratio corresponds to a lower displacement response; however, a higher mass ratio also results in a higher acceleration response bounded by $\beta/(1+\beta)$. Therefore, although the displacement response can be mitigated by increasing the mass ratio, it cannot decrease the acceleration response. A feasible range of mass ratio varying from 0.1 to 0.3 is considered in this paper.

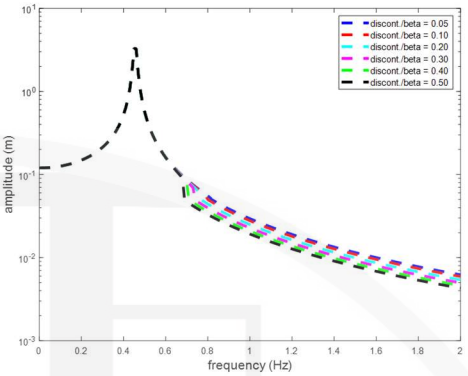

Fig. 4 Sensitivity of mass ratio on displacement frequency responses.

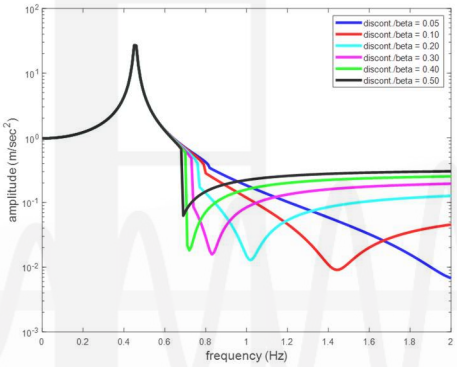

Fig. 5 Sensitivity of mass ratio on acceleration frequency responses.

Shaking Table Testing

A small-scale shaking table test was conducted to verify the analytical model and simulation results. The specimen of the entire system consisted of a base plate, four single-curvature guides, an inerter, and an isolation platform, as shown in Figs. 6 and 7. The isolation system consisted of a platform with four wheels and a frictional plate, and the total weight was 18.11 kg. This isolation system rolls on guides with a curvature of 1.2 m, which provides a $\pm$ 15 cm isolation displacement. The subsystem of the inerter consisted of two driven rollers, flywheels, screws, and a base. Each driven roller had a diameter of 20 mm and thickness of 30 mm and weighed 0.025 kg. The flywheel had a diameter of 120 mm, a thickness of 20 mm, and a weight of 0.6 kg, with each flywheel providing an additional mass ratio of 0.125. The specific length of the frictional plate, determined by the parameter δ, was used to trigger the inerter subsystem.

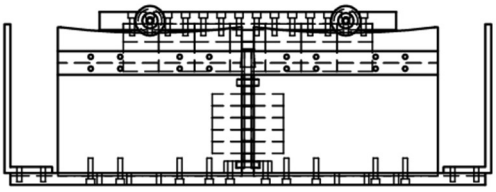

Fig. 6 Front view of design drawing.

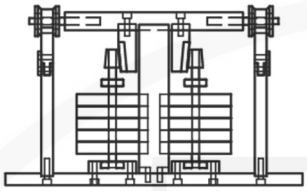

Fig. 7 Side view of design drawing.

A uniaxial small-scale shaking table at the National Center for Research on Earthquake Engineering (NCREE) was used. The table had dimensions 1000 mm × 800 mm and an actuator stroke of ± 150 mm. The setup of the specimen is shown in Fig. 8. For the sensor layout, three uniaxial accelerometers were used, two of which were mounted at the front and back of the platform and one on the shaking table. Additionally, a displacement transducer was adopted to measure the isolation displacement.

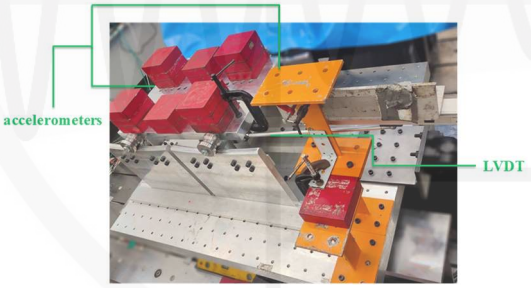

Fig. 8 Specimen setup and sensor layout.

For the input to the shaking table, several domestic ground motions, including those of the 1999 Chi-Chi, 1999 Chiayi, 2002 Hualien, 2006 Hengchun, and 2016 Meinong earthquakes, were considered. The measurements of the shaking table test were compared with the resimulation results to verify the analytical model. For the Chi-Chi earthquake, the resimulation results (shown in Fig. 9) closely align with the experimental results. This implies that the dynamic behavior of the proposed isolation system with a discontinuous inerter can be represented by the mathematical model, thus preliminarily verifying the feasibility of the mechanism.

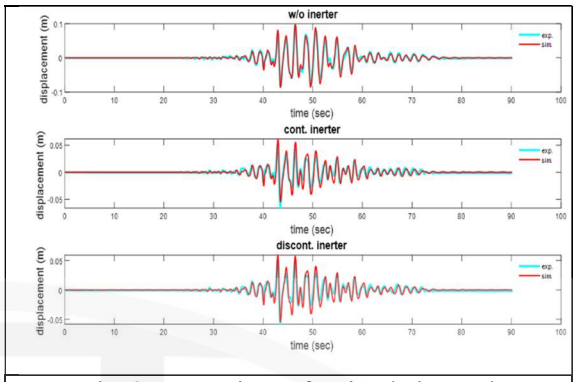

Fig. 9 Comparison of resimulation and experimental results (Chi-Chi, TCU107, E-W).

Conclusions

In this paper, the feasibility of the proposed concept and mechanism of an isolation system that incorporates a discontinuous inerter was preliminarily investigated and verified. The idea was inspired by the continuous inerter but modifications were made by introducing an effective length to improve control performance. With the appropriate design, the proposed isolation system with a discontinuous inerter can effectively mitigate the isolation displacement under minor to moderate earthquakes. Additionally, the system can reduce both the acceleration and isolation displacement under a beyond-design-basis earthquake. Experimental verification confirms the correctness and feasibility of the proposed mechanism.

References

Kuroda, H., Arima, F., Baba, K., & Inoue, Y. (2000). Principles and characteristics of viscous damping devices (gyro-damper), the damping forces which are highly amplified by converting the axial movement to rotary one. In 12th World Conference on Earthquake Engineering.

Smith, M. C. (2002). “Synthesis of mechanical networks: the inerter.” IEEE Transactions on Automatic Control, 47(10), 1648-1662.

Zhang, Z., Zhang, YW. Y., & Ding, H. (2020). "Vibration Control Combining Nonlinear Isolation and Nonlinear Absorption." Nonlinear Dyn 100, 2121-2139.

Jensen, H. A., & Sepulveda, A. E. (2000). Optimal design of uncertain systems under stochastic excitation. AIAA journal, 38(11), 2133-2141.

Di Paola, M. and Navarra, G. (2009), Stochastic seismic analysis of MDOF structures with nonlinear viscous dampers. Struct. Control Health Monit., 16: 303-318. https://doi.org/10.1002/stc.254

Chen, Wei-Kai (2024), “Preliminary Study of Isolation Bearing with Discontinuous Inerters for Seismic Protection of Essential Equipment and Components,” Master Thesis, National Taiwan University.

Seismic Performance for Confinement of the Reinforced Concrete Kernel-Confined Column

Kai-Ning Chi[1], Ker-Chun Lin[2], Sheng-Jhih Jhuang[1], and Chen Hao[3]

紀凱甯[1]、林克強[2]、莊勝智[1]、陳顥[3]

Abstract

In high-rise buildings, lower-story columns that must withstand high axial loads may experience issues such as poor concrete placement and detailing conflicts due to reinforcement congestion. Under seismic forces, spalling of the concrete cover exposes the outer longitudinal reinforcement, thus reducing its buckling strength. This phenomenon adversely affects the seismic performance of column members, compromising the overall structural safety. This study tests six full-scale reinforced-concrete column specimens with a cross-section of 600 × 600 mm, utilizing concrete with a compressive strength of 42 MPa, SD 550W longitudinal reinforcement, and SD 785 transverse reinforcement. It is proposed to relocate part of the outer longitudinal reinforcement to the confined concrete core, forming a kernel-confined (KC) steel-bar column to address deficiencies in practical reinforcement detailing. The column design follows the confinement provisions for axial force control in accordance with ACI 318-19 and axial loading is applied based on the actual confined reinforcement ratio. Experimental results indicate that the KC column configuration increases the spacing between outer longitudinal bars, effectively resolving construction difficulties caused by conflicts in transverse reinforcement. All six specimens exhibit axial-compression failure modes. However, specimens with f_c' less than 70 MPa and transverse reinforcement with f_{yt} of 690 MPa failed to achieve the expected strength and deformation capacity. This was due to the inconsistency between the ultimate lateral strain of concrete and the strain required for the transverse reinforcement to develop its design strength. Thus, the compatibility of lateral deformation between concrete and confinement reinforcement is a critical factor influencing the deformation capacity of column members.

Keywords: reinforced-concrete column, kernel-confined column, confinement, deformation compatibility

Research Motivation and Objectives

In current domestic structural-design practice, the cross-sections of columns must balance economic efficiency and functionality. To maximize usable space, the column cross-section should not be excessively large. Meanwhile, to enhance the flexural design capacity, longitudinal reinforcement is typically arranged along the outer edges. Although lower-story columns require higher ductility, space constraints often result in a high longitudinal-reinforcement ratio exceeding 4%, leading to reinforcement congestion, poor concrete placement, and detailing conflicts. Under seismic loading, spalling of the concrete cover exposes the outer longitudinal reinforcement, while deformation of transverse reinforcement reduces the buckling resistance of the longitudinal bars. These effects negatively impact the seismic performance of columns and compromise structural safety.

This study investigates the performance of special moment-frame columns under high axial loads according to the Building Concrete Structural Design Code (Ministry of the Interior, 2023) and ACI 318-19 (ACI, 2019). This study adopts a transverse-reinforcement design strength of 790 MPa and explores various longitudinal-reinforcement configurations and confinement-reinforcement details to develop kernel-confined (KC) columns, which are both constructible and functionally efficient. The KC column design aims to increase the spacing between outer longitudinal bars, thus addressing construction

[1] Assistant Researcher, National Center for Research on Earthquake Engineering
[2] Research Fellow, National Center for Research on Earthquake Engineering
[3] Master, National Taiwan University of Science and Technology

challenges caused by reinforcement congestion, such as improving concrete placement and resolving conflicts at transverse-reinforcement hooks. Additionally, KC bars are introduced to delay inelastic buckling of longitudinal reinforcement, thereby mitigating deficiencies observed in current column-design practices.

Confinement-Reinforcement Design for Reinforced-Concrete Column Members

According to the Building Concrete Structural Design Code and Section 18.7.5 of ACI 318-19, the confinement-reinforcement requirements for rectangular columns in special moment-frame systems are specified as follows:

The purpose of Eq. (1), below, is to ensure that, after spalling of the concrete cover, the transverse ties can provide adequate confinement for the core concrete, allowing it to sustain high compressive stress. For ease of discussion, this equation is denoted as $R_{t,(a)}$ in this study. However, when designing confinement reinforcement for large column cross-sections, using Eq. (1) alone may lead to an insufficient amount of transverse reinforcement, owing to the small value of ($A_g/A_{ch} - 1$). Therefore, an additional equation, Eq. (2), is used to define the lower limit of confinement reinforcement, denoted as $R_{t,(b)}$. To ensure that column members subjected to high axial loads can still accommodate a lateral drift demand of 3%, ACI 318-19 recommends that, when using high-strength concrete ($f_c' > 70$ MPa) or when the axial load exceeds $P_u > 0.3A_gf_c'$, each longitudinal-reinforcement bar must be confined using seismic hooks (135° or 180° hooks) in closed ties or cross ties to meet the confinement requirements. Additionally, in confinement-reinforcement design, the required amount of confinement reinforcement must satisfy Eq. (1) and Eq. (2), and an additional comparison must be made using Eq. (3). The final design must adopt the largest value among the three equations. Equation (3) was proposed by Paultre and Légeron (2008), based on the concrete-confinement effect model developed by Mander *et al*. (1988). The purpose of this equation is to prevent axially loaded column members from undergoing compression-controlled failure, which could negatively impact lateral deformation capacity. This issue is particularly critical when the axial load exceeds $P_u > 0.3\ A_gf_c'$ or when high-strength concrete ($f_c' > 70$ MPa) is used. In this study, Eq. (3) is denoted as $R_{t,(c)}$. The three equations are as follows:

$$R_{t,(d)} = \frac{A_{sh}}{sb_c} \geq \begin{cases} R_{t,(a)} = 0.3\dfrac{f_c^{'}}{f_{yt}}\left(\dfrac{A_g}{A_{ch}} - 1\right), & (1) \\ R_{t,(b)} = 0.09\dfrac{f_c^{'}}{f_{yt}}, \text{ and} & (2) \end{cases}$$

$$\left| \begin{array}{l} R_{t,(c)} = 0.2k_f k_n \dfrac{P_u}{f_{yt}A_{ch}} \\ \Uparrow when \begin{array}{l} P_u \geq 0.3A_g f_c^{'} \\ f_c^{'} \geq 70MPa \end{array} \end{array} \right| , \quad (3)$$

where A_{sh} is the total area of transverse reinforcement (mm^2), s is the spacing of transverse reinforcements (mm), b_c is the distance between the outermost transverse reinforcements (mm), A_g is the gross cross-sectional area (mm^2), A_{ch} is the core concrete area enclosed by the outermost transverse reinforcement (mm^2), f_c' is the compressive strength of concrete (MPa), f_{yt} is the yield strength of transverse reinforcement (MPa), P_u is the axial load applied to the column member (N), k_f is the concrete strength factor, k_n is the effective confinement factor, and finally n_l is the number of longitudinal-reinforcement bars confined by 90° stirrups and seismic hooks along the outer perimeter of the core concrete.

Experimental Design for Column Members

The experimental design parameters include longitudinal-reinforcement configurations, transverse-reinforcement strength, and confinement detailing. By varying the proportion of core longitudinal reinforcement and adopting different confinement-reinforcement detailing based on various code requirements, this study investigates the seismic performance of KC columns.

A total of six full-scale reinforced-concrete (RC) column specimens were designed. The materials used include concrete with a compressive strength of 42 MPa, SD 550W longitudinal reinforcement, and SD 785 transverse reinforcement. The column specimens have an aspect ratio of 3, and the transverse-reinforcement detailing follows common industry-standard seismic-tie configurations, including 135° closed stirrups, ties with one end bent at 90° and the other at 180°, and SD 785 welded closed stirrups (Power-Ring). The detailed specimen configurations are shown in Figure 1.

To better simulate the behavior of actual buildings under seismic forces, tests were conducted at the National Center for Research on Earthquake Engineering (NCREE) using the Multi-Axial Testing System (MATS). A constant axial load was applied while performing cyclic lateral displacement loading in a double-curvature bending configuration. The seismic performance tests were conducted with a target drift ratio of 3%, as illustrated in Figure 2. The displacement history used in the tests is shown in Figure 3, with peak drift angles of ±0.125%, ±0.25%, ±0.375%, ±0.5%, ±0.75%, ±1%, ±1.5%, ±2%, ±3%, ±4%, and ±5%, each repeated for three loading cycles. Lateral loading was applied at three different rates:

drift ratio 0.125% to 0.5% at a loading rate of 0.5 mm/s; drift ratio 0.75% to 3% at a loading rate of 2 mm/s; and drift ratio 4% to 5% at a loading rate of 3 mm/s.

Analysis and Discussion of Test Results

- **Strength Response and Failure Modes**

The shear strengths of all specimens significantly decreased after reaching the peak drift angle of 1.5%. Compared to the specimens with all longitudinal reinforcement placed at the edges, the KC column had fewer longitudinal reinforcements at the edges, resulting in a more limited flexural strength. Observations of the crack patterns indicated that the concrete cracks in all six specimens primarily developed along the axial direction, differing from typical flexural-shear failure and flexural failure modes. Therefore, it is concluded that the six specimens failed as a result of axial compression. Detailed crack patterns are shown in Figure 4. The shear–displacement relationships for each specimen are shown in Figure 5.

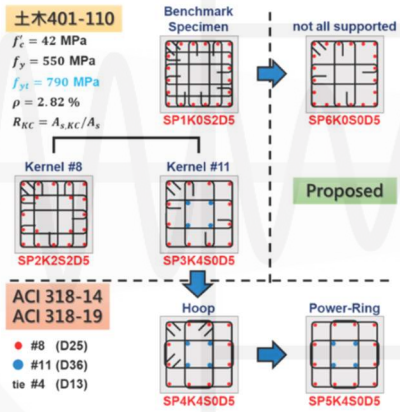

Fig. 1. Comparison of specimen configurations.

Fig. 2. Test setup.

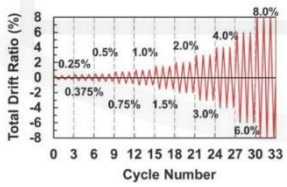

Fig. 3. Loading protocol.

- **Deformation Performance**

For all six specimens, the average drift ratio at 80% of maximum shear strength after the strength dropped by 80% in both positive and negative directions was below the target deformation capacity of 3% drift. The results of the strength and deformation tests are summarized in Table 1.

Fig. 4. Failure modes of specimens after 3% drift angle displacement (east view).

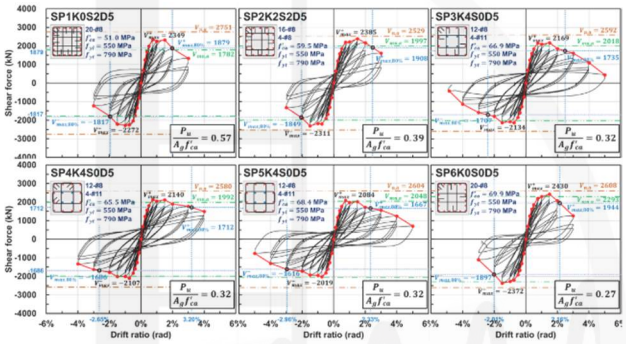

Fig. 5. Horizontal shear-force–displacement relationships for each specimen.

Table 1. Summary of test results (*DR*: drift ratio).

Specimen	f'_{ca} (MPa)	DCR	Side	DR_{max} (%)	V_{max} (kN)	$V_{max,avg}$ (kN)	$DR_{80\%}$ (%)	$DR_{80\%,avg}$ (%)
SP1K0S2D5	51.04	1.00	+	0.75	2349	2311	1.97	1.96
			−	-1.00	-2272		-1.95	
SP2K2S2D5	59.51	1.00	+	1.50	2385	2348	2.46	2.26
			−	-1.50	-2311		-2.06	
SP3K4S0D5	66.91	1.00	+	1.50	2169	2152	2.48	2.44
			−	-0.75	-2134		-2.41	
SP4K4S0D5	65.49	0.87	+	0.75	2140	2124	3.20	2.93
			−	-0.75	-2107		-2.65	
SP5K4S0D5	68.41	0.87	+	0.75	2084	2052	2.33	2.65
			−	-0.75	-2019		-2.96	
SP6K0S0D5	69.88	0.87	+	1.50	2430	2401	2.16	2.09
			−	-1.50	-2372		-2.01	

- **Confinement Performance Discussion**

Specimens SP4K4S0D5 and SP5K4S0D5, with f_{yt} = 690 MPa used as the design strength for transverse reinforcement, did not achieve the target deformation capacity of 3% drift angle even when complying with the confinement requirements of ACI 318-19. A comparison of the experimental results from this study with previous research (Huang, 2021) is shown in Figure 6, highlighting significant differences in the deformation performance of column specimens under high-strength and normal-strength concretes.

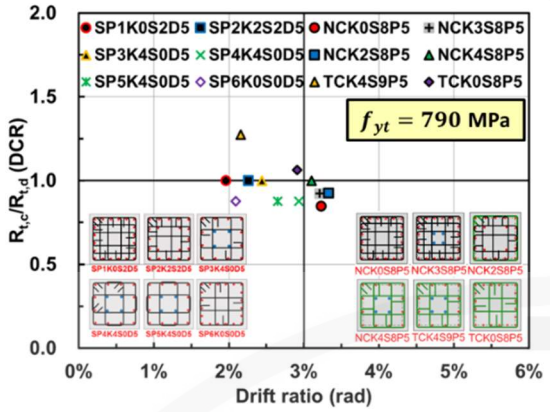

Fig. 6. Relationship between confinement reinforcement and deformation for the specimens.

- **Material Strain Compatibility**

The development of transverse stress and strain in both unconfined and confined concrete, as well as the longitudinal stress–strain relationship of transverse reinforcement, are illustrated in Figure 7. Since the experimental results show that the average drift ratio at 80% strength for all specimens did not achieve the target deformation of 3% drift, it is concluded that confined concrete cannot provide sufficient strength and deformation capacity beyond approximately 2% drift. For further details, please refer to the past work (Chen 2022).

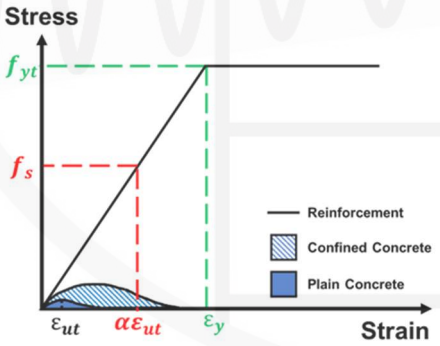

Fig. 7. Schematic diagram of the stress–strain relationships for confinement reinforcement and concrete.

Conclusion and Recommendations

The purpose of this study was to investigate the seismic behavior of column members subjected to high axial loads. Based on the $R_{t,(c)}$ confinement formula controlled by axial force in ACI 318-19, the axial pressure was applied according to the actual confinement-reinforcement volume calculation. The column-reinforcement materials used were SD 550W longitudinal bars and SD 785 transverse bars, with the actual compressive strength of the concrete ranging between 51 to 69 MPa. The main conclusions are as follows:

1. The deformation results for column specimens with concrete strengths not exceeding 70 MPa showed that, when applying the axial force calculated based on the $R_{t,(c)}$ confinement formula, the specimens could not achieve a 3% drift lateral deformation capacity, regardless of whether the transverse-reinforcement design strength was 690 MPa or 790 MPa. However, increasing the amount of confinement steel by lowering the design strength of the transverse reinforcement contributed to improving the deformation capacity.

2. The confinement reinforcement and concrete strength used in the column members should maintain an appropriate matching ratio. The strain developed in the confinement steel at design strength should not exceed the ultimate lateral tensile strain that the core concrete can provide.

3. For columns bearing high axial pressure, at the limit state, the likelihood of yielding of the longitudinal bars in tension is lower. Conventional longitudinal bars placed at the outer edges of column members may increase the potential for compressive buckling, owing to the loss of the concrete cover. This study showed that, when the KC bar accounts for 40% of the total longitudinal reinforcement, it can still delay the onset of buckling in the longitudinal bars.

References

ACI Committee 318 (2019), "*Building Code Requirements for Structural Concrete and Commentary*," American Concrete Institute (ACI), Farmington Hills.

J. B. Mander, M.J.N. Priestly, and R. Park, (1988), "*Theoretical Stress-Strain Model For Confined Concrete*," Journal of Structural Engineering, 114(8), pp. 1804-1826.

Paultre, P., and Légeron, F., (2008), "*Confining Reinforcement Design for Reinforced Concrete Columns*." Journal of Structural Engineering, ASCE, V. 134, No. 5, May, pp.738-749.

Construction and Planning Agency Ministry of the Interior (2023), *Specifications for Design of Concrete Structures*, Taipei, Taiwan.

Huang Jun-Kai (2022), "Study on High-Strength Rectangular RC Columns with Kernel Confined Rebars," National Taiwan University of Science and Technology, Master Thesis, Advisor: Ker-Chun Lin.

Chen Hao (2022), "Study on Seismic Performance for Confinement of RC KC Column," National Taiwan University of Science and Technology, Master Thesis, Advisor: Ker-Chun Lin.

Experimental Behavior of Steel Pipe with a Single Wave Feature

Ker-Chun Lin[1], Tsu-Wei Yuan[2], Sheng-Jhih Jhuan[3], Kai-Ning Chi[3], Gee-Yu Liu[1], and Chui-Hsin Chen[4]

林克強[1]、袁祖威[2]、莊勝智[3]、紀凱甯[3]、劉季宇[1]、陳垂欣[4]

Abstract

Steel pipe with a wave feature is designed for crossing faults. This pipe is capable of significant deformation and is suitable for crossing faults with large displacement deformation; it is referred to as steel pipe crossing fault (SPF). The SPF discussed in this study has a specific wave feature designed to absorb axial and bending deformation caused by fault displacement, with a nominal diameter of 800 mm, a wall thickness of 8 mm, and a single wave form with a wave height (h_F) of 115 mm. The experiment on this single-wave pipe is divided into deformation tests and a hydraulic pressure test. The deformation tests include axial compression, axial tension, and four-point bending tests. The results of axial compression test indicated that the specimen developed a maximum load of 660 kN, after which the strength gradually decreased; when the deformation reached 120 mm, the strength was 454 kN. In the axial tension test, the specimen's strength increased with deformation; when the tensile displacement reached 119 mm, the strength increased to 3922 kN. In the four-point bending test, the wave segment exhibited elastic–plastic and hardening behavior; when the deformation angle of the wave segment reached 12.6°, the plastic bending moment strength was 214 kN-m, and the hardening strength reached 527 kN-m as the deformation progressed to 17.9°. After the loading tests were completed, the three specimens were subjected to a hydraulic pressure test. Under a water pressure of 1.2 MPa (12.5 kgf/cm²) maintained for 300 seconds, none of the specimens exhibited leakage.

Keywords: fault-crossing steel pipe, water transmission pipe, wave feature, fault displacement, seismic design

1. Introduction

Under orogenic movement caused by compression between the Philippine Sea Plate and the Eurasian Plate, Taiwan Island has developed a geological fault structure that is primarily oriented in a north–south direction. According to a 2021 announcement by the Central Geological Survey of the Ministry of Economic Affairs in Taiwan, there is a total of 36 Category I and II faults on the island (Lin et. al., 2021). For large-scale underground lifelines in Taiwan, it is difficult to avoid crossing these faults and to mitigate the impacts of fault displacement. When pipelines intersect faults, they may experience axial compression, tension, bending, or a combination of deformation modes, depending on the fault type and the angle between the pipeline and the fault. Historically, pipeline systems in Taiwan have consisted of straight pipes and various flexible joints. However, as fault displacement increases, these pipeline systems may be subjected to issues such as pipe fracture, buckling, damage, and joint failure, ultimately leading to economic losses and public livelihood problems. A report on an investigation of pipeline damage from the 1999 Chi-Chi earthquake categorized damage to water supply pipelines into straight pipe failure, joint failure, and component failure, with 58% of the damage occurring in straight pipes. This indicates that for water transmission pipelines located near or crossing faults, the straight

[1] Research Fellow, National Center for Research on Earthquake Engineering (NCREE)
Professor, Department of Civil and Construction Engineering, National Taiwan University of Science and Technology
[2] Engineer, Shie-Ho Engineering Consultant LTD
[3] Assistant Researcher, National Center for Research on Earthquake Engineering (NCREE)
[4] Associate Professor, Department of Civil Engineering, National Yang Ming Chiao Tung University

pipe sections do not meet the seismic deformation requirements. Therefore, it is critical for water transmission pipelines that cross faults to maintain their functionality during fault displacement.

To address the loss of functionality in water transmission pipelines due to fault displacement, Japan's JFE Corporation developed a fault-crossing steel pipe with a wave-shaped geometry, known as the steel pipe crossing fault (SPF), as shown in Figure 1(a). The wave feature is integrally formed, with h_F denoting the wave height. According to the Japan Water Steel Pipe Association (2014), the axial deformation capacity of SPF is specified as 1.0 hF, and the allowable design rotational deformation is 8°. The wave feature utilized in this study is formed by welding two symmetrical half-wave shapes at the wave crest, as shown in Figure 1(b). The two symmetrical half-wave steel plates are shaped by cold (room temperature) stamping.

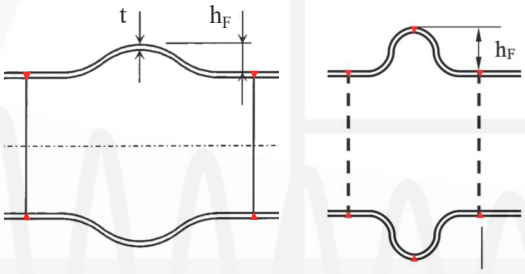

(a) JFE wave feature, (b) wave feature used in this study

Fig. 1. Wave features of JFE and this study

This study aims to investigate the experimental behavior of the SPF shown in Figure 1(b) under monotonic loading. Axial compression, axial tension, and bending tests were conducted to examine the axial and flexural mechanical behavior of the SPF. After these loading tests, all three specimens underwent a hydraulic pressure test to verify whether any leakage occurred under sustained water pressure of 1.2 MPa (12.5 kgf/cm²) for 300 seconds.

2. Test Program

In this study, three tests were conducted on SPF steel pipes: axial compression, axial tension, and four-point bending, designated as SPF-C1, SPF-T1, and SPF-B1, respectively. Each SPF specimen comprises a wave segment and two straight segments on either side. The wave segment was fabricated by welding two cold-stamped half-wave components together at the wave crest using single-sided V-groove full-penetration welds. The joints between the wave segment and the two straight segments were also constructed using the same full-penetration welds. The size and details are illustrated in Figure 2. All three specimens share the same pipe diameter and material specifications. The outer diameter of the steel pipe was 812.8 mm, the wall thickness was 8 mm, and the wave height (h_F) at the center of the wave segment was 115 mm. The pipe material was SS400 steel. The specimen dimensions are provided in Table 1.

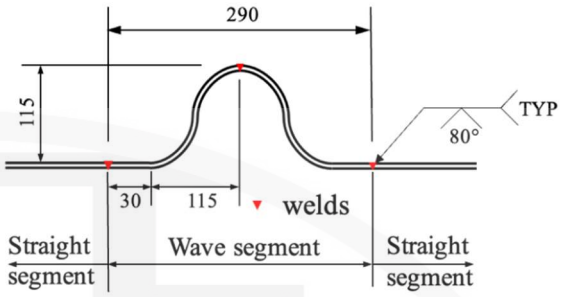

Fig. 2. Size and welding details of SPF used in this study

Table 1 Specimen dimension table.

Specimens	SPF-B1	SPF-C1 SPF-T1
Designation (1)	800A	800A
Outer diameter D_o, mm	812.8	812.8
Wall thickness, mm	8	8
Wave height h_F, mm	115	115
Total length L, mm	6820	1500

(1) Designation specified in the catalog of Japan Water Steel Pipe Association (2014)

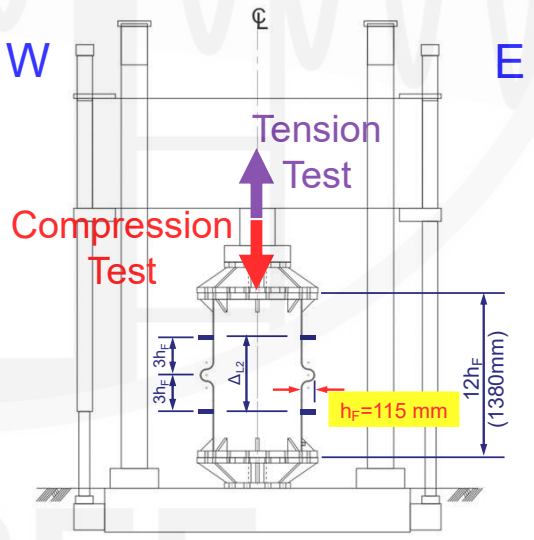

Fig. 3. Setup of axial compression and tension tests

Axial compression and tension tests

The axial compression and tension tests were conducted using a 500-ton universal testing machine at the National Center for Research on Earthquake Engineering (NCREE). Both tests employed the same setup, as shown in Figure 3. The specimens were positioned vertically, with the top and bottom ends connected to the testing machine via transition fixtures.

The tests were performed under displacement control, with displacement applied and measured by the displacement transducer of the testing machine. The deformation of the specimen was represented by the relative displacement measured over two lengths of $3h_F$ each, extending upward and downward from the center of the wave feature. The test results confirmed that the deformation displacement measured over the total $6h_F$ gauge length across the wave crest closely matched the total deformation displacement of the specimens.

Four-point bending test

The setup for the four-point bending test is shown in Figure 4. The specimen was placed horizontally. The distance between the upper loading roller supports was 1150 mm ($10h_F$), and the distance between the lower reaction roller supports was 5290 mm ($46h_F$). The upper loading rollers were connected to two hydraulic actuators through a transition beam, while the lower reaction rollers were connected to fixed supports anchored to the strong floor. At both the upper and lower hinge supports, the SPF specimen was clamped using two semicircular fixtures, each 500 mm wide. Between the contact surfaces of the semicircular fixtures and both the upper loading supports and lower fixed supports, polytetrafluoroethylene (Teflon) plates and steel rods were used to create roller supports that allowed for both rotation and sliding. The test results confirmed that the sum of the angles measured by two tiltmeters, placed at positions $3h_F$ on either side of the wave feature center, matched the relative rotation between the two straight segments of the specimen.

3. Test Results and Discussion

Axial compression test

Figure 5 shows the relationship between axial compressive force and the displacement measured over the $6h_F$ gauge length $6h_F$ (345 mm) above and below the wave feature center) for specimen SPF-C1. The displacement (Δ_{L2}) represents the average of measurements taken from the east and west sides of the specimen (as shown in Figure 3). The test results indicate that specimen SPF-C1 provided axial compression deformation capacity exceeding one wave height (h_F = 115 mm). The test was terminated at a displacement of 120 mm, with a corresponding axial compressive force of 434 kN. The peak axial compressive strength of 660 kN occurred at a displacement of 8.9 mm. In addition, deformation analysis revealed that the specimen's deformation was fully concentrated within the $6h_F$ region. These findings suggest that within approximately one wave height of compressive deformation, the specimen exhibited elastic–plastic behavior.

Axial tension test

Figure 6 shows the relationship between axial tensile force and displacement for specimen SPF-T1. The displacement (Δ_{L2}) was measured over the same $6h_F$ gauge length as in the axial compression test and was taken as the average of that of the east and west side measurements (as shown in Figure 3). The test results show that specimen SPF-T1 provided axial tension deformation capacity exceeding 115 mm. The test was terminated at a displacement of 119 mm, at which point the tensile strength reached 3922 kN. Based on the axial tension test results, the specimen exhibited increasing strength with displacement within approximately one wave height of deformation, and the force–displacement response demonstrated a bilinear behavior, as shown in Figure 6.

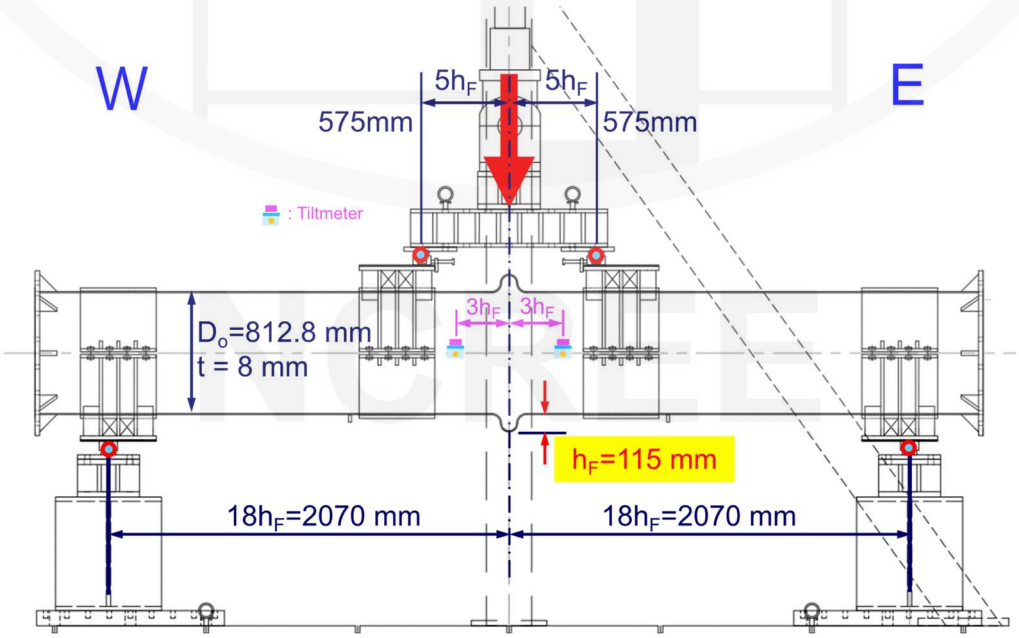

Fig. 4. Setup of four-point bending test

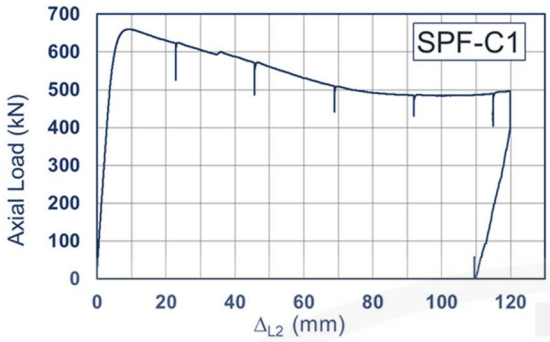

Fig. 5. Relationship between force and displacement for specimen SPF-C1

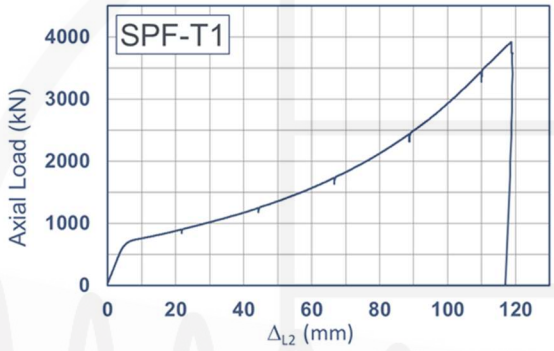

Fig. 6. Relationship between force and displacement for specimen SPF-T1

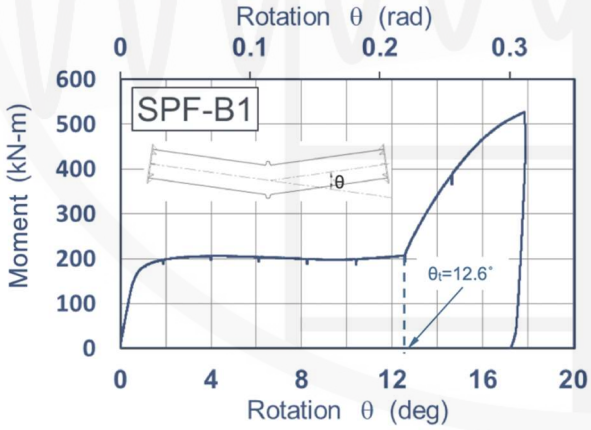

Fig. 7. Relationship between bending moment and rotational angle for specimen SPF-B1

Four-point bending test

Figure 7 shows the relationship between bending moment and rotational deformation angle for specimen SPF-B1. The rotational deformation angle (θ) represents the relative angular displacement between the straight segments on both sides of the wave segment. It was the sum of the angles measured by two tiltmeters installed at positions $3h_F$ (345 mm) on either side of the wave feature center. The test results indicate that specimen SPF-B1 had a relative rotational deformation capacity of up to 16° (0.279 rad). The test was terminated at a deformation angle of 17.9°, at which point the maximum bending moment at the midspan reached 527 kN-m. Figure 7 shows that a significant change in the strength response occurred at a deformation angle of θ_t = 12.6°, corresponding to a midspan bending moment of 214 kN-m. When the deformation angle was less than θ_t, the specimen exhibited elastic–plastic behavior, with the elastic rotational limit approximately 0.5°. After the deformation exceeded θ_t, it is presumed that contact occurred on the compression side (upper side of the wave segment) during bending, which increased resistance and resulted in a subsequent rise in bending strength.

Hydraulic pressure test

After the loading tests, specimens SPF-C1, SPF-T1, and SPF-B1 were subjected to hydraulic pressure testing. The test results confirmed that under a sustained internal water pressure of 12.5 kg/cm² (1.2 MPa) for 300 seconds, none of the three specimens experienced rupture or leakage.

4. Conclusions and Recommendation

Based on the results of the tests conducted in this study, the following conclusions can be drawn for the SPF with the wave feature adopted in this study (see Figure 1(b)).

1. According to the deformation test results, specimen SPF-C1 achieved a total compressive deformation of 120 mm, specimen SPF-T1 reached a total tensile deformation of 121 mm, and specimen SPF-B1 achieved a rotational deformation of 17.9°. These results satisfy the deformation requirements of axial deformation up to 1.0 h_F (115 mm) and a rotational deformation limit of 16° specified in Japan (WSP, 2014).

2. After undergoing maximum deformation, all three specimens successfully passed the hydrostatic pressure test, showing no rupture or leakage under a sustained internal pressure of 12.5 kg/cm² for 300 seconds.

References

Lin, Qi-Wen), Liu, Yen-Chiu), Chou, Pin-Shan and Lin,Yen-Hui (2021), "Recent development of active fault investigations of Taiwan," *Bulletin of the Central Geological Survey*, Number 34, 1-40 (in Chinese).

WSP, (2014). *WSP Steel Pipe for Fault Zones (Flexible Structure Type), WSP 077 Supplement-2014*. Japan Water Steel Pipe Association (in Japanese)

Wang, Bing-Xin (王炳鑫) (2000), "Damage report on public water supply pipeline facilities during the 1999 Chi-Chi Earthquake in Taiwan," *Taiwan Water Works Association Journal*, 19(1), 64–81 (in Chinese).

Introduction of the Steel-core Wall Structure Shaking Table Test

Pu-Wen Weng[1], Chia-Chen Lin[2], Fu-Pei Hsiao[3], Yu-Chen Ou[4], and Chung-Chan Hung[5]

翁樸文[1]、林佳蓁[2]、蕭輔沛[3]、歐昱辰[4]、洪崇展[5]

Abstract

In the Taiwan Building Code for the Design of Reinforced Concrete Structures, both Special Moment Frames and Special Structural Walls are recognized as permissible structural systems for resisting lateral forces. However, the Taiwanese engineering community predominantly adopts Special Moment Frames, wherein only beam and column components are designed to withstand seismic forces. Consequently, moment-resisting frame structures constructed in accordance with current regulations tend to exhibit large columns, deep beams, and dense reinforcement detailing. This excessive reinforcement congestion within confined spaces adversely impacts constructability, which in turn affects the seismic performance of structural components and raises concerns regarding their seismic resilience. Therefore, there is a pressing need to identify suitable seismic-resistant structural systems.

Given the current challenges faced by building structures in Taiwan, this study employs large-scale structural testing using a shaking table to investigate the behavior of advanced steel structures and coupled wall systems, along with corresponding mitigation strategies. This approach enhances the understanding of the overall structural behavior under seismic conditions and facilitates future applications in the numerical simulation of analogous structural systems. Furthermore, this research involves international collaboration with the New Zealand QuakeCoRE earthquake engineering research center, the University of Canterbury, and the University of Auckland. Collectively, these research teams aim to develop simulation and analysis methodologies for advanced steel and coupled wall structural systems, while refining experimental techniques for hybrid seismic testing and nonlinear dynamic analysis. This paper provides an overview of advanced steel-core wall structures, as well as the large-scale structural experiments conducted on a shaking table.

Keywords: shaking table test, coupled wall, coupling beam, buckling restrained brace

Taiwan is situated in a seismically active region with numerous active faults. If the near-fault zone is defined as the area within 10 km on either side of an active fault, over 8.6 million people—approximately one-third of Taiwan's population—live within this zone. Due to the characteristics of near-fault earthquakes, such as high-velocity pulses and significant surface displacements, buildings subjected to near-fault effects may experience more severe damage compared to typical seismic events. While extensive research has been conducted on the collapse behavior of reinforced concrete buildings, most studies have focused on the commonly used Special Moment Frame system, with limited exploration of other structural systems.

To address this gap, this study employs large-scale shaking table collapse experiments to investigate

[1] Associate Researcher, National Center for Research on Earthquake Engineering

[2] Associate Technologist, National Center for Research on Earthquake Engineering

[3] Research Fellow, National Center for Research on Earthquake Engineering; Joint Professor, Department of Civil Engineering, National Cheng Kung University

[4] Director General, National Center for Research on Earthquake Engineering; Professor, Department of Civil Engineering, National Taiwan University

[5] Professor, Department of Civil Engineering, National Cheng Kung University

the behavior of advanced steel structures and coupled wall systems, along with corresponding mitigation strategies. A key component of this research is a shaking table collapse test on a five-story steel-core wall structure. The test specimen is manufactured in modular units and assembled on the earthquake simulation shaking table, offering advantages such as interchangeable lateral load-resisting systems and rapid assembly and disassembly. This paper provides an overview of the shaking table experiment and its research objectives.

Literature Review on Shaking Table Structural Experiments

Shaking table experiments can accurately capture the seismic behavior of structures under earthquake loading. To better understand the planning of shaking table tests, we reviewed past large-scale structural experiments conducted on shaking tables.

In 2018, a large-scale collapse experiment on a seven-story weak-story frame structure was conducted at the NCREE Tainan Laboratory (Lin et al., 2021). This test incorporated ground motion records from the 1999 Chi-Chi earthquake (CHY015) and the 2016 Meinong earthquake (CHY063) to compare the structural responses induced by far-field and near-fault seismic events. The test specimen, shown in Figure 1, was uniquely designed using a modular approach, where different segments of the structure were constructed separately. From 2018 to 2020, NCREE collaborated internationally with the New Zealand QuakeCoRE earthquake research center and the University of Auckland to develop seismic vulnerability assessment and resilience enhancement techniques for mid-to-high-rise buildings. This project focused on the torsional behavior of structures subjected to earthquake-induced damage, specifically investigating the torsional failure mechanisms of ductile and non-ductile reinforced concrete (RC) frame structures. The test specimens for this research were also designed using a modular approach (Figure 2) (Suzuki, 2021).

Fig. 1 Seven-story weak-story frame structure

Fig. 2 Torsional behavior of frame structure

This study investigates the seismic behavior of a hybrid structural system composed of steel frames and coupled walls. Drawing from the design principles of past large-scale shaking table experiments, the test specimen is constructed using a modular approach. The modularity of the specimen allows for a systematic examination of the effects of rigid and flexible lateral load-resisting components on the seismic response of the structure. The following section provides an overview of the experimental study on the steel-core wall structural system. For details regarding numerical simulation and analysis, refer to Lin et al. (2025).

Specimen Design

In the major cities of New Zealand, such as Christchurch and Auckland, structures with hybrid lateral load-resisting systems have become increasingly common. In Taiwan, there has been a gradual shift toward developing coupled wall structural systems to withstand strong seismic forces. Consequently, this study's test specimen was conceptualized using an advanced steel-core wall structural system. The structural design focuses on a hybrid system that conforms to seismic design codes for targeted earthquakes and various component types, with an additional emphasis on post-earthquake repairability. The goal of repairability is achieved through a combination of resilient design and seismic detailing.

The test specimen is intended for general office purposes and is located in Wellington, New Zealand. According to the NZS 1170.0 (2002) standard, the seismic design importance level is set to 2, and the near-fault factor N(T,D) is assumed to be 1.0, based on the NZS 1170.5 (2004) standard. This factor accounts for near-fault effects on buildings with a natural period of less than 1.5 seconds (based on the analysis of the test building's natural vibration period). According to the current NZS 1170.5, it is assumed that the building is located on Class C soil (shallow soil), with a hazard factor (Z) of 0.4, which corresponds to a return period factor (R) of 1.0 for the design earthquake hazard. This corresponds to earthquake motion with a 500-year return period for the seismic design level associated with this importance level. The structural performance factor (Sp) is assumed to be 1.0, based on design considerations for lateral stability against sliding and overturning.

The test specimen utilized in this study is designed as a hybrid structural system comprising a steel frame and coupled wall configuration. It consists of five floors, each with a plan dimension of 5.4 m × 5.4 m. Each floor is designed with a height of 2.5 m, resulting in a total building height of 13.75 m, inclusive of a foundation measuring 75 cm in thickness. The building configuration was selected after several

iterations of prototype design, taking into account the objectives of the testing, cost, scale considerations, and the capabilities of the testing facility. The dimensions of the structural members are not designed to full scale but are instead modeled at an approximate ratio of 2/3. Key constraints impacting the design include the load-bearing capacity and overturning moment limitations of the shaking table, which are critical when considering the building's weight and the size of the structural members. Additionally, to facilitate fabrication and assembly, the specimen is segmented into three components, which are manufactured externally to the laboratory and subsequently transported and assembled on the shaking table.

The structural design can be categorized into several components, specifically the steel buckling-restrained braces (SBRB), coupled walls, shear connection beams, and non-structural components. The RC coupled core wall and SBRB provide lateral resistance in the x-direction, while the RC core wall resists lateral forces in the y-direction. The surrounding structural steel frames are primarily designed to support gravity loads, with the exception of the beam located on the fifth floor at the interface with the SBRB system frame, which replaces the SBRB on this level and is specifically designed to withstand bending moments. Each floor uses a composite steel deck floor system, wherein the steel deck serves as a permanent formwork for a concrete slab with a thickness of 110 mm. The concrete slab is supported by the surrounding frame, angular steel braces installed along the RC walls, and secondary steel beams aligned with the RC core wall in the y-axis. Shear studs are employed to connect the floor slab to all steel beams, and the reinforcement of the slab is welded to the extended reinforcement of the RC core wall.

The test specimen is constructed in three modular components, which are then transported to the seismic simulation shaking table and vertically stacked for testing. Figure 3 shows the sectional view of the segmented modular design. The test modules will be lifted by a crane using chains and shackles connected to lifting mechanisms. These lifting mechanisms are installed in the core walls and connected to concrete blocks to reduce the risk of structural damage and deflection during transportation.

Fig. 3 Modular test specimen

Conclusions

The NCREE Tainan Laboratory has established various experimental facilities dedicated to earthquake engineering, all equipped with the most advanced control systems available globally. A large-scale hybrid structural system test specimen is planned for testing on the shaking table at the Tainan Laboratory. The primary objectives of this experiment are to evaluate the interaction between the structural system and the lateral load-resisting system at the system level, to verify and refine design and building simulation methods, and to assess the impacts of seismic performance while developing effective mitigation strategies.

This study employs large-scale shaking table collapse experiments to investigate the behavior of an advanced steel-core wall structural system, along with associated mitigation measures. The research team is currently collaborating with the New Zealand QuakeCoRE, the University of Canterbury, and the University of Auckland to discuss the design of the test specimen and the sequences of seismic loading. The planned shaking table collapse experiment involving a five-story steel-core wall structure is set to be conducted at the NCREE Tainan Laboratory in April 2025.

Acknowledgments

The successful execution of this large-scale international collaborative experiment was made possible with the support of the National Institutes of Applied Research, the New Zealand QuakeCoRE, the University of Canterbury, and the University of Auckland. The authors would like to express their sincere gratitude to the personnel involved from these institutions for their invaluable assistance. Additionally, the authors extend their appreciation to Professor Chung-Che Chou of the Department of Civil Engineering at National Taiwan University for his contributions to the design of the SBRB used in this project.

References

Lin J. L., Chen W. H., Hsiao F. P., Weng Y. T., Shen W. C., Weng P. W., Chao, S. H., Chung L. L. and Hwang, S. J. (2021), “Effects of Hysteretic Models on the Seismic Evaluation of A Collapsed Irregular Building from Bidirectional Near-Fault Ground Motions on A Shake Table,” Engineering Structures, Vol. 247, No. 15.

Tomomi Suzuki, Aishwarya Y Puranam, Kenneth J Elwood, Hung-Jen Lee, Fu-Pei Hsiao, Shyh-Jiann Hwang (2021), “Shake table tests of seven-story reinforced concrete structures with torsional irregularities: Test program and datasets” Earthquake Spectra.

Lin H. Z., Weng P. W., Yeh S. W., Shen W. C., Hsiao F. P., Ou Y. C., Hung C. C., Will Pollalis, Santiago Pujol and Rick Henry (2025), “Shake-Table Test and Numerical Simulation on a Hybrid Structural Steel-Reinforced Concrete Coupled Wall Building,” Structural Engineering. (accepted)

Flexural-Shear Response of Existing Reinforced Concrete Columns Subjected to Varying Axial Loads

Wen-Cheng Shen*, Pu-Wen Weng†, Yi-An Li‡, and Yu-Ting Hwang§

沈文成* 翁樸文† 李翼安‡ 黃裕庭§

Abstract

During the period of rapid economic growth in Taiwan, a large number of reinforced concrete (RC) buildings were constructed. However, insufficient seismic design concepts at the time resulted in the widespread use of non-ductile reinforcement detailing. In mid- to high-rise buildings, the ground-story columns are subjected to high axial forces while simultaneously resisting cyclic lateral loading induced by seismic events. This effect is particularly pronounced in exterior and corner columns, which may experience axial force reveals from compression to tension, which would further compromise their seismic performance.

In this study, the seismic behavior of six RC column specimens designed to experience flexural failure under varying axial forces and cyclic lateral loading are examined. The key design parameters include longitudinal and transverse reinforcement ratios. Transverse reinforcement spacings were set to 100 mm, 150 mm, and 200 mm. The longitudinal reinforcement configurations consist of either all D25 bars or a combination of D25 and D32 bars. The transverse reinforcement consisted of D10 and D13 bars. Experimental results demonstrate that non-ductile RC columns exhibit rapid strength degradation after reaching their peak strength, and their deformation capacity was limited.

Keywords: flexural-shear failure; varying axial load; non-ductile detailing; reinforced concrete column

Introduction

Rapid urban development in Taiwan from the 1970s to the 1990s led to the construction of numerous mid- to high-rise reinforced concrete (RC) buildings. However, the ground-story columns of these buildings often lack sufficient transverse reinforcement despite being subjected to high axial forces. Post-earthquake investigations in recent years have demonstrated that this deficiency leads to flexural-shear failure after the flexural strength is reached. Under seismic loading, the exterior and corner columns experience significant axial force fluctuations (i.e., varying axial forces), which raises concerns about their ability to withstand cyclic axial and lateral loads when transverse reinforcement is inadequate.

The 2024 Hualien earthquake confirmed that seismic retrofitting can significantly improve structural resilience. However, the existing seismic assessment guidelines (Chiou et al., 2020; Sung and Tsai, 2017) in Taiwan are primarily designed for low-rise buildings and may not fully apply to taller structures. Furthermore, research on the effects of varying axial forces on RC columns is limited. This study aims to addresses these gaps through experimental investigations of RC columns designed for flexural-shear failure under cyclic lateral loading and varying axial forces. The findings are expected enhance our understanding of their seismic behavior and support the development of improved seismic assessment models.

Specimen Design

Six RC column specimens were designed and fabricated to investigate their seismic behavior. Each specimen had a cross-section of 500×500 mm and a net height of 2000 mm, as illustrated in Fig1. Two longitudinal reinforcement configurations were adopted: (1) 12-D25 bars and (2) a

* Assistant Researcher, National Center for Research on Earthquake Engineering
† Associated Researcher, National Center for Research on Earthquake Engineering
‡ Assistant Professor, Department of Civil Engineering, National Chung-Hsing University
§ Master Student, Department of Civil Engineering, National Chung-Hsing University

combination of 4-D32 bars and 8-D25 bars. The transverse reinforcement consisted of closed stirrups with two 90°-135° crossties comprising either D10 or D13 bars with spacings of 100 mm, 150 mm, and 200 mm. The specimens were designed to reach flexural strength before transitioning to shear-dominated failure, ensuring a flexural-shear failure mode.

The axial force ratio ($P / A_g f_c'$) applied to the specimens ranged from 0.6 to -0.1, and the concrete compressive strength (f_c') determined based on measured values obtained on the test day. The design parameters and material properties are summarized in Tables 1 and 2, respectively.

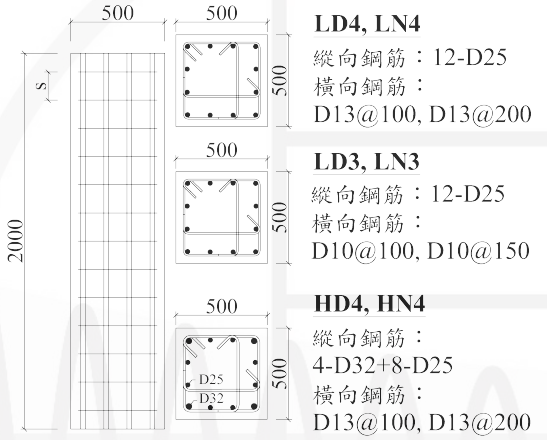

Fig. 1. Elevation view and steel layouts (unit: mm)

Table 1. Summary of design parameters

Specimen	Longitudinal steel	Transverse steel
LD4	12-D25 (r_l = 2.43%)	D13@100mm r_t = 0.76%
LN4		D13,200mm 0.38%
LD3		D10@100mm r_t = 0.43%
LN3		D10@150mm r_t = 0.29%
HD4	4-D32+ 8-D25 (r_l = 2.92%)	D13@100mm r_t = 0.76%
HN4		D13@200mm r_t = 0.38%

Table 2. Material properties

Specimen	f_{yl} (MPa)	f_{yt} (MPa)	f_c' (MPa)
LD4	456 (D25)	463 (D13) 458 (D10)	31.4
LN4			31.7
LD3			29.7
LN3			28.5
HD4	456 (D25) 452 (D32)		30.8
HN4			30.3

Test Setup

Tests were conducted at the National Center for Research on Earthquake Engineering (NCREE) by using the Multi-Axial Testing System to simulate the double-curvature deformation of RC columns under simultaneous varying axial and lateral loading. The interstory drift levels were applied by following the provisions of ACI 374.2R-13 (ACI, 2013), with three loading cycles per drift level in the sequence of 0.25%, 0.375%, 0.5%, 0.75%, 1.0%, 1.5%, 2.0%, 3.0%, 4.0%, 5.0%, and 6.0%. The loading protocol is illustrated in Fig. 2.

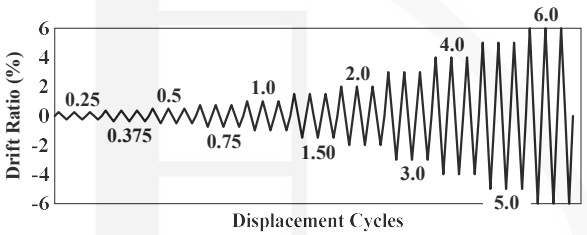

Fig. 2. Loading protocol

The axial loads were applied by following the recommendations of Hassan (Hassan, 2011). At the beginning of the experiment, an initial axial load ($0.25 A_g f_c'$) was applied to each specimen. Before the peak strength was reached, the axial load was cyclically applied between the maximum axial compression value ($0.6 A_g f_c'$) and the maximum axial tension value ($-0.1 A_g f_c'$), adhering to a fixed slope. Once the specimen reached its peak strength, the loading slope was adjusted based on the interstory drift level to maintain the axial force within the range of maximum axial compression and maximum axial tension.

Crack Patterns

Figure 3 illustrates the crack patterns observed at peak strength in the positive loading direction, where all specimens exhibited clear diagonal cracks. Figure 4 shows the crack patterns at peak strength in the negative loading direction, highlighting the formation of circumferential diagonal tension cracks during the tensile axial loading phase. As the lateral displacement increased, the crack propagation accelerated, resulting in concrete spalling at the column ends owing to crushing. Eventually, the specimens completely lost their load-carrying capacity, and at this point, the test was terminated.

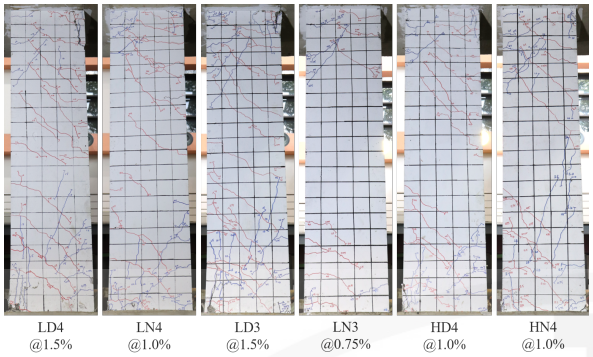

Fig. 3. Crack patterns at peak strength in the positive direction

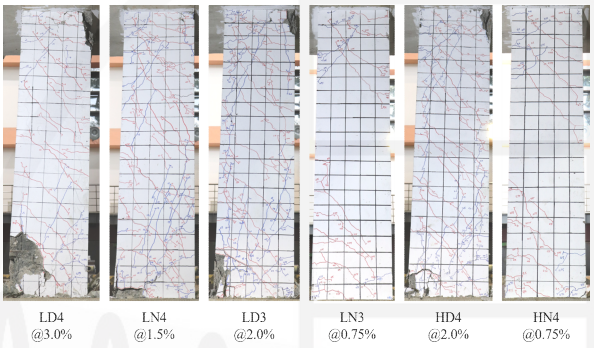

Fig. 4. Crack patterns at peak strength in the negative direction

Hysteretic Response

Figure 5 presents the lateral force-displacement hysteresis loops, with the data corrected for platen friction, P-Δ effects, and foundation rotation. The red solid lines in Fig. 5 represent the hysteresis envelope curves corresponding to the first loading cycle at each interstory drift level.

The test results demonstrate that all specimens exhibited limited ductility, as characterized by a rapid degradation in strength after reaching peak strength. Notably, Specimen HD4 exhibited the highest lateral strength in the positive direction, while Specimen LD4 achieved the highest lateral strength in the negative direction. Figure 6 provides a comparative analysis of the hysteresis envelope curves for all specimens, allowing for a clearer understanding of the differences in their seismic performance. This comparison illustrates the variations in the strength and energy-dissipation capabilities of the specimens, highlighting the effects of different reinforcement configurations.

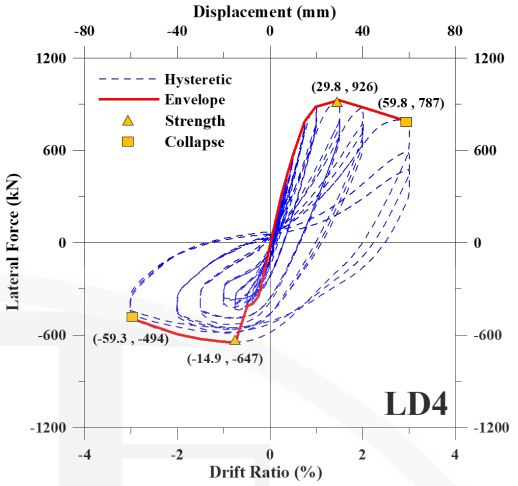

(a) Specimen LD4

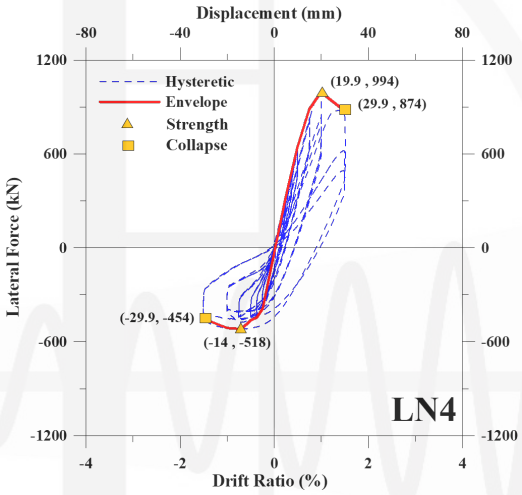

(b) Specimen LN4

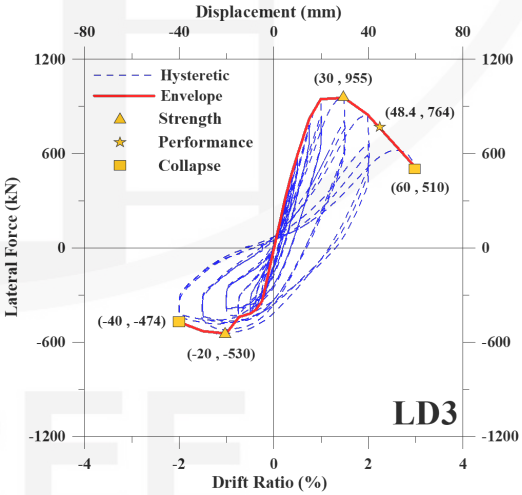

(c) Specimen LD3

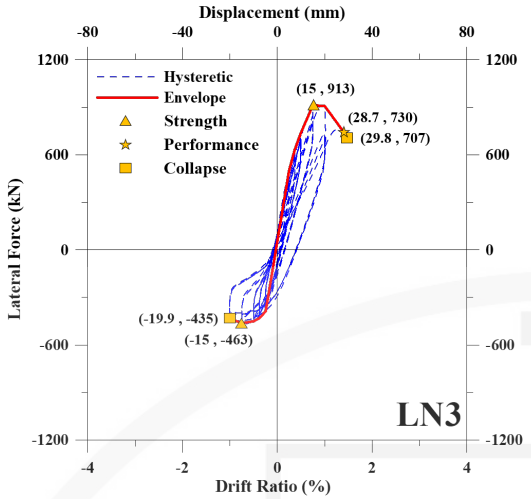

(d) Specimen LN3

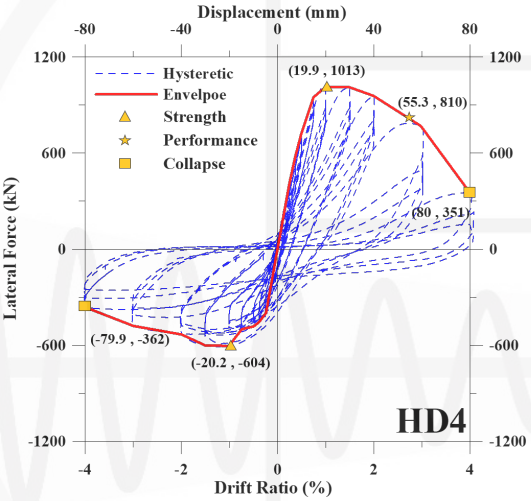

(e) Specimen HD4

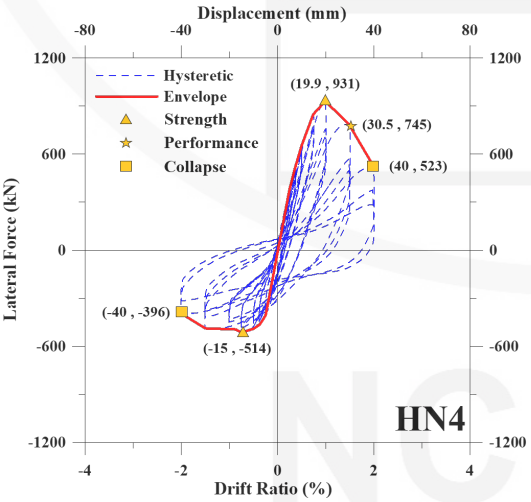

(f) Specimen HN4

Fig. 5. Hysteresis responses

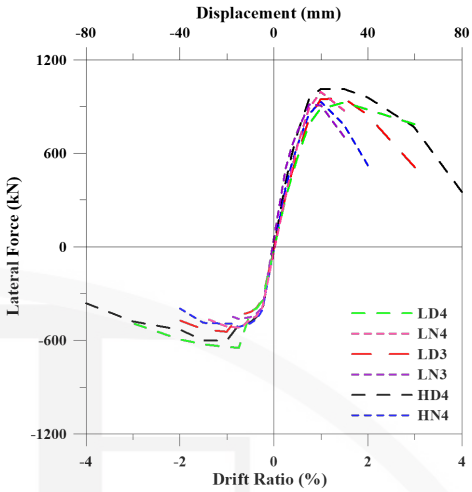

Fig. 6. Comparison of skeleton curves

Conclusions

(1) Specimens subjected to varying axial forces experienced rapid strength degradation after reaching their peak strength and had limited deformation capacity.

(2) Increased transverse reinforcement significantly enhances specimen ductility, as observed in the comparison of D- and N-series specimens with different transverse reinforcement spacings.

(3) Increasing longitudinal reinforcement in Specimens LD4, LN4, HD4, and HN4 had minimal impact on seismic performance.

(4) Reduced transverse reinforcement at the same spacing in Specimens LD4 and LN4 resulted in poorer ductility than in LD3 and LN3.

References

Chiou T. C. et al., “Technical Handbook for Taiwan Earthquake Assessment and Strengthening of Structures by Pushover Analysis (TEASPA V4.0),” NCREE Technical Report, NCREE-20-005, Taipei, 2020, 445 pp.

Sung Y. C. and Tsai I. C., “Seismic Evaluation of RC Buildings (SERCB) - Theoretical Background and System Operation,” Chinese Institute of Civil and Hydraulic Engineering, Taipei, 2017, 203 pp.

ACI (American Concrete Institute), “Guide for Testing Reinforced Concrete Structural Elements under Slowly Applied Simulated Seismic Loads (ACI 374.2R-13),” ACI Committee 374, Farmington Hills, Michigan, 2013, 18 pp.

Hassan, W. M., “Analytical and Experimental Investigation of Seismic Vulnerability of Beam-Column Joints without Transverse Reinforcement in Concrete Buildings,” PhD Dissertation, University of California, Berkeley, 2011, 471 pp.

Investigation of Nonlinear Hinge Behavior of Concrete-Filled Steel Tube Columns

Min-Lang Lin [1], Yu-Chieh Tseng [2], Chao-Hsun Huang [3], Tsung-Chih Chiou [4], Li-Lai Zhong [5], Yuan-Tao Weng[1], Te-Kuang Chou[6], and Mojtaba Fathisepahvand[7]

林敏郎[1]、曾俞傑[2]、黃昭勳[3]、邱聰智[4]、鍾立來[5]、翁元滔[1]、周德光[6]、法慕杰[7]

Abstract

In this study, we investigate a nonlinear hinge model for concrete-filled steel tube columns (CFST), which are increasingly used in Taiwan's steel structures alongside steel rectangular hollow structural sections (SRHS). The inclusion of concrete within steel columns increases both cross-sectional strength and column stiffness. However, research on the nonlinear hinge behavior of CFST columns remains limited. To address this gap, based on domestic experimental data, a regression-based nonlinear hinge model is proposed herein. We then evaluate seismic performance of a 15-story steel moment-resisting frame (MRF) through pushover analysis to compare the seismic behavior of SRHS with CFST columns, revealing improved ductility and reduced residual drift in CFST systems.

Keywords: Steel frame, Moment-resisting frame, Concrete-filled steel tube column, Nonlinear hinge model, Seismic capacity assessment, Nonlinear pushover analysis

Introduction

Concrete-filled steel tube columns (CFST) are used extensively in steel-structured building projects in Taiwan. However, there is a lack of nonlinear hinge models for these components in both domestic and international research. In this study, we compile relevant experimental data on steel columns from Taiwan to propose suitable nonlinear hinge models. Eleven sets of experimental data on CFST columns are analyzed. Based on the experimental hysteretic responses, the corresponding envelope curves are obtained, and a regression analysis is performed to derive the suggested nonlinear hinge models. Finally, to illustrate the application of the proposed model with CFST column, we conduct a nonlinear pushover analysis on a 15-story moment-resisting frame (MRF), and the results were compared with those of steel rectangular hollow structural sections (SRHS) to evaluate its seismic performance.

Nonlinear Hinge Model of Concrete-Filled Steel Tube Columns

In this study, the backbone curve of the rectangular steel column is defined based on Taiwan Earthquake Assessment for Structures by Pushover Analysis-Steel (TEASPA-S) [1], as shown in Figure 1. The curve comprises five points, labeled A through E. Point A represents the origin, point B the yield strength, point C the ultimate strength, point D the residual strength, and point E the strength loss. The nonlinear behavior of the member is characterized using three parameters: a, b, and α. Parameter a represents the nonlinear rotation between points B and C, b represents the nonlinear rotation between points B and

[1] Associate Researcher, National Center for Research on Earthquake Engineering (NCREE)
[2] Master's, Department of Civil Engineering, National Taipei University of Technology (NTUT)
[3] Associate Professor, NTUT
[4] Joint Researcher, NCREE
[5] Honorary Consultant, NCREE
[6] Associate Technologist, NCREE
[7] PhD Fellow, NTUT

D, and α is the strain hardening parameter ($\alpha = \frac{M_{max}}{M_y}$) that quantifies the strength increment from point B to C.

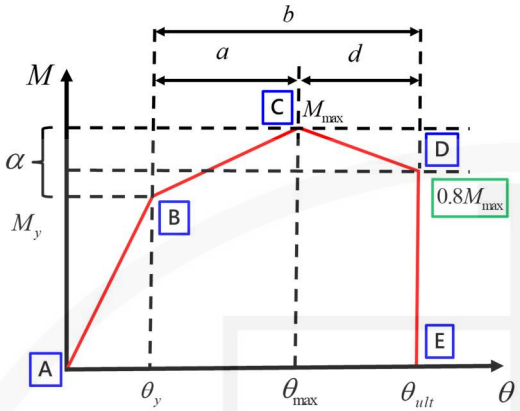

Fig. 1. Proposed development diagram of nonlinear hinge model

The yield strength at point B, yield rotation, and shear deformation factor are defined in accordance with ASCE 41-17 [1]. The calculation formulas are as follows:

$$M_y = M_p \quad (1)$$

$$\theta_y = \frac{M_y L(1+\eta)}{6EI} \quad (2)$$

$$\eta = \frac{12EI}{L^2 G A_s} \quad (3)$$

The flexural strength M_p of the CFST columns is determined based on relevant design codes. Given that the Taiwan Steel Reinforced Concrete Structure Design Code and Commentary (2011) [2] and the Taiwan Steel Structure Limit State Design Code (2010) [3] are relatively outdated, and the ongoing revision of the Taiwan Steel Structure Design Code for Buildings [4] primarily references the latest versions of AISC 360 and AISC 341, we adopt the provisions of the most recent AISC 360-22 [5] for calculating the strength of composite sections.

To calculate the yield rotation and shear deformation factor, the section's EI value is computed using the effective composite section $(EI)_{eff}$, as expressed in equation (3).

Axial Compressive Strength:

$$P_{n0} = P_p = F_y A_s + 0.85 f'_c A_c \quad (1)$$

$$P_e = \frac{\pi^2 (EI)_{eff}}{L_c^2} \quad (2)$$

$$EI_{eff} = E_s I_s + C_3 E_c I_c \quad (3)$$

$$C_3 = 0.45 + 3\left(\frac{A_s}{A_g}\right) \le 0.9 \quad (4)$$

$$When \ \frac{P_{n0}}{P_e} \le 2.25,$$

$$P_n = P_{n0}\left(0.658^{\frac{P_{n0}}{P_e}}\right) \quad (5)$$

$$When \ \frac{P_{n0}}{P_e} > 2.25,$$

$$P_{n,c} = 0.877 P_e$$

Axial Tensile Strength:

$$P_{n,t} = A_s F_y \quad (6)$$

Flexural Strength (M_p) :

Flexural strength is derived considering the stress distribution illustrated in Figure 2 and incorporating the contributions of the steel plates and the concrete infill.

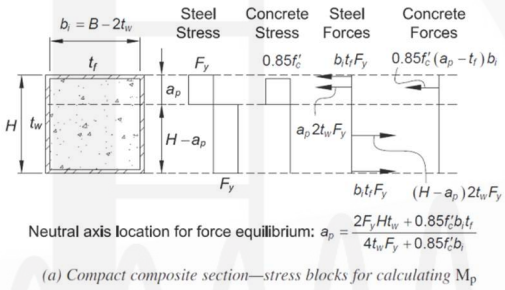

Fig. 2. Stress distribution of composite section (AISC 360-22 [5]).

The nonlinear parameters a, b, and α were determined through regression analysis based on the dataset of 11 experimental specimens. To avoid unreasonable results when applying the derived formulas in future applications, we identified the extreme values by substituting the full regression range into Equations (7)–(9) and established these as the upper limits of the equations.

The regression range of the test specimens was $18 \le b/t \le 48$ and $14.1\% \le P/P_{ye} \le 41\%$. By substituting the maximum and minimum values, the extreme values of each equation were obtained. The three parameters were then assigned their respective maximum values, rounded down for conservatism. The regression formulas of these three parameters are as follows:

$$\alpha = 10^{0.025}\left(\frac{b}{t}\right)^{0.057}\left(1 - \frac{P}{P_{ye}}\right)^{-0.578} - 0.140 \le 1.75(\text{unitless}) \quad (7)$$

$$a = 10^{1.097}\left(\frac{b}{t}\right)^{-0.384}\left(1 - \frac{P}{P_{ye}}\right)^{1.897} - 0.348 \le 3.0(\%\, rad) \quad (8)$$

$$b = 10^{0.760}\left(\frac{b}{t}\right)^{0.011}\left(1 - \frac{P}{P_{ye}}\right)^{1.549} - 0.886 \le 4.5(\%\, rad) \quad (9)$$

Comparison between Experimental Envelope and Proposed Nonlinear Hinge Model

The nonlinear hinge parameters proposed herein were compared to the experimental envelope curves. The comparison was categorized as low axial force conditions (axial force ratio ≤ 20%), as illustrated in Figure 3, and high axial force conditions (axial force ratio > 20%), as illustrated in Figure 4. The results indicated that the proposed nonlinear hinge model for CFST columns closely aligned with the experimental data. However, in terms of strength and ductility predictions, the model tended to be slightly conservative, generally underestimating both aspects relative to the experimental results.

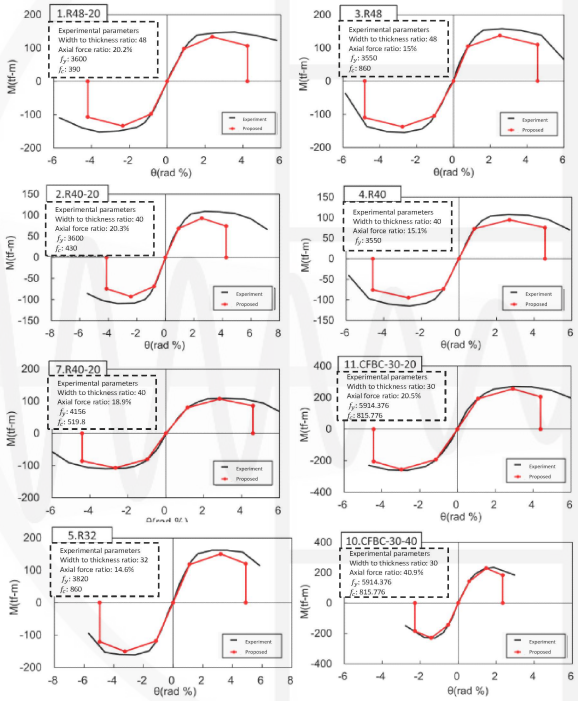

Fig. 3. Comparison between the proposed model and experimental curves (low axial force).

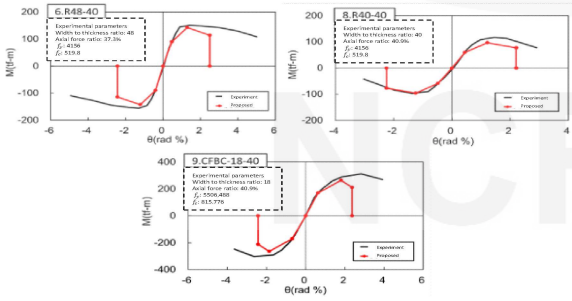

Fig. 4. Comparison between proposed model and experimental curves (high axial force).

Nonlinear Pushover Analysis

A 15-story MRF structure with five spans in the X-direction and three spans in the Y-direction was investigated. The structural specifications are detailed in Table 1, and a three-dimensional representation is provided in Figure 5. Two analytical models were developed: in Model 1, the columns were designed as SRHS, while the beams were H-shaped sections. The nonlinear hinge properties of the beams and columns were modeled based on the recommendations in TEASPA-S V2.0 [1]. In Model 2, the structural component dimensions remained identical to those in Model 1. However, the steel columns were filled with concrete, and the proposed nonlinear hinge model for CFST columns, as developed in this study, was implemented. Nonlinear pushover analyses were then performed using the ETABS structural analysis software to compare the seismic performances of the two models.

Table 1. Beam and column cross-sectional dimensions (Unit: mm).

Floor	Column Dimensions	Beam Dimensions (with enhanced connection details)
RF	BOX 300 × 300 × 16 (SN490C)	H500 × 200 × 10 × 16 (SM490B)
15F	BOX 450 × 450 × 22 (SN490C)	H600 × 300 × 12 × 22 (SM490B)
14F		
13F		
12F	BOX 500 × 500 × 22 (SN490C)	
11F		
10F		
9F	BOX 550 × 550 × 25 (SN490C)	H700 × 300 × 13 × 24 (SM490B)
8F		
7F		
6F	BOX 600 × 600 × 25 (SN490C)	
5F		
4F		
3F	BOX 650 × 650 × 28 (SN490C)	
2F		
1F		

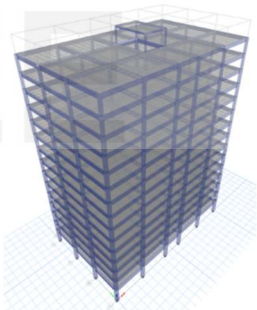

Fig. 5. Fifteen-story MRF model.

Nonlinear pushover analyses of both models were performed, and their capacity curves and nonlinear hinge developments are shown in Figures 6 and 7. The results indicate that the structural strength of the SRHS column model is governed by flexural failure at the column base on the first floor, resulting in a column-dominated failure mode. The design performance targets of this model are a ground acceleration of $A_p = 0.789\,g$ and a capacity-to-demand ratio (CDR) of 1.794. By contrast, the structural strength of the CFST column model is controlled by flexural failure of the steel beams on the third and fourth floors, leading to a beam-dominated failure mode. Its design performance targets are a ground acceleration of $A_p = 0.856\,g$ and a CDR of 1.946. A comparison between the two models suggests that the CFST marginally enhance the seismic performance of the building.

Conclusions

1. A regression analysis based on 11 sets of domestic experimental data was performed to propose nonlinear hinge parameters for CFST columns. According to the results, the proposed parameters can reasonably and conservatively predict the nonlinear behavior of the components.

2. The seismic performance of two steel structure models was compared: one comprising SRHS columns with H-shaped beams and the other incorporating CFST columns in the original configuration. The results of a pushover analysis indicate that the SRHS model is governed by column failure and exhibits poorer seismic performance, whereas the CFST column model is governed by beam failure, resulting in enhanced seismic capacity.

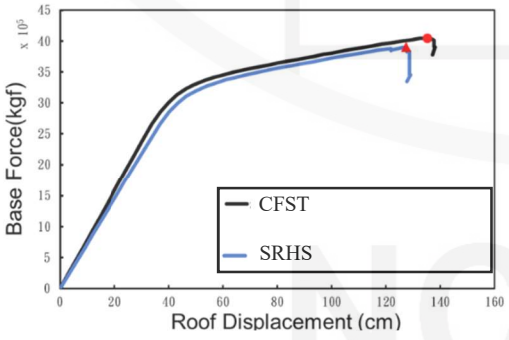

Fig. 6. Capacity Curve

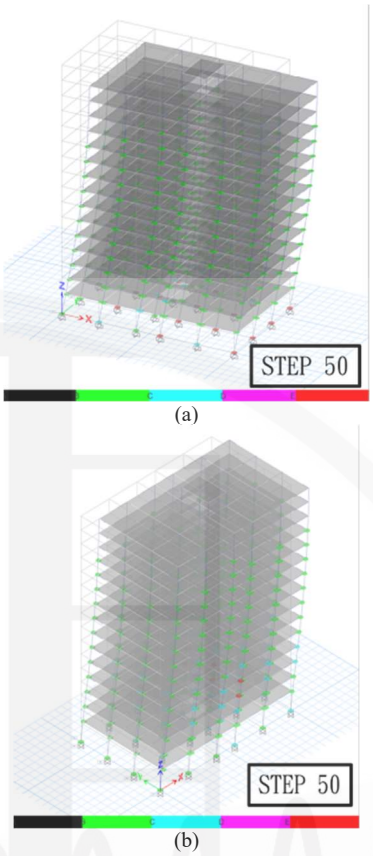

Fig. 7. Nonlinear hinge development and failure mode: (a) SRHS column model and (b) CFST column model.

References

[1] Lin, M.-L., Chiu, C.-C., Chung, L.-L., Chou, T.-K., Weng, Y.-T., Chung, K.-H., Chang, H.-Y., & Tseng, Y.-J. (2023). Seismic Evaluation Technical Manual for Steel Structural Buildings (TEASPA-S V2.0). National Center for Research on Earthquake Engineering, Report No. NCREE-23-012.

[2] Construction and Planning Agency, Ministry of the Interior. (2011). Design Code and Commentary for Steel-Reinforced Concrete Structures (Revised ed.).

[3] Construction and Planning Agency, Ministry of the Interior. (2010). Limit State Design Code and Commentary for Steel Structures (Revised ed.).

[4] Architectural Research Institute, Ministry of the Interior. (2021). Revision Study of the Steel Structure Design Code for Buildings (Fiscal Year 110 Report).

[5] American Institute of Steel Construction (AISC). (2022). ANSI/AISC 360-22: Specification for Structural Steel Buildings. American National Standard.

Scaled Model Tests on Pile–soil Interaction in Liquefied Ground

Kuan-Yu Chen[1], Chih-Chieh Lu[2], Yuan-Chang Deng[1], Shang-Yi Hsu[3], and Jin-Hung Hwang[4]

陳冠羽[1]、盧志杰[2]、鄧源昌[1]、許尚逸[3]、黃俊鴻[4]

Abstract

The issue of soil liquefaction has garnered significant attention in Taiwan since the 1999 Chi-Chi earthquake and the 2016 Meinong earthquake. In bridge and large building projects, appropriate pile foundation design is commonly used for resisting liquefaction. However, due to the complex mechanisms of soil liquefaction, liquefiable soil layers are often treated by reducing the modulus and strength of the soil as seismic design parameters for pile foundations in liquefied ground. Consequently, developing appropriate reduction factors is a major concern in geotechnical engineering. Currently, the design and analysis of anti-liquefaction pile foundations in Taiwan rely heavily on foreign literature, resulting in a significant lack of representative research for reference. Thus, it is essential to thoroughly verify the validity of reduction factors through scientific evidence and establish suitable soil reduction factors applicable to Taiwan. These efforts will aid in revising soil liquefaction-related seismic design criteria. This study aims to investigate the interaction behavior of liquefied soil, piles, and superstructures through a series of 1-g shaking table tests. With an integrated approach, this study explores the soil-pile-superstructure interaction, clarifies this complex mechanical mechanism, evaluates the impact of liquefied soil on the seismic performance of pile foundations, and proposes reasonable reduction factors for liquefiable soil sites that can be referenced for seismic design guideline development. This paper provides a detailed description of the apparatus installation, model design, and input motion. It also examines the natural frequency identification results of the saturated soil specimens and model structures in their initial state.

Keywords: liquefaction, 1-g shaking table test, soil-structure interaction, physical modeling

Introduction

In past earthquakes, there have been numerous cases of damage to pile foundations caused by soil liquefaction, such as during the 1964 Niigata earthquake in Japan, the 1989 Loma Prieta earthquake in the United States, the 1990 Luzon earthquake in the Philippines, and the 1995 Kobe earthquake in Japan. These earthquakes resulted in structural damage and deformation of pile foundations of buildings and bridge piers due to ground liquefaction. Deep foundations are crucial geotechnical structures, and their seismic performance design in liquefiable ground is a significant concern for various sectors. However, the interaction behavior of liquefied soil, piles, and superstructures is complex and is often simplified in engineering practice using the pseudo-static method, which accounts for the weakening (softening) behavior of soils during liquefaction. This design method involves reducing the modulus and strength of liquefied soil to determine the lateral resistance of the pile foundation. The Japan Road Association code of practice (JRA 1990, 1996) proposes reduction factors (D_E) for soil parameters based on variables such as the factor of safety against liquefaction, cyclic shear strength ratio, and depth of the liquefied soil layer. The Architectural Institute of Japan (AIJ 1988) also proposes a conservative reduction factor based on the same concept. The reduced soil parameters are the horizontal coefficient of subgrade reaction (k_h) and the ultimate lateral soil resistance (p_u). However, due to the lack of data for evaluation and understanding of their physical mechanisms, there is considerable uncertainty in the analysis and design of pile

[1] Assistant Researcher, National Center for Research on Earthquake Engineering
[2] Research Fellow, National Center for Research on Earthquake Engineering
[3] Associate Researcher, National Center for Research on Earthquake Engineering
[4] Professor, Department of Civil Engineering, National Central University

foundations in liquefied ground. Therefore, many previous studies have conducted physical model experiments, such as 1-g shaking table tests or centrifuge tests, to further clarify the mechanism of soil–pile–structure interaction during the liquefaction process. In this study, a series of 1-g shaking table tests and numerical simulations were performed to provide reasonable recommendations for geotechnical parameter reduction. These findings serve as a reference for revising seismic performance design standards.

Experimental Setup

In this study we conducted a 1-g scaled model shaking table test that simulates the complex interaction behavior between steel pipe piles and liquefied soil layers, closely resembling in situ conditions. The experiment focused on investigating the seismic response of superstructure-type foundations with varying fundamental vibration periods in liquefied soil layers. The design of the fundamental vibration periods of the model's superstructure adheres to seismic design regulations, specifically considering the definitions of long-period (T = 1.0 s) and short-period (T = 0.3 s) structures.

(1) Apparatus installation

A schematic illustration of the model pile and apparatus is shown in Figs. 1 and 2. The model pile was fixed at the base of the laminar box (fixed-end), and strain gauges were attached to the pile body to monitor variations in bending moment along the depth during motion. Using the theory of elastic beams, the rotation, deflection, shear force, and soil resistance of the pile were estimated from its bending moment. To capture dynamic responses during loading, precision accelerometers, piezometers, linear displacement transducers, and a laser displacement sensor were installed in the soil specimen to measure dynamic responses, such as acceleration, pore water pressure, lateral displacement, and vertical settlement.

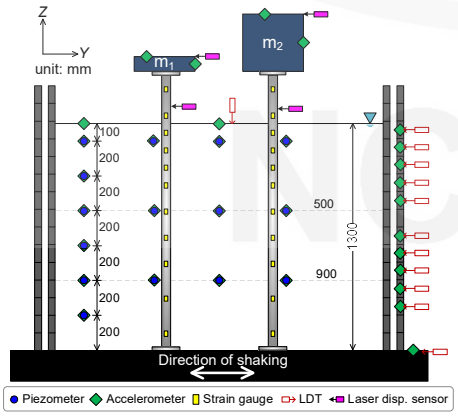

Fig. 1. Schematic illustration of the apparatus used in the shaking table test

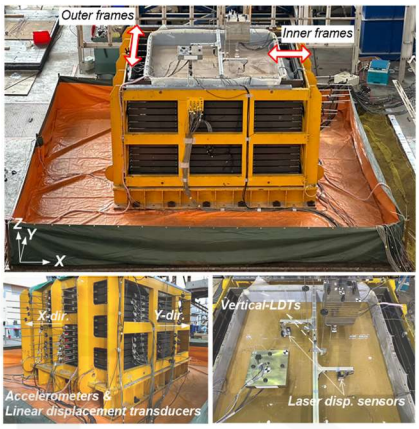

Fig. 2. Actual experimental set-up of the shaking table test

(2) Saturated soil specimen

The experiment used clean quartz sand as the soil specimen, and the wet pluviation method was applied to prepare the specimen. The remolded specimen was constructed in seven equal layers, and the initial relative density of the specimen was approximately Dr = 48%. The basic physical properties of the soil material are shown in Fig. 3.

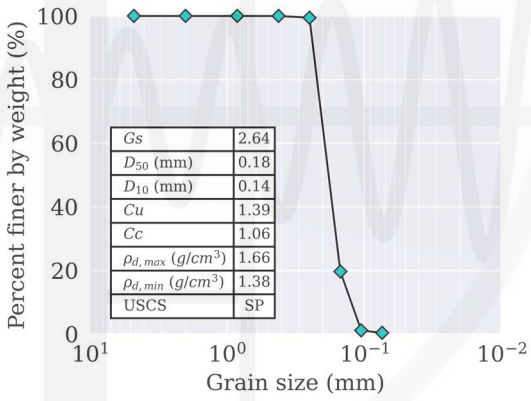

Fig. 3. Physical properties of soil material

Scaling Law

Due to limitations in environmental and test equipment, the size and confining stress conditions of 1-g model tests may differ from those in the field. To ensure a reasonable simulation of soil–pile–superstructure interaction behavior, it is necessary to consider the similarity between the model and the prototype and create a physically scaled model based on the size, boundary conditions, and stress conditions of the prototype pile–soil system. In this study, the experimental model was scaled using the scaling laws proposed by Iai (1989), Iai and Nakahara (2005), and Wood et al. (2002). The physical model was scaled based on three main scale factors: length, density, and gravity. By using these three variables, other physical quantities, such as force, mass, and stress, can be derived. In this study, the length scale factor for the experimental model was λ = 16 (prototype/model).

The soil material used in the model was assumed to be the same as in the prototype, resulting in a density scale factor of $\lambda\rho = 1$. Since the experiment was conducted under a 1-g gravitational field, the gravity (acceleration) scale factor was $\lambda g = \lambda\ddot{u} = 1$.

Furthermore, under small strain conditions ($\gamma \le 10^{-4}$), the relationship between the shear modulus of the model and prototype soil layers and the shear strain scale factor is:

$$\begin{cases} (G_o)_m = (\tau)_m/(\gamma)_m = (\rho)_m \cdot (V_s)_m^{\,2} \\ (G_o)_p = (\tau)_p/(\gamma)_p = (\rho)_p \cdot (V_s)_p^{\,2} \end{cases}$$

$$\lambda_\varepsilon = \frac{(\gamma)_p}{(\gamma)_m} = \lambda \Big/ \left[(V_s)_p \cdot (V_s)_m^{-1} \right]^2$$

where G_o is the initial shear modulus, τ is shear stress, γ is shear strain, ρ is soil density, V_s is shear wave velocity, and the subscripts m and p denote model and prototype, respectively.

The objective of the experiment was to simulate the flexural behavior of a prototype steel pipe pile with Young's modulus $(E)_p \approx 210$ GPa. To achieve this, the material of the model pile was chosen as aluminum alloy $(E)_m \approx 70$ GPa, which is approximately 1/3 of the prototype value. Therefore, by adjusting the wall thickness of the model pile, the flexural rigidity of an actual steel pipe pile can be approximately simulated. The scaling relationships of the physical quantities between the model and prototype are summarized in Table 1 for reference.

Table 1. Scale factors for 1-g model test

Physical quantity	Units	Scaling factor (prototype/model)
Length	[L]	λ=16
Density	[ML^{-3}]	λ_ρ=1
Gravity	[LT^{-2}]	λ_g=1
Acceleration	[LT^{-2}]	$\lambda_{\ddot{u}}$=1
Stress	[ML^{-1}T^{-2}]	$\lambda_\sigma=(\lambda_\rho\cdot\lambda^3\cdot\lambda_{\ddot{u}})\cdot\lambda^{-2}=\lambda$
Strain	[-]	λ_ε
Moduli	[ML^{-1}T^{-2}]	$\lambda_{mod.}=\lambda_\sigma/\lambda_\varepsilon=\lambda/\lambda_\varepsilon$
Flexural rigidity	[FL^2]	$\lambda_{EI}\approx\lambda^4$
Dynamic time	[T]	$\lambda_t=(\lambda\cdot\lambda_{\ddot{u}})^{0.5}=\lambda^{0.5}$
Frequency	[T^{-1}]	$\lambda_f=\lambda_t^{-1}=\lambda^{-0.5}$

Input Motion

The experiment employed both white noise excitation and sinusoidal loading to conduct system identification and investigate the dynamic characteristics of the liquefied ground and the model structure. The frequency bandwidth and peak acceleration amplitude of the white noise signal were 0.1–50 Hz and 20 gal, respectively. For the sinusoidal loading, an acceleration signal with a frequency of 2 Hz and an amplitude of 20 gal was applied for 60 cycles. The main seismic events were simulated using real earthquake records: a near-fault ground motion from the 1999 Chi–Chi earthquake (station TCU052) and a far-field ground motion from the 2002 Yilan-Hualien earthquake (station ILA050). These input motions were used to examine the effects of different earthquake characteristics on the pile–soil interaction behavior in the liquefied soil layer. Fig. 4 presents the input earthquake motions of the shaking table. Whether the scaled earthquake motion retains its impulsive nature was determined using the method proposed by Shahi and Baker (2014). As shown in Fig. 4(a), the east–west ground motion recorded at station TCU052 remains classified as pulse-like motion after scaling.

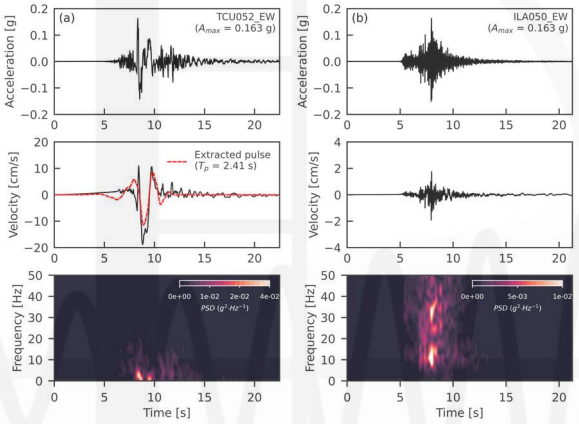

Fig. 4. Input motion: (a) pulse-like motion; (b) non-pulse-like motion

Preliminary Results

Fig. 5 illustrates the results of identifying the saturated sandy soil specimen in its initial state. The figure shows that the predominant frequency of the soil layer, estimated at approximately $f_{0,soil} = 12.45$ Hz through the transfer function, was close to the results obtained from the theoretical solution of the amplification function for a uniform, isotropic, damped, linear elastic soil layer on a rigid base. This validates the accuracy of estimating the natural frequency of the soil specimen using white noise sweeps. The targeted fundamental vibration frequencies of the model piles were $(T_0)_{p1} = 0.075$ s and $(T_0)_{p2} = 0.25$ s, respectively, with boundary conditions commonly used in engineering practices by assuming the ground surface as a fixed-end to calculate the fundamental frequency of the superstructure. However, soil behaves as an elastoplastic material, not rigid, so when the structural foundation is on soft ground, the deformation of the substructure increases, leading to a decrease in the fundamental vibration frequency of the superstructure. Fig. 6 presents the results of identifying the natural frequencies of the model pile foundation using white

noise shaking. The fundamental frequencies of single-pile-supported structures in soil were approximately 4.8 Hz and 1.5 Hz.

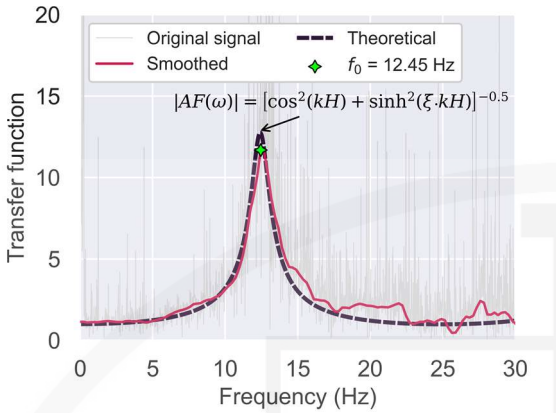

Fig. 5. Predominant frequency of saturated soil specimen

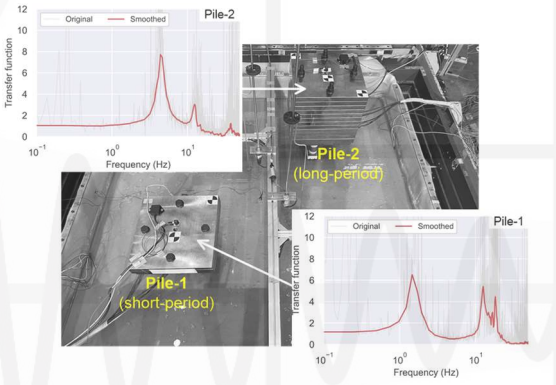

Fig. 6. Natural frequency of the model piles: (a) Pile-1; (b) Pile-2

Summary

This study presents the experimental results using a pulse-type earthquake as the input motion (TCU052_EW, A_{max} = 0.16 g), focusing on the evolution of excess pore water pressure in the saturated sandy ground and the acceleration response of the pile–soil system during shaking. Fig. 7 displays the acceleration response and the variation of the pore water pressure ratio (r_u) at different depths during shaking. The figure illustrates the variation of excess pore water pressure at different depths within the free-field array of the soil specimen. The results indicate that full liquefaction occurred at approximately 9.0 s into the shaking event. The results show that before liquefaction, the upward propagation of seismic waves led to an amplification of acceleration amplitude. However, once liquefaction (or softening) occurred, the acceleration amplitude decreased across all depths, demonstrating a significant damping effect.

Based on the preliminary analysis of the test results, the following conclusions can be drawn. (1) After liquefaction, the fundamental frequency (f_0) of both the ground and the single-pile-supported structure decreases significantly. (2) During shaking, the acceleration amplitude exhibits an amplification effect before liquefaction, whereas a distinct damping effect is observed after liquefaction.

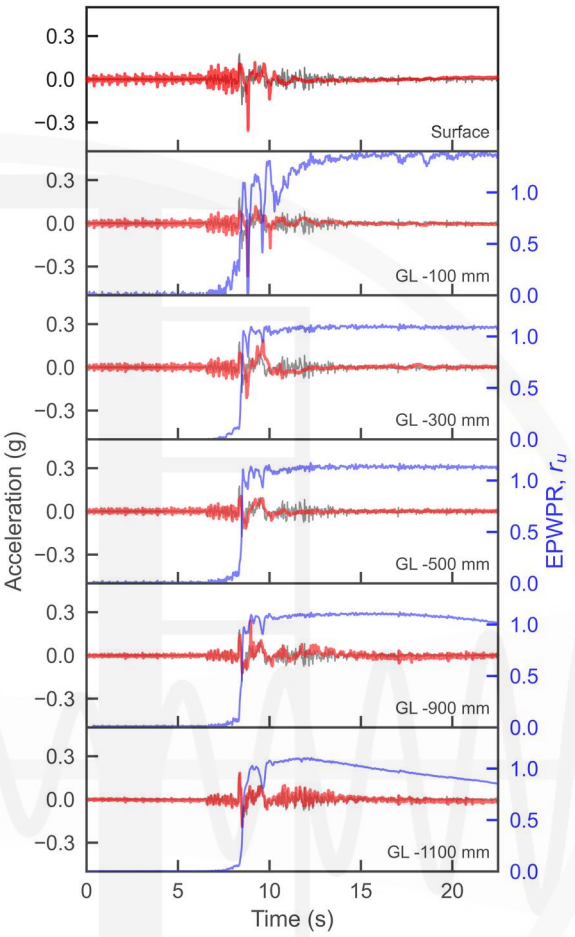

Fig. 7. Acceleration and EPWPR-time histories at different depths in the soil layer

References

Iai, S., "Similitude for shaking table tests on soil-structure-fluid model in 1g gravitational field," *Soils and Foundations*, 29(1), pp. 105 — 118 (1989).

Iai, S., and Nakahara, T., "Generalized scaling relations for dynamic centrifuge tests," *Géotechnique*, 55(5), pp. 355–362 (2005).

Wood, D.M., Crewe, A., and Taylor, C., "Shaking table testing of geotechnical models," *International Journal of Physical Modelling in Geotechnics*, 2(1), pp. 01–13 (2002).

Shahi, S.K. and Baker, J.W. "An Efficient Algorithm to Identify Strong-Velocity Pulses in Multicomponent Ground Motions," *Bulletin of the Seismological Society of America*, 104(5), pp. 2456–2466 (2014).

Influence and Trend of Fault Displacements on the Behavior of Fault-crossing Buried Pipelines

Che-Yu Chang[1] and Wei-Kuang Chang[2]

張哲瑜[1]、張為光[2]

Abstract

This study evaluates the behavior of fault-crossing buried pipelines. The commercial software SAP2000 is utilized to conduct the analyses, with a focus on the influence of strike-slip fault movements on the buried pipelines as well as the dimension effects on the pipeline's behavior.

Keywords: buried pipeline, fault-crossing, fault displacement, SAP2000

Introduction

Damage to buried pipelines caused by seismic events, such as strong ground motion, permanent ground movement, and soil liquefaction, can be severe. Interruptions in water supply may lead to inconvenience and sanitary issues, while damage to gas or oil pipelines could result in fatal incidents. Figure 1 shows several failure modes of buried pipelines resulting from ground movements. Many studies have been conducted on this important issue of damage to fault-crossing buried pipelines (Sarvanis et al. 2017; Demirci et al. 2018; Demirci et al. 2021).

Considering that current replacement pipelines are mostly made of steel and polyethylene (PE), this study evaluates the fault-crossing behavior of steel pipelines. Analyses are performed using the software SAP2000. Strike-slip fault movement is simulated and the influence and trends of fault displacements and pipe dimensions are estimated.

Numerical Model

The behavior of fault-crossing pipelines is analyzed using SAP2000 in this study. Figure 2 displays a finite element model that employs beam elements to represent the pipeline and springs to represent the soil effects. Soil springs are applied at each node of the beam elements. Strike-slip fault movement is simulated by applying displacement to half the length of the pipeline while the other half remains fixed, as shown in Figures 2 and 3. Both the dip angle of the fault and the angle between the fault displacement direction and the pipe's axial direction are set at 90 degrees. Fault displacements are gradually applied from 0.02 m to 2 m in the +Y direction as shown in Figure 2.

Table 1 shows the material properties of the steel pipeline used in this study. Table 2 lists the pipe diameters and thicknesses for the 18 cases examined. The yield strength (F_y) of the steel pipeline is 195 MPa, and the tensile strength (F_u) is 320 MPa.

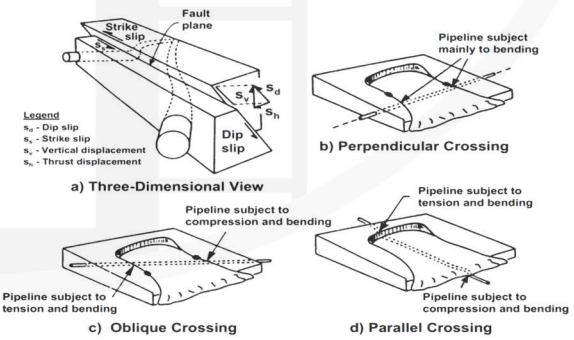

Fig.1. Failure modes of buried pipelines resulting from ground movements (Argyrou et al., 2020).

The soil condition is assumed to be dense sand. Table 3 summarizes the continuous soil spring stiffness for each case. The lateral and axial directions correspond to the Y and X directions shown in Figure 2, respectively. The spring stiffness applied at each node of the beam elements is defined as follows:

[1] Assistant Research Fellow, National Center for Research on Earthquake Engineering

[2] Associate Research Fellow, National Center for Research on Earthquake Engineering

$$k_d = \frac{k_c L}{N} \quad (1)$$

where k_d is the discrete soil spring stiffness, k_c is the continuous soil spring stiffness, L is the total length of the pipeline, and N is the total number of pipeline nodes.

Analysis Results

The analysis results are presented in terms of the pipelines' von Mises stress. Figure 4 shows the von Mises stress distribution for Case 1, which has a 21.7 mm diameter pipeline. The strike-slip fault movement has a 90-degree dip angle, and the angle between the fault movement and the pipeline's axial direction is also 90 degrees. The horizontal axis represents the position along the pipeline, while the vertical axis indicates the von Mises stress. The results include the pipeline stresses due to fault displacements ranging from 0 m to 2 m. The yield strength is shown as a red solid line, and the tensile strength is shown as a blue dashed line for reference.

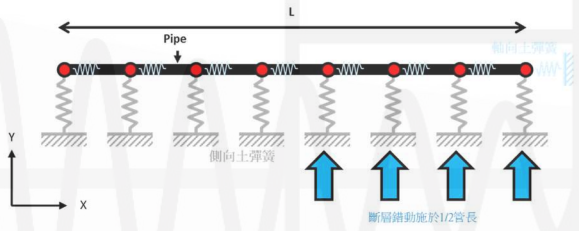

Fig.2. Pipeline finite element model.

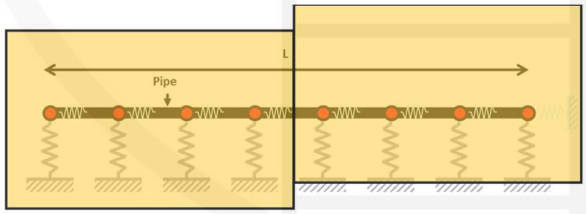

Fig.3. Strike-slip movement scheme.

Table 1. Material properties of steel pipe

Young's modulus (N/mm^2)	0.206×10^6
Density (kg/mm^3)	7850×10^{-9}
Poisson's ratio	0.3

Table 2. Steel pipe dimensions

Case	Outer diameter (mm)	Thickness (mm)
1	21.7	2.8
2	27.2	2.8
3	34.0	3.2
4	42.7	3.5
5	48.6	3.5
6	60.5	3.8
7	76.3	4.2
8	89.1	4.2
9	114.3	4.5
10	139.8	4.5
11	165.2	5.0
12	216.3	5.8
13	267.4	6.6
14	318.5	6.9
15	355.6	7.9
16	406.4	7.9
17	457.2	7.9
18	508.0	7.9

Table 3. Stiffness of soil springs

Case	Continuous lateral soil stiffness (N/mm^2)	Continuous axial soil stiffness (N/mm^2)
1	0.492	0.196
2	0.585	0.247
3	0.691	0.309
4	0.817	0.390
5	0.897	0.445
6	1.047	0.556
7	1.225	0.706
8	1.357	0.829
9	1.586	1.074
10	1.787	1.327
11	1.962	1.584
12	2.255	2.115
13	2.487	2.665
14	2.673	3.236
15	2.784	3.662
16	2.912	4.262
17	3.016	4.882
18	3.100	5.520

Figures 5–7 show the von Mises stress distribution for Case 6 (pipeline diameter of 60.5 mm), Case 12 (pipeline diameter of 216.3 mm), and Case 18 (pipeline diameter of 508.0 mm), respectively. The results indicate that as the pipeline diameter increases, the von Mises stress decreases because of the increased stiffness of the pipeline. Consequently, the fault displacement that the pipeline can withstand before reaching yield strength and tensile strength increases with larger diameters.

Figures 8–11 show the relationship between yield length and fault displacement for Case 1 (pipeline diameter of 21.7 mm), Case 6 (pipeline diameter of 60.5 mm), Case 12 (pipeline diameter of 216.3 mm), and Case 18 (pipeline diameter of 508.0 mm), respectively. In these figures, the horizontal axis represents the applied fault displacement, and the vertical axis represents the yield length of the pipeline. As the applied fault displacement increases, the von Mises stress in the pipeline reaches the yield strength level. The length of the yielding portion increases with increased applied fault displacement, eventually leading to the pipeline stress reaching the tensile strength. The yield length at which tensile strength is attained is indicated by a circle in Figures 8–11.

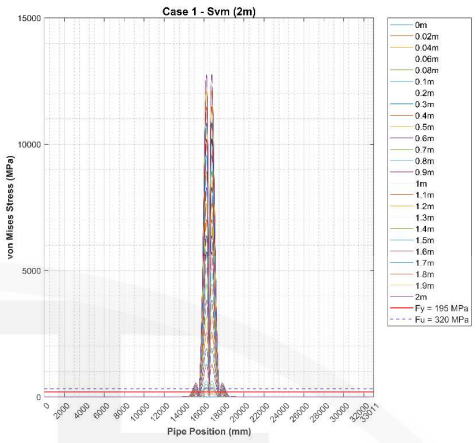

Fig.4. Case 1 pipeline von Mises stress distribution.

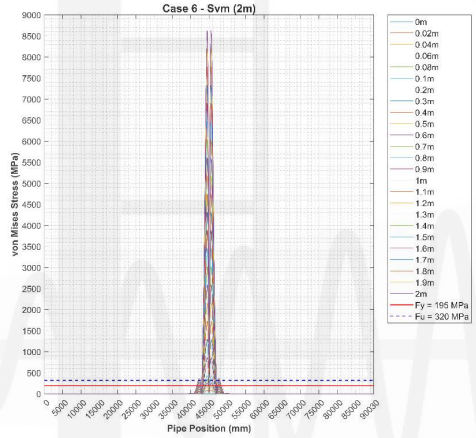

Fig.5. Case 6 pipeline von Mises stress distribution.

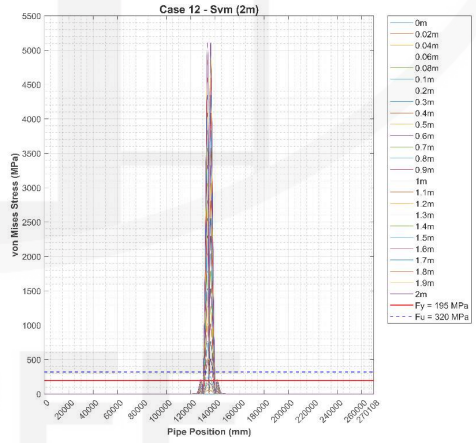

Fig.6. Case 12 pipeline von Mises stress distribution.

Conclusions

This study conducted numerical analyses using SAP2000 to assess the behavior of fault-crossing buried pipelines. The analysis focused on steel pipelines subjected to strike-slip fault movement at a dip angle of 90 degrees, with the fault movement direction aligned perpendicularly to the pipeline axial direction. The pipeline was modeled using beam elements, and discrete soil springs were applied at each beam element node. The results show that as the pipeline diameter increased, the von Mises stress decreased due to enhanced stiffness. In addition, the yield length at which tensile strength was reached increased with larger diameter pipelines, allowing for greater sustainable fault displacement.

References

Argyrou, C., O'Rourke, T.D., Pariya-Ekkasut, C., and Stewart, H.E. "Ductile iron pipeline response to earthquake-induced ground rupture." Earthquake Spectra, 2020, pp.1-24.

Demirci, H.E., Bhattacharya, S., Karamitros, D. & Alexander, N. "Experimental and numerical modeling of buried pipelines crossing reverse faults," Soil Dynamics and Earthquake Engineering, 2018, pp.198-214.

Demirci, H.E., Karaman, M. & Bhattacharya, S. "Behaviour of buried continuous pipelines crossing strike-slip faults: Experimental and numerical study," Journal of Natural Gas Science and Engineering, 2021, 103980.

Sarvanis, G.C., Karamanos, S.A., Vazouras, P., Mecozzi, E., Lucci, A. & Dakoulas, P. "Permanent earthquake-induced actions in buried pipelines: Numerical modeling and experimental verification," Earthquake Engineering Structural Dynamics, 2017, pp.1-22.

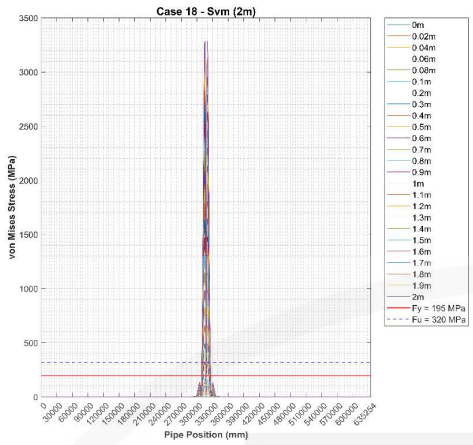

Fig.7. Case 18 pipeline von Mises stress distribution.

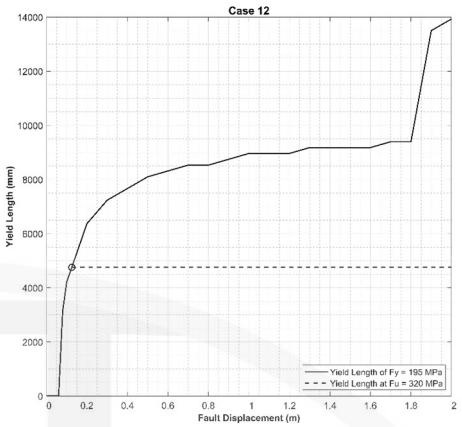

Fig.10. Case 12 pipeline yield length versus fault displacement.

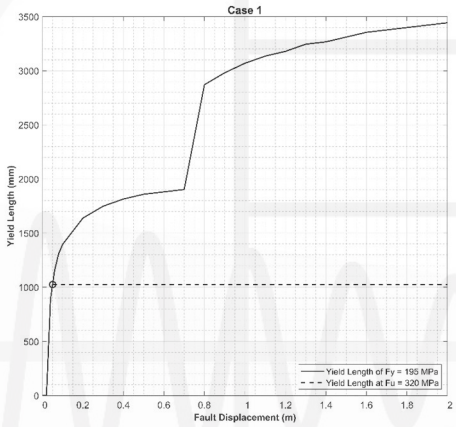

Fig.8. Case 1 pipeline yield length versus fault displacement.

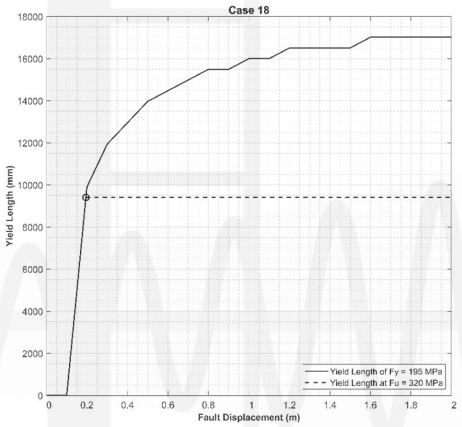

Fig.11. Case 18 pipeline yield length versus fault displacement.

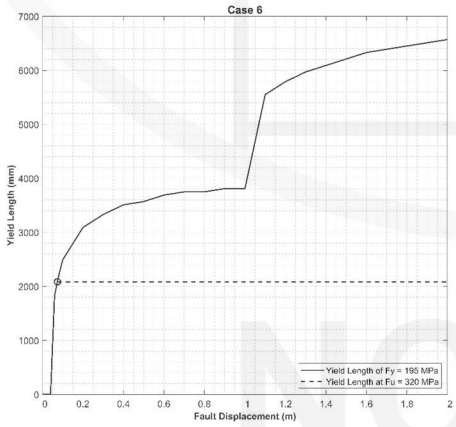

Fig.9. Case 6 pipeline yield length versus fault displacement.

Seismic Design of Constant-Section Truss-Confined Buckling-Restrained Braces

An-Chien Wu[1] and Ming-Chieh Chuang[1]

吳安傑[1]、莊明介[1]

Abstract

The key feature of a truss-confined buckling-restrained brace (TC-BRB) is the use of an additional truss-confining system attached outside the central steel casing. This truss system is composed of several steel open-web truss frames that provide the required restraining rigidity while reducing the size of the central casing section size and the amount of infilled mortar. The overall self-weight of the proposed TC-BRB is lower than that of conventional buckling-restrained braces (BRB), especially in long-span and large-force-capacity BRB applications. A simplified approach to determine the buckling load and design recommendations for the constant-section TC-BRB are provided for use in engineering practice.

Keywords: buckling-restrained brace, truss-confined restrainer, effective rigidity, buckling load

Introduction

The key feature of truss-confined buckling-restrained braces (TC-BRBs) is the use of an additional truss confining system that is attached outside the central steel casing. This truss system is composed of several open-web steel truss frames that provide the required restraining rigidity while reducing the size of the central casing section and the amount of infilled mortar. The hysteresis behavior of TC-BRBs in terms of truss member response, ability to resist buckling, and cumulative deformation capacity have been investigated by conducting cyclic loading tests on physical specimens having different yield capacities, truss frame shapes, and sizes. The results confirmed that the proposed TC-BRB can be designed and fabricated to achieve excellent seismic performance (Guo *et al*., 2017a, 2017b; Chen *et al*., 2021, 2022; AISC 2016; Wu *et al*. 2023). In this study, a simplified approach to determine the ultimate compressive strength and design recommendations for constant section TC-BRBs are provided for use in engineering practice.

Key Experimental Results

Details of the six TC-BRB specimens, test setup, loading procedure, hysteresis responses, and failure modes can be found in a previous experimental study (Wu *et al*. 2023). As illustrated in Figure 1, specimens CT and 2CT were equipped with a constant-section truss-confining system. The design dimensions of their steel cores and truss-confined restrainers are listed in Tables 1 and 2. Specimens CT and 2CT had nominal tensile yield capacities P_{yn} of 1016 and 853 kN, respectively, and they were made from CNS SN490B steel plates, which has a nominal yield stress of 325 MPa. The expected maximum compressive strength P_{max} was 2060 kN for specimen CT and 1730 kN for specimen 2CT, considering material over-strength, strain hardening, and compression strength adjustment factors of 1.2, 1.3, and 1.3, respectively. The axial deformation versus force relationships plots of the two specimens and their failure modes are presented in Figures 2 and 3, respectively. Additionally, their cyclic peak responses, including maximum tensile strength (T_{max}), compressive strength (C_{max}), core strain (ε_c), and cumulative inelastic deformation (CID) capacity, are listed in Table 3.

Table 1. Design dimensions of the steel cores.

Specimen	t_c (mm)	B_c (mm)	B_j (mm)	L_c (mm)	L_t (mm)	L_x (mm)	L_n (mm)	L_{pp} (mm)	L_B (mm)
CT	25	75	120	4878	50	250	120	6120	6270
2CT		65		4638	60	360			

[1] Associate Researcher, National Center for Research on Earthquake Engineering

Table 2. Design dimensions of the restrainers.

Specimen	Central casing (mm)	Chord (mm)	Post (mm)	Diagonal & transverse (mm)	L_{sc} (mm)	h_0 (mm)
CT	139.6×4	42.5×3	42.5×3	26.9×2.5	5478	200
2CT		48.4×3.2	48.4×3.2	33.8×2.8		220

Table 3. Key experimental results.

Specimen	Failure mode	T_{max} (kN)	C_{max} (kN)	Max. ε_c (%)		Max. P_T/P_y	Max. P_C/P_T	CID
				Positive	Negative			
CT	Buckling	1375	1378	0.60	0.34	1.15	-	-
2CT	Buckling	1447	1635	2.12	1.82	1.39	1.12	208

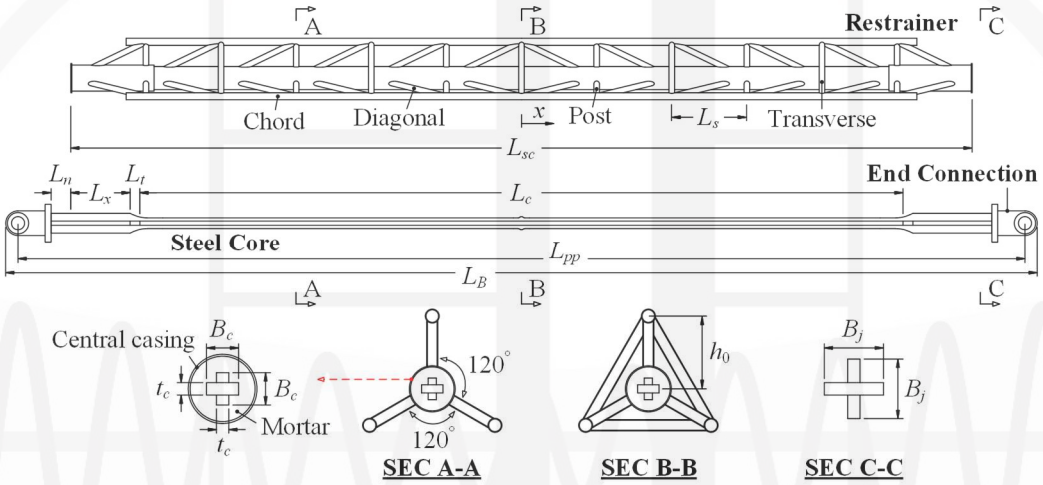

Fig. 1. Details of constant section TC-BRB.

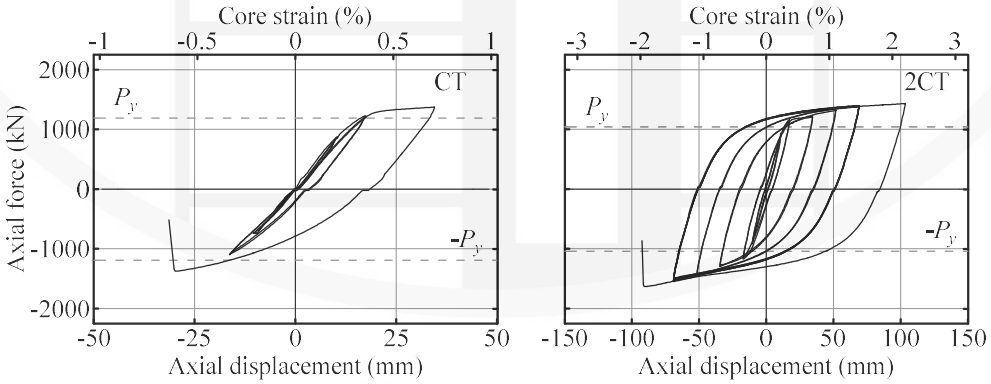

Fig. 2. Experimental responses of specimens.

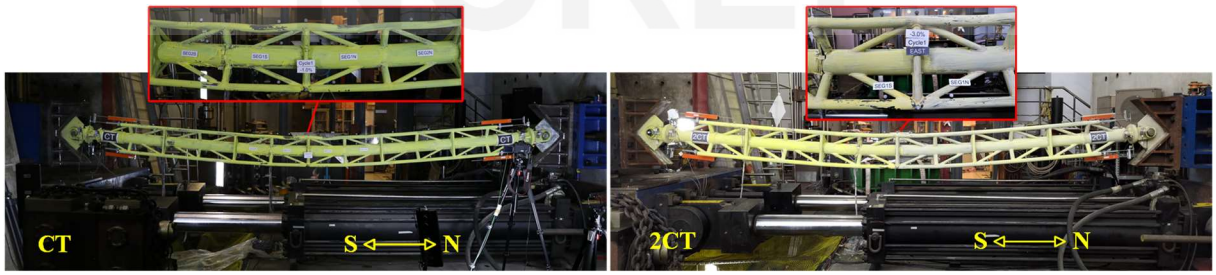

Fig. 3. Failure of the specimens.

Buckling Load

During specimen design, the buckling resistance of the constant-section truss-confining system was estimated using a previously described analytical method (Guo et al. 2017a). By considering the buckling direction, the flexural stiffness EI_{tr} of the constant-section truss-confining system comprising three identical plane truss frames with an equal incline angle between each other can be determined using the following equation:

$$EI_{tr} = 3EI_{ch} + 1.5E\left(A_{ch} + A_d\cos^3\theta_d\right)h_{eff}^{\ 2} \quad (1)$$

where E = 200 GPa is the elastic modulus of steel; I_{ch} is the moment of inertia of each chord about its own neutral axis; h_{eff} is the effective center-to-center distance between the central casing and the chord; θ_d is the diagonal inclination; and A_{ch} and A_d are the cross-sectional areas of each chord and diagonal, respectively. The shear stiffness K_v of the TC-BRB truss-confining system was determined as follows:

$$K_v = \frac{1.5EA_d\sin^2\theta_d\cos\theta_d}{1 + A_d\sin^3\theta_d / A_{po} + A_d\cos^3\theta_d / A_{ch}} \quad (2)$$

where A_{po} is the cross-sectional area of each post. The elastic buckling resistance P_{cr} of the TC-BRB was determined by considering the effect of shear deformation on the truss-confining system, as follows:

$$P_{cr} = P_{cr,e} + \lambda\frac{P_{cr,tr}}{1 + P_{cr,tr} / K_v},$$

$$\lambda = 0.14 + 1.22\left(\frac{K_v}{EA_d}\right)^2 + 2.35\sqrt{\frac{1}{n_s}} \quad (3)$$

where λ is a modification factor calibrated by performing finite element model analyses, and n_s is the number of truss segments. The elastic buckling resistance of the central casing ($P_{cr,e}$) and the truss-confining system ($P_{cr,tr}$) were determined as follows:

$$P_{cr,e} = \frac{\pi^2 EI_e}{L_{sc}^{\ 2}},\ P_{cr,tr} = \frac{\pi^2 EI_{tr}}{L_{sc}^{\ 2}} \quad (4)$$

where I_e is the moment of inertia of the central casing. After yielding of the steel core, the flexural resistance contributed by the core is relatively small owing to a substantial decrease in its stiffness. Consequently, the contribution of the core is excluded from the calculation of the elastic buckling resistance P_{cr} in Equation (3).

The assessed buckling resistance values of the restrainers used in specimens CT and 2CT are listed in Table 4. In conventional BRB design practice, a restraining ratio (P_{cr}/P_{yn}) greater than the product of the three considered over-strength factors is often adopted as a criterion (Tsai *et al*. 2014, Chuang *et al*. 2015) to prevent flexural buckling against the expected maximum compressive strength P_{max}. In this study, the product of the three considered over-strength factors is 1.2 × 1.3 × 1.3 = 2.03. According to Table 4, the calculated elastic buckling resistance P_{cr} of specimen 2CT is greater than the expected strength P_{max}, whereas the resistance of specimen CT is considerably lower than the expected compressive demand.

To demonstrate the efficiency of material usage in constant-section truss-confining systems, two types of BRBs were designed for the prototype mega braced frame. The cross-sectional layout of the steel cores used in for the design examples is identical to that of the specimens given in Figure 1 with a total length L_B of approximately 18 m. The dimensions of the steel cores used in the design examples are listed in Table 5. The nominal yield strength P_{yn} of the steel core is 7638 kN using SN490B steel with a calculated weight of W_c = 4.13 tonne. The buckling restrainers L_{sc} is 16m-long and the detailed dimensions are given in Table 6. The CT-BRB is essentially a TC-BRB designed with a constant-section truss-confining system by following the aforementioned analytical method. The restraining ratio of the CT-BRB is slightly higher than 3.0. CONV-1 and CONV-2 are conventional BRBs designed with 812.8 mm × 14 mm and 711.2 mm × 16 mm circular pipes, resulting in restraining ratios of 2.83 and 2.13, respectively. The estimated steel (W_r) and mortar (W_m) weights of the three restrainers are given in Table 6; a mortar density of 2.0 ton/m^3 is assumed. The amounts of steel used in the restrainers of CT-BRB and CONV-1 with a restraining ratio of approximately 3.0 are similar. However, the weight of the infilled mortar in CONV-1 is more than thrice that in CT-BRB. From the design examples, the total weight of the restraining system, including that of the steel restrainer and mortar, of the TC-BRB is approximately 40% less than that of a conventional BRB (100 × (13.79 - 23.15)/23.15 = -40.4% for CT-BRB). Even when compared to CONV-2, which was designed with a restraining ratio that was only slightly higher than the considered over-strength factor of 2.03 (= 1.2 × 1.3 × 1.3), the total weight of the restraining system the TC-BRB was still approximately 28% lower (100 × (13.79 - 19.24)/19.24 = -24.9% for CT-BRB).

The test results obtained from the buckled specimens in Table 3 revealed that the calculated critical loads P_{cr} in Table 4 significantly over-estimated the resistance of specimens CT and 2CT. Although the restraining ratio P_{cr}/P_{yn} of specimen 2CT was higher than the product of the considered over-strength factors (1.2 × 1.3 × 1.3 = 2.03), global instability was observed during the cyclic loading test. As stated in a previous study (Guo et al. 2017a), the limit values of restraining ratios for BRBs with different cross-sectional characteristics or end connections can differ. From the test results of specimen 2CT, it appears that further experimental research is warranted before lowering the limit value of the restraining ratios of the TC-BRB with constant-section truss-confining systems from 3.0 to the product of the over-strength factors.

Table 4. Buckling resistance assessments of the restrainers.

Specimen	h_{eff} (mm)	h_{eff} / h_0	θ_d (radian)	EI_{tr} (kN-m^2)	K_v (kN)	$P_{cr,e}$ (kN)	$P_{cr,tr}$ (kN)	λ	P_{cr} (kN)	P_{cr} / P_{yn}
CT	200	1.00	0.41	6278	5935	258	2065	0.848	1556	1.53
2CT	220	1.00	0.45	9562	9336		3145	0.854	2267	2.66

Table 5. Steel core dimensions of the design examples.

Type	t_c (mm)	B_c (mm)	B_j (mm)	L_c (mm)	L_t (mm)	L_x (mm)	L_n (mm)	L_{pp} (mm)	L_B (mm)	W_c (tonne)
CT-BRB CONV-1 CONV-2	50	260	445	12570	185	1530	225	17120	17570	4.13

Table 6. Restrainer dimensions of the design examples.

Type	Central casing (mm)	Chord (mm)	Post & Diagonal (mm)	Transverse (mm)	L_{sc} (mm)	a	h_0 (mm)	P_{cr} (kN)	P_{cr} / P_{yn}	W_r (tonne)	W_m (tonne)
CT-BRB	500×12	190.7×6	139.8×6	101.6×4		0	700	23531	3.08	4.84	4.82
CONV-1	812.8×14	-	-	-	16000	-	-	21614	2.83	4.41	14.61
CONV-2	711.2×16	-	-	-		-	-	16287	2.13	4.39	10.72

Conclusions

The proposed restraining system offers remarkable advantages in terms of its efficient flexural rigidity, lower self-weight, and improved architectural appearance when adopted as a large load-carrying and long-span brace in mega-braced frame structures. It is recommended that the restraining ratio be greater than 3.0 to develop the full capacity of the steel core for severe seismic service. The constant-section TC-BRB is considerably lighter than conventional BRBs in long-span applications. Compared to conventional BRBs, the appearance of the constant-section TC-BRB may be more attractive to some designers and building owners. This analytical and experimental investigation of the buckling load, hysteresis behavior, and failure mechanism have established the fundamentals for the further development of a comprehensive design method for the proposed TC-BRB.

References

Guo YL, Zhou P, Wang MZ, Pi YL, Bradford MA. Numerical studies of cyclic behavior and design suggestions on triple-truss-confined buckling-restrained braces. Engineering Structures 2017a; 146: 1-17.

Guo YL, Zhou P, Wang MZ, Pi YL, Bradford MA, Tong JZ. Experimental and numerical studies of hysteretic response of triple-truss-confined buckling-restrained braces. Engineering Structures 2017b; 148: 157-174.

Chen C, Lin YC, Wu AC, Chen LA, Tsai KC. Long-span buckling-restrained braces using truss-confined restrainers. Structural Engineering 2021; 36: 5-50. (in Chinese)

Chen LA, Wu AC, Chen C, Tsai KC. A Study of BRBs using Varying Section Steel Truss Restrainers. Structural Engineering 2022; 37: 27-47. (in Chinese)

American Institute of Steel Construction (AISC). Seismic Provisions for Structural Steel Buildings (AISC 341-16). AISC: Chicago, Illinois, 2016.

Wu AC, Tsai KC, Chen C, Chen LA, Lin YC, Experimental behavior of truss-confined buckling-restrained braces. Earthquake Engineering & Structural Dynamics 2023; 52: 624-640.

Tsai KC, Wu AC, Wei CY, Lin PC, Chuang MC, Yu YJ, Welded end-slot connection and debonding layers for buckling-restrained braces. Earthquake Engineering & Structural Dynamics 2014; 43: 1785-1807.

Chuang MC, Tsai KC, Lin PC, Wu AC, Critical limit states in seismic buckling-restrained brace and connection designs. Earthquake Engineering & Structural Dynamics 2015; 44: 1559-1579.

Deep-Learning-Driven Nonlinear Response-History Analysis and Structural Cross-Section Design Optimization

Kuang-Yao Li[1], I-Hsiang Chang[1], Wei-Tze Chang[2], Yin-Nan Huang[3] and Chuin-Shan Chen[4]

黎光曜[1]、張壹翔[1]、張慰慈[2]、黃尹男[3]、陳俊杉[4]

Abstract

In recent years, artificial intelligence technologies such as machine learning and deep learning have advanced rapidly, demonstrating fast computation and highly generalized simulation capabilities. These characteristics have led to their widespread adoption in various fields. In structural analysis and design, the existing practical approaches encounter several challenges. One major challenge is the adoption of nonlinear response-history analysis. Although this analysis method is more accurate than static and response spectrum analyses, it is significantly more time-consuming. Another challenge is heavy reliance on engineers' experience, which limits exploration and innovation in design solutions. To address these challenges, deep learning methods—including graph neural networks (GNNs), long short-term memory (LSTM) models, and reinforcement learning (RL) - are applied herein to develop solutions for two key objectives. Specifically, a nonlinear response-history prediction model is proposed for seismically isolated reinforced concrete structures and steel structures, and an optimal cross-section design model is developed. The results demonstrate the high accuracy and efficiency of these models, highlighting their potential for use in practical structural engineering applications.

Keywords: deep learning, steel structure, base-isolated structure, nonlinear response-history analysis, cross-section design

Introduction

In this project, various deep learning techniques are applied to structural engineering and earthquake engineering for overcoming the current limitations, accelerate analysis, and increase efficiency. The focus is on two primary topics: predicting the nonlinear response-history analysis of seismically isolated reinforced concrete structures and optimizing the cross-section design of steel moment-resisting frames.

The core technology used in both cases is graph neural networks (GNNs) (Scarselli et al., 2009), which, unlike traditional neural networks, can process flexible input structures. Graph data, consisting of nodes and edges, aligns well with structural topology (joints and members), while the message-passing mechanism (Gilmer et al., 2007) captures the dependencies between elements, thereby resembling force transmission in structures. Owing to these advantages, GNNs have been widely used in structural analysis, including static response simulations (Chang et al., 2020; Chou et al., 2024).

For nonlinear response prediction in seismically isolated concrete structures, GNNs are integrated with long short-term memory (LSTM) networks (Hochreiter et al., 1997) in this study to model time-dependent structural responses under earthquake loading. The proposed model predicts joint displacement, velocity, acceleration, member forces, and isolator behavior. It generalizes across various structural geometries and seismic records.

For cross-section optimization in steel moment-resisting frames, a GNN is combined with reinforcement learning (RL) to automate design decisions for

[1] M.S. Student, National Taiwan University
[2] Associate Researcher, National Center for Research on Earthquake Engineering
[3] Associate Professor, National Taiwan University
[4] Distinguished Professor, Department of Civil Engineering, Department of Materials Science and Engineering, National Taiwan University

minimizing material costs while fulfilling structural strength requirements.

Prediction and Design of Nonlinear Response-History Analysis of Base-Isolated Reinforced Concrete Structures

Prediction of Nonlinear Response-History Analysis

In this study, nonlinear response-history analyses of 4,650 randomly generated base-isolated reinforced concrete structures are conducted using the OpenSees finite-element software to establish a training dataset. The isolation system consists primarily of lead-rubber bearings, natural rubber bearings, and fluid viscous dampers. The overall design scope is detailed in Tables 1 and 2. The graph-LSTM framework (Chou et al., 2024), which utilizes a graph attention network (GAT) to extract structural topology features and integrates an LSTM network to predict the time-history responses of all structural nodes and member forces, is used in this study.

Table 1. Design scope of lead-rubber bearings

Characteristic strength Q_d	$3\%W$-$9\%W$
Post-yield period T_2	3.0-4.5
Pre-yield stiffness K_1	$max[10K_2, F_y/1\ cm]$

Table 2. Design scope of viscous damper

ζ (%)	0	5	10	15
α	0.4	0.7		1

Training Results of Nonlinear Response-History Analysis Prediction Model

The trained Graph-LSTM model achieved high prediction accuracy, with R^2 values exceeding 0.96 for most response time series and peak values compared to the simulation data. Figure 1 presents the best-performing response-history prediction from the entire test set, where the predicted responses closely match those obtained from the OpenSees analysis. Furthermore, compared to traditional finite-element methods, the Graph-LSTM model improves the computational efficiency substantially, achieving speedups of up to 860 times. These results highlight its potential for use in practical applications.

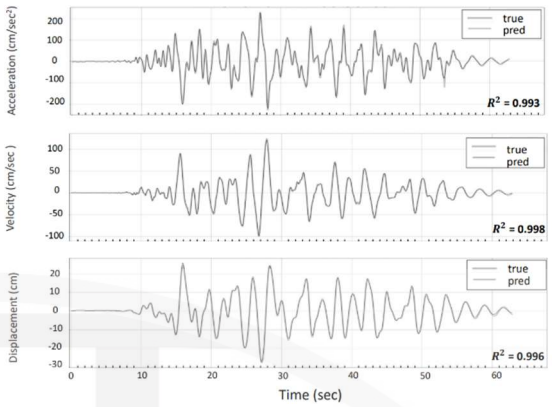

Fig. 1. Comparison of response-history prediction between a test case and finite-element analysis results.

Dimensionality Reduction and Reliability Analysis of Model

A dimensionality reduction and visualization analysis of the graph embedding was conducted. As illustrated in Figure 2, the graph embedding is closely correlated to the fundamental vibration period of the building structure, thereby demonstrating that the model effectively captures the critical features essential to structural dynamic behavior. This further validates the reliability of the graph-LSTM framework.

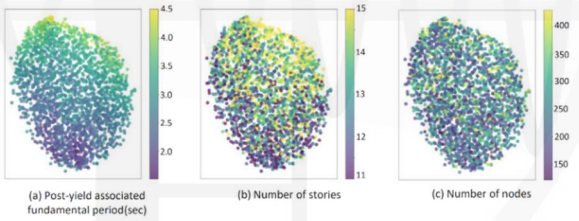

Fig. 2. Visualization of dimensionality reduction of graph embedding.

Design Optimization of Base-Isolated Structure

By integrating the aforementioned fast nonlinear dynamic analysis model with a multi-objective optimization algorithm, this study aims to optimize the design of base-isolated structures. Based on extensive simulations of various isolation design schemes, the proposed approach effectively addresses the trade-off between isolator displacement and superstructure acceleration. It identifies a Pareto optimal set, which provides engineers with clear and meaningful decision-making guidance, thereby advancing the development of performance-based design for base-isolated structures.

Cross-Section Design Optimization of Steel Structure

Reinforcement learning is a deep learning approach that allows a model to accumulate experience

through interactions with its environment and learn to make optimal decisions for maximizing or minimizing specific objectives by receiving rewards. Japanese researchers (Hayashi et al., 2022) developed a graph-based reinforcement learning framework for optimizing the cross-sectional design of two-dimensional steel frames. Compared to other optimization methods, this framework exhibits high generalizability.

Model Construction and Design Target

In this study, the aforementioned approach to three-dimensional steel moment-resisting frames is extended by developing an AI-assisted cross-section optimization framework called graph-RL. This framework is designed to optimize the cross section of structures with varying numbers of stories (4–7 stories), spans (2–6 bays), and bay widths (6–8 m) with the aim of minimizing the total volume of structural components (material usage). The design strength is evaluated on the basis of Taiwan's static design regulations and different load combinations.

The reinforcement learning algorithm employed herein is the Deep Q-Network (DQN) (Mnih et al., 2013), which is designed to solve discrete action space problems. During optimization, the DQN predicts the Q-values of each group of beam and column members, which represent the expected cumulative reward associated with the selection of a particular component. By leveraging these predicted Q-values, the model gradually identifies the optimal members for reduction, ultimately minimizing the total material cost.

Model Training and Inference Process

Figure 3 illustrates the overall workflow of the Graph-RL framework. During training, structures with various geometric configurations serve as inputs, and all structural members are initially assigned the largest possible cross sections.

In each design iteration, the environment (finite-element structural analysis software) evaluates the strength of the current design. If the design satisfies the code-based strength requirements, the model selects a group of beam or column members based on the current state of the structure by following the epsilon-greedy strategy to reduce their cross-sectional sizes. The environment then calculates the reduction in material volume as a reward and outputs the structural analysis results for the updated design. A sequence of states, actions, and rewards is stored, allowing the graph-RL model to sample data and update its parameters.

During the inference stage, the process remains largely the same, except that the model strictly follows a greedy strategy and selects only the best possible action while keeping its parameters unchanged.

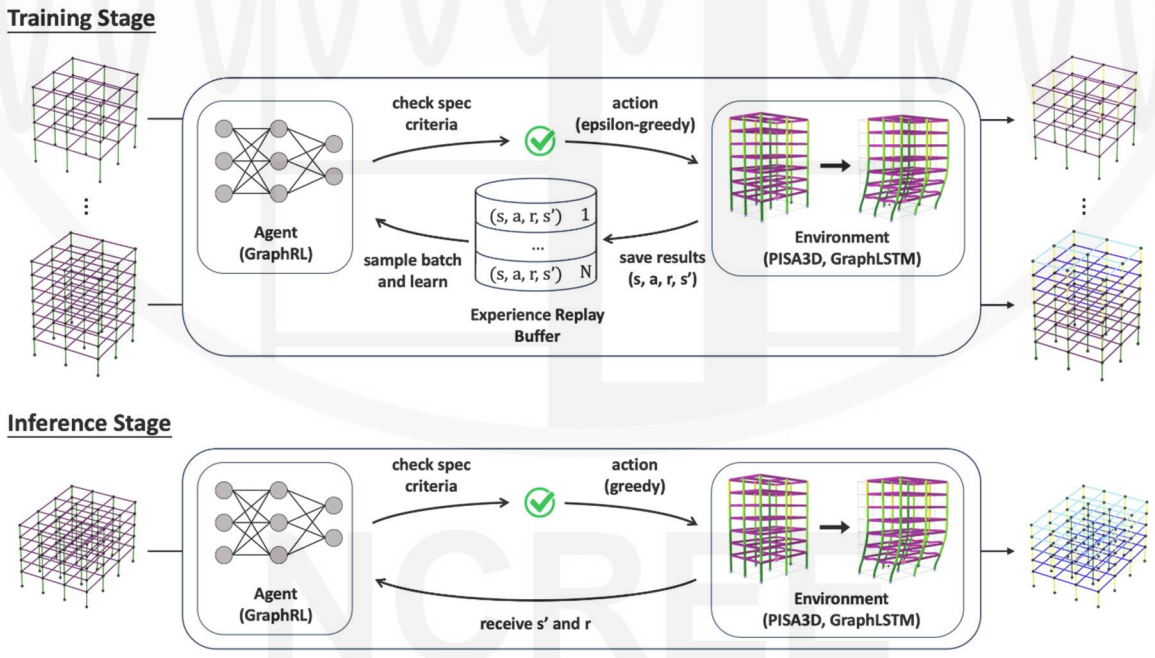

Fig. 3. Training and inference workflow of graph-RL model.

Performance Evaluation of Graph-RL Model

To evaluate the design performance of the Graph-RL model during training, a fixed-geometry structure (with predetermined spans, bays, and story count) is designated as the test structure. After a certain number of training episodes, the model performs inference on this test structure.

Figure 4 depicts the total cumulative reward obtained in each training episode (black dashed line). Because the input structures vary continuously, no clear

trend is observed. However, the cumulative reward from the test inferences (red solid line) shows a distinct upward and stabilizing trend. This indicates that throughout training, the model progressively learns how to optimize the cross-section design while fulfilling strength constraints, resulting in more efficient material usage.

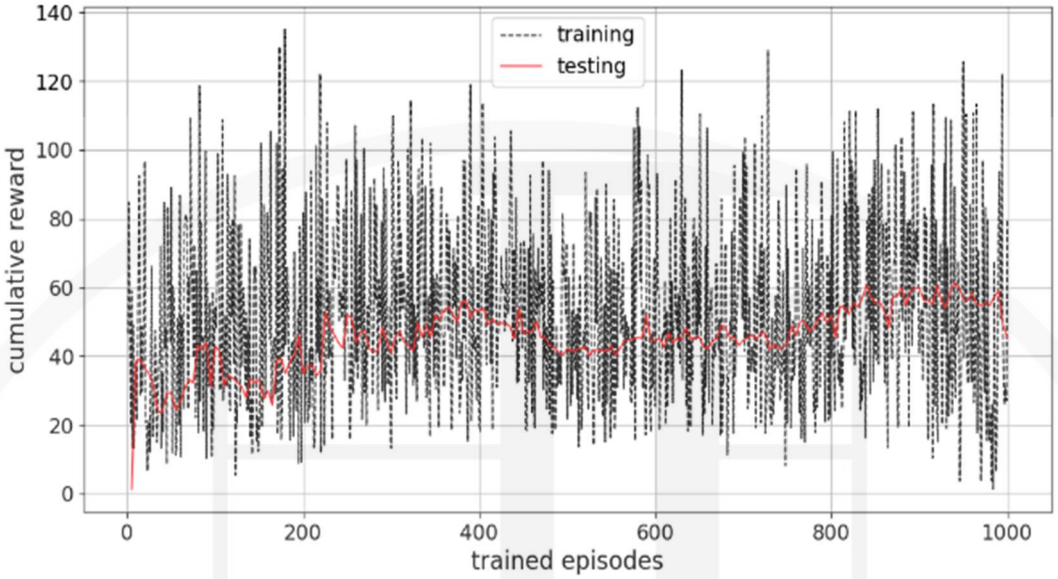

Fig. 4. Cumulative reward of training and inference stage for each episode.

Conclusions

This study aimed to optimize structural design by training AI models to perform rapid nonlinear response-history analysis. Successful applications were demonstrated for both steel structures and base-isolated reinforced concrete structures. The graph-LSTM model accurately predicts nonlinear time-history responses, while the reinforcement learning-based graph-RL model effectively optimizes the cross-section design of steel structures.

However, the current models are limited to the specific structural types considered herein. Future research should extend its applicability to a broader range of materials and building types to broaden practical use cases and accelerate seismic engineering analysis and design processes.

References

Scarselli, F., Gori, M., Tsoi, A. C., Hagenbuchner, M., and Monfardini, G., "The Graph Neural Network Model," IEEE Transactions on Neural Networks, 2009, 20(1), pp. 61-80. doi:10.1109/TNN.2008.2005605.

Gilmer, J., Schoenholz, S. S., Riley, P. F., Vinyals, O., and Dahl, G. E., "Neural Message Passing for Quantum Chemistry," arXiv, 2017. doi:10.48550/ARXIV.1704.01212.

Battaglia, P. W., Hamrick, J. B., Bapst, V., et al., "Relational Inductive Biases, Deep Learning, and Graph Networks," arXiv, 2018. doi:10.48550/ARXIV.1806.01261.

Chang, K. H., and Cheng, C. Y., "Learning to Simulate and Design for Structural Engineering," arXiv, 2020. doi:10.48550/ARXIV.2003.09103.

Chou, Y. T., Chang, W. T., Jean, J. G., Chang, K. H., Huang, Y. N., and Chen, C. S., "StructGNN: An Efficient Graph Neural Network Framework for Static Structural Analysis," Computers & Structures, 2024, 299, 107385. doi:10.1016/j.compstruc.2024.107385.

Hochreiter, S., and Schmidhuber, J., "Long Short-Term Memory," Neural Computation, 1997, 9(8), pp. 1735-1780.

Chou, Y.-T., Kuo, P.-C., Li, K.-Y., Chang, W.-T., Huang, Y.-N., and Chen, C.-S., "Inductive Graph-Based Long Short-Term Memory Network for the Prediction of Nonlinear Floor Responses and Member Forces of Steel Buildings Subjected to Orthogonal Horizontal Ground Motions," Earthquake Engineering & Structural Dynamics, 2024, pp. 1-17. doi:10.1002/eqe.4264.

Hayashi, K., and Ohsaki, M., "Graph-Based Reinforcement Learning for Discrete Cross-Section Optimization of Planar Steel Frames," Advanced Engineering Informatics, 2022, 51, p. 101512. doi:10.1016/j.aei.2021.101512.

Mnih, V., Kavukcuoglu, K., Silver, D., et al., "Playing Atari with Deep Reinforcement Learning," arXiv, 2013.

Bridge Inspection Assessment and Automated Defect Detection Using UAV-Based Computer Vision Framework

Kuan Yen[1] and Chia-Ming Chang[2]

嚴寬[1]、張家銘[2]

Abstract

Bridge integrity is critical for infrastructure safety, especially because aging and natural disasters can compromise the structural performance of bridges. Traditional bridge inspections are essential but often slow, labor-intensive, and unable to access certain components such as abutments and the undersides of bridge decks. Recent advances in unmanned aerial vehicles (UAVs) have markedly improved the efficiency of bridge inspection. This study proposes a systematic UAV-based framework for automated visual inspection of bridges by integrating deep learning and computer vision. First, UAV-captured images are localized by converting camera coordinates into global (GPS) coordinates on the basis of azimuth and camera-to-object distance data. Next, an instance segmentation model is used to detect and delineate cracks, concrete spalling, and exposed reinforcement, and each defect is tagged with precise spatial coordinates. Finally, photogrammetric techniques are used to quantify the three-dimensional geometric parameters of the identified defects. A demonstration case is used to confirm that the proposed framework substantially increases inspection efficiency and produces comprehensive, high-resolution condition data, including defect location, type, and size, that improve bridge inspection by incorporating spatial positioning and defect quantification.

Keywords: Unmanned aerial vehicles, bridge inspection, computer vision, deep learning, defect quantification

Introduction

The structural integrity of bridges is a critical safety concern in infrastructure management because both natural disasters and structural aging can induce bridge deterioration, subsequently compromising public safety. Hence, regular inspection and assessment of bridge conditions are indispensable. However, Taiwan experiences a notable challenge, where the number of bridges far exceeds the availability of professional inspectors, rendering traditional visual inspection methods inefficient due to insufficient field engineering expertise. Furthermore, it is often difficult for field engineers to visually inspect specific bridge components, such as piers spanning rivers or the undersides of bridge decks, which necessitates reliance on inspection vehicles or small inflatable boats.

In recent years, the application of unmanned aerial vehicles (UAVs) has substantially enhanced the efficiency of bridge inspection. This study proposes a comprehensive computer-vision-based bridge inspection framework comprising three key processes: image localization, defect detection, and damage quantification. By integrating ultra-wideband (UWB) and real-time kinematic (RTK) technologies, the framework can precisely determine the azimuth and distance from the camera to the target, thus effectively localizing the images captured by UAVs. This hybrid positioning method employs two-way ranging (TWR) techniques to simulate satellite functionality for UAVs operating in areas with weak GNSS signals.

For defect identification, the framework utilizes deep learning models with instance segmentation capabilities to effectively identify critical defects, including cracks, concrete spalling, exposed reinforcement, and water seepage, which substantially enhances image analysis capabilities. To validate the practicality of the proposed framework and apply it under actual field conditions, technical parameters are continuously adjusted and optimized according to

[1] Doctoral Student, National Taiwan University
[2] Research Fellow, National Center for Research on Earthquake Engineering

real-world scenarios to ensure system reliability and applicability.

Compared to conventional manual visual inspection, UAV-based methods provide more comprehensive deterioration detection results and facilitate inspection from multiple angles (e.g., cap beams and main girders) that would otherwise be inaccessible. Moreover, the bridge defect locations detected using deep learning algorithms can be documented in bridge assessment reports to provide more scientific and comprehensive bases for bridge maintenance management.

Smart Bridge Inspection Framework

This study presents a smart bridge inspection framework, as illustrated in Fig. 1. The framework comprises three principal processes: automated image data acquisition using unmanned aerial vehicles, development of bridge defect detection models through deep learning techniques, and integration of the detection results with bridge assessment ratings. Through UAV automation, visible-light images of a bridge's exteriors are acquired; subsequently, instance segmentation models are established to detect four specific defect types, i.e., cracks, concrete spalling, exposed rebar, and water seepage, to allow for precise localization of structural deficiencies. After detection, image geometry extraction methods are combined with standardized evaluation criteria to derive the corresponding D.E.R.&U. values, which facilitates the assessment of structural safety and determination of urgency classifications.

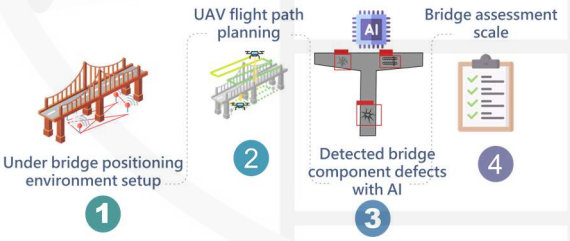

Fig. 1. Smart bridge inspection framework.

To acquire the structural imagery of bridges, the open-source flight planning software Mission Planner is employed herein as an instrument for generating UAV-readable flight paths (Chintanadilok et al., 2022). During this process, it is essential to ensure that the captured images contain the scale, geometric transformation, and coordinate data necessary for subsequent safety assessments. Moreover, the UAV flight paths must be planned meticulously to accommodate bridge substructure environments with insufficient GNSS signals, necessitating the implementation of UWB networks to capture critical component images, including girder webs, diaphragms, and bearing systems. The UWB positioning network is established using multiple UWB transmitters. These fixed ground-based UWB units generate virtual GNSS signals that effectively replace actual GNSS signals, which are obstructed by structural elements. The system calculates relative coordinates and transmits them to mobile aerial UWB units, allowing the UWB devices mounted on aerial UAVs to obtain absolute coordinates and complete spatial positioning, as depicted in Fig. 2.

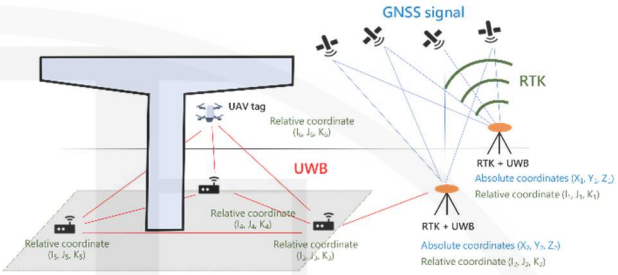

Fig 2. UWB network layout on a bridge.

The data for this study consists of two primary sources: independently collected bridge imagery and professional datasets from engineering consulting firms. To build a reliable training base, selected images from the Mapillary Vistas dataset (Neuhold et al., 2017) were extracted, focusing on explicit depictions of bridge structures. These images were supplemented with a self-annotated dataset of concrete bridge defects. The study focuses on four key defect types: concrete cracks, concrete damage, exposed reinforcement, and seepage. After rigorous screening and quality control, a final training set of around 1,000 images with clearly defined defect features was compiled.

For model development, the Detectron2 library (Wu et al., 2019) was used as the core framework. Built on PyTorch (Paszke et al., 2019) and developed by Facebook AI Research (FAIR), Detectron2 offers a modular structure that supports fast experimentation, parameter tuning, and future scalability. Using this framework, a Mask Region-Based Convolutional Neural Network (Mask R-CNN) was implemented for automated defect detection and segmentation, achieving accurate and scalable bridge defect identification.

According to the domestic "Highway Bridge Inspection and Reinforcement Specifications," periodic inspections of highway bridges employ the D.E.R.&U. visual inspection assessment criteria. In this methodology, comprehensive evaluations of bridge structural deterioration are conducted across four dimensions: "Degree," "Extent," "Relevancy to bridge structural safety and serviceability," and "Urgency of repair." A key advantage of the D.E.R.&U. assessment methodology is its requirement to evaluate only the components that exhibit signs of deterioration. This requirement eliminates redundant inspections of components in good condition, effectively streamlining the inspection workflow and precisely highlighting critical components with structural damage.

UAV Smart Bridge Inspection Test

The Wanshou Bridge in Taipei City was selected as a demonstration site for this study, and a UWB positioning system was established along its structure. This 166-meter-long bridge was equipped with 27 UWB sensors along its span. Because the bridge crosses the Jingmei River, the distance between piers exceeded the communication range of the UWB equipment. Therefore, to enhance positioning accuracy during UAV traversal over the river, additional UWB devices were installed on both riverbanks to provide stable positioning signals throughout the inspection process.

Bridge data were collected by means of UAV inspection, with a focus on critical defects including cracks, concrete spalling, exposed rebar, and seepage. These data formed the basis for training specialized segmentation models for bridge visual inspection. AI-based deterioration recognition technology employing computer vision was used to conduct an in-depth analysis of bridge imagery with the aim of automatically identifying various types of damage and precisely delineating the locations and extents of deterioration. As illustrated in Fig. 3, the blue and red bounding boxes indicate crack and concrete spalling regions, respectively. This intelligent inspection methodology significantly reduced both inspection time and cost while simultaneously increasing detection accuracy. Unlike traditional manual inspection methods, AI-based deterioration recognition is unaffected by subjective factors. Its assessment criteria are based on data analysis and machine learning algorithms, and therefore, it provides more objective and accurate results. Fig. 3 depicts how the deep learning model precisely localizes specific defects: cracks (blue bounding boxes), concrete spalling (red bounding boxes), exposed reinforcement (green bounding boxes), and moisture infiltration (yellow bounding boxes). This technology provides not only clearly defined defect identification frames but also measurements of the overall extent of deterioration and basic dimensional information, as illustrated in Fig. 4. Therefore, it can be used to obtain concrete reference data for subsequent reinforcement and repair schedules.

Conclusions

The next-generation intelligent bridge inspection methodology developed in this project addresses the enhancement of bridge structural safety, a critical public-infrastructure-related concern. In terms of data acquisition, we established a comprehensive UAV flight planning protocol. The most significant innovation is the implementation of a UWB network system that effectively resolves the technical challenge of collecting imagery from beneath bridge structures—a persistent limitation in conventional inspection approaches. Another key technological component is the UAV-based image processing, analysis, and management system, which integrates deep learning and computer vision technologies to construct a robust bridge inspection framework. This system enables engineering personnel to perform inspection tasks with enhanced efficiency and precision.

Fig. 3. Smart bridge inspection framework.

Fig. 4. Smart bridge inspection framework.

The AI recognition process comprises three essential processes: image localization, deterioration identification, and damage assessment. Unlike previous works, which focused primarily on deterioration recognition, this project establishes a comprehensive, integrated framework for bridge inspection that effectively assists engineers in conducting routine inspection operations. By establishing a robust connection between AI-driven outcomes and the current bridge inspection standards—specifically the D.E.R.&U. evaluation methodology—the proposed approach provides inspection technicians with objective and reliable preliminary assessment criteria.

Regarding future work, this project will continue to explore innovative applications of advanced technologies in bridge inspection to further increase the efficiency and accuracy of inspections. Notably, the proposed technological framework is not limited to bridge inspection but can be adapted to various other domains: factory inspection (utilizing UAVs for elevated inspections to complement the limited vertical perspective of autonomous ground vehicles, thereby achieving comprehensive technological inspection coverage); solar panel inspection (integrating thermal infrared sensing technology to precisely monitor solar panel generation efficiency, enabling immediate fault resolution, and enhancing overall power generation performance); and inspection of other infrastructure facilities (employing UAV-assisted periodic facility inspections to significantly reduce labor costs and operational risks). These extended applications support the development of comprehensive, intelligent technological inspection protocols across multiple infrastructure domains.

References

1. Chintanadilok, J., Patel, S., Zhuang, Y., & Singh, A. (2022). Mission Planner: An open-source alterna-tive to commercial flight planning software for unmanned aerial systems. EDIS, 2022(4).
2. Zhou, F., Wen, G., Qian, G., Ma, Y., Pan, H., Liu, J., & Li, J. (2022). A high-efficiency deep-learning-based antivibration hammer defect detection model for energy-efficient transmission line inspection systems. International journal of antennas and Propagation, 2022.
3. Gong, Y., Zhou, W., Wang, K., Wang, J., Wang, R., Deng, H., & Liu, G. (2023). Defect detection of small cotter pins in electric power transmission system from UAV images using deep learning tech-niques. Electrical Engineering, 105(2), 1251-1266.
4. He, K., Gkioxari, G., Dollár, P., & Girshick, R. (2017). Mask R-CNN. In Proceedings of the IEEE In-ternational Conference on Computer Vision (pp. 2961-2969).
5. Kim, S., Kim, D., Jeong, S., Ham, J. W., Lee, J. K., & Oh, K. Y. (2020). Fault diagnosis of power transmission lines using a UAV-mounted smart inspection system. IEEE Access, 8, 149999-150009.
6. Moore, M., Phares, B. M., Graybeal, B., Rolander, D., Washer, G., & Wiss, J. (2001). Reliability of visual inspection for highway bridges, Volume I (No. FHWA-RD-01-105). Turner-Fairbank Highway Research Center.
7. Munawar, H. S., Ullah, F., Shahzad, D., Heravi, A., Qayyum, S., & Akram, J. (2022). Civil infrastruc-ture damage and corrosion detection: An application of machine learning. Buildings, 12(2), 156.
8. Neuhold, G., Ollmann, T., Rota Bulo, S., & Kontschieder, P. (2017). The mapillary vistas dataset for semantic understanding of street scenes. In Proceedings of the IEEE International Conference on Computer Vision (pp. 4990-4999).
9. Paszke, A., Gross, S., Massa, F., Lerer, A., Bradbury, J., Chanan, G., … & Chintala, S. (2019). Pytorch: An imperative style, high-performance deep learning library. Advances in Neural Infor-mation Processing Systems, 32.
10. Savino, P., & Tondolo, F. (2023). Civil infrastructure defect assessment using pixel-wise segmentation based on deep learning. Journal of Civil Structural Health Monitoring, 13(1), 35-48.
11. Liu, Y., Dong, J., Li, Y., Gong, X., & Wang, J. (2022). A UAV-based aircraft surface defect inspection system via external constraints and deep learning. IEEE Transactions on Instrumentation and Meas-urement, 71, 1-15.
12. Yoshikura, M., Minami, T., Fukuoka, T., Fujiu, M., & Takayama, J. (2022, March). Assessment of bridge engineers on output display size in automatic detection of free lime using deep learning. In 7th International Conference on Road and Rail Infrastructure.

(This report is adapted and paraphrased from the content of "Framework of UAV bridge inspection with computer vision and deep learning". For full details, please refer to: Kuan, Yen, and Chia-Ming Chang. 2024. *Framework of UAV Bridge Inspection with Computer Vision and Deep Learning*, Pp. 862-869 in.)

Urban Rescue Networks and Disaster Information Integration

Cheng-Tao Yang[1], Lien-An Chen[2], Ya-Chu Tsao[3], Yi-Chang Chu[4], and Shih-Hsuan Huang[2]

楊承道[1]、陳蓮安[2]、曹雅筑[3]、朱易昌[4]、黃士軒[2]

Abstract

This project uses urban road networks to integrate disaster text analysis, road and urban block risk assessment, and image recognition technologies for increasing the precision of decision-making support in disaster response. The key developments under this project in 2024 are as follows: (1) Disaster text mining, wherein temporal and spatial analyses are applied to improve the timeliness and structure of disaster data; (2) expansion of the road and urban block risk assessment model by applying it to the Miaoli–Taichung–Changhua–Nantou areas to verify its applicability; and (3) integration of image recognition, as tested during the 0403 Hualien earthquake, to enhance road damage detection.

Keywords: Rescue routes, Text mining, Image recognition

Introduction

As climate change intensifies, densely populated urban areas face greater disaster risks because of high concentration of buildings and complex infrastructure. Therefore, increasing the precision of disaster response and improving rescue route management have emerged as critical challenges in disaster prevention efforts.

In this project, we integrate numerical road networks, urban block maps, rescue points, transportation nodes, and population distribution. By using large language models (LLMs), we analyze disaster messages to extract address and event-type information, and their classification and severity grading is aligned with user-defined categories. These data are then subjected to temporal and spatial analysis. Additionally, image recognition techniques are applied to identify impacted regions and critical assets, thereby improving the structure and timeliness of disaster data. The proposed system is validated in Taichung and Hualien regions, as presented in the following applications.

Disaster Text Mining

In this project, LLMs are applied to process disaster-related text for increasing the speed and accuracy of information management during emergencies. Unlike traditional manual classification, which assigns only one disaster type per message, LLMs can automatically extract address information and identify multiple disaster types within a single message. Moreover, they assign severity levels based on user-defined criteria, thereby allowing for more efficient resource allocation.

After classification, temporal analysis is performed to compare reporting patterns between earthquakes and typhoons. For example, during the April 3 earthquake (Fig. 1), the number of messages spiked abruptly and declined slowly, exhibiting a long-tail pattern linked to prolonged structural repairs. By contrast, the reports related to Typhoon Gaemi (Fig. 2) were generated primarily during daytime, coinciding with the storm's active period. These patterns underscore the need for hazard-specific response strategies. In addition, spatial analysis is conducted. The addresses extracted from the messages without coordinates are geocoded using the Ministry of the Interior's address database. Based on the classification results, hotspot maps are generated for various disaster types, such as building collapse, humanitarian crises, gas incidents (Fig. 3), and elevator entrapments (Fig.

[1] Associate Researcher, National Center for Research on Earthquake Engineering
[2] Research Assistant, National Center for Research on Earthquake Engineering
[3] Student, Department of Civil Engineering, National Taiwan University
[4] Former Research Assistant, National Center for Research on Earthquake Engineering

4), to help identify high-risk areas and guide response planning.

Miaoli–Taichung–Changhua–Nantou

To assess the effects of earthquake-induced road blockages caused by damage to or collapse of roadside buildings along Central Taiwan's major rescue routes, this project compiled the road network data of Taichung City, Nantou County, Changhua County, and Miaoli County. The Tgbs module of the TELES system was used to simulate building damage due to a large-scale earthquake. The analysis additionally incorporated a post-earthquake road blockage risk assessment method proposed by Chu et al. [1][2], which employs quantitative indicators to identify high-risk segments. These indicators include (1) the dispersal width of building debris, (2) affected length ratio of each road segment, and (3) overall blockage severity. The results serve as a basis for evaluating road passability and guiding emergency response planning following an earthquake.

As illustrated in Fig. 5, the Taichung–Changhua Fault runs in the north–south direction. In the simulated seismic scenario, densely built areas near the fault, particularly in Taichung City, Changhua County, and Nantou County, are more prone to extensive building collapse, which can potentially lead to temporary traffic paralysis. The red-highlighted roads represent segments with reduced serviceability or elevated blockage risk, which would significantly affect traffic functionality. It is recommended that alternate routes be pre-planned for these high-risk segments to maintain emergency access and regional connectivity in the event of a major earthquake.

Key High-Risk Roads Identified:

Nantou County: Chenggong Rd., Taiping Rd., Zhangnan Rd., Nangang 2nd Rd., Daming Rd.

Changhua County: Shatian Rd., Zhongshan Rd., Jinhua Rd., Jiancheng Rd., Zhongxing Rd., Zhongzheng Rd.

Taichung City: Zhonghua Rd., Sanfeng Rd., Zhongzheng Rd., Zhongqing Rd., Beitun Rd., Minsheng Rd., Jinma 3rd Rd., Zhongshan 3rd Rd.

Hualien

Before April 2024, this project completed a seismic road blockage risk assessment for Hualien by using a displacement scenario along the north–south trending Milun Fault. High-risk urban blocks were identified by cross-referencing three datasets: (1) roadside building composition, (2) estimated road blockage risk, and (3) the spatial distribution of buildings by seismic design code era. These assessments were used to identify highly exposed areas for targeted disaster prevention planning.

On April 3, 2024, a magnitude 7.1 earthquake struck Hualien. As depicted in Figure 6, the distribution of red- and yellow-tagged buildings after the event strongly correlated to the high-risk urban blocks and road segments identified by this project. This demonstrates the practical value of earthquake risk modeling based on the seismic vulnerability of buildings.

In 2024, the project further applied image recognition techniques to assess road damage from the 0403 Hualien earthquake to facilitate rapid post-disaster evaluation. The core technology was remote sensing-based damage detection using satellite, aerial, and UAV imagery, enhanced using deep learning models. Traditional methods such as field inspection and public reporting are often time-consuming and constrained by labor and environmental conditions. To address this challenge, the project adopted Chen & Lin's method [3], which uses generative adversarial networks (GANs) to create synthetic training datasets and Siamese neural networks to improve detection performance.

Additionally, experiments were conducted using synthetic datasets possessing diverse features to improve the model's generalization ability in different application scenarios, thus effectively addressing the shortage of road damage samples in satellite imagery.

In the 0403 Hualien case, image data were obtained from the Aerial Survey and Remote Sensing Branch. The aerial imagery had a resolution of 0.25 m, with each image covering an area of approximately 8 km². Each image was processed in approximately 3 min. As depicted in Figure 7, in urban areas, the model successfully identified road damage near the collapsed Uranus Building. In mountainous regions, such as Taroko, the model detected multiple landslides and falling rocks, thereby effectively outlining the affected road segments and their impact zones.

These results were further integrated with numerical road networks to assess the extent of road blockage and guide alternative route planning. In the future, this technology can be applied to support disaster response strategies, relief material distribution, and resident alert provision, thereby improving the efficiency of emergency response and decision making. Moreover, the image recognition module was integrated into the "Disaster-Oriented Digital Twin Model for Automated Rescue Simulation" to support digital twin–based road damage analysis and visualization.

Conclusion

This project integrates digital twin technology, text mining, and AI-based image recognition for earthquake disaster prevention applications. These technologies are extended to multiple regions to provide enhanced decision-making support to government agencies and disaster response institutions. Our key achievements in 2024 include disaster information text analysis, risk assessment of roads and urban blocks, and testing of image recognition techniques—all of which have been implemented and validated in Kaohsiung, Hualien, Yunlin–Chiayi–Tainan, and Miaoli–Taichung–Changhua–Nantou.

References

1. Chu, Yi-Chang, Yang, Cheng-Tao, Yeh, Chin-Hsun, & Lin, Szu-Yun. (2023). Multi-index assessment of road blockage risk due to seismic event-induced building debris. Earthquake Spectra, 39(4), 2193–2211.
2. 楊承道、曹雅筑、吳文元、朱易昌。(2022 年 12 月)。《救援路網規劃與震損風險評估原型軟體發展—QGIS Python Plugin 開發者技術手冊（第一版)》。財團法人國家實驗研究院國家地震工程研究中心(NCREE-2022-019)。
3. Chen, Lien-An, & Lin, Szu-Yun. (2025). Enhancing road damage identification in satellite images through synthetic data. International Journal of Disaster Risk Reduction, 116, 105091.

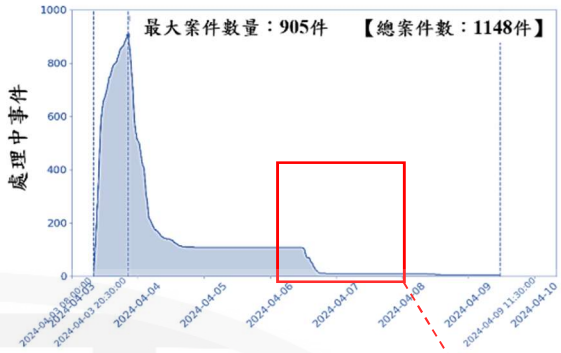

Fig. 1. Temporal distribution of disaster reports during the 0403 earthquake.

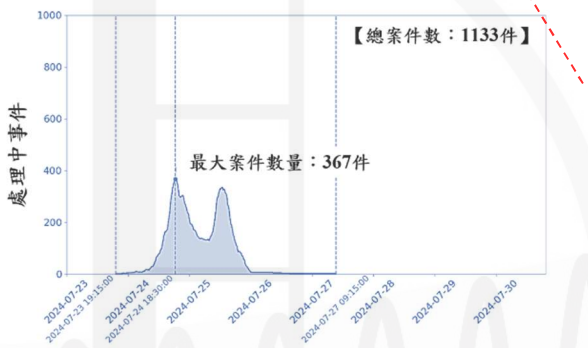

Fig. 2. Temporal distribution of disaster reports during Typhoon Gaemi.

Fig. 3. Gas-related disaster heatmap for the Taipei area during the 0403 earthquake.

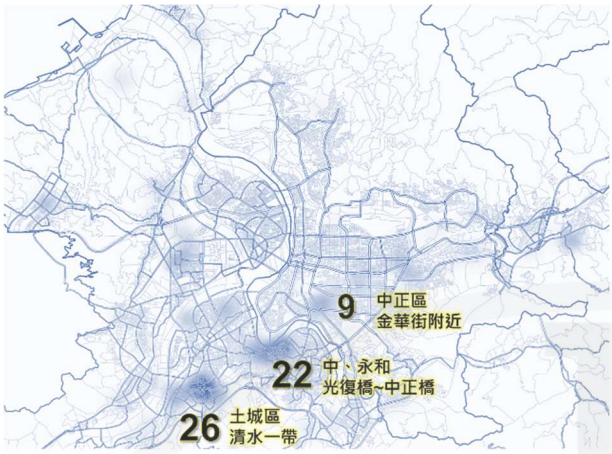

Fig. 4. Elevator entrapment heatmap for the Taipei area during the 0403 earthquake.

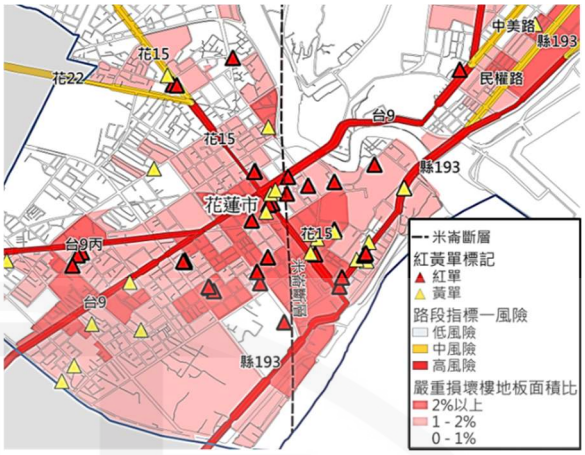

Fig. 6. Comparison between predicted high-risk urban blocks and actual building damage in Hualien.

Fig. 5 Road blockage risk analysis for Miaoli–Taichung–Changhua–Nantou

Fig. 7 0403 Hualien earthquake: Image recognition for road damage detection.

Intelligent Analysis and Recognition Module for Infrasound Signals of Tatun Volcano Group

Jye-Hwang Lo[1], Wei-Tze Chang[2], Ya-Chuan Lai[2], Min-Hung Shih[3], Cheng-Horng Lin[4], Jen-Yu Han[5], and Chuin-Shan Chen[6]

羅傑鯨[1]、張慰慈[2]、賴雅娟[2]、史旻弘[3]、林正洪[4]、韓仁毓[5]、陳俊杉[6]

Abstract

In this study, we develop an intelligent analysis and recognition module for infrasound signals of the Tatun Volcano Group. By integrating deep learning and machine learning, the module increases the accuracy and efficiency of abnormal signal detection. By using the infrasound data acquired from the Xiaoyoukeng observation site in October 2023, a comprehensive dataset comprising 836 time-frequency spectrograms and 1,153 annotated signals was constructed. Based on their unique time-frequency characteristics, the signals were classified into four distinct categories: Bar, wave, curve, and trapezoid. In the module, we use YOLOv9 as the core image recognition model. Performance evaluation through back-testing on the test dataset validated the detection and anomaly-identification capabilities of the module, with a mean average precision of 0.898. To further enhance the characterization of infrasound signals, Power Spectral Density analysis was performed, followed by a comparative evaluation of the clustering performance of two unsupervised learning algorithms: K-means and DBSCAN. The results indicated a high degree of consistency between the YOLOv9 detections and the clusters identified by DBSCAN, with the latter exhibiting superior noise reduction and improved accuracy in abnormal signal identification. The proposed intelligent analysis and recognition module demonstrates the feasibility of using AI technologies for volcanic activity monitoring. By robustly and efficiently supporting volcanic anomaly detection, the module contributes significantly to the advancement of volcanic monitoring and early warning systems.

Keywords: Tatun volcano group, Infrasound monitoring, YOLOv9

Introduction

Recent studies conducted using various geophysical and geochemical monitoring techniques have highlighted active hydrothermal circulation and deep magmatic activity beneath the Tatun Volcano Group, suggesting the potential for future volcanic activity [1]. Among these phenomena, phreatic eruptions have attracted considerable attention in global volcanic monitoring and disaster prevention owing to their sudden and unpredictable nature. The catastrophic phreatic eruption of Japan's Mount Ontake in 2014, which resulted in severe casualties, underscores the need for real-time monitoring and early warning systems for such volcanic events [2]. In the advancement of volcanic monitoring technologies, infrasound has emerged as a critical tool for detecting volcanic gas emissions and explosive activity owing to its high sensitivity to volcanic processes [3]. Infrasound waves propagate through the atmosphere over long distances and effectively capture abnormal changes in volcanic

[1] Assistant Researcher, National Center for Research on Earthquake Engineering

[2] Associate Researcher, National Center for Research on Earthquake Engineering

[3] Assistant Researcher, National Center for Research on Earthquake Engineering

[4] Distinguished Research Fellow, Institute of Earth Sciences, Academia Sinica

[5] Professor, Department of Civil Engineering, National Taiwan University

[6] Distinguished Professor, Department of Civil Engineering, Department of Materials Science and Engineering, National Taiwan University

degassing, thereby providing additional diagnostic information for volcanic activity monitoring.

With the advancement of artificial intelligence (AI), particularly in terms of deep learning and machine learning, AI technologies have demonstrated strong potential for use in volcanic monitoring and infrasound signal analysis. AI applications have proved to be effective at signal processing and anomaly detection, contributing to improvements in the accuracy and responsiveness of monitoring systems [4][5]. The integration of infrasound monitoring with AI-based analysis enhances the reliability and timeliness of volcanic monitoring, thereby reducing the risk of early warning failure due to delays in manual analysis. This study investigates volcanic fumarole activity in the Tatun Volcano Group by establishing a high-density, real-time infrasound monitoring system. Additionally, an AI-driven intelligent analysis and recognition module for infrasound signals has been developed to increase the accuracy and efficiency of volcanic activity monitoring.

The objectives of this study are constructing an infrasound signal dataset and developing an AI-based intelligent analysis and recognition module for infrasound signals to enhance real-time data processing capabilities. Through this research, we aim to enhance our understanding of the volcanic mechanisms of the Tatun Volcano Group and contribute to the advancement of volcanic monitoring technology and disaster mitigation strategies.

Infrasound Signal Image Dataset

We constructed an infrasound signal image dataset by using the data collected from the Xiaoyoukeng infrasound observation network in October 2023. Given that there are no recorded explosive eruptions of the Tatun Volcano Group for direct analysis, for classification purposes, we referred to the internationally recognized time-frequency characteristics of volcanic infrasound signals. We categorized these signals into four distinct types: Bar, wave, curve, and trapezoid.

The bar category is characterized by high-amplitude signals of short durations, resembling the explosive eruption patterns observed at Fuego Volcano. By contrast, the wave category displays stable low-frequency oscillations, comparable to the continuous degassing activity at Reventador Volcano [6]. Although the curve and trapezoid categories could not be directly correlated to specific volcanic signals from existing international datasets, their distinctive time-frequency characteristics suggest they may represent lesser-studied volcanic activity patterns. These categories may serve as valuable references for future infrasound monitoring and signal classification studies.

The dataset established herein comprises 836 time-frequency infrasound spectrograms with 1,153 annotated signals across the four categories. This dataset serves as a foundational resource for ongoing volcanic infrasound research, and it can be used to train machine learning and deep learning models, thereby contributing to the automation and accuracy enhancement of volcanic activity monitoring.

Intelligent Analysis and Recognition Module for Infrasound Signals

In this study, YOLOv9 [7] is used as the foundational model for detecting infrasound signal images. YOLOv9 is one of the most advanced real-time object detection frameworks to date. Its backbone architecture comprises multiple convolutional layers alongside repeated asymmetric convolutional structures to facilitate hierarchical feature extraction. Through the integration of spatial pyramid pooling and upsampling mechanisms, the model effectively fuses multi-scale information, which enhances its ability to detect objects of varying sizes. The final detection output benefits from feature concatenation and successive convolutional operations, which collectively improve feature integration and recognition accuracy.

A total of 168 images were used to backtest the proposed method. The experiments were conducted on an NVIDIA GeForce RTX 2080 Ti GPU. The average inference time was approximately 41.5 ms per 640 × 640 image. The model's detection performance was quantitatively evaluated using standard metrics, including mean average precision (mAP), precision, recall, and F1-score. The detailed detection outcomes are presented in Table 1 and Figs. 1–4.

Table 1. Infrasound signal model detection results (performance metrics).

Class	Precision	Recall	F1 score	mAP50
Bar	0.951	0.846	0.895	0.967
Wave	0.823	0.705	0.759	0.831
Curve	0.904	0.815	0.857	0.892
Trapezoid	0.875	0.846	0.860	0.9
All	0.888	0.803	0.843	0.898

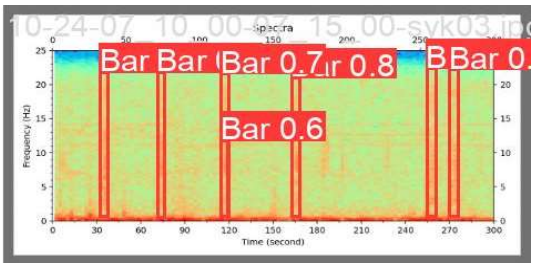

Fig. 1. Building seismic attribute data.

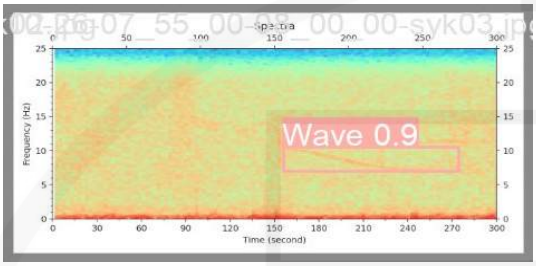

Fig. 2. Potential tsunami inundation area.

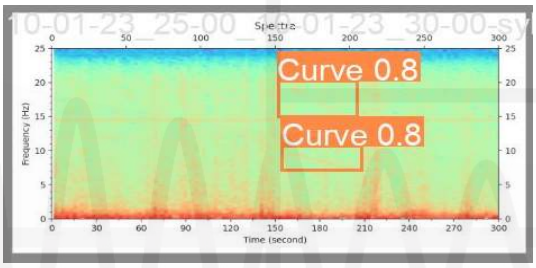

Fig. 3. Percentage of buildings exceeding severe damage.

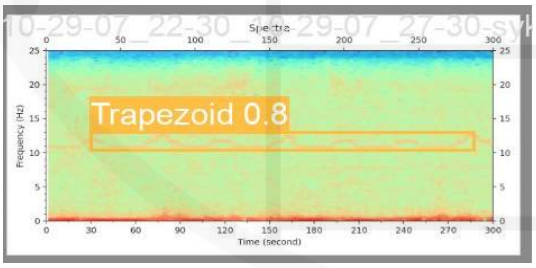

Fig. 4. LLMs combined with line group conversation.

To further analyze the infrasound signals, we used power spectral density (PSD) as the basis for comparative analyzing two unsupervised clustering algorithms: K-means and DBSCAN. PSD is widely used as a frequency-domain analytical tool to describe how the power of a signal is distributed over frequency, as defined in Equation (1). By applying PSD-based visualization, the spectral characteristics of infrasound signals can be examined more effectively, thereby enhancing the capability to identify anomalous events.

$$PSD(f) = \frac{|X(f)|^2}{N} (N = sec * F_s) \quad (1)$$

Here, $PSD(f)$ denotes the PSD at frequency f; $X(f)$is the Fourier transform of the signal, representing it in the frequency domain; and N refers to the total number of signal samples.

In the clustering analysis, the K-means algorithm is suitable for identifying signal groups with distinct features, while DBSCAN can detect clusters of arbitrary shape, in addition to identifying and excluding outliers, which do not belong to any cluster. As illustrated in Fig. 5, we compare the anomaly detection performance of K-means and DBSCAN within the frequency range of 18.0–18.5 Hz. K-means divided the data into 20 clusters, whereas DBSCAN identified 17 clusters. A time-series statistical analysis revealed that variations in the intensity of anomalous infrasound signals show a degree of correlation with environmental parameters such as atmospheric pressure, wind speed, and rainfall. Specifically, during certain periods, fluctuations in pressure and increases in wind speed may affect the background of the signal, while rainfall may introduce additional noise. DBSCAN, with its density-based clustering mechanism, effectively filters out these meteorological background noises, thereby providing a more concentrated distribution of anomalous signals and improved detection accuracy.

Furthermore, the anomalies detected by YOLOv9 show a high degree of consistency with the DBSCAN clustering results (as illustrated in Figure 6). This consistency supports the validity of the detected anomalous infrasound features and facilitates the exclusion of non-volcanic interference sources, such as meteorologically induced noise.

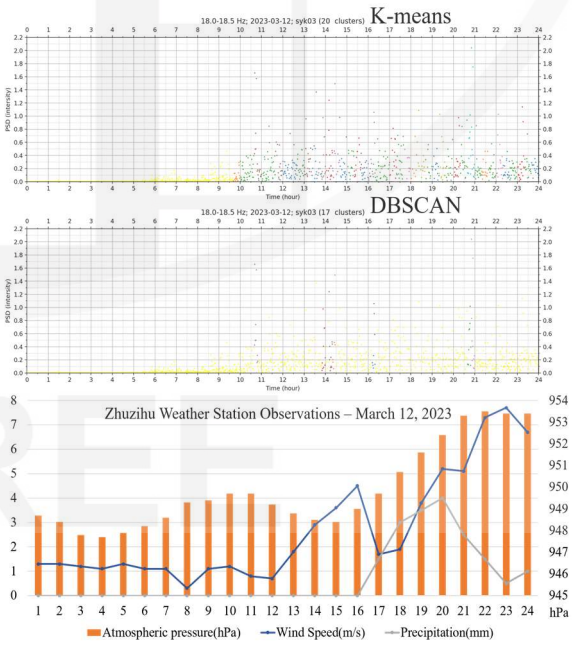

Fig. 5. K-means vs. DBSCAN clustering results.

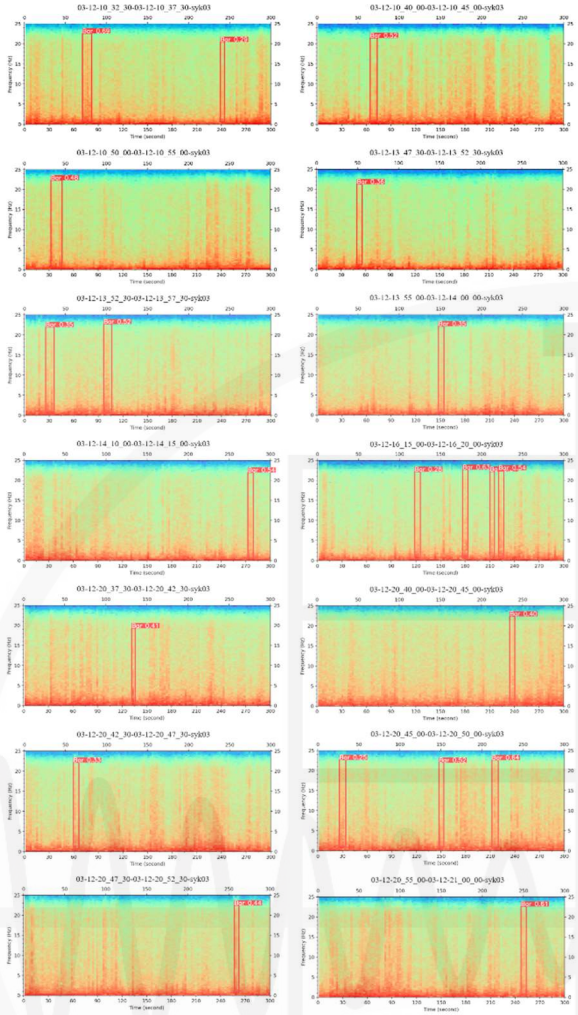

Fig. 5. Infrasound model detection–2023/03/12

Overall, the supervised deep learning model YOLOv9 and the unsupervised clustering algorithm DBSCAN demonstrate high consistency in anomalous signal detection and complementary strengths. DBSCAN, through its density-based approach, offers significant advantages in processing unstructured data and effectively identifying and excluding external interferences. By contrast, YOLOv9 enhances localization precision and visualization of anomalous signals, thereby improving the accuracy of anomaly recognition. These findings validate the effectiveness of both methods in the detection of infrasound anomalies and contribute to increasing the accuracy of volcanic infrasound data analysis, thus providing more reliable technical support for volcanic activity monitoring.

Conclusions

The YOLOv9-based infrasound signal detection model developed herein achieved automated detection and efficient classification of anomalous infrasound events, and its mAP on the test dataset was 0.898. The model demonstrated high computational efficiency, processing approximately 24 images per second; this makes it suitable for use in real-time monitoring applications. According to the experimental results, YOLOv9 outperformed traditional clustering methods on anomaly recognition accuracy and had a high degree of consistency with the results produced by DBSCAN, which further validated its robustness and practical utility in anomaly detection tasks. The findings suggest that the proposed YOLOv9-based intelligent analysis and recognition module for infrasound signals of the Tatun Volcano Group substantially increases the accuracy of anomaly identification, provides a more robust data analysis framework, and offers strong technical support for volcanic activity monitoring.

References

1. Lin, C. H. (2016). Evidence for a magma reservoir beneath the Taipei metropolis of Taiwan from both S-wave shadows and P-wave delays. *Scientific Reports*, *6*(1), 39500.
2. Kato, A., Terakawa, T., Yamanaka, Y., Maeda, Y., Horikawa, S., Matsuhiro, K., & Okuda, T. (2015). Preparatory and precursory processes leading up to the 2014 phreatic eruption of Mount Ontake, Japan. *Earth, Planets and Space*, *67*, 1-11.
3. Fee, D., & Matoza, R. S. (2013). An overview of volcano infrasound: From Hawaiian to Plinian, local to global. *Journal of Volcanology and Geothermal Research*, *249*, 123-139.
4. Dye, B. C., & Morra, G. (2020). Machine learning as a detection method of Strombolian eruptions in infrared images from Mount Erebus, Antarctica. *Physics of the Earth and Planetary Interiors*, *305*, 106508.
5. Bishop, J. W., Blom, P. S., Webster, J., Reichard-Flynn, W., & Lin, Y. (2022). Deep learning categorization of infrasound array data. *The Journal of the Acoustical Society of America*, *152*(4), 2434-2445.
6. Johnson, J. B., & Ripepe, M. (2011). Volcano infrasound: A review. *Journal of Volcanology and Geothermal Research*, *206*(3-4), 61-69.
7. Yeh, C. H., Loh, C. H., & Tsai, K. C. (2006). Overview of Taiwan earthquake loss estimation system. Natural hazards, 37, 23-37.

5D Smart City Disaster Prevention & Relief Platform (3)

Ren-Zuo Wang[1], Chih-Shian Chen[2], and Jui-Mien Lin[2]

王仁佐[1]、陳志賢[2]、林瑞綿[2]

Abstract

To further enhance urban disaster prevention and response capabilities, this study focuses on establishing the foundational framework of the 5D Smart City Disaster Prevention and Response Platform. The development includes a module for monitoring building structural health and a module for displaying rescue road information with the aim of improving the platform's 3D data visualization capabilities and strengthening its application in local government command centers. This development aligns with national digital-twin technologies and incorporates highly visualized big-data presentation techniques. Furthermore, it integrates structural-health monitoring data, bridge monitoring data, and disaster-prevention road information, thereby enabling the platform to interface with dynamic monitoring data, ensuring the widespread adoption and practical implementation of disaster-prevention technologies.

Keywords: Smart City, Digital Twin, Smart Disaster Prevention and Response Platform

Introduction

With the increasing frequency of extreme weather events and natural disasters, the safety monitoring of urban infrastructure has become more critical than ever. Taiwan, located in the Pacific Ring of Fire, faces long-term seismic and climatic impacts on building structures, making structural health monitoring an urgent priority for enhancement. This project leverages the 5D Smart City Disaster Prevention and Response Platform to develop a module for monitoring building structural health, utilizing digital-twin technology for dynamic monitoring and structural safety assessment. This initiative aims to strengthen a city's disaster-response capabilities. Additionally, the platform will integrate rescue road information, ensuring that, in the event of a disaster, optimal traffic routes can be provided in real time, thereby improving emergency response efficiency.

Building-Structural-Health Monitoring Function Module

To enhance building structural safety and further improve the accuracy and predictive capabilities of the monitoring system, this function module focuses on a building-structural-health monitoring system. The key components include micro-vibration measurement, a structural-analysis model, modal analysis, and the structural-health monitoring system, detailed as follows.

1. **Conducting Micro-Vibration Measurements for Structural Frequency Calculation:**

   A. **Installing Micro-Vibration Sensors to Measure Structural Frequency:**

   Micro-vibration sensors will be installed at key locations in the building to measure small vibrations and calculate the structural frequency response. These micro-vibration data are critical for assessing the structural health of the building.

   B. **Obtaining Approval and Ensuring Proper Removal of Equipment:**

   Before conducting the above micro-vibration measurements, prior approval must be obtained from the building management unit. Measurement equipment should be inspected regularly and removed immediately after the measurement is completed to avoid interfering with the building's daily operations and maintenance.

[1] Research Fellow, National Center for Research on Earthquake Engineering

[2] Assistant Researcher, National Center for Research on Earthquake Engineering

2. Establishing the Structural Analysis Model:

A. Creating a 3D Geometric Structural Model Using 3D Modeling Software:

Advanced 3D modeling software will be used to develop a precise geometric representation of the building structure.

B. Implementing Finite-Element Analysis with Beam and Rod Elements:

Based on the characteristics of different structural components, suitable finite-element methods will be applied for structural modeling. Commonly used elements include solid elements, beam–column elements, and shell elements, which effectively describe various structural properties of the building.

C. Assigning Material Properties Based on Structural Elements:

Different material properties (*e.g.*, concrete, steel, wood) will be assigned to various structural components such as beams, columns, and slabs to ensure the accuracy of the structural analysis model.

3. Conducting Structural Modal Analysis:

A. Developing the Structural-Analysis Model and Defining Boundary Conditions:

After the structural-analysis model is completed, the necessary boundary conditions will be set. For instance, the base of the building will be modeled as a fixed boundary to simulate real-world structural support conditions.

B. Performing Modal Analysis and Calculating Structural Frequency:

Modal analysis will be conducted using the developed structural model to calculate the modal frequencies. These frequency values must closely match the structural frequency data obtained from micro-vibration measurements in order to validate the accuracy of the structural-analysis model and ensure it correctly reflects the actual building conditions.

4. Establishing the Structural-Health Monitoring System:

A. System Hardware and Software Planning & Integration:

Based on the requirements of structural-health monitoring, appropriate hardware and software components will be planned and selected. The hardware includes various types of sensors, while the software is responsible for data-processing, visualization, and early-warning system operations. The system will integrate structural-health monitoring data, 3D modeling, and analysis results to enable data visualization, real-time monitoring, and predictive analysis.

B. System Installation:

After finalizing the hardware and software plans, system installation will be carried out, ensuring that all equipment is correctly installed and functioning properly. This process includes installation of sensors, set up of the data-transmission system, and development of the monitoring platform.

The structural-health-monitoring system architecture is illustrated in Fig. 1. All equipment is powered through an uninterruptible power supply (UPS). Measurement data is transmitted to the monitoring computer and, before being uploaded to the database, it passes through a firewall to ensure data security.

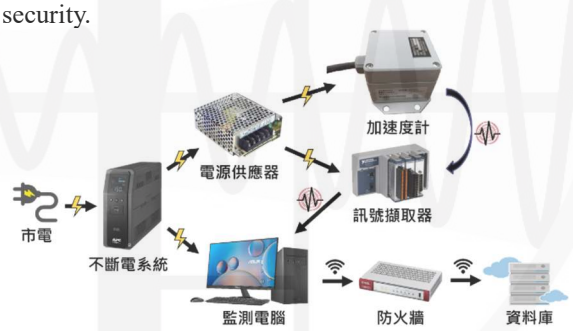

Fig. 1. The structural-health-monitoring system architecture.

The monitoring data can be displayed on the Smart Disaster Prevention and Response Platform. Figure 2 shows the building-structural-health monitoring signals displayed on the platform. Next to the 3D model of the building within the platform, a real-time data panel is shown, which displays the peak acceleration (unit: gal) from the accelerometer and the data transmission time.

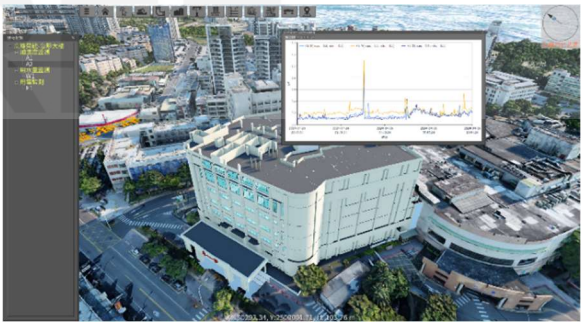

Fig. 2. Screen of the structural-health monitoring platform.

5. Automatic Notification Function of the Health Monitoring System:

In addition, when conducting seismic simulations for buildings, the seismic records from the KAU058 station during the 921 earthquake were selected for duration analysis. After evaluation, the alert value for post-earthquake inspection was set to Level 4 and the action value was set to Level 5.

After an earthquake event, the structural-health monitoring system will automatically transmit monitoring results and notifications of the earthquake event. The notification will include not only the seismic information released by the Central Weather Bureau but also, more importantly, the actual seismic intensity monitored in the building, providing relevant authorities with data for decision making and response handling, as shown in Fig. 3.

Fig. 3. Notification of earthquake event information for structural monitoring.

Rescue-Road-Information Display Function Module

The development of the rescue-road-information display function module for the Zuoying District of Kaohsiung City aims to provide critical road information during post-disaster rescue operations, assisting in rapid decision-making and resource allocation. This module integrates multiple data sources and visualizes road conditions, bridge damage, and alternative route planning in order to enhance the timeliness and accuracy of disaster response actions.

This function module collaborates with the Earthquake Disaster Simulation Group of the National Center for Research on Earthquake Engineering and the Earthquake Disaster Decision Support System at Kaohsiung University, ensuring real-time updates of disaster information and decision-making support. With data validation and technical support provided by the teams, the system can quickly integrate the latest damage information, optimize rescue route planning, and support relevant agencies in resource allocation and disaster response execution.

1. Earthquake Simulation and Damage Prediction

A. Based on the active fault data published by the Central Geological Survey of the Ministry of Economic Affairs (2023) (see Fig. 4), the Chihshan Fault, Xiaogangshan Fault, and Chaozhou Fault were selected as the study area. Earthquake simulations were conducted based on parameters such as fault length, rupture mechanism, and rupture depth.

B. The Taiwan Earthquake Loss Estimation System (TELES), Bridge Damage Assessment Software (Tgbs), and (Thighway) were utilized, combined with Geographic Information System (GIS) technology, to conduct earthquake scenario simulations and risk assessments.

C. The simulation results will be displayed on the platform, including the post-earthquake conditions of major communication routes, bridge damage, and the risk of building collapse along these routes. This data will serve as a critical basis for post-disaster road rescue planning, in turn enhancing rescue efficiency and supporting disaster-prevention response strategies.

Fig. 4. Active faults within the Kaohsiung City region.

2. Establishment of the Building Seismic Attribute Database

A. Integrate Kaohsiung City's Zuoying District property tax data and address location data to

establish a building seismic attribute database.

B. Import building attributes (such as construction year, structure, number of floors, and usage) and spatial coordinate information as the foundation for earthquake damage estimation.

C. Ensure that the building data supports earthquake-damage loss assessments and post-disaster response analysis.

3. Bridge Seismic-Damage Assessment and Rescue-Route Blockage Analysis

A. Establish seismic-damage assessment data for twenty major bridges in Zuoying District, including construction year, most recent maintenance year, and seismic retrofitting status.

B. Supplement and verify the bridge data to ensure completeness and use it as a basis for determining bridge usability after an earthquake.

C. Calculate the seismic-damage risk for the bridges and assess its impact on rescue routes, ensuring the availability of viable routes during a disaster.

4. Identification of High-Risk Rescue Routes

A. Compile data for major roads in Zuoying District and conduct risk analysis based on road classifications (1E, 1U, 1W, 2U, and 2W).

B. Use the TELES subsystem Tgbs to assess the impact of building collapses after an earthquake and identify potentially blocked routes.

C. Mark medium- and high-risk rescue routes based on the risk assessment results to ensure the accuracy of disaster-response planning.

5. Integration with Earthquake-Disaster Decision Support System

A. Integrate the rescue route earthquake disruption risk analysis results into the Earthquake Disaster Decision Support System.

B. Perform route analysis using the ArcGIS Online Directions widget to ensure the system can avoid blocked routes and provide the optimal rescue path.

C. Export the analysis results (Shape File) for display on the platform, providing real-time visual information to decision-makers.

Conclusions

This year, the 5D Smart City Disaster Prevention and Response Platform has successfully integrated multiple data sources, thus enhancing disaster-monitoring, early-warning, and disaster-response decision-making capabilities. Through features such as earthquake-damage simulation, rescue-route planning, and building seismic assessment, the platform provides accurate and real-time decision support to disaster response units, effectively strengthening urban resilience. Collaboration with local governments and research institutions has improved the data accuracy and applicability of the platform, ensuring the effectiveness of response measures.

In the future, the model algorithms will be further optimized to improve disaster-risk calculation accuracy and strengthen integration with GIS and AI technologies to provide more immediate disaster-response capabilities. Additionally, the application scope of the platform will be expanded to establish cross-regional disaster-prevention collaboration mechanisms and promote the standardization of smart-city disaster-prevention and response technologies to enhance overall response efficiency, thereby creating a safer and more resilient urban environment.

Reference

Ren-Zuo Wang, & Chih-Shian Chen. (2024). Resilient City Infrastructure Management and Decision Support Platform Final Report. Kaohsiung City Government Public Works Bureau, Kaohsiung.

Application of Large Language Models to Post-Disaster Support Visits

Jye-Hwang Lo[1], Wei-Tze Chang[2], and Chun-Yao Yang[3]

羅傑鯨[1]、張慰慈[2]、楊鈞堯[3]

Abstract

As climate change intensifies and the frequency of natural disasters increases, post-disaster support visits have become a crucial task for social service organizations. However, traditional interview methods are limited by challenges such as labor shortages, difficulties in synchronizing records, and inefficient information management. To increase interview efficiency and enhance decision-making support, an automated interview recording and analysis system based on artificial intelligence (AI) and large language models (LLMs) is developed in this study. The proposed system uses a LINE Bot as its front-end interface, in addition to Pyannote.audio for speaker diarization and WhisperX for high-accuracy speech-to-text conversion. This allows the system to achieve accurate time alignment while maintaining the contextual integrity of interview transcripts. Additionally, the system uses OpenAI's LLM for semantic analysis, topic classification, and key information extraction. By integrating retrieval-augmented generation (RAG), the system is able to retrieve and update relevant knowledge in real-time, thereby increasing the accuracy of information retrieval and improving decision-making support. The proposed system can generate real-time interview summaries, thereby assisting social workers in quickly understanding interviewees' needs and providing intelligent suggestions. By ensuring the completeness of interview content and reducing manual processing, the system increases overall operational efficiency.

Keywords: Post-disaster support visits, Speech-to-text, Large language models

Introduction

In traditional post-disaster support visits, social workers predominantly conduct face-to-face interviews to evaluate the needs of affected households and gather essential data. However, this approach presents numerous challenges that limit the efficiency of interviews and compromise the integrity of information management. A primary issue is the increasing shortage and aging of the volunteer workforce. As the demographic composition of social workers skews older, and younger generations participate in limited numbers in volunteer activities, the available number of workers is often insufficient to cater to the increased demand for support visits during disasters. This imbalance causes operational strain, reducing the timeliness and coverage of the necessary interventions.

Moreover, the manual nature of data collection and documentation presents additional obstacles. Social workers are often required to simultaneously conduct interviews and record information, whether through handwritten notes or digital input. This dual-tasking not only increases cognitive and physical workload but also decreases the accuracy and completeness of records. The absence of a streamlined recording process further complicates the timely extraction of actionable insights. These challenges are compounded by deficiencies in information management and analysis. Interview data are traditionally stored in fragmented paper-based formats or decentralized digital files, as opposed to a standardized database infrastructure. Such disorganized data storage impairs the efficient consolidation and analysis of information, which undermines the precision and responsiveness of real-time decision-making in post-disaster scenarios.

In recent years, the application of artificial intel-

[1] Assistant Researcher, National Center for Research on Earthquake Engineering
[2] Associate Researcher, National Center for Research on Earthquake Engineering
[3] Research Assistant, National Center for Research on Earthquake Engineering

ligence (AI) technologies to disaster response operations has garnered considerable attention, particularly in domains such as speech recognition, automated transcription, and data analysis. These advancements offer promising avenues for improving the operational efficiency, accuracy, and decision-support capabilities of post-disaster support visits. Notably, the emergence of large language models (LLMs), exemplified by the GPT series, introduces substantial opportunities for automated processing and in-depth analysis of interview data. Given their advanced understanding of natural language and semantic interpretation capacities, LLMs can extract key information, generate concise summaries, and classify topics. These capabilities considerably improve the organization, accessibility, and practical utility of interview data, thereby enhancing the overall effectiveness of post-disaster interventions.

To address the inherent limitations of the traditional support visit models, we collaborate with the Tzu Chi Charity Foundation to integrate AI technologies and LLMs into the post-disaster support visits process. By using automated speech recognition, real-time transcription, and semantic analysis, the proposed system increases the accuracy and efficiency of interview documentation. Furthermore, the implementation of a standardized data management system facilitates the seamless integration and analysis of interview data, which strengthens the existing decision-support mechanisms.

The use of AI and LLM technologies is expected to remarkably enhance the effectiveness and reach of post-disaster social services. Through increased data usability and transparency, decision-makers will obtain a more accurate and comprehensive understanding of the specific needs of affected households. Ultimately, this innovation aims to facilitate more informed and responsive disaster relief efforts, thereby contributing to the broader goals of sustainable social reconstruction and resilience-building in post-disaster environments.

Post-Disaster Support Visits Assistant

In this study, cloud technology and AI algorithms are used to realize the automated collection, processing, and analysis of interview speech data with the aim of enhancing the efficiency and informational value of speech records. Overall, LINE is the most widely used instant messaging application in Taiwan. Therefore, a speech transcription and analysis system based on a LINE Bot is developed [1] to improve user convenience and acceptance.

The system architecture, illustrated in Fig. 1, uses the LINE Bot as the front-end communication interface to receive and store voice messages while performing speech recognition and transcription. To realize highly accurate speech processing and semantic analysis, several advanced AI technologies are integrated, namely Pyannote.audio [2], WhisperX [3], and OpenAI's large language model (LLM) [4]. These technologies increase the accuracy, readability, and analyzability of interview speech data while providing real-time retrieval and decision-support functions.

In the speech processing phase, the proposed system uses Pyannote.audio for speaker diarization to accurately distinguish the utterances of different speakers during the interview. This significantly improves the accuracy of transcription and semantic analysis. Pyannote.audio is an open-source speech processing framework based on deep learning, and it employs recurrent neural networks (RNNs) for speech representation learning. Moreover, it incorporates features such as voice activity detection (VAD), speaker change detection (SCD), and overlapped speech detection (OSD), which allow it to achieve high accuracy even in multi-speaker interactions. In volunteer interview scenarios, where conversations often involve multiple participants and overlapping speech, speaker diarization effectively separates and processes individual speech contributions. Following speaker separation, the system uses WhisperX for speech-to-text (STT) transcription and generates word-level timestamps to ensure temporal alignment and contextual integrity. WhisperX, an improved version of the standard Whisper model, employs VAD and forced alignment to increase timestamp accuracy. Its batch inference capability further increases processing efficiency, which makes the model particularly suitable for transcribing long audio recordings. This ensures that the transcription results are not only accurate but also well-synchronized with the original audio.

Subsequently, a comprehensive semantic analysis of the transcribed texts is performed using OpenAI's LLM. Built on a transformer architecture, the LLM uses a self-attention mechanism to capture and model long-range dependencies between words, which improves its contextual understanding and reasoning abilities. Herein, the LLM is used for topic classification and keyword extraction to generate interview summaries and support decision-making. This allows volunteers or decision-makers to quickly grasp interviewees' core needs.

To enhance the timeliness and accuracy of the LLM-generated content, Retrieval-Augmented Generation (RAG) [5] technology is incorporated into the proposed model. By combining knowledge retrieval and language model generation, the proposed system can dynamically access relevant information from relational databases during semantic analysis. This includes past case records, policy documents, or domain-specific knowledge, which ensures that the analysis results are not solely based on the LLM’s pretrained knowledge. Instead, they are continually updated, thereby enhancing the applicability and reliability of semantic understanding.

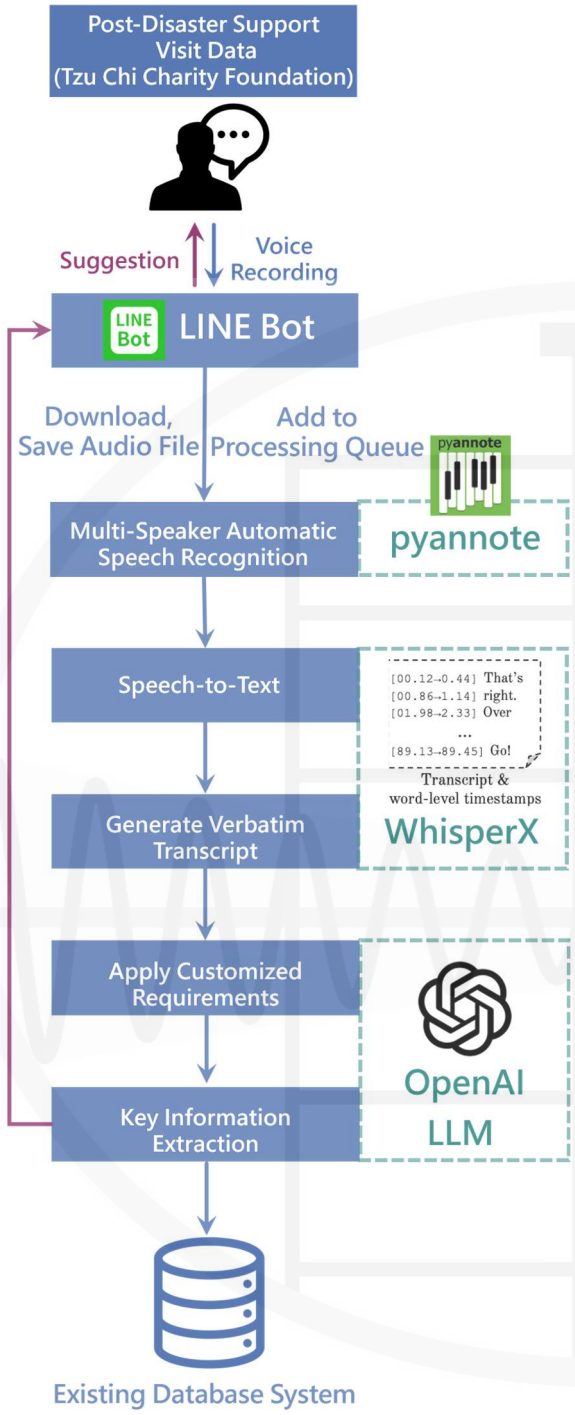

Fig. 1. Architecture of interview speech transcription and analysis system.

The proposed system features a highly scalable and modular design, and it supports multiple languages and various application modes, making it suitable for volunteer interviews, meeting transcription, and knowledge management scenarios. It facilitates efficient data collection, accurate transcription, and structured storage of interview information, thereby providing decision-makers with real-time, high-quality information support. As illustrated in Fig. 2, the LINE Bot interface offers an intuitive user experience, which allows users to upload voice messages and receive transcription results and summary information in real time. Additionally, users can select between the volunteer mode and meeting mode based on their specific interview needs, which further enhances the flexibility and applicability of the speech processing system.

Fig. 2. LINE bot user interface.

Fig. 3 illustrates the results of the volunteer interview speech transcription and summary generation. The system automatically identifies different speakers and transcribes the interview into a verbatim transcript while clearly differentiating the statements of various participants. Additionally, it extracts key information and summarizes 19 essential points from the interview (e.g., household population, family background, and property damage) to provide volunteers and relevant personnel with a quick reference for verification. This ensures completeness of the interview content and facilitates real-time supplementation of missing information or the provision of suggestions and reminders. To improve the timeliness and accuracy of interviews and disaster response efforts, the system offers real-time interaction capabilities. During volunteer interviews and emergency response operations, it can provide immediate prompts, such as "Remember to inquire about medical needs," to facilitate comprehensive information gathering and prevent the omission of critical questions. Moreover, the system can be used in training and educational settings to offer real-time feedback for reinforcing learning outcomes. This use case allows volunteers and professionals to receive

comprehensive guidance during simulated training exercises and practical operations.

Furthermore, the system can autonomously extract derivative information to offer suggestions to medical resources, track the latest weather and disaster updates, verify emergency administrative orders related to disaster prevention and response, and identify social assistance and reconstruction resources. By automating the organization and analysis of key information, the system significantly improves decision-making efficiency and enhances response capabilities.

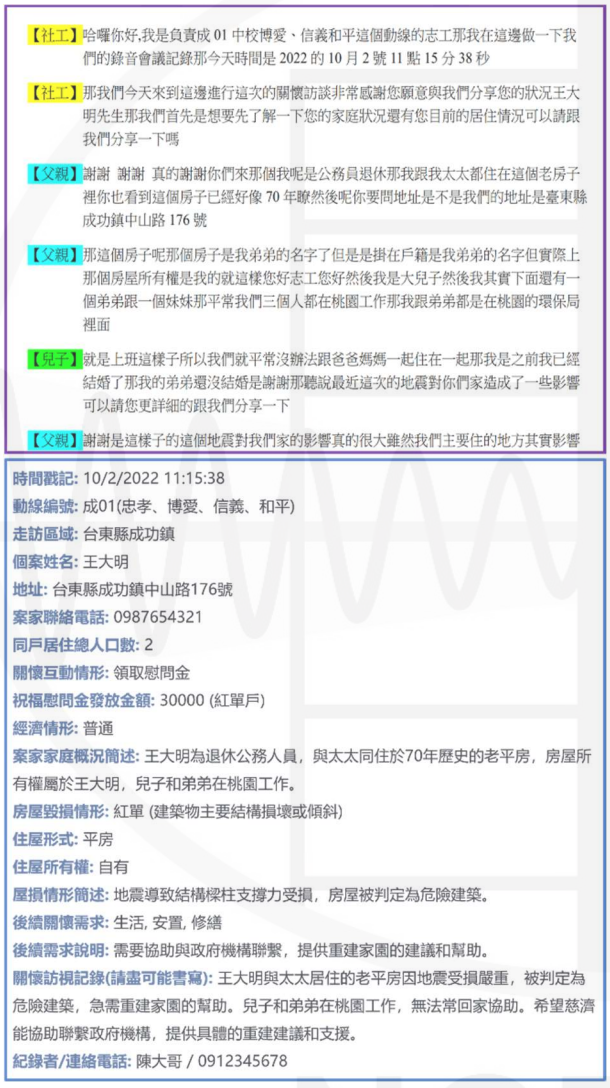

Fig. 3. Transcript and key summary (Chinese).

Conclusions

In this study, artificial intelligence (AI) and large language models (LLMs) are integrated to develop a high-performance speech processing and semantic analysis system for post-disaster support visits. The proposed system addresses the limitations of traditional interview methods, including the burden on human resources, difficulties in information recording, and challenges in data analysis. By using automated speech recognition and semantic processing, the system transcribes and structures interview content in real-time while extracting key information. This allows volunteers and decision-makers to quickly grasp the main points of interviews, which enhances information management and increases decision-making efficiency. The system not only improves the completeness and accessibility of interview data but also reduces the manual processing workload through intelligent summarization and semantic analysis. Ensuring the timely consolidation and application of critical information supports disaster response and recovery efforts more effectively.

With the continuous advancement of AI technologies, the system can be further refined to improve its semantic understanding and contextual reasoning capabilities. This would allow it to automatically adjust its analytical approach to different interviewees, thereby providing more detailed semantic insights and decision-making recommendations. Additionally, the expansion of its multilingual speech recognition and semantic analysis capabilities will be a key development direction, which would allow the system to cater to the demands of international disaster relief, cross-border social services, and humanitarian assistance, thereby extending its applicability and impact.

References

1. LINE Corporation. (n.d.). Messaging API documentation. LINE Developers. Retrieved March 20, 2025, from https://developers.line.biz/en/docs/messaging-api/
2. Bredin, H., Yin, R., Coria, J. M., Gelly, G., Korshunov, P., Lavechin, M., ... & Gill, M. P. (2020, May). Pyannote. audio: neural building blocks for speaker diarization. In *ICASSP 2020-2020 IEEE International conference on acoustics, speech and signal processing (ICASSP)* (pp. 7124-7128). IEEE.
3. Bain, M., Huh, J., Han, T., & Zisserman, A. (2023). Whisperx: Time-accurate speech transcription of long-form audio. *arXiv preprint arXiv:2303.00747*.
4. OpenAI. (n.d.). *OpenAI API documentation*. Retrieved March 20, 2025, from https://platform.openai.com/docs/
5. Lewis, P., Perez, E., Piktus, A., Petroni, F., Karpukhin, V., Goyal, N., ... & Kiela, D. (2020). Retrieval-augmented generation for knowledge-intensive NLP tasks. *Advances in neural information processing systems*, *33*, 9459-9474.

Development and Application of Advanced Experimental Technologies in Earthquake Engineering

Keh-Chyuan Tsai[1], Chia-Ming Chang[1], Huang, Shieh-Kung[2], Shiang-Jung Wang[3], Yong-An Lai[4], Yuan-Sen Yang[5], Shih-Yu Chu[6], Pei-Ching Chen[3], and Kung-Juin Wang[7]

蔡克銓[1]、張家銘[1]、黃謝恭[2]、汪向榮[3]、
賴勇安[4]、楊元森[5]、朱世禹[6]、陳沛清[3]、王孔君[7]

Abstract

Various experimental technologies in earthquake engineering simulation, including measurement technology, signal processing, numerical modeling and calculation methods, and integration of heterogeneous hardware and software, significantly affect the quality of simulation and experiments. In addition, a thorough understanding of the characteristics of the specimen is critical. This project aims to improve different aspects of earthquake engineering simulation technologies and to evaluate and verify the characteristics and performance of novel seismic isolation and reduction technologies.

Keywords: earthquake engineering, large-scale structural testing, experimental technology, numerical simulation, hybrid simulation, isolation, seismic reduction

Introduction

The research content includes numerical and experimental simulation conducted to verify the performance of technologies of seismic isolation and reduction. The research topics and results are described below.

Application of Inerter and MR Dampers

This study presents a novel semi-active control law for magnetorheological (MR) dampers used to reduce the seismic response of structures. A hybrid simulation was conducted to verify the effectiveness of this control law. In addition, this study investigated increasing the performance of tuned mass dampers (TMDs) by incorporating inerters, springs, and damping devices. This study establishes design methodologies for single-degree-of-freedom (DOF) or multiple-DOF systems. Extensive numerical analyses were performed to verify the effectiveness of the proposed design methodologies.

The proposed semi-active control law linearizes the behavior of the MR damper within each time step. The input and the output of the linearized model is the input voltage and the estimated damping force, respectively. This approach enhances the conventional two-stage semi-active control method by enabling the estimation of optimum input voltage based on the current status. Consequently, a more flexible semi-active control characterized by higher adaptability to varying earthquake input scenarios is achieved. Figure 1 shows the sequence of real-time hybrid simulation for a system using the semi-active control law.

[1] Professor, Department of Civil Engineering, National Taiwan University
[2] Associate Professor, Department of Civil Engineering, National Chung Hsing University
[3] Professor, Department of Civil and Construction Engineering, National Taiwan University of Science and Technology
[4] Associate Professor, Department of Civil Engineering, National Central University
[5] Professor, Department of Civil Engineering, National Taipei University of Technology
[6] Professor, Department of Civil Engineering, National Cheng Kung University
[7] Principal Engineer, National Center for Research on Earthquake Engineering

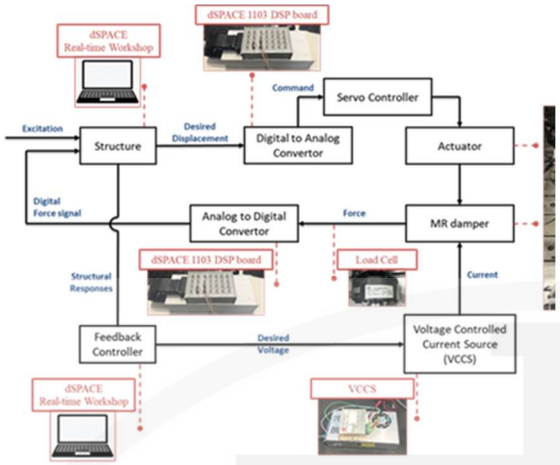

Fig. 1. Real-time hybrid simulation using the semi-active control algorithm.

Integration of TMD and Base Isolation

Base-isolated systems have elongated vibration periods to avoid resonant responses during seismic events. However, when the ground acceleration has lower frequency content or when the displacement magnitude is large (such as in near-fault excitation), base-isolated structures can experience excessive displacement responses due to resonance effects or a lack of sufficient damping. A highly effective method to suppress such excessive displacement response is the incorporation of an adjustable TMD or inerter in the structural system.

This research project studied the seismic performance of a base-isolated system equipped with an adjustable TMD through shaking table tests conducted at the National Center for Research on Earthquake Engineering (NCREE). The specimen was a three-story steel frame, seismically isolated using a friction pendulum system. As shown in Figure 2, the effective mass of the TMD was adjusted by changing the number of inerters.

The effectiveness of the base isolation and the TMD was assessed using two performance indices: maximum inter-story drift (which directly relates to maximum inter-story shear) and maximum absolute acceleration (which indicates comfort and structural safety). Compared with the results obtained from a conventional system that lacked base isolation and an adjustable TMD, the base-isolated system with adjustable TMD proved to be more effective in reducing both performance indices.

In addition, it was observed that different intensities of ground motion necessitated varying effective masses for the TMD. This further indicated the benefit of integrating an adjustable TMD with a base isolation system to enhance protection for buildings under seismic risk.

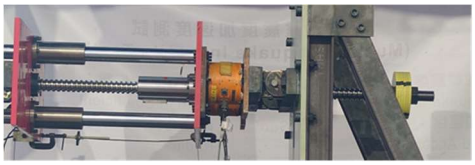

Fig. 2. The inerter as the adjustable TMD in an base-isolated system.

Sloped Rolling-type Bearing and Inerter

A sloped rolling-type bearing (SRB) has a simple structure. Its maximum acceleration is a constant value that can be fully determined once the slope and frictional damping are established. Hence, it can effectively reduce the acceleration response of the superstructure. However, similar to other types of base isolation systems, the use of an SRB as a seismic isolation system can result in excessive displacement responses of the superstructure when ground motion contains significant low-frequency content or when the ground displacement is too large. To address this issue, this study investigated the performance of a hybrid system consisting of an SRB and an inerter controlled by a clutch (i.e., SRB with clutch-based inerter, SRBCI). The SRBCI is expected to reduce the displacement response of the superstructure while maintaining a relatively low transmitted acceleration response.

This study proposed a velocity control model for the clutch that can reasonably estimate the difference in instantaneous velocities between the input and output points at any given moment. During performance tests, it was found that the acceleration response of an SRBCI was relatively large, accompanied by unintended vibrations when the inerter began functioning. This phenomenon could be attributed to the collision between the inerter and the clutch. Therefore, this research proposed a pulse vibration model that simulates the vibrations using a single DOF system and identifies related model parameters. Figure 3 shows the performance tests and the comparison between experimental and numerical simulations.

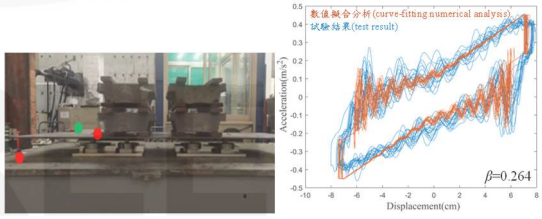

Fig. 3. SRBCI performance test and simulation comparison

Sky Hook Control Law for Active Isolation for Devices

Seismic isolation applied to the structure itself is not the most efficient method for high-tech factories because in additional to large vibrations it is also required to reduce or eliminate unwanted small vibrations. Fortunately, the concept of seismic isolation can be directly applied to devices with good performance. Among the currently available isolation technologies, active vibration isolation is especially effective in reducing the transferred acceleration to the isolated superstructures or devices (Liu and Wu, 2013).

A sky hook damper was used to develop a novel control method for an active vibration isolation system. This method can convert a conventional linear servo-controlled sliding platform into an active vibration isolation system. The control method uses the measured base acceleration and the relative velocity of the isolation layer as inputs to calculate the optimal active control force on a real-time basis. In addition, the effective damping coefficient can be adjusted by the control method to achieve higher stiffness during non-earthquake events. When an earthquake occurs, the properties of the isolation system can be adjusted accordingly to minimize the transferred acceleration and restrict the maximum relative displacement for maximizing protection for the isolated devices.

The research involved developing the control algorithm for the sky hook damper and conducting a series of characteristic, parametric, frequency, and time-history analyses to fully understand the dynamic properties and seismic performance of the isolation system. Subsequently, a series of shake table tests was conducted to verify its effectiveness. Test results indicated that the proposed control method and the resulting active vibration isolation system provided excellent performance in protecting the isolated devices by isolating input excitation. No resonance was observed during the tests. The isolation system was able to function effectively even during small earthquakes. The relatively low cost required to build such isolation systems also helps to achieve wider applications in the industry.

Application of Image-processing-based Measurement Technologies

Technologies for accurate and comprehensive displacement measurement are one of the most important prerequisites for large-scale structural testing. However, as the complexity of large-scale structural testing has been continuously increasing, traditional measuring methods and devices have struggled to meet measurement demands. Conversely, thanks to the increasing resolution of photographs and continuous improvements in image-processing algorithms, image-based displacement measurement technologies are playing increasingly important roles in structural testing. This study developed several image-processing-based technologies, which were successfully utilized in various large-scale structural testing projects.

1. A method for measuring dynamic three-dimensional (3D) displacement in seismic isolation systems. This method has the following features.

    a. Single-camera measurement. Only one camera is required to accurately capture the 3D dynamic displacement of the base isolation system located on the shake table.

    b. Higher efficiency. This method successfully avoids the difficulty of synchronization between multiple cameras, thereby significantly improving the overall working efficiency.

    c. Reduced measurement error. By utilizing the physical properties of the measured 3D displacement (the x-, y-, and z-components of the base isolation system constrained by a known sliding surface), the analysis procedure is greatly simplified, the required time and computation power to calculate the 3D displacement are minimized, and the magnitudes of the errors are also significantly minimized.

2. Calibration method for multiple cameras. This method has the following features.

    a. Easier calibration. Instead of using a large-scale calibration board, the geometric properties of the specimens and testing environment are used in the calibration procedure. This leads to less preparation work and higher overall working efficiency.

    b. More flexible adjustments in the calibration procedure. By using 3D projection technology, adjusting the parameters of the image processing procedure becomes easier and the accuracy of the measurement results is improved.

Practical examples of using the aforementioned image-processing based measurement technologies in large-scale structural tests include:

1. Shake table tests of a friction pendulum isolation system. The dynamic 3D relative displacement of the isolation system (as shown in Figure 4) was measured. The characteristics of the measured error were investigated through a series of error analyses, and identified error characteristics were used to further increase the accuracy of the measurement results.

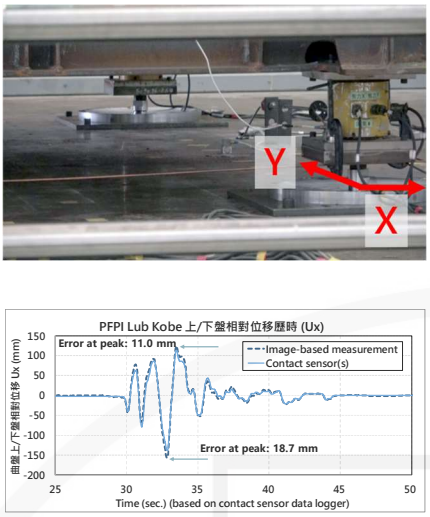

Fig. 4. Shake table test of a friction pendulum isolation system and the measurement result.

2. Cyclic loading tests of buckling-restrained braces (BRBs). The significantly large deformation of a BRB under extreme loading conditions can be accurately and effectively measured. Multiple cameras were used in this testing project, and the calibration procedure was conducted using 3D projection technology.

Finally, this research also aimed to develop a general-purpose software framework that integrates all the developed image-processing-based measurement technologies for facilitating their application in structural testing in the future.

Analog and Digital Hardware in the Loop in Hybrid Simulation

The "hardware in the loop" technology is frequently used in the fields of aerospace and electrical engineering. This study used SCRAMNet as the communication method to minimize latency in data transmission. By eliminating the necessary analog-digital (A/D) and digital-analog (D/A) operations common in traditional hybrid simulation environments, this study aimed to build a purely digital environment capable of supporting various advanced research topics in earthquake engineering, including structural health monitoring, structural vibration control, novel structural testing methods, and hybrid simulation.

The validity of the developed digital environment was verified by comparing the results of shake table tests (STTs) and real-time hybrid simulation tests (RTHSTs). The specimen used was a base-isolation system with a piezoelectric friction controllable mass damper (PFCMD). The base isolation employed a rolling pendulum system (RPS). A piezoelectric friction damper (PFD) was used to adjust the initial sliding friction of the PFCMD, enabling it to provide the desired semi-active control. Test results indicated that the outcomes from an RTHST, based on the proposed digital testing environment, closely matched those obtained from the STT.

Utilizing Machine Learning in Nonlinear Real-time Hybrid Simulation

RTHSTs can be used to investigate the seismic performance of velocity-dependent structural components or systems (Chen and Chen, 2023). One of the challenges in conducting RTHSTs is that the calculation time for the numerical substructure must be strictly limited to a specified duration. This study proposed using machine learning technology to replace full-fledged nonlinear numerical modeling and analysis in an attempt to reduce computing time. To this end, an OpenSees model was created for a single-bay, three-story steel frame with a viscous damper installed on all three stories. Nonlinear time history analysis was performed across numerous cases to generate a substantial dataset for training a recursive long short-term memory (LSTM) model at a later stage. Various time delays associated with experimental activities, including actuator motion control and data acquisition, were also incorporated into the training process. The trained model was subsequently used to replace nonlinear time history analysis in the RTHST. Various verification tests were conducted, and the results indicated that RTHSTs could be executed stably and successfully.

Conclusions

Several advanced structural testing technologies were developed and successfully applied in a number of experimental projects.

References

Chen, P. C. and Chen, P. C., 2023. Real-Time Hybrid Simulation for Seismic Control Performance Evaluation of an Active Inerter Damper System, Engineering Structures, Engineering Structures, 294, 116760.

Liu Y. H. and Wu W. H. "Active vibration isolation using a voice coil actuator with absolute velocity feedback control," International Journal of Automation and Smart Technology, 3(4):221-226 (2013).

Damage Estimation of Natural Gas Service Pipes Following an Earthquake

Gee-Yu Liu[1] and Pao-Ching Chou[2]

劉季宇[1] 周寶卿[2]

Abstract

Natural gas systems supply gas to households as well as commercial and industrial customers, making them most convenient heating energy sources. The gas service pipes are short pipe segments that connect the distribution pipelines to end users. This study proposes an earthquake damage estimation model for these pipes, which includes a formula for calculating the probability of pipe damage due to earthquake ground motions, along with two correction factors that reflect various pipe fragilities and the effects of soil liquefaction. Using central Taiwan counties as a demonstration, damage estimation of an M7.6 earthquake scenario is conducted.

Keywords: natural gas systems, gas service pipes, damage estimation, scenario earthquake

Introduction

Natural gas systems supply gas to households as well as commercial and industrial customers, making them extremely convenient sources of heating energy. Along with water and electricity, they are essential lifelines for the daily livelihoods of people. According to the Energy Administration of the Ministry of Economic Affairs, there are 3.885 million gas customers in Taiwan as of September 2023, as illustrated in **Figure 1**, demonstrating high penetration rates nationwide. Utility gas pipes can be classified into two categories: distribution pipelines and service pipes. Due to the broad and dense distribution of gas pipelines, they are exposed to high seismic risk. Studies of major earthquakes from 1964 to 1995 reveal that damage to natural gas systems accounts for 20%–50% of post-earthquake fire incidents (ASCE, 2002), underscoring the need for seismic risk assessment and management. In a previous study, the authors developed an earthquake damage assessment model for gas distribution pipelines. The model incorporated a standard repair rate formula and a set of repair rate correction factors for pipelines with varying pressure ratings and pipe types (Liu et al., 2025). This study further proposes a model for service pipes, given the extensive number of service pipes and their substantial contribution to pipeline seismic damage following earthquakes.

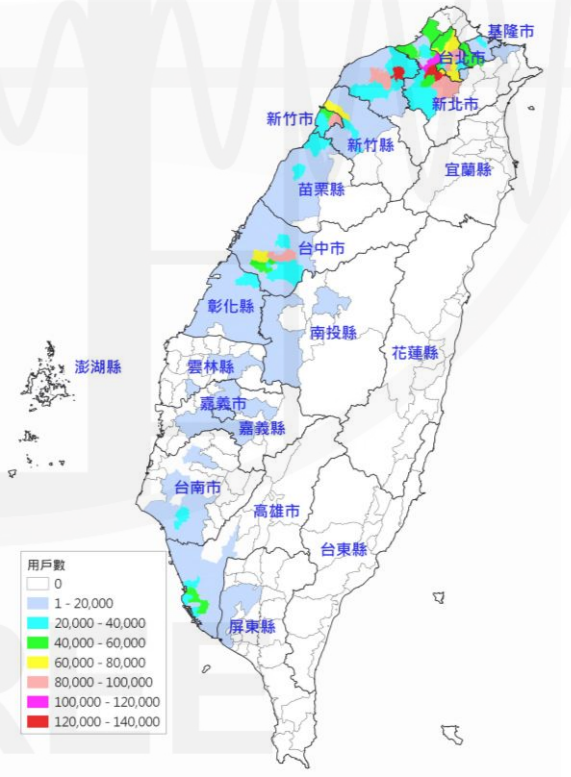

Fig. 1. Distribution of natural gas customers in Taiwan by township (Energy Administration, September 18, 2023).

[1] Research Fellow, National Center for Research on Earthquake Engineering
[2] Assistant Researcher, National Center for Research on Earthquake Engineering

Gas Service Pipes and Damage Model

Figure 2 depicts the typical alignment of gas distribution pipelines and service pipes in an urban area. Distribution pipelines are buried beneath the pavement of roadways, alleys, or building back lanes, exhibiting a relatively extensive linear distribution. Service pipes connect distribution pipelines to end users at the gas meters. Notably, they are short pipe segments, and their installation diverges from standard buried pipelines, thus distinguishing them from distribution pipelines in various aspects.

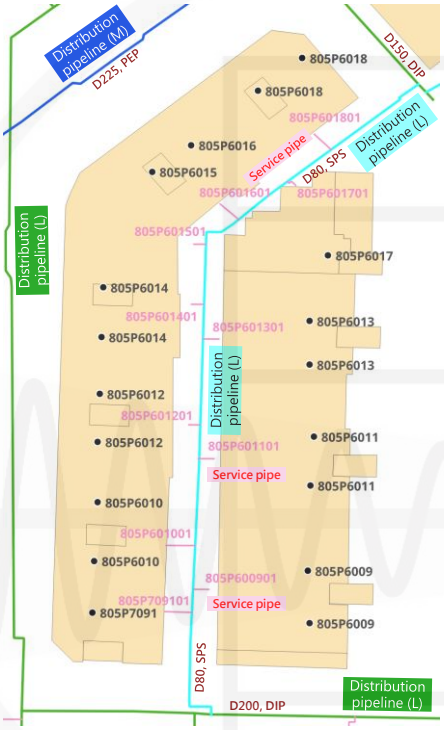

Fig. 2. Typical urban roadways, building outlines, gas distribution pipelines, and gas service pipes.

As the development and implementation of natural gas systems in Taiwan are very similar to those in Japan, studies on the damage model for gas service pipes in Japan is most informative. These studies are mainly based on experience from the 1995 Kobe earthquake, which resulted in tremendous damage in major urban areas and received extensive attention. Major findings have been summarized in two reports by the "日本損害保険料率算出機構" (2014, 2022). According to these reports, the damage probability of a service pipe can be expressed as:

$$RR = R_f \cdot C_p \cdot C_g$$

where R_f stands for the standard damage probability, and C_p and C_g are the two correction factors that account for the seismic fragility of the pipe type and the soil liquefaction hazard level at the site. In this expression, the formula for R_f is a function of the spectral intensity (SI, units of cm/s) of earthquake ground motions as defined by Housner (1965), which is not a popular index for measuring ground motion intensity. In this study, a conversion was performed to transform SI into the peak ground velocity (PGV, units of cm/s). The new expression is:

$$R_f = \begin{cases} 0 & PGV < 20 \\ 2.42\times10^{-4}\cdot(PGV-20)^{1.16} & 20 \le PGV < 100 \\ 0.03903 & PGV \ge 100 \end{cases}$$

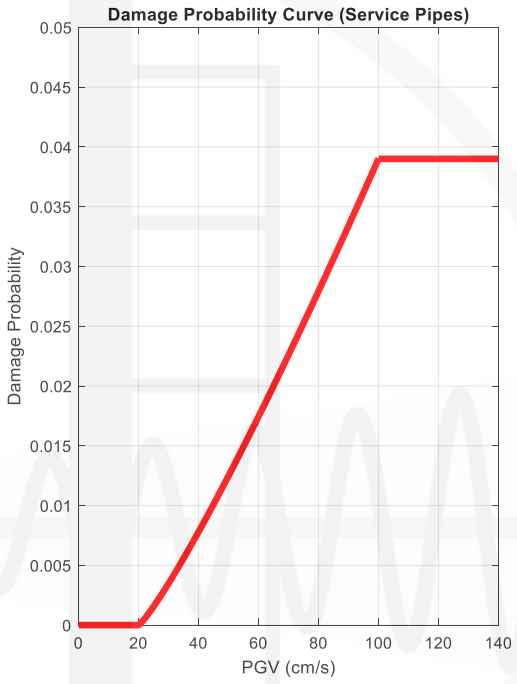

Fig. 3. Standard damage probability of gas service pipes plotted against the peak ground velocity (日本損害保険料率算出機構，2014, 2022).

This expression, depicted in **Figure 3**, predicts that the gas service pipe will be damaged only when the PGV value exceeds 20 cm/s. The damage probability increases monotonically with PGV up to 100 cm/s, beyond which it saturates at a probability of 0.03903.

Correction Coefficients

There are two types of gas service pipes, namely threaded steel pipes and polyethylene (PE) pipes, which have completely different seismic fragility. According to the compilation by the "日本損害保険料率算出機構" (2014, 2022), the pipe-type correction coefficients C_p are 1.00 and 0.00, respectively for steel and PE pipes. However, this study employs a value of 0.05 for PE pipes to be more conservative, reflecting the likely inferior detailing in service pipe installation in Taiwan.

Regarding the liquefaction correction coefficient, the limited availability of domestic seismic damage data precludes the establishment of a robust correlation between natural gas pipeline damage and soil liquefaction hazards in Taiwan. Consequently, this study references the Japanese model provided of "日本損害保險料率算出機構" (2014, 2022). The adjusted liquefaction correction factor C_g is a function of the liquefaction potential index (PL) at the site, as shown in **Figure 4**. When conducting damage estimation, this factor must be applied in conjunction with the probability of soil liquefaction occurrence $Prob_{Lqf}$ at the site. According to **Figure 4**, when the PL value is less than 5, the site is deemed to exhibit negligible or minimal liquefaction, and the correction factor C_g is set to 1.0. When the PL value exceeds 15, the site is susceptible to severe liquefaction, and the multiplier C_g reaches a saturation value of 8.0 with no further amplification. For PL values between 5 and 15, the multiplier is derived through linear interpolation.

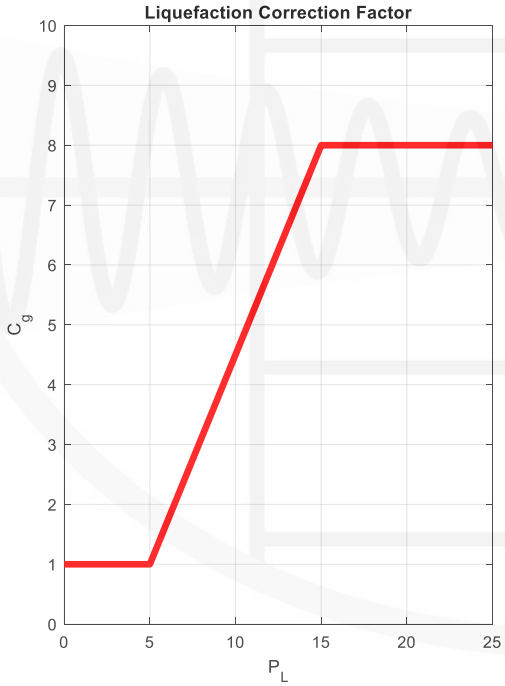

Fig. 4. Liquefaction modification coefficient for natural gas service pipe damage assessment.

Density of Gas Service Pipes for Number Estimation

According to the current legal regulations for gas utilities, establishment of a GIS database of the gas distribution pipelines is compulsory, while that of service pipes is discretionary. In practice, most utilities do not maintain their own database of service pipes. As a result, the number of service pipes in an area may not be available for damage estimation. To address this issue, this study developed an empirical formula that relates the "density of service pipes" to the "penetration." The "density of service pipes (y)" is the ratio of the number of service pipes to the number of customers in an area, essentially representing the number of service pipes per customer. The "penetration (x)" is the ratio of the number of customers to the total number of households in an area. The empirical formula, illustrated in **Figure 5**, is as follows:

$$y = -0.002021x + 0.4003$$

This formula enables the estimation of the number of service pipes in any spatial unit of a gas utility where a database of service pipes does not exist.

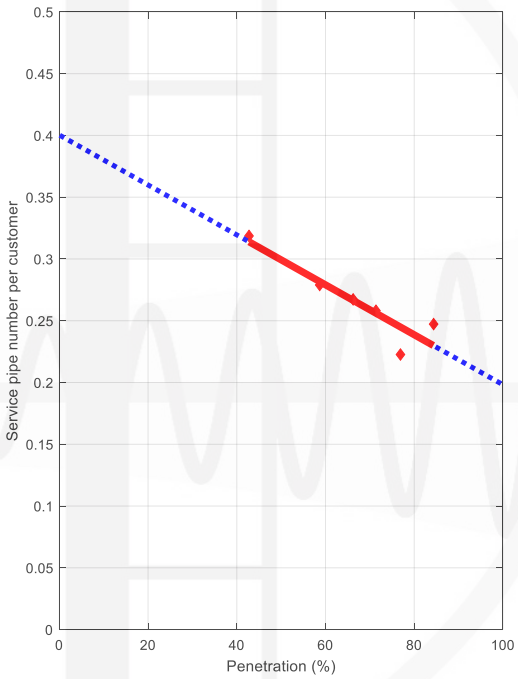

Fig. 5. The empirical formula that relates the "density of service pipes" to the "penetration."

Damage Estimation in a Spatial Unit

To estimate damage to natural gas service pipes, the Taiwan Earthquake Loss Estimation System (TELES) of the National Center for Research on Earthquake Engineering (NCREE) is used, with villages (村里) serving as the spatial units. First, the number of service pipes Num in each village is attained from the database (or estimated if data are unavailable). Next, based on the seismic source parameters of the scenario earthquake, an earthquake hazard potential analysis is conducted to determine the PGV and the PL for each village, as well as the probability of soil liquefaction $Prob_{Lqf}$. If the PL value for a village is less than 5, as shown in **Figure 6(a)**, only the PGV needs to be considered, without

accounting for liquefaction damage. Conversely, when the PL value exceeds 5, the TELES model assumes that the village has areas where liquefaction does not occur $(1-Prob_{Lqf})$ and areas where it may occur $Prob_{Lqf}$, with their respective area proportions shown in **Figure 6(b).** For the latter areas, liquefaction-induced damage must also be considered. In this case, the expected damage to the service pipes in the village can be represented (assuming the same pipe type) as:

$$N = Num \cdot R_f \cdot C_p \cdot \left[\left(1 - Prob_{Lqf}\right) + Prob_{Lqf} \cdot C_g \right]$$

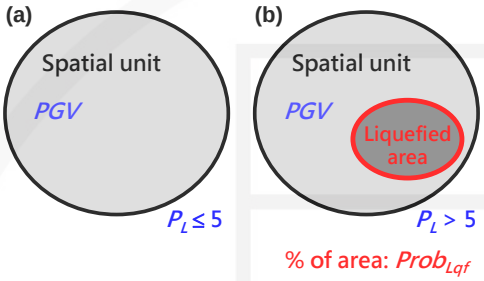

Fig. 6. Damage estimation in a small spatial unit (a) without and (b) with soil liquefaction hazard.

Case Study

A hypothetical scenario involving a magnitude 7.6 earthquake along the Changhua fault system is analyzed. The Changhua fault system, an amalgamation of the Dajia and Changhua Faults, is characterized as a reverse fault with a rupture length of 82.5 km, extending from Dajia, Taichung, to Gukeng, Yunlin. The central region of Taiwan, encompassing Taichung, Changhua, and Nantou counties, is serviced by four natural gas companies, Shin Chung, Shin Chang, Shin Lin, and Jun-Min, catering to approximately 700,000 users. Using TELES, the estimated service pipe damage across approximately 182,000 pipe segments, based on penetration data, yields around 4,550 damage cases. Damage hotspots include the Beitun, Xitun, and Nantun districts in Taichung City, as well as Changhua City in Changhua County, as illustrated in **Figure 7.**

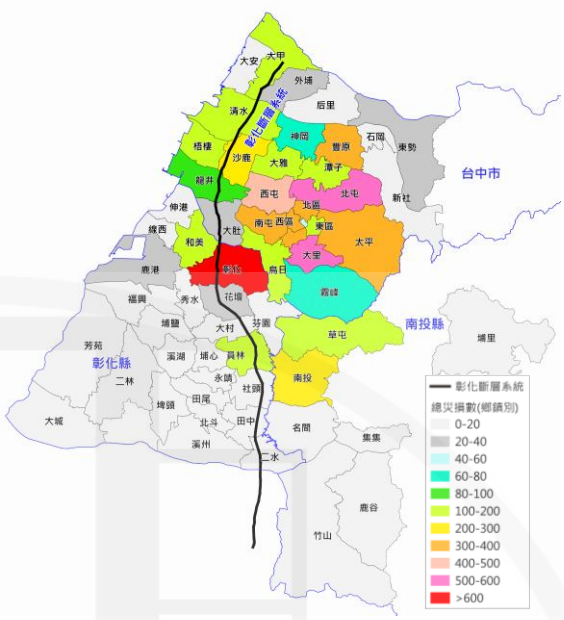

Fig. 7. A thematic map of the number of gas service pipe damage cases in Central Taiwan by township under a M7.6 Changhua fault system earthquake scenario.

References

American Society of Civil Engineers (ASCE) (2002), Improving Natural Gas Safety in Earthquakes.

Housner, G.W. (1965), "Intensity of Ground Shaking Near the Causative Fault," Proc. World Conf. Earthquake Eng., 3rd, New Zealand, 3, 94-109.

日本損害保険料率算出機構(2014)，「国・自治体の地震被害想定における被害予測手法の調査(地震保険研究 27，2013 年度調査)」。

日本損害保険料率算出機構(2022)，「国・自治体の地震被害想定における被害予測手法の調査(地震保険研究 37，2021 年度調査)」。

Liu, G.-Y., Chou, P.-C., and Hung, H.-Y., (2025), Earthquake Damage Assessment Model for Natural Gas Distribution Pipelines, Structural Engineering, Vol. 40, No. 1, pp.69-86 (in Chinese).

Seismic Loss Assessment Technique with Multiple Ground Motion Prediction Models

Lee-Hui Huang[1] and Chin-Hsun Yeh[2]

黃李暉[1]、葉錦勳[2]

Abstract

Seismic disaster scenario simulation technology relies on ground motion prediction equations (GMPEs) to estimate the hazard potential of ground motion. In the "Reevaluation of Probabilistic Seismic Hazard of Nuclear Facilities in Taiwan Using SSHAC Level 3 Methodology" project, multiple new GMPEs applicable to Taiwan were developed. In this study, four GMPEs suitable for crustal earthquakes and four for subduction earthquakes are selected and integrated into the existing seismic disaster scenario simulation framework. Additionally, weighted combinations of these four GMPEs are provided to comprehensively evaluate the effects of multiple GMPEs on earthquake damage estimation. By incorporating multiple GMPEs, the proposed approach reduces the biases associated with a single model, thereby preventing underestimation or overestimation of damage. This methodology more accurately reflects the uncertainties in ground motion distributions. In seismic disaster prevention planning, it enhances the understanding of uncertainty in damage estimation results. In probabilistic seismic risk assessment, the proposed approach helps generate more reliable risk assessment results.

Keywords: ground-motion prediction equation, risk assessment, TELES, TERA

Background

The Taiwan Earthquake Loss Assessment System (TELES) is an earthquake disaster scenario simulation software developed by the National Center for Research on Earthquake Engineering (NCREE). TELES can estimate earthquake hazard potential (e.g., ground motion, soil liquefaction), building damage, and casualties based on the specific source parameters of an earthquake scenario. Moreover, it can be used in combination with the Taiwan earthquake source hazard model to analyze probabilistic earthquake risk. TELES assists governments and organizations in developing disaster prevention plans and earthquake risk management strategies.

To assist the Taiwan Power Company in assessing earthquake hazards at nuclear facilities, NCREE established the Taiwan Earthquake Hazard Advanced Model. In this project, strong ground motion data were collected from significant earthquake events in Taiwan, and 12 new ground motion prediction equations (GMPEs) were developed, including 9 for crustal earthquakes and 3 for subduction earthquakes.

Among these, the Chao (2019) GMPE, developed by Dr. Chao, can be applied to both crustal and subduction earthquakes. The aforementioned GMPEs are based on seismological principles, and they consider key factors such as moment magnitude (Mw), source type (crustal or subduction), faulting style, path effects, and site effects. By accounting for various earthquake ground motion phenomena, this model provides more accurate earthquake motion estimation results.

In this study, several of the aforementioned GMPEs specific to Taiwan are combined with the existing wide-area site effect models in TELES, and the resulting combination is incorporated into earthquake disaster scenario simulation technology, as summarized in Table 1. In this table, the year in the brackets denotes the original model's publication year, and "adj" indicates that the GMPE parameters have been adjusted based on Taiwan's strong ground

[1] Assistant Researcher, Seismic Disaster Simulation Division, NCREE

[2] Research Fellow and Division Head, Seismic Disaster Simulation Division, NCREE

motion data.

In addition, ground motion is predicted using four GMPEs, where weighted values are employed for crustal and subduction earthquakes. This approach, called combined GMPE, allows users to comprehensively evaluate the influence of multiple GMPEs in earthquake damage assessments.

Table 1 GMPEs Integrated into TELES.

Name	Source Type	Remarks
ASK (2014) adj	Crustal	Hanging Wall Effects
CB (2014) adj	Crustal	Hanging Wall Effects
Idriss (2014) adj	Crustal	
Chao (2019)	Crustal and subduction	
Phung (2018)sb	Subduction	
LL (2008) adj	Subduction	
AGA (2016) adj	Subduction	Forearc/Backarc

Scenario Simulations Using Different GMPEs

For an earthquake of magnitude 7.5 on the Dajia Fault, the ground motion distributions estimated using different GMPEs are presented in Figure 1. The numerical value in the upper-right corner of each figure represents the maximum estimated value, indicating the extreme prediction. For the spectral acceleration 0.3 s, the Idriss model yields the highest estimate while the Chao model produces the lowest. For the spectral acceleration of 1.0 s, the CB model yields the highest estimate while the Chao model yields the lowest. Owing to the large hanging wall region, the ASK and CB models, which account for hanging wall effects, predict high ground motion values over a wider area compared to the other models. The Combined GMPE results consistently fall within the range of these four models.

In further analysis, the distribution and seismic vulnerability of different building types are considered in estimating building damage. The numbers of severely damaged buildings in Taichung City estimated using different GMPEs are listed in Table 2.

The Taichung Metropolitan Area is located on the hanging wall of the Dajia–Changhua Fault, and it contains a considerable number of high-rise buildings. Because the CB and ASK models consider the hanging wall effect, their estimated damage values for these high-rise buildings are higher. Additionally, the ASK model provides higher estimates for short-period spectral acceleration. The areas with higher estimated values tend to contain greater numbers of old, low-rise buildings, and therefore, the estimated damage to low-rise structures is greater.

The Idriss model, too, predicts relatively high short-period spectral acceleration values but does not account for the hanging wall effects. Consequently, it predicts a smaller high-motion region, and the estimated damage to low-rise buildings is lower.

The Chao model yields the lowest ground motion estimates. Because it does not consider the hanging wall effects, the predicted high-motion region is more limited, and therefore, the estimated damage to low-rise buildings is the lowest.

For a magnitude 7.6 scenario earthquake on the Chelungpu Fault, the ground motion distributions estimated using different GMPEs are illustrated in Figure 2, and the corresponding numbers of severely damaged buildings in Taichung City are listed in Table 3. Because the eastern side of the Chelungpu Fault consists mainly of hills and mountains, with relatively few buildings in the hanging wall region, the predicted number of damaged buildings is lower.

Table 2 Estimated number of severely damaged buildings in Taichung city for the Dajia–Changhua Fault earthquake scenario (Mw 7.5).

Attn_type	Low-rise (1–3F)	Mid-rise (4–7F)	High-rise (8–18F)	Super-high-rise (above 19F)	Total
Combined	51,937	5,705	339	16	57,996
Chao(2019)	29,148	4,096	254	12	33,510
ASK(2014)	70,982	6,222	371	17	77,591
CB(2014)	53,847	8,134	572	27	62,581
Idriss(2014)	53,667	5,469	289	13	59,438

Table 3 Estimated number of severely damaged buildings in Taichung City for the Chelungpu Fault earthquake scenario (Mw 7.6).

Attn_type	Low-rise (1–3F)	Mid-rise (4–7F)	High-rise (8–18F)	Super-high-rise (above 19F)	Total
Combined	22,138	2,776	137	4	25,054
Chao(2019)	18,488	2,982	165	6	21,641
ASK(2014)	22,017	2,104	97	3	24,220
CB(2014)	8,004	1,549	122	4	9,679
Idriss(2014)	44,373	4,397	203	7	48,979

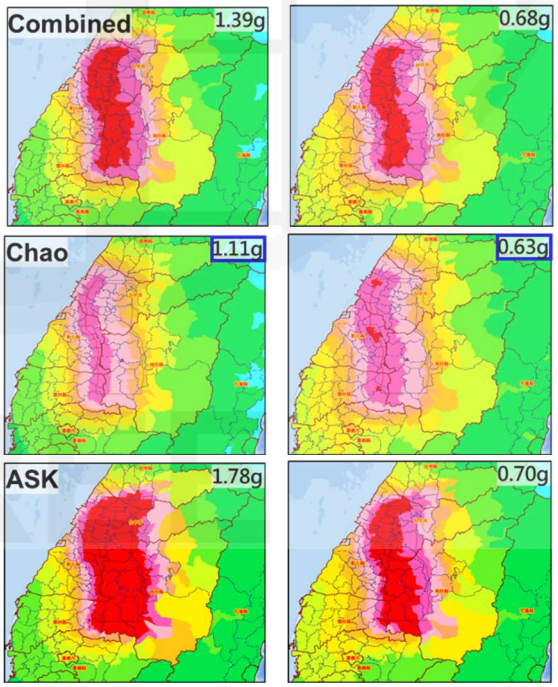

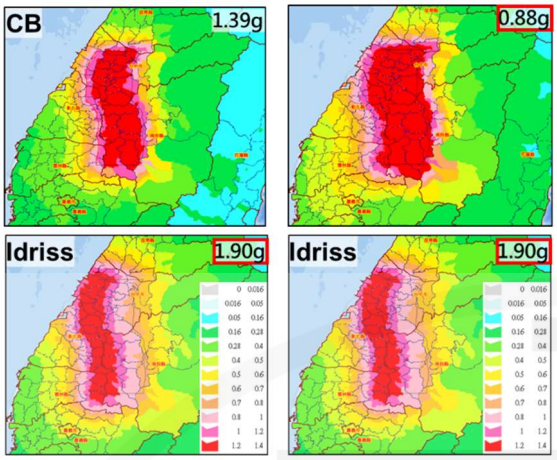

(a) T = 0.3 s (b) T = 1.0 s

Fig. 1. Comparison of spectral acceleration estimation results obtained using different GMPEs in the Dajia–Changhua Fault earthquake scenario (Mw 7.5).

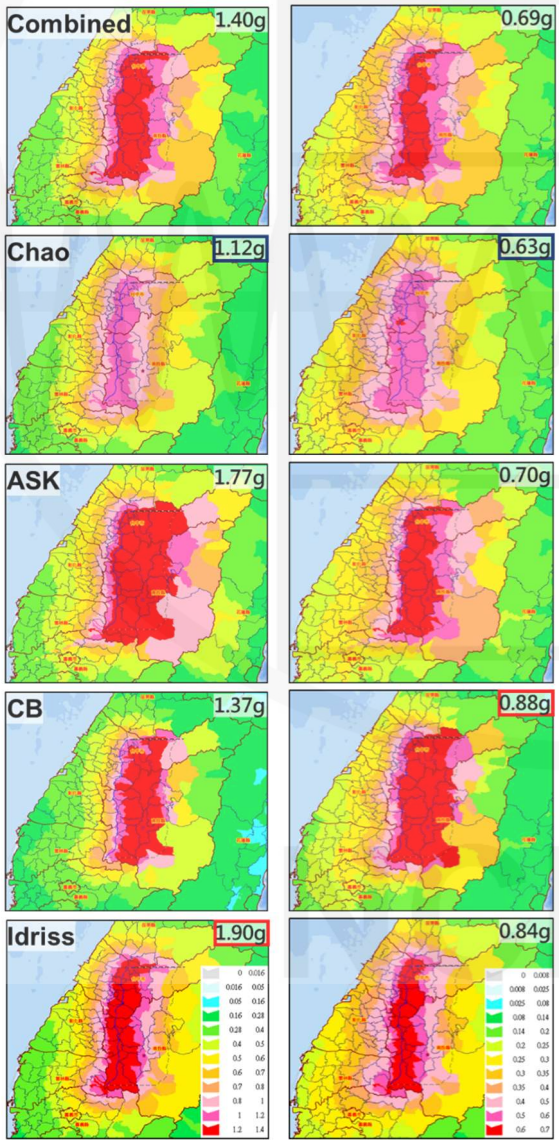

(a) T = 0.3 s (b) T = 1.0 s

Fig. 2. Comparison of spectral acceleration estimation results obtained using different GMPEs in the Chelungpu Fault earthquake scenario (Mw 7.6)

Probabilistic Risk Assessment Considering Multiple GMPEs

In 2023, the National Center for Research on Earthquake Engineering (NCREE) developed the Taiwan Earthquake Risk Assessment System for Insurance (TERA-ins). TERA-ins is a probabilistic earthquake insurance risk assessment software based on seismic disaster scenario simulations, and it is currently used by the Taiwan Residential Earthquake Insurance Fund. The system provides risk assessment results for residential earthquake insurance, including annual average losses, loss standard deviation, probable maximum loss, occurrence exceedance probability (OEP), and aggregate exceedance probability (AEP), among others. It supports the annual review of insurance premiums and the risk spreading mechanism. Additionally, the single-event scenario simulations generated using TERA-ins help the fund to conduct emergency response drills.

To protect the interests of over three million policyholders and ensure the accuracy and reliability of TERA-ins, the fund compared its performance to those of other internationally recognized earthquake insurance risk assessment models; according to the comparison results, TERA-ins is highly effective.

Probabilistic earthquake risk assessments require that Taiwan's seismic hazard source models be integrated to simulate a series of earthquake events and generate the corresponding loss data tables. The seismic disaster scenario simulations of individual fault hazard earthquake events are conducted using four different GMPEs. Accordingly, the number of simulation results for fault hazard earthquake events quadruples. The annual average occurrence rates of the original fault hazard earthquake events are allocated according to the weightings assigned to each of the four GMPEs. In other words, each fault hazard earthquake event is analyzed using all the four GMPEs, and each resulting estimate is treated as an independent seismic scenario. The annual average occurrence rate of the original fault hazard earthquake event is then divided among the four GMPE-based estimates based on their respective weightings.

In this way, any probabilistic earthquake risk assessment can comprehensively consider the results obtained using multiple GMPEs, thereby reflecting the uncertainty in the distribution of ground motion predictions.

Conclusion

Multiple GMPEs are integrated into seismic disaster scenario simulation techniques. All these GMPEs are based on Taiwan's strong ground-motion data, making them applicable to Taiwan. However, even for the same fault geometry and source parameters, the ground motion intensity distributions predicted by different GMPEs can vary significantly.

The damage estimation results consider the ground motion intensity estimated using the GMPEs, in addition to the distribution of buildings and population. If the distribution of ground motion intensity is consistent with the distribution of buildings, higher damage estimates are expected. For example, certain GMPEs consider the hanging wall effect, and metropolitan areas may be located on the hanging wall side of the fault rupture (e.g., ASK/CB models of the Dajia–Changhua Fault). Conversely, some GMPEs do not consider the hanging wall effect, and most buildings are located on the footwall side of the rupture (e.g., Chao/Idriss models of the Chelungpu Fault).

The use of a single GMPE may lead to either underestimation or overestimation of the actual damage. The use of multiple GMPEs mitigates bias in loss estimation resulting from reliance on a single ground motion intensity estimate, thereby preventing both underestimation and overestimation of damage predictions.

The "minimum-maximum damage estimate range" derived from the different GMPEs reflects the uncertainty inherent in damage estimation. This range enhances the robustness of disaster prevention planning and supports the formulation of more comprehensive response strategies.

In probabilistic earthquake risk assessments, considering multiple GMPEs helps reflect the uncertainty in ground motion distribution and yields more reliable risk assessment results.

References

1. Chao, S.-H., B. Chiou, C.-C. Hsu, P.-S. Lin (2019). Development of Horizontal and Vertical Ground Motion Models for Crustal Earthquakes and Subduction Earthquakes in Taiwan. NCREE-19-003.
2. Idriss, I. M. (2014). An NGA-West2 empirical model for estimating the horizontal spectral values generated by shallow crustal earthquakes. Earthquake Spectra, 30(3), 1155-1177.
3. Campbell, K. W., & Bozorgnia, Y. (2014). NGA-West2 ground motion model for the average horizontal components of PGA, PGV, and 5% damped linear acceleration response spectra. Earthquake Spectra, 30(3), 1087-1115.
4. Abrahamson, N. A., Silva, W. J., & Kamai, R. (2014). Summary of the ASK14 ground motion relation for active crustal regions. Earthquake Spectra, 30(3), 1025-1055.
5. Abrahamson, N. A., Gregor, N., & Addo, K. (2016). BC Hydro Ground Motion Prediction Equations for Subduction Earthquakes. Earthquake Spectra, 32(1), 23-44.
6. Van-Bang Phung, Chin Hsiung Loh, Shu Hsien Chao, and Abrahamson, N. A. (2020). Ground Motion Prediction Equation for Taiwan Subduction-Zone Earthquakes. Earthquake Spectra, 36(3), 1331-1358.
7. Lin, P.-S., & Lee, C.-T. (2008). Ground-motion attenuation relationships for subduction-zone earthquakes in northeastern Taiwan. Bulletin of the Seismological Society of America, 98(1), 220–240.
8. Lee-Hui Huang, Chin-Hsun Yeh, Yin-Nan Huang, Shu-Hsien Chao, (2023),"Study on Application of the Ground Motion Model for Wide-area Seismic Damage Assessment", NCREE-2023-025 ◦ (In Chinese)
9. Chin-Hsun Yeh, Lee-Hui Huang, Hsiang-Yuan Hung, Gee-Yu Liu, (2023), " Taiwan Residential Earthquake Insurance Risk Assessment Model", NCREE-23-024 ◦ (In Chinese)

Application of Speech and Language AI Models for Key Information Extraction in Disaster Reporting

Chi-Hao Lin[1], Xing-Yi Huang[2], and You-Xuan Lin[2]

林祺皓[1]、黃馨儀[2]、林祐萱[2]

Abstract

After a large-scale earthquake, large quantities of disaster information are collected from various sources. Rapidly understanding the disaster situation and its distribution is the top priority for emergency response. Currently, the Fire Agency's Emergency Management Information Cloud (EMIC) provides disaster-reporting functions, but it relies on manual processing and registration, which limits efficiency. This study aims to develop an AI-based disaster-reporting assistance system that utilizes automatic speech recognition and natural language processing to enhance information collection and processing efficiency. We integrate Google's Speech-to-Text and OpenAI's Whisper to ensure disaster reports function in both online and offline environments. Additionally, text analysis techniques incorporating named-entity recognition and an address recognition model (ARM) automatically extract key disaster information, such as disaster type, description, and location, thereby improving reporting accuracy. The results show that this system significantly reduces disaster-reporting time, minimizes human errors, and provides emergency-response units with real-time, structured information to enhance disaster-response efficiency.

Keywords: Natural language processing, disaster reporting, speech recognition, earthquake.

Introduction

After an earthquake, fast and accurate disaster reporting is crucial for the allocation of rescue resources and the efficiency of emergency response. The ability to quickly assess the extent of damage, identify affected locations, and determine the severity of incidents can significantly impact the effectiveness of disaster relief operations. The Fire Agency's Emergency Management Information Cloud (EMIC) currently requires personnel to manually sort reports, identify key content (such as disaster type, description, and location), and enter it into the system. However, this process relies heavily on human labor, which is not only time-consuming but also prone to errors due to the overwhelming volume and complexity of incoming information. As disaster reports pour in from various sources, inconsistencies in terminology, lack of structured formats, and delays in processing can hinder swift decision-making. Therefore, improving the automation of disaster reporting through AI technology is the core objective of this study.

This study develops an AI-based earthquake disaster-reporting assistance system that leverages Automatic Speech Recognition (ASR) and text analysis to improve efficiency and accuracy of information processing. ASR plays a fundamental role in this system by transcribing spoken reports into text, which can then be systematically processed and analyzed. Google's Speech-to-Text and OpenAI's Whisper are chosen as core ASR technologies to meet different environmental conditions. Google's Speech-to-Text utilizes cloud computing to provide real-time speech transcription, supports multiple languages, and includes noise reduction and contextual adaptation features, making it highly effective for structured data entry in connected environments. Meanwhile, Whisper operates on local devices, making it suitable for post-disaster environments where internet access may be unavailable, thus offering stable offline speech-to-text capabilities. By integrating both online and offline ASR solutions, this system ensures that disaster reporting remains functional across a wide range of conditions.

Furthermore, to ensure the completeness and accuracy of disaster reports, natural-language-

[1] Associate Researcher, National Center for Research on Earthquake Engineering
[2] Research Assistant, National Center for Research on Earthquake Engineering

processing (NLP) techniques are integrated to extract critical information from transcribed text. Disaster reports often contain unstructured data, requiring intelligent text analysis to identify relevant details efficiently. This study utilizes the CKIP named-entity recognition (NER) model from Academia Sinica and the address recognition model (ARM) developed by the National Center for Research on Earthquake Engineering (NCREE) to enhance data extraction and processing. The NER model automatically identifies key entities such as location names, facilities, and organization names, allowing for structured categorization of disaster-related information. Meanwhile, ARM enhances address recognition using deep-learning models such as BERT and BiLSTM, significantly improving the accuracy of geolocation extraction from informal or inconsistently formatted text inputs. By combining ASR and NLP technologies, this system aims to streamline disaster-information processing, reduce human error, and support emergency responders in making timely and data-driven decisions during crisis situations.

Speech Recognition Model

The disaster-reporting assistance tool integrates two widely adopted ASR models: one designed for online environments and another optimized for offline use. This dual-system approach ensures efficient disaster reporting across diverse scenarios, whether in urban centers with stable internet access or remote, disaster-stricken areas where connectivity is disrupted. The online ASR system utilizes Google's Speech-to-Text, a robust cloud-based service that delivers high-accuracy, real-time transcription while supporting over 125 languages and dialects. Its advanced capabilities make it particularly useful for emergency response operations, where clarity and speed are crucial. One of its key features is noise reduction, which filters out background sounds such as sirens, crowd noise, or environmental disturbances, significantly improving recognition accuracy in chaotic disaster environments. Additionally, it supports multi-channel recognition, allowing the system to differentiate between multiple speakers, which is essential in scenarios where multiple emergency responders or eyewitnesses are providing simultaneous information. Another notable advantage is its custom vocabulary function, which enables users to train the model to recognize domain-specific terminology related to earthquake disaster management. For example, words such as "collapse," "epicenter," and "seismic intensity" can be added to enhance transcription accuracy in emergency communications. These capabilities make Google's Speech-to-Text an indispensable tool for real-time speech processing, streamlining information intake for disaster response teams and improving situational awareness.

In contrast, the offline ASR system leverages OpenAI's Whisper, a Transformer-based sequence-to-sequence model that is trained on extensive multilingual datasets. Unlike cloud-based solutions, Whisper is designed to function without an internet connection, making it an ideal choice for post-disaster environments where network infrastructure may be damaged or unavailable. One of Whisper's greatest strengths is its robust language processing, which allows it to transcribe speech with high accuracy across various accents, dialects, and speaking styles. This feature is particularly beneficial in emergency response, as distress calls or disaster reports often involve diverse linguistic patterns and speech variations. Additionally, Whisper's on-device processing capabilities ensure that speech-to-text conversion remains functional even in severe disaster conditions where network-dependent services are inaccessible. This independence from cloud connectivity not only enhances reliability but also ensures data security and privacy, as all processing occurs locally without transmitting sensitive information over the internet. By integrating both Google's Speech-to-Text and OpenAI's Whisper, this system ensures a seamless, adaptable disaster-reporting mechanism that is capable of functioning efficiently in both well-connected urban environments and remote, infrastructure-compromised regions. Through this hybrid approach, emergency responders can swiftly process and relay critical disaster information, thereby enhancing overall coordination and response efficiency.

Text Analysis

Once user statements are converted into text via ASR, text extraction models analyze the information to extract key disaster-related data. The text analysis models applied in this study include:

(1) Named Entity Recognition:

The NER model developed by the CKIP Knowledge Group at Academia Sinica is designed for open-source word segmentation, part-of-speech tagging, and NER. Leveraging NLP techniques, NER automatically identifies and labels meaningful terms within text, such as personal names, geographical locations, and institutional names. This technology plays a crucial role in semantic understanding, information extraction, and text classification. In this study, we focus on applying NER for recognition of geographic information to enhance the extraction and analysis of location-related data in textual content.

The CKIP NER model defines eighteen categories of entity labels, with four specifically related to geographic information:

FAC (Facility): Refers to buildings or facilities with specific functions, such as "Taipei 101," "Chiang

Kai-shek Airport," and "Kaohsiung MRT Red Line."

GPE (Geo-Political Entity): Represents politically defined regions, such as "Taipei City" and "Banqiao District, New Taipei City."

LOC (Location): Encompasses general geographical regions, including natural landscapes, landmarks, or areas not defined by administrative divisions, such as "Alishan" and "Sun Moon Lake."

ORG (Organization): Refers to institutions closely related to geographic spaces, such as the "National Center for Research on Earthquake Engineering" and the "Ministry of the Interior's Mapping Center."

In this study, the CKIP NER model is applied to extract geographic information from textual data, particularly focusing on automatically tagging and structuring location-related features described in natural language. By integrating the NER model, this research enables the automated extraction of crucial geographical details from disaster reports processed through speech recognition.

(2) Address Extraction Model:

The ARM developed by NCREE aims to complement and enhance CKIP Transformers in identifying address strings. The model is designed to extract geographic location-related text from a given string while ensuring precise address recognition across different linguistic contexts. During training, the model identifies continuous address strings within sentences and classifies them into three categories using sequence tagging: "Address (A)," "Non-Address (NA)," and "Start or End of a Continuous String (E)" (Fig. 1). To improve recognition performance, the model architecture incorporates the pre-trained bidirectional encoder representations from transformers (BERT), leveraging its deep language comprehension and rich contextual understanding to enhance classification capabilities.

Text	<E>	他	在	新	厝	里	新	富	一	街	169	號	人	口	處	<E>
Labels	E	NA	NA	A	A	A	A	A	A	A	A	A	NA	NA	NA	E

Fig. 1. Sequence labeling method for text strings.

The greatest advantage of the BERT model lies in its bidirectional encoding mechanism, which allows it to consider both preceding and following words in a sentence. This enables the model to accurately distinguish between place names and general nouns when analyzing address strings. For example, the term "Nanjing" in "Nanjing East Road, Taipei City" refers to a location, whereas in "Nanjing Treaty," it has a completely different meaning. BERT utilizes contextual information to correctly interpret such distinctions. Additionally, its self-attention mechanism dynamically adjusts the weight of input sequences, strengthening the impact of key terms based on context. This feature is particularly useful for handling common challenges in Chinese address recognition, such as abbreviated place names, irregular expressions, or typographical errors. Compared to traditional rule-based address extraction methods, BERT effectively processes informal text, including colloquial expressions found in social media or user inputs. For instance, "Taipei Nangang" and "Nangang Taipei" have different word orders but refer to the same geographic location, a distinction that BERT can correctly identify.

To further enhance model performance, this study integrates a bidirectional long short-term memory (BiLSTM) neural network to process contextual dependencies. This approach enables the model to learn long-term relationships and effectively capture the syntactic structure of addresses (Figure 2). Regarding training data generation, address data was randomly selected from a street address positioning dataset to create a final training set of 2,000 samples. Among them, 1,617 samples included contextual information around the address string, consisting of 637 sentences with random non-meaningful context and 980 with meaningful, manually designed natural language sentences (196 unique sentences, each duplicated five times to expand the dataset). The remaining 383 samples contained no surrounding context, with 276 being standalone addresses and 107 being sentences without addresses. This data design aimed to train the model to recognize extreme cases. By incorporating diverse training samples, the model improves its adaptability to both formal and informal texts, ensuring higher accuracy and generalization in real-world applications.

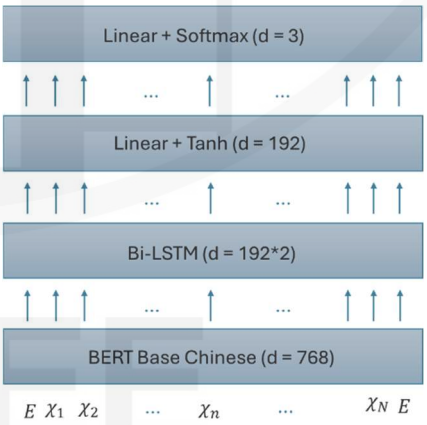

Fig. 2. Address extraction model.

(3) Address Field Segmentation Model:

The address field segmentation model is designed to identify the specific address components within an input string, categorizing each character into fields such as county, township or district, village, road, lane,

alley, number, and floor, or labeling it as "other." The core architecture of this model is based on a bi-directional recurrent neural network (BiRNN), combined with an active-learning training approach to address the challenge of insufficient labeled data and improve the model's adaptability to new samples. Since RNNs are particularly effective in processing sequential data, they consider the contextual information of the input string, allowing the model to retain the structural and semantic integrity of address components. For example, while "Xinyi District, Taipei City, Songren Road" and "Songren Road, Xinyi District, Taipei City" have different word orders, BiRNN can leverage its bidirectional learning mechanism to incorporate both preceding and following text, thus enhancing segmentation accuracy. Compared to traditional rule-based methods, RNNs can learn the inherent patterns of place names, in turn reducing reliance on manually designed rules and providing greater flexibility in handling variations in address formats.

To overcome the challenge of limited labeled data, this study adopts an active-learning training approach. Traditional supervised learning depends on a large amount of labeled data, but manually annotating address information is time-consuming and costly. To mitigate this issue, an initial model was trained using 8,530 pre-labeled address field data samples. The model then processed a large batch of unlabeled address data, selecting samples with the highest uncertainty based on classification confidence scores ($1 - \max p_{label}$). The selected samples were manually labeled and fed back into the training dataset to retrain the model, improving its adaptability to difficult classification cases. This method significantly reduces the required amount of labeled data while effectively enhancing model performance.

For data selection, the study divided the unlabeled address data into batches according to geographical regions. For example, Taipei City's address data was split into 83 sub-datasets, while New Taipei City's data was divided into 84. In each iteration, five unlabeled samples were selected from one sub-dataset, ensuring that different address formats from various regions were evenly incorporated into the learning process. The process continued until all sub-datasets had been evaluated by the model. As a result of this iterative learning strategy, the training dataset expanded to 9,365 samples. The final model was tested using a reserved validation set, achieving an accuracy rate of 0.99 (Fig. 3).

CityName	TownName	Tract	Neighborhood	Road	Lane	Alley	No	Floor
台北市	大安區			辛亥路三段			200號	
				大學路二段			2002號	
台北市	大安區			辛亥路三段			188號	

Fig. 3. Address field segmentation results.

Conclusion

This study successfully integrated AI-based speech recognition and text analysis techniques to enhance disaster information collection and processing efficiency. Google's Speech-to-Text and OpenAI's Whisper ensure disaster reports can be transcribed in varying network conditions, while named-entity recognition and address recognition models improve the accuracy of geographic information extraction. The results indicated that this system significantly reduces reporting time, lowers human-error rates, and enhances emergency response capabilities.

Moreover, the combination of automatic speech recognition and natural-language-processing technologies present new possibilities for intelligent disaster response. Future improvements could focus on refining speech-recognition accuracy and expanding applications to other disaster types such as typhoons and floods. This research demonstrates the potential of AI in earthquake disaster reporting, providing a more efficient solution for post-disaster information management.

References

Vaswani, A., Shazeer, N., Parmar, N., Uszkoreit, J., Jones, L., Gomez, A. N., Kaiser, L., & Polosukhin, I. (2017). "Attention is all you need," 31st Conference on Neural Information Processing Systems (NIPS 2017), Long Beach, CA. USA.

Mohamed, A. R., Hinton, G., & Penn, G. (2012). understanding how deep belief networks perform acoustic modelling," 2012 IEEE International Conference on Acoustics, Speech and Signal Processing (ICASSP), Kyoto, Japan. https://doi.org/10.1109/ICASSP.2012.6288863

Yang, M. & Ma, W. Y. (2023) CKIP Transformers. https://github.com/ckiplab/ckip-transformers?tab=readme-ov-file

Analysis of the Relationship between Risk- and Hazard-based Ground Motions

Hsun-Jen Liu[1] and Yin-Nan Huang[2]

劉勛仁[1]、黃尹男[2]

Abstract

Building a resilient society is a global trend for strengthening sustainable development. To assess seismic resilience, structural design must satisfy performance levels defined under specific seismic levels or risk objectives throughout the structure's service life, employing a uniform risk approach. The Taiwan Building Code primarily adopts a uniform hazard approach, which specifies three seismic levels based on return periods of 30, 475, and 2500 years and corresponding seismic design objectives (i.e., no damage under minor earthquakes, repairable damage under moderate earthquakes, and absence of collapse under severe earthquakes). This study evaluates the relationship between uniform risk and uniform hazard ground motions through theoretical and analytical studies. Specifically, it examines the ratio between risk-targeted ground motion and uniform hazard ground motion, known as the risk coefficient (C_r), under different hazard curve and fragility curve conditions. The theoretical analysis is based on risk estimation formulas derived from simplified seismic hazard curves, while the analytical study uses probabilistic seismic hazard analysis results from 200 test sites in Taiwan. A comprehensive understanding of C_r provides a preliminary basis for transitioning seismic design from hazard-based to risk-based approaches.

Keywords: resilient society, risk coefficient, risk-targeted ground motion, hazard slope, fragility uncertainty

Introduction

While globalization has driven rapid advancements in economy, technology, and culture, it has also introduced challenges such as population shifts, geopolitical instability, resource disparities, and extreme natural disasters. These factors contribute to increased social and security instability. Instead of relying solely on resistance-based strategies, modern approaches prioritize enhancing crisis adaptability and fostering a resilient society.

The term "resilience" originates from the Latin word "resilire," meaning to rebound or recover, and signifies a system's adaptability and capacity to recover when faced with hazards. A resilient society focuses on coexisting with risks rather than avoiding them, aiming to quantify risks and manage disasters to maintain predefined safety and reliability targets, even in challenging situations.

In civil engineering, seismic design principles already incorporate resilience concepts, requiring buildings to possess adequate strength and ductility to withstand design-level earthquakes. Strength ensures appropriate structural dimensions and system integrity, corresponding to adaptability, while ductility allows structures to absorb seismic energy and sustain inelastic deformation, reflecting recovery capacity.

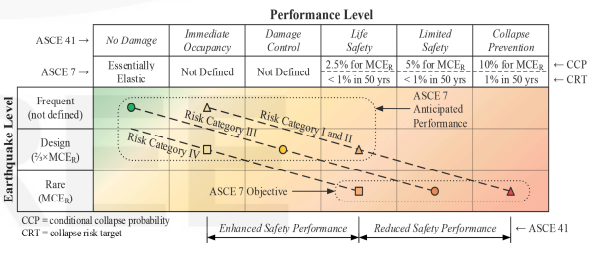

Fig. 1 Seismic performance objectives based on risk categories in ASCE 7 (Speicher and Harris, 2021).

To assess seismic resilience, structural design must

[1] Assistant Research Fellow, National Center for Research on Earthquake Engineering

[2] Associate Professor, National Taiwan University

satisfy predefined performance levels for specific seismic levels or risk objectives throughout the design service life. According to the American Society of Civil Engineers (ASCE) 7 Standard, the risk objective is set such that the collapse probability of buildings within 50 years under Risk-Targeted Maximum Considered Earthquake (MCE_R) ground motion is set at 1%, following a uniform risk approach. Figure 1 illustrates the seismic performance level targets for different risk categories as outlined in ASCE 7 (Speicher and Harris, 2021).

The Taiwan Building Code (Ministry of the Interior, 2024) primarily follows a uniform hazard approach, defining three seismic levels based on return periods of 30, 475, and 2500 years and the corresponding seismic design objectives: minor earthquakes should cause no damage, moderate earthquakes should result in repairable damage, and major earthquakes should not cause collapse. While the code does not explicitly specify risk objectives, it provides performance-based design levels.

Uniform hazard ground motion (UHGM) is determined based on seismic hazard curves, which identify seismic intensity measures corresponding to specific exceedance frequencies (or return periods). In contrast, risk-targeted ground motion (RTGM) is derived through an iterative process that integrates seismic hazard curves with structural fragility curves to achieve predefined risk targets. Seismic hazard curves are obtained from complex seismic source models and ground motion prediction models. Fragility curves, typically represented as lognormal distributions, require the definition of two parameters: the median capacity (C_{50}) and the logarithmic standard deviation (β). C_{50} represents the seismic intensity at which the probability of structural collapse reaches 50%, while β reflects the variability in structural seismic capacity.

This study investigates the relationship between RTGM and UHGM and identifies differences under various seismic hazard conditions and structural damage models. By employing theoretical and analytical studies, this research aims to explore variations in the risk coefficient (C_r), providing a foundation for transitioning seismic design from a hazard-based to a risk-based approach.

Theoretical C_r

Seismic risk (P_F) can be calculated by combining the hazard curve $H(a)$ with the fragility curve $P_{F|a}(a)$, as expressed in the following theoretical formula (McGuire, 2004; Kennedy and Short, 1994):

$$P_F = \int_0^\infty H(a) \left(\frac{\mathrm{d}P_{F|a}(a)}{\mathrm{d}a}\right) \mathrm{d}a \quad (1)$$

where a represents the intensity measure (e.g., spectral acceleration). The seismic hazard curve $H(a)$ can be expressed as a power function in a logarithmic scale:

$$H(a) = K_I a^{-K_H} \quad (2)$$

where K_I is a constant and K_H is the slope of the hazard curve. The fragility function $P_{F|a}(a)$ follows a lognormal distribution:

$$P_{F|a}(a) = \left[\left(a\beta\sqrt{2}\right)\exp\left(\frac{(\ln a - \ln C_{50})^2}{2\beta^2}\right)\right]^{-1} \quad (3)$$

Substituting Equations (2) and (3) into Equation (1) and applying the variable transformation $x = \ln a$, we obtain:

$$P_F = \frac{K_I}{\beta\sqrt{2\pi}} \int_{-\infty}^{\infty} \exp\left(-K_H x - \frac{(x - \ln C_{50})^2}{2\beta^2}\right) \mathrm{d}x \quad (4)$$

Expanding and simplifying Equation (4), yields:

$$P_F = K_I \exp\left(-K_H(lnRTGM + 1.28\beta) + \frac{(K_H\beta)^2}{2}\right) \quad (5)$$

According to the current ASCE 7 definition of structural fragility, a 10% probability of collapse under MCE_R ground motions is assumed. Thus, C_{50} can be rewritten as:

$$C_{50} = RTGM \ \exp(1.28\beta) \quad (6)$$

Here, $RTGM$ represents the seismic intensity that satisfies the risk target. Substituting Equation (6) into Equation (5) and rearranging yields:

$$RTGM = \left(\frac{K_I}{P_F}\right)^{\frac{1}{K_H}} \exp(0.5K_H\beta^2 - 1.28\beta) \quad (7)$$

Furthermore, $UHGM$ is defined as the seismic intensity corresponding to a given annual exceedance frequency H_f. From Equation (2), we obtain:

$$UHGM = \left(\frac{K_I}{H_f}\right)^{\frac{1}{K_H}} \quad (8)$$

The risk coefficient C_r is defined as the ratio of Equation (7) to Equation (8), yielding:

$$C_r = \left(\frac{H_f}{P_F}\right)^{\frac{1}{K_H}} \exp(0.5K_H\beta^2 - 1.28\beta) \quad (9)$$

For the maximum considered earthquake level and a 1% probability of collapse within 50 years, the values of H_f and P_F are 4×10^{-4}/year (return period of 2500 years) and 2×10^{-4}/year, respectively. Thus, Equation (9) simplifies to:

$$C_r = 2^{\frac{1}{K_H}} \exp(0.5K_H\beta^2 - 1.28\beta) \quad (10)$$

Analytical C_r

The case study utilizes seismic hazard curves for

spectral acceleration at a period of 0.3 seconds under reference-rock conditions (V_{S30} = 760 m/s) across 200 test sites distributed in Taiwan. The UHGM corresponding to a 2500-year return period is directly identified. Then, using Equation (1) and the ASCE 7 risk target, the RTGM is determined, allowing for the calculation of analytical C_r.

The probabilistic seismic hazard analysis (PSHA) relies on a seismic source characterization (SSC) model that incorporates recently updated fault sources in Taiwan, as documented by the Central Geological Survey (2020) and Taiwan Power Company (2019). It also includes areal seismic sources and subduction zone sources, as defined by Taiwan Power Company (2019) under the project "Reevaluation of Probabilistic Seismic Hazard of Nuclear Facilities in Taiwan Using SSHAC Level 3 Methodology." The ground motion characterization (GMC) model utilizes six crustal-source and four subduction-zone-source ground motion prediction equations (GMPEs), also from Taiwan Power Company (2019).

The structural fragility curve follows the reliability target condition set in Equation (6). Figure 2 illustrates the RTGM calculation, combining the seismic hazard curve and the structural fragility curve. The dashed line represents the initial estimate of RTGM based on UHGM, and the solid line represents the final RTGM, which satisfies the 1% collapse probability within 50 years, aligning with the ASCE 7 risk target.

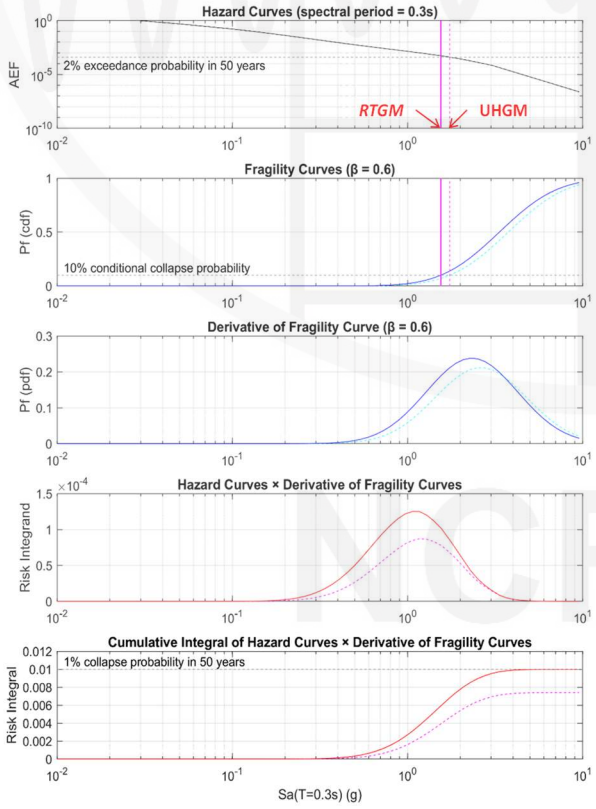

Fig. 2 Example of risk-targeted ground motion (RTGM) calculation.

Discussion on Theoretical C_r and Analytical C_r

From Equation (10), the key parameters influencing C_r are the hazard curve slope (K_H) and the fragility curve standard deviation (β). The three-dimensional relationship among these factors is illustrated in Figure 3. When β is fixed at 0.6, as referenced in ASCE 7, the relationship between C_r and K_H is depicted by the red curve in Figure 4.

In general, a larger β indicates greater uncertainty in seismic resistance, leading to a wider range of possible failure intensities. Consequently, the annual occurrence rate of RTGM should decrease (i.e., the return period increases) to achieve the required risk target. Additionally, a larger K_H implies a steeper hazard curve slope, which corresponds to higher seismic activity, resulting in a higher RTGM.

The distribution of C_r values across 200 test sites is shown as colored dots in Figures 3 and 4, where different colors represent UHGM values at a 2500-year return period for a 0.3-second spectral acceleration. The analysis considers five β values: 0.4, 0.5, 0.6, 0.7, and 0.8. The calculation of K_H is based on return periods ranging from 475 to 2500 years, with the variation falling between 2 and 6. Observations indicate that most K_H values in Taiwan fall between 3 and 3.5, which is close to the ASCE 7 reference value of 4.0, derived from the regulation that the Design Earthquake (DE) is 2/3 of the Maximum Considered Earthquake (MCE_R). Furthermore, for a given K_H, a higher UHGM corresponds to a lower C_r, aligning with its definition as the ratio of RTGM to UHGM.

Comparing theoretical and analytical C_r values, the former is consistently higher than the latter, with the difference increasing as K_H and β increase. This discrepancy arises because the theoretical C_r assumes a single-slope hazard curve, leading to an overestimation of hazard at lower seismic intensity levels compared to conventional calculations, thus making theoretical C_r larger than analytical C_r.

Figures 3 and 4 mark the critical C_r = 1 boundary (pink plane in Figure 3 and black dashed line in Figure 4), which helps estimate the relative relationship between RTGM and UHGM. In Figure 4, where β = 0.6, the critical K_H values corresponding to C_r = 1 are approximately 3 for the theoretical model and 3.5 for the case study. When K_H is below these values, RTGM is expected to be lower than UHGM. The critical C_r boundary for the theoretical model (white line in Figure 3) can be derived from Equation (10) as follows:

$$K_H\beta = 1.778 \tag{11}$$

Figure 5 illustrates the relationship between UHGM, C_r, and K_H across 200 test sites. The overall C_r values range from 0.85 to 1.2, indicating that RTGM may increase or decrease relative to UHGM, depending on the hazard curve slope (K_H). This variability suggests

an uncertainty margin of approximately 20% in RTGM estimation.

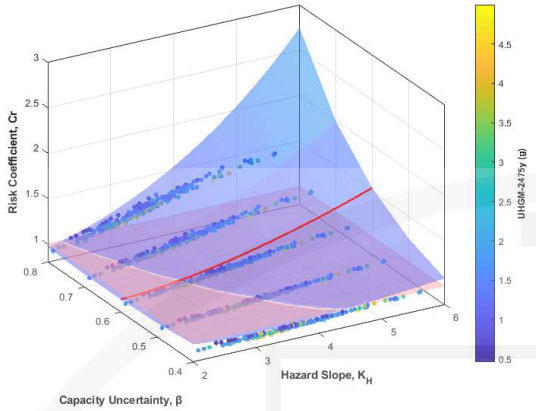

Fig. 3 Distribution of theoretical C_r (surface) and analytical C_r (colored points) for different K_H and β.

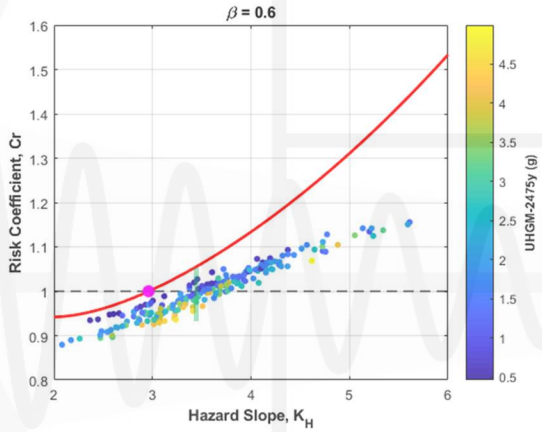

Fig. 4 Distribution of theoretical C_r (red line) and analytical C_r (colored points) for $\beta = 0.6$.

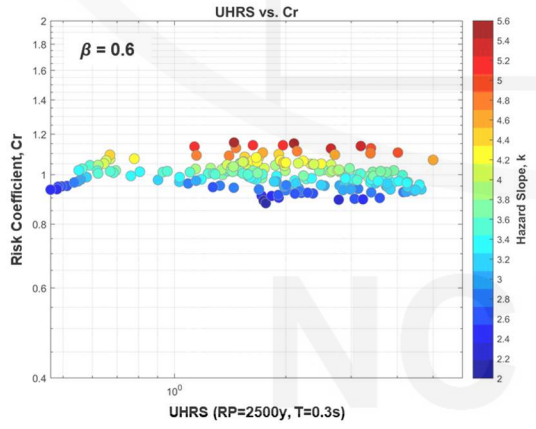

Fig. 5 Relationship between UHGM, C_r, and K_H across 200 test sites.

Conclusions

With the increasing emphasis on resilient societies, risk-targeted ground motion (RTGM) is expected to become a key focus in the future of seismic design. This study provides a preliminary analysis and comparison of the risk coefficient C_r for risk-targeted and hazard-targeted ground motions, using both theoretical formulations and analytical case studies.

The theoretical C_r was derived from a simplified hazard curve-based risk estimation model (McGuire, 2004), whereas the analytical C_r was obtained from probabilistic seismic hazard analysis (PSHA) conducted at 200 test sites across Taiwan. The results indicate that the theoretical C_r tends to be overestimated due to the assumption of a linear hazard curve (single-slope).

To improve accuracy, future work will focus on developing a dual-slope hazard curve model, which will better reflect the actual ground motion. This will allow for a more realistic formulation of C_r, facilitating a more direct transition from hazard-based to risk-based design ground motions.

References

ASCE/SEI 7-22, (2022). "Minimum Design Loads and Associated Criteria for Buildings and Other Structures", American Society of Civil Engineers, Reston, Virginia.

ASCE/SEI 43-05, (2005). "Seismic Design Criteria for Structures, Systems, and Components in Nuclear Facilities", American Society of Civil Engineers, Reston, Virginia.

CGS, (2020). "Improvement of the Active Fault Potential Map of Taiwan and Seismic Source Characterization – Final Report", Central Geological Survey, Ministry of Economic Affairs, Taiwan. (in Chinese)

Kennedy, R.P. and Short, S., (1994). "Basis for Seismic Provisions of DOE-STD-1020", U.S. Dept. of Energy, UCRL-CR-111478.

McGuire, R.K., (2004). "Seismic Hazard and Risk Analysis", Earthquake Engineering Research Institute Publication, No. MNO-10, Oakland, California.

NLMA, (2024). "Seismic Design Code for Buildings in Taiwan", National Land Management Agency, Ministry of the Interior, Taiwan. (in Chinese)

Speicher, M. and Harris, J., (2021). "Advancing First-Generation Performance-based Seismic Design for Steel Buildings – Part 1: Background and Motivation", *STRUCTURE Magazine,* Vol. 28, No. 10.

Taiwan Power Company, (2019). "Reevaluation of Probabilistic Seismic Hazard of Nuclear Facilities in Taiwan Using SSHAC Level 3 Methodology – Volume 4: Hazard Input Documents", prepared by National Center for Research on Earthquake Engineering.

Parameters for Seismic Hazard Assessment
Statistical Analysis of the Geometry of the Changhua Fault System in Taiwan

Kuan-Yu Chen[1], You-Chia Lee[2], Yu-Wen Chang[3], Hsun-Jen Liu[1], and Chih-Wei Chang[4]

陳冠宇[1]、李宥葭[2]、張毓文[3]、劉勛仁[1]、張志偉[4]

Abstract

Dip angle is a key parameter for describing the down-dip fault geometry in a probabilistic seismic hazard assessment (PSHA). Estimators had to make a forced suggestion with higher uncertainty ranges for fault dips due to the scarcity of data from geological and geophysical surveys.

In this study, we adopt two approaches, statistical and stacked 2D inferred fault geometries, to evaluate the down-dip geometry of a seismogenic fault and discuss the difference between aleatoric uncertainty (from data distribution) and epistemic uncertainty (decision making) and their ranges.

We collected fault dip angle values from geological and geophysical surveys conducted along the Changhua fault system to establish a tabulated and visualized database. By using a quantile-quantile plot, a graphical tool, to confirm the normality of the obtained dip data distribution, the dip of the Changhua fault system was estimated to be 17/30/43° with weights of 0.3/0.4/0.3 when using the extended Swanson–Megill method and 14/30/46° with weights of 0.2/0.6/0.2 when using the extended Pearson–Tukey method. According to the stacked 2D fault geometries, the shallow dip angle is 20/30/45°, and the deep dip angle values are 2° and 5°.

Keywords: PSHA, Dip, Changhua Fault, Weighting

Introduction

Different probabilistic seismic hazard assessment (PSHA) evaluation teams have proposed several alternative geometric models (including mean, uncertainty range and weights) of seismogenic faults. For the Changhua fault system, the single dipping angle is given as 20/30/40° by Hu et al. (2016), 45° by TEC (Shyu et al., 2016; 2020), and 35/45/55° by NCREE (2019); two dipping angles are given as 20(8.5)/25(5)/30(10)° by Yen et al. (2020); and three dipping angles are given as 35(20)[5]/45(30)[10]/55(40)[15]° by Shyu et al. (2017). We believe that the subjective opinions of researchers unconsciously influence the evaluation process, resulting in the development of various geometric models by different PSHA teams.

We tabulated and visualized the fault dip database from the collected dip angles and locations of geological and geophysical surveys. After confirming the normality of the dip distribution, we used statistical analysis to comply with the characteristics of the normal distribution curve to obtain the mean value, uncertainty range (confidence interval), and their corresponding weights. A visualized two-dimensional (2D) profile of stacked fault geometries is useful for effectively determining the down-dip geometry of seismogenic faults.

[1]Assistant Researcher, National Center for Research on Earthquake Engineering
[2] Research Assistant, National Center for Research on Earthquake Engineering
[3] Research Fellow, National Center for Research on Earthquake Engineering
[4] Assistant Technologist, National Center for Research on Earthquake Engineering

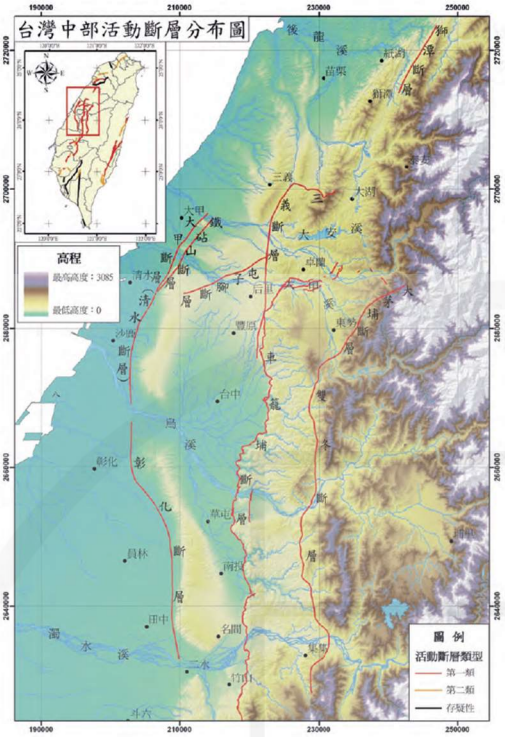

Fig. 1. Active fault map of central Taiwan. The Changhua fault system considered herein consists of the Dajia, Cingshui, and Changhua faults on the west of this active fault map (Lin et al., 2008).

We believe that adopting these approaches could minimize subjectivity in the evaluation process or decision making.

Changhua Fault System

The Changhua fault system consists of three faults: the Dajia and Cingshui faults on the west side of the Baguashan tableland and the Changhua fault on the west side of the Dadushan tableland, with their lengths being 30, 22, and 36 km, respectively. The total length of the Changhua fault system is up to 88 km.

Geological survey results indicate the absence of surface faulting and features along the Changhua fault system (Lin et al., 2008). The location of the Changhua fault system is mapped by geographical features (scarps) (Lin, 1957; Ku, 1963; Shi et al., 1984; Shi and Yang, 1985; Shen et al., 2005). According to shallow subsurface geophysical technical surveys, as well as borehole (Chen et al., 2006; Chen et al., 2008; Lin et al., 2008) and reflection seismic data (Chen, 1971; Hsiao, 1968; Wang et al., 2002; Shi et al., 2000; 2002; 2003; Hsiao, 2002; Chen and Su, 2002; Wang and Kuo, 2003; Dong et al., 2006), the Changhua fault system is consider as a blind fault.

There is a 13-km-long branch fault called the Tiehchenshan fault (also called the Dajiadong fault) is located at the northern tip of the Dajia fault and be considered as a back-thrust of Dajia fault. This fault is excluded from the Changhua fault system in this study.

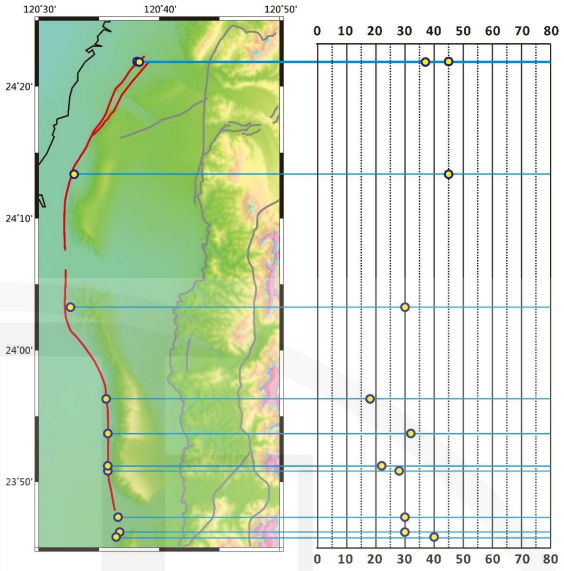

Fig. 2 Distribution of investigation sites with dip angle along the Changhua fault system.

Data Integration

The dip angles obtained from geological (field surveys, borehole, trenching) and geophysical (reflection seismic surveys and electrical resistivity surveys) surveys along the Changhua fault system are listed in a table with results of dip angel (refer to the NCREE 2024 technical report for more details regarding the table). Figure 2 presents the statistically determined survey points and the corresponding dip angles along the Changhua fault system, which will help us observe the dip variations along the fault.

Normal Distribution Test

The quantile-quantile plot (Q-Q plot) is a graphical tool that helps determine whether the dip data quantiles (Y-axis) are approximately distributed as the normal distribution quantiles (- axis). If the dataset follows (or is similar to) a normal distribution, the Q-Q plot (blue dots) will (approach) the X=Y line (red line). The high coefficient of determination (R^2 = 0.987, Fig. 3) indicates that the dip data quantiles fit well to the normal distribution quantiles.

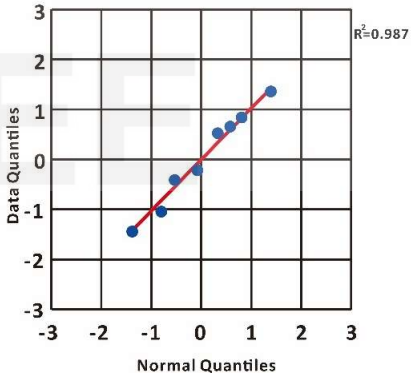

Fig. 3 Quantile-quantile plot of dip angle of the Changhua fault system.

Dip Assessment

After confirming that the filtered dip data follow a normal distribution, statistical analysis can be performed to comply with the characteristics of the normal distribution curve to obtain the mean value, uncertainty range (confidence interval), and their respective weights by using two common methods (Hammond and Bickel, 2013; Megill, 1984; Bickel et al., 2011; Pearson and Tukey, 1965; Keefer and Bodily, 1983): (a) the extended Swanson–Megill (ESM) method, which assigns weights of 0.3, 0.4, and 0.3 to the 10th, 50th, and 90th percentiles (as 80% confidence intervals within the 1.282 standard deviation of the mean) and (b) the extended Pearson–Tukey (EPT) method, which assigns weights of 0.185, 0.630, and 0.185 (generally 0.2, 0.6, and 0.2) to the 5th, 50th, and 95th percentiles (as 90% confidence intervals within the 1.645 standard deviation of the mean). Figure 4 depicts the confidence intervals and their corresponding standard deviations, as well as the weights of the ESM (green) and EPT (navy) methods.

Statistical Results

The statistically determined dip angles of the Changhua fault system are 17/30/43° with the weights of 0.3/0.4/0.3 when using the ESM method and 14/30/46° with the weights of 0.2/0.6/0.2 when using the EPT method (presented in Fig. 5).

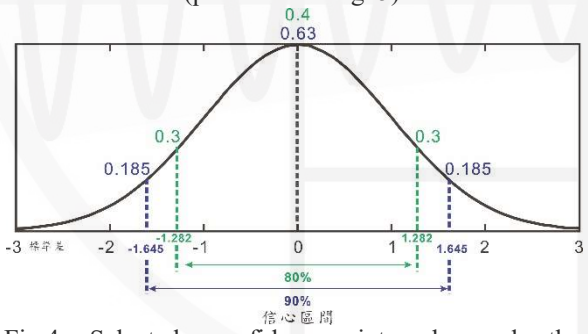

Fig.4 Selected confidence intervals and the corresponding standard deviations and weights of the ESM (green) and EPT (navy) methods.

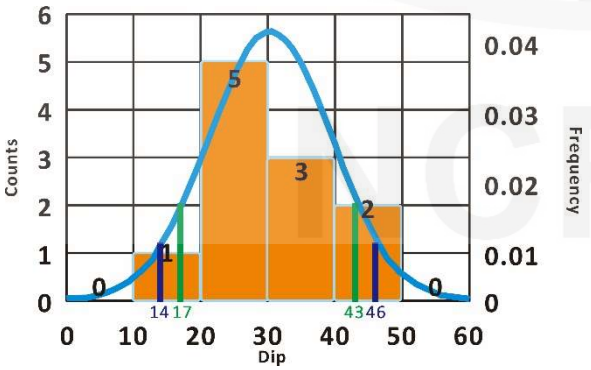

Fig.5 Statistical histogram and normal distribution (blue curve) of the Changhua fault system. The green and navy bars and values represent the evaluation results obtained using the ESM and EPT methods, respectively.

2D Fault Geometry and Discussion

The stacked cross section of the selected 2D fault geometries illustrates that there are two dip angles in the Changhua fault system. The shallow dip angle is 20/30/45° and the deep dip angle is 2°–5°. A comparison of our model with other models developed by different PSHA teams indicated that the geometric models (including mean, uncertainty range, and weights) of seismogenic faults vary across different PSHA evaluations (Hu et al., 2016; Shyu et al., 2017; Yen et al., 2020). We believe that this epistemic uncertainty can be attributed to the subjective opinions of the members involved in the evaluation process.

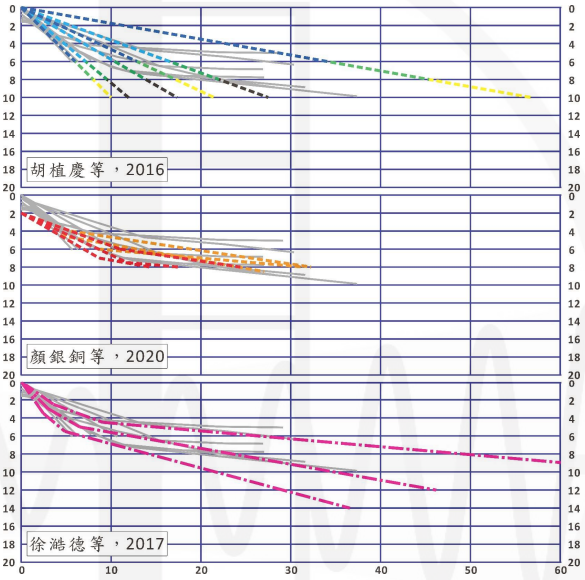

Fig.6 Comparison of the cross section of stacked geometries of the Changhua fault system. The visualized 2D profile of fault geometries is helpful for effectively determining the down-dip geometry of seismogenic faults.

Future Works

This project aims to establish a dip angle database with references, survey locations, and results of all active (seismogenic) faults announced by GSMMA in (on land) Taiwan. The use of a statistical approach and the 2D profile of stacked fault geometries is helpful for effectively determining the down-dip geometry, seismogenic depth, and decollement depth of seismogenic faults. We have completed the database of most of the active faults in Western Taiwan (from Taipei to Pingtung), except for the active faults in Eastern Taiwan (from Ilan to Taitung).

Reference

1. Bickel, J. E., L. W. Lake, J. Lehman. 2011. Discretization, Simulation, and Swanson's (Inaccurate) Mean. SPE Economics and Management 3(3) 128-140.
2. Chen, J.S. (1971) A comparative study of the

refraction and reflection seismic data obtained on the Changhua Plain to the Peikang Self, Petrol. Geol. Taiwan, No. 15, P. 199-217.Hsiao, P. T., 1968. Seismic Study of the Taichung Area, Taiwan, Petrol. Geol. Taiwan, 6, 209-218.

3. Chen, M. M., H. W., Chen, H. T. Chu, K. S. Shieh (2008) Based On Borehole Data To Interpret The Characters Of The Changhua Fault. Special Publication of the Central geological survey, No.20, P.33-48.
4. Chen, T. S., F. C. Su, (2003) The structural type of Northern Changhua fault. CPC Corporation, Taiwan.
5. Chen, W. S., Y. G., Chen, H, C, Yang (2006) Earthquake Geological Investigation And Data Bank Establishment On Active Faults- Trenching and Paleo-seismic research (5/5). Report of Central geological survey. No.95-08, pp.133.
6. Dong, L. D., Y. H. Lee, W. S. Chen (2006) Earthquake Geological Investigation And Data Bank Establishment On Active Faults-Geophysical prospecting program (5/5) Report of Central geological survey, No. 95-09, pp. 187.
7. Hammond, Robert & Bickel, J. (2013) Reexamining Discrete Approximations to Continuous Distributions. Decision Analysis. 10. 6-25. 10.1287/deca.1120.0260.
8. Hsiao, J. W. (2002) Investigating the shallow structures around the Chinshui Fault, West-Central Taiwan. Master Thesis of Geophysical Institute of National Central University. pp. 104
9. Hu, J. C., C. C. Liu, T. Y. Yang, K. E., Jing, C. T. Cheng (2016) Fault activity observation study Phase III- Fault integration observation and potential analysis. Annual Report of Central geological survey No.105-02. Pp.468.
10. Keefer, D. L., S. E. Bodily. 1983. Three-point Approximations for Continuous Random Variables. Management Science 29(5) 595-609.
11. Ku, C.C. (1963) Photogeologic study of terraces in northwestern Taiwan. Proc. Geol. Soc. China, no. 6, 51-60.
12. Lin, C. C. (1957) Topography of Taiwan. Historical Records Committee of Taiwan Provincial Government Publication. pp. 424
13. Lin, C. W., S. T. Lu, S. T. Shih, W. H. Lin, Y. C. Liu, P. T. Chen (2008) The active faults of Central Taiwan. Central geological survey special publication, No. 21, pp. 148.
14. Megill, R. E. 1984. An Introduction to Risk Analysis, Second edition. PennWell, Tulsa, OK.
15. NCREE (National Center for Research on Earthquake Engineering) (2019) Reevaluation of probabilistic seismic hazard of nuclear facilities in Taiwan using SSHAC level 3 methodology. NCREE Report-Volume 2: Seismic Source Characterization Technical Report. Available at: http://sshac.ncree.org.tw
16. Pearson, E. S., J. W. Tukey. 1965. Approximate Means and Standard Deviations Based on Distances between Percentage Points of Frequency Curves. Biometrika 52(3/4) 533-546.
17. Shen, S. M., J. C., Chang, G. S., Yang (2005) Earthquake Geological Investigation And Data Bank Establishment On Active Faults- Analysis of topography of active faults and database establishment. Annual Report of Central geological survey, No. 94-13, pp. 80
18. Shih, R. C., J. M. Hsieh, Y. C. Lin (2003) Shallow Seismic Reflection Images of the ChangHua Fault. Proceeding of 2003 Annual conference of Geological society. P. 139-143.
19. Shih, R. C., P. H. Chen, H. Y. Yen, C. H. Lin (2000) Active fault geophysical survey program-Geophysical prospecting of active faults in Central and Taitung areas of Taiwan (3/5). Annual Report of Central geological survey, pp.80.
20. Shih, R. C., P. H. Chen, M. T. Lu, W. S. Chen (2002) Earthquake Geological Investigation And Data Bank Establishment On Active Faults-Shallow geophysical prospecting (1/5) Annual Report of Central geological survey, No. 95-09, pp. 166.
21. Shih, T. T., G. S. Yang (1985) The Active Faults And Geomorphic Surfaces Of Pakua Tableland In Taiwan. Geographical Research. No.11. P. 173-186.
22. Shih, T. T., J. J. Chang, K. H. Tang, C. D. Shih, G. S. Yang, M. Y. Hsu (1984) A geomorphological study of active fault in western and southern Taiwan. Geographical Research No.10, P. 49-94.
23. Shyu, J. B. H., Y.-R. Chuang, Y.-L. Chen, Y.-R. Lee, and C.-T. Cheng (2016) A new on-land seismogenic structure source database by the Taiwan Earthquake Model (TEM) project for seismic hazard analysis of Taiwan, Terr. Atmos. Ocean. Sci. in this vol.
24. Shyu, J. B. H., Yin, Yu-Hsuan, Chen, Cheng-Hung, Chuang, Yi-Rung, Liu, Sze-Chieh. (2020) Updates to the on-land seismogenic structure source database by the Taiwan Earthquake Model (TEM) project for seismic hazard analysis of Taiwan. Terrestrial Atmospheric and Oceanic Sciences. 31. 469-478. 10.3319/TAO.2020.06.08.01.
25. Wang, C. Y., Kuo, S.Y., Shyu, W.L., and Hsiao, J.W. (2003) Investigating Near-surface Structures under the Changhua Fault, West-central Taiwan by the Reflection Seismic Method, TAO, 14(3), 343-367.
26. Wang, C.Y., H. Y., Kuo (2003) Detecting The Tiehchanshan Fault By The Seismic Reflection Method. Special Publication of the Central Geological Survey, No.14, P77-87.
27. Wheeler D. (2011) Problems with skewness and kurtosis Part one and part two. Quality Digest Daily.
28. Yen, Y. T., Shyu, J. B. H., Y. R. Lee, B.S. Hsieh, M. C. Hsieh, Y. R. Chuang (2020) Taiwan Seismic Hazard Potential of active faults and evaluation of the characteristics of the seismic source. Annual Report of Central Geological survey No.109-45. pp.423.

Soil–gas Radon Monitoring Data and its Association with the M_L 7.1 Hualien Earthquake of April 2024

Vivek Walia[1] and Shih-Jung Lin[2]

瓦里亞[1]、林世榮[2]

Abstract

This report investigates soil–gas radon anomalies as possible precursors to the magnitude 7.1 Hualien earthquake sequence that struck eastern Taiwan on April 3, 2024 and aftershocks. We analysed radon data from a network of monitoring stations across active fault zones, alongside meteorological parameters and seismic events. Radon anomalies were detected at Jiaosi, Sanjie, Hsinchu, and Qingshui monitoring stations prior to the earthquake, often exceeding 3-sigma thresholds. The results suggest that radon emissions can serve as reliable indicators of tectonic stress and impending seismic events. This study emphasizes the importance of integrating real-time radon monitoring to enhance earthquake preparedness in geologically active regions like Taiwan.

Keywords: radon monitoring, earthquake precursors, Hualien earthquake, Taiwan tectonics

Introduction

The scientific community has long studied various geochemical parameters that may be precursors of earthquakes. These precursors are often found in active fault zones and volcanic areas. Common precursors include gases such as radon, carbon dioxide, and helium and stable isotope ratios such as δ^2H and $\delta^{18}O$. Numerous studies have documented changes in these parameters prior to seismic events (Igarashi et al., 1995; Yang et al., 2006). Among these, radon is one of the most extensively researched precursor. It is a noble gas produced by the decay of uranium in the Earth's crust. Due to its inertness, short lived, and natural release from the ground, radon is ideal for monitoring. Several studies have reported that radon levels often rise or fall near fault zones before earthquakes (Fu et al., 2019).

These studies typically utilise time-series data to detect changes in radon concentrations. However, background noise in the data can complicate the identification of genuine earthquake-related signals. To address this issue, researchers employ various statistical methods. The most commonly used method is the "mean ± nσ" approach, where values that fall beyond a defined number of standard deviations from the mean are considered anomalous (Virk & Walia, 2001). Another important consideration in these studies is the selection criteria for earthquakes. Some researchers analyze events occurring within a specific radius (e.g., 20–40 km) from radon monitoring sites (Walia et al., 2013), whereas others use the distance-based equation proposed by Dobrovolsky et al. (1979) to filter relevant seismic events (Kumar et al., 2020). Alternatively, some studies focus exclusively on events along known fault lines.

Taiwan lies at a highly complex tectonic boundary where different tectonic plates converge. The Philippine Sea Plate moves toward the Eurasian Plate at a rate of about 80–90 mm per year. In the southwest, the South China Sea Plate subducts beneath the Philippine Sea Plate. Because of these tectonic movements, Taiwan experiences numerous earthquakes each year. Global Navigation Satellite System (GNSS) data indicate that the Longitudinal Valley suture zone absorbs approximately 30 mm/yr of NNW-SSE crustal shortening (Hsu et al., 2009).

Taiwan has experienced several massive earthquakes in the past century. Notable seismic events include the 1951 Hualien-Taitung earthquakes, a powerful earthquake near Chengkung in 2003, another near Hualien in 2018, and a series of events near Chihshang in 2022. Most recently, on April 3, 2024 a magnitude 7.1 earthquake struck near Hualien, marking the most powerful tremor in the region since

[1] Research Fellow, National Center for Research on Earthquake Engineering, walia@niar.org.tw
[2] Assistant Researcher, National Center for Research on Earthquake Engineering, sjlin@niar.org.tw

1951, according to the Central Weather Administration (CWA) (cwa.gov.tw). The island's seismicity is largely driven by two major fault systems along the Longitudinal Valley in eastern Taiwan: the east-dipping Longitudinal Valley Fault and the west-dipping Central Range Fault. These two faults delineate the boundary where the Philippine Sea Plate collides with the Eurasian Plate. Their close proximity results in complex fault interactions, with both potentially rupturing during a single seismic event (Fig. 1) (Cheloni et al., 2024).

Seismological studies indicate that the 2022 Chihshang earthquakes primarily released stress along the Central Range Fault, while stress continued to accumulate on the Longitudinal Valley Fault. Prior to 2024, this fault was believed to be capable of producing earthquakes with magnitudes between 7.3 and 7.6. Recent research has revealed increasingly complex fault geometries, particularly north of Ruisui, where the Central Range Fault becomes more dominant.

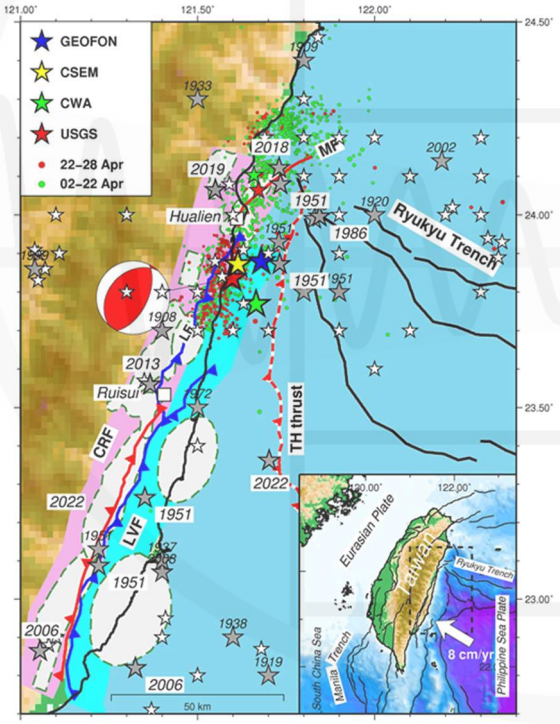

Fig. 1. Seismotectonic framework of Eastern Taiwan. Major fault systems (solid lines) are shown. The aftershock sequence (colored dots) occurred during April 2-28, 2023 according to the Central Weather Administration catalog. The ML 7.1 mainshock and ML 6.5 aftershock are marked by colored stars, and historical earthquakes are indicated by gray stars ($6.0 \leq M < 6.5$) and white stars ($M \geq 6.5$). Shaded regions represent rupture zones of significant earthquakes along the Longitudinal Valley Fault (light blue) and Central Range Fault (pink). The inset map shows Taiwan's regional tectonic setting with the main study area highlighted. Key fault abbreviations: CRF (Central Range Fault), LVF (Longitudinal Valley Fault), MF (Milun Fault), LF (Lingding Fault), and TH (Takangkou High) (from Cheloni et al., 2024).

The April 3, 2024 earthquake occurred at 07:58 TST at a depth of 19.7 km, with its epicenter located 13.6 km south of Hualien city. A magnitude 6.5 aftershock followed just 13 minutes later. This event initiated a sequence of aftershocks, over 240 with magnitudes ≥4 within the first five days and mostly propagating north-northeast of the mainshock. Another notable cluster occurred on April 23, including two moderate events (M 6.1 and 6.2) at shallower depths.

According to the U.S. Geological Survey, the mainshock exhibited reverse faulting, consistent with the region's compressive tectonic regime and a crustal contraction rate of approximately 30 mm/year. The fault systems display varying interactions along their length, reflecting the region's transitional tectonic environment, shaped by both arc-continent collision and subduction dynamics near the Ryukyu Trench. These findings underscore the seismic complexity and ongoing hazard potential in eastern Taiwan.

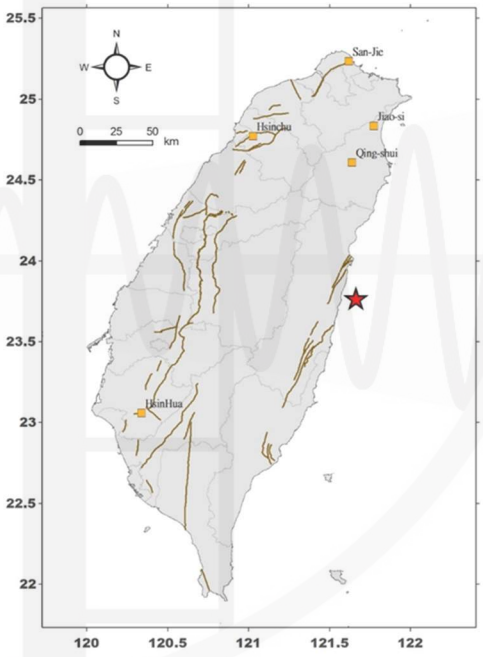

Fig. 2. Radon monitoring station network along different fault zones and the location of seismic event.

Results and Discussion

Our research group has extensively investigated soil gas radon as a potential precursor to earthquakes, utilizing a network of monitoring stations strategically established across various active fault zones in Taiwan (Fig. 2) (Arora et al., 2017; Walia et al., 2013). Through this monitoring network, we detected anomalous patterns in soil radon concentrations at some monitoring stations before some significant earthquakes occurred within the study region. To distinguish genuine seismic precursors from weather-related fluctuations, we developed robust tectonic models using advanced nonlinear analysis methods, specifically empirical mode decomposition and

singular spectrum analysis. These techniques allowed us to effectively isolate and validate true pre-seismic radon signals (Kumar et al., 2020). We analyzed data for soil–gas radon anomalies as potential precursors to the magnitude 7.1 Hualien earthquake sequences that struck eastern Taiwan on April 3, 2024. The study adopted the Dobrovolsky et al. (1979) equation to analyze the relationship between epicentral distance (R) and the anomaly distance (D), calculating the D/R ratio to assess the potential of radon emissions as an earthquake precursor.

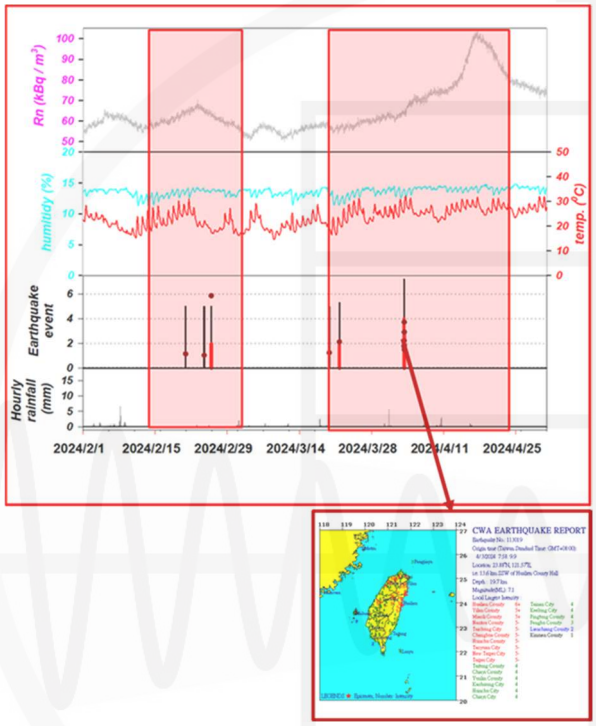

Fig.3. Radon monitoring data at the Jiaosi Station along with other parameters from February 1 to April 30, 2024. Red boxes represent probable precursory anomalies.

At the Jiaosi Station (JS), situated approximately 118 km from the earthquake epicenter, radon levels exhibited significant fluctuations over the course of two months (Fig. 3). Two distinct episodes were observed. The first began around February 12 and lasted nearly three weeks, followed by another surge in mid-March that persisted through April. These anomalies exceeded the 3-sigma threshold, marking them as statistically significant and indicative of stress accumulation in the crust. During a notable event on February 25 (M 5.1, depth of 7.6 km), the D/R ratio reached 5.9 with an epicentral distance of 22 km. This station thus meets the intensity criterion (≥5) and distance requirement (≤120 km), aligning well with theoretical expectations.

The Hsinchu Station (HC), approximately 130 km from the epicenter, also recorded marked radon fluctuations during February and March (Fig. 4). Although some data were lost due to technical issues, the remaining readings confirmed substantial increases that matched the seismic timeline. The trend, characterized by rising radon levels, continued through the end of March. The station fulfilled the criteria of intensity (≥4) and distance (≤130 km), supporting the presence of a precursory anomaly. Additionally, these fluctuations were corroborated by similar signals at other northern and eastern stations, highlighting a broader regional pattern of radon elevation ahead of the seismic event.

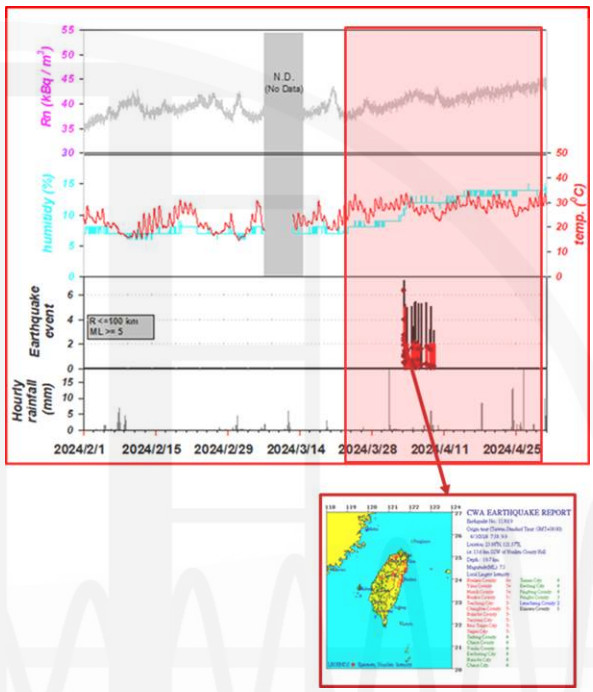

Fig. 4. Radon monitoring data at the Hsinchu Station along with other parameters from February 1 to April 30, 2024. Red boxes represent probable precursory anomalies.

The Sanjie Station (SJ), with a qualifying intensity of ≥4 and distance of ≤150 km, experienced two notable radon elevation episodes, beginning in late February and peaking around mid-March (Fig. 5). These episodes were accompanied by variations in humidity, which may have contributed to the fluctuations. However, the persistent upward trend in radon levels, despite intermittent dips, suggests a precursory signal consistent with crustal stress buildup. Technical challenges in data upload and download were encountered but did not obscure the broader trend, which remains ongoing. The sustained rise in radon levels implies that full stress release had not yet occurred.

The Qingshui Station (QS), located less than 100 km from the epicenter and positioned within a geothermal park, is not yet integrated into the real-time monitoring network. It displayed pronounced radon variability over the three-month observation period (Fig. 6). Data recorded from March 1 indicate that the elevated radon values were not correlated with temperature or humidity fluctuations, suggesting that the high radon concentration may represent a precursory anomaly associated with the recent significant seismic event. A sudden spike was noted

after the earthquake, confirming its role as a valuable indicator of seismic precursors, particularly in geothermal environments.

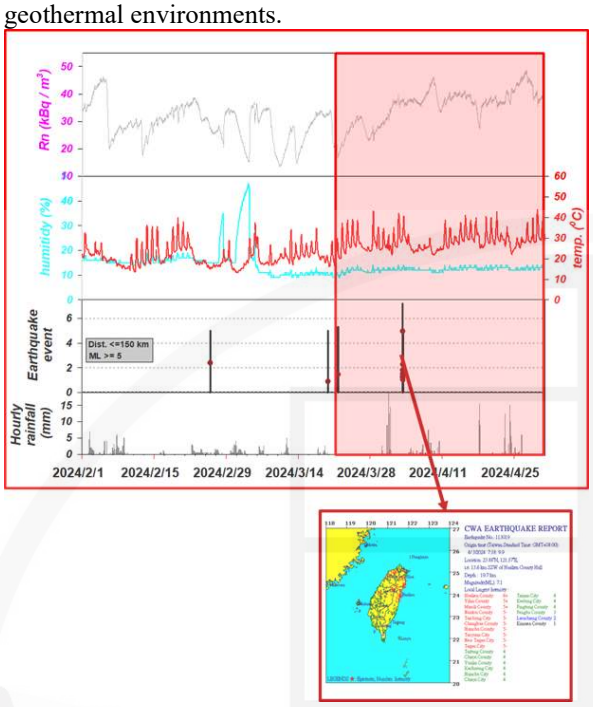

Fig. 5. Radon monitoring data at the Sanjie Station along with other parameters from February 1 to April 30, 2024. Red boxes represent probable precursory anomalies.

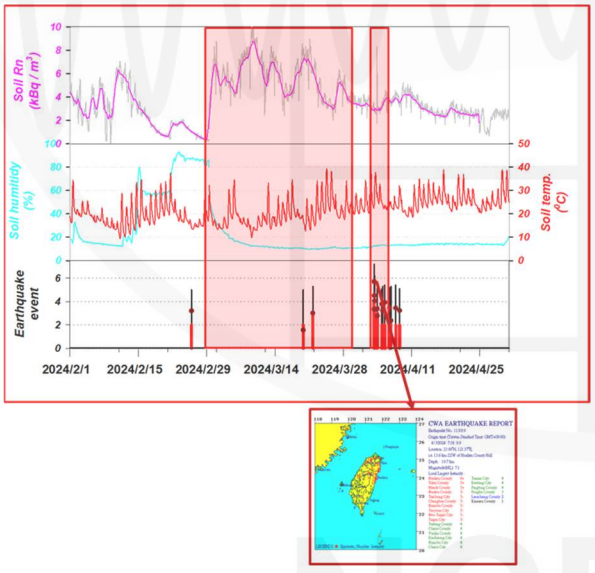

Fig. 6. Radon monitoring data at the Qingshui Station along with other parameters from February 1 to April 30, 2024. Red boxes represent probable precursory anomalies.

Our soil radon monitoring network found strong correlations between radon anomalies and seismic events during the April 2024 Hualien earthquake sequences. Four stations (SJ, JS, QS, and HC) showed precursory signals simultaneously, confirming radon's potential as a predictive indicator. JS and QS displayed especially notable trends, while SJ and HC maintained high radon levels after the earthquake, suggesting ongoing tectonic stress. Hsinhua station (HH) showed no clear signal, indicating spatial variation in radon responses.

These findings highlight the need to expand real-time monitoring and integrate high-sensitivity stations into prediction models. Continuous data collection and verification across multiple stations help distinguish between noise and genuine precursory patterns. Current rising trends at several stations may indicate potential aftershocks or continued seismic activity, requiring careful monitoring. Improving the D/R model, data quality, and sensor placement will be essential for enhancing earthquake early warning systems in Taiwan and similar regions.

References

Arora, B.R., Kumar, A., Walia, V., Yang, T-F., Fu, C-C., Liu, T-K., Wen, K-L., Chen C-H., Cleaning Soil-gas Radon at Hsinchu, Taiwan for Contamination from Meteorological and Hydrological Parameters: A Step Forward to Identify Earthquake Precursors. J Asian Earth Sci 149:49-63, 2017.

Cheloni, D., Famiglietti, N. A., Caputo, R., Tolomei, C., Vicari, A., A composite fault model for the 2024MW 7.4 Hualien earthquake sequence in eastern Taiwan inferred from GNSS and InSAR data. Geophysical Research Letters, 51, e2024GL110255. https://doi.org/10.1029/ 2024GL110255, 2024.

Dobrovolsky, I.P., Zubkov, S.I., Miachkin, V.I., Estimation of the size of earthquake preparation zones: Pure and Applied Geophysics PAGEOPH, 117, p. 1025–1044, doi: 10.1007/BF00876083, 1979.

Fu, C.C., Lee, L.C., Yang, T.F., Lin, C.H., Chen, C.H., Walia, V., Liu, T.K., Ouzounov, D., Giuliani, G., Lai, T.H., Wang, P.K. and Wang, Y., 2019. Gamma ray and Radon anomalies in Northern Taiwan as a possible preearthquake indicator around the plate boundary: Geofluids, 2019, doi: 10.1155/2019/4734513

Hsu, Y.-J., Yu, S.-B., Simons, M., Kuo, L.-C., Chen, H.-Y. Interseismic crustal deformation in the Taiwan plate boundary zone revealed by GPS observations, seismicity, and earthquake focal mechanisms. Tectonophysics, 479(1–2), 4–18. https://doi.org/10.1016/j.tecto.2008.11.016, 2009.

Kumar, A., Walia, V., Lin, S-J., Fu. C-C., Real-time database for geochemical earthquake precursory research. Natural Hazards 104: 1359-1369, 2020.

Igarashi, G., Saeki, S., Takahata, N., Sumikawa, K., Tasaka, S., Sasaki, Y., Takahashi, M., Sano, Y., Ground-water radon anomaly before the kobe earthquake in Japan: Science, 269, p. 60–61, doi: 10.1126/science.269.5220.60, 1995.

Virk, H.S., Walia, V., Helium/radon precursory signals of Chamoli Earthquake, India: Radiation Measurements, 34, p. 379–384, doi: 10.1016/S1350-4487(01)00190-1, 2001.

Yang, T.F., Fu, C. C., Walia V., Seismo-geochemical variations in SW Taiwan: multi-parameter automatic gas monitoring results, Pure and Applied Geophysics, 163(4)693–709, 2006.

Walia, V., Yang, T-F, Lin, S-J., Kumar, A., Fu, C-C., Chiu, J-M., Chang, H-H., Wen, K-L., Chen, C-H., Temporal variation of soil gas compositions for earthquake surveillance in Taiwan. Radiat Meas 50:154–159, 2013.

Field Inspection of Buildings after the M_L 7.2 Hualien Earthquake of April 3, 2024

Ming-Chieh Chuang[1], Jui-Liang Lin[2], Kai-Ning Chi[3], Gee-Jin Yu[4], Huang-Zuo Lin[5], An-Chien Wu[1], Chung-Chun Ma[6], and Bai-Yi Huang[7]

莊明介[1]、林瑞良[2]、紀凱甯[3]、於積瑨[4]、林皇佐[5]、
吳安傑[1]、馬忠駿[6]、黃百誼[7]

Abstract

At 7:58 a.m. on April 3, 2024, Taiwan time, an earthquake with a magnitude of ML 7.2 struck Shoufeng Township, Hualien County, marking the largest earthquake in Taiwan since the 921 earthquake in 1999. Due to continuous aftershocks, strong tremors of magnitude 6.0 and 6.3 occurred in the early morning of April 23, 2024, Taiwan time, which exacerbated seismic damage and caused the collapse of many buildings. To assess the damage to buildings in Hualien after the major earthquake and its continuous strong aftershocks, as well as the progress of post-disaster recovery, researchers from the National Earthquake Engineering Research Center (NCREE) visited the Hualien area in early May 2024. They collaborated with experts and scholars from Mexico, Canada, and Taiwan to investigate the seismic damage. At the end of May 2024, NCREE researchers, along with experts from the Earthquake Engineering Research Institute in the USA and the New Zealand Society for Earthquake Engineering, traveled to Hualien to survey the damaged buildings, meet with officials from the Hualien County Government, and learn about local post-disaster recovery efforts. The research team collected relevant information through a seismic damage survey of buildings impacted by the April 3 Hualien earthquake to understand the causes of building damage and the challenges of post-disaster recovery.

Keywords: Field Inspection, damaged buildings, retrofit, collapse

Introduction

On April 3, 2024, at 7:58:09 a.m. Taiwan time, an earthquake with a Richter magnitude of M_L 7.2 (referred to as the 0403 Hualien earthquake) struck Shoufeng Township, Hualien County (Fig. 1) [CWA, 2024]. This earthquake is the largest to hit Taiwan since the Chi-Chi earthquake (921 earthquake) in 1999. The seismic intensity in Heping Village, Xiulin Township, reached 6+, while Hualien City and Taroko reported intensities of 6-. The 0403 Hualien earthquake caused structural damage to many buildings in Hualien, and aftershocks persisted. On April 23, 2024, at 2:26 a.m. and 2:32 a.m. Taiwan time, strong aftershocks measuring 6.0 and 6.3 on the Richter scale occurred, respectively, with the maximum seismic intensity in the Hualien area reaching 5 weak. These aftershocks exacerbated the damage to many buildings, leading to even collapses. According to statistics from the Hualien County Government [Hualien County Government, 2024], as of June 5, 2024, there were 90 red-tagged and 89 yellow-tagged buildings in Hualien.

To assess the damage to buildings in the Hualien area after the 0403 Hualien earthquake and its continuous and strong aftershocks, as well as to evaluate the progress of post-disaster recovery, an international survey team named Team S (S for “Stick together”) was formed. This team consisted of researchers from the National Center for Earthquake

[1] Associate Researcher, National Center for Research on Earthquake Engineering
[2] Division Director, Building Engineering Division, National Center for Research on Earthquake Engineering
[3] Assistant Researcher, National Center for Research on Earthquake Engineering
[4] Associate Technologist, National Center for Research on Earthquake Engineering
[5] Research Assistant, National Center for Research on Earthquake Engineering
[6] Former Research Assistant, National Center for Research on Earthquake Engineering
[7] Assistant Researcher, National Center for Research on Earthquake Engineering

Engineering of the National Institute of Experimental Research (NCREE), five scholars from the Mexican Society of Earthquake Engineering, Prof. David Lau from Carleton University in Canada, and several industry experts and scholars in structural engineering from Taiwan. The team visited damaged buildings in the Hualien area between May 8 and May 11, 2024, to study the effects of the earthquake and examples of building reinforcement and earthquake resistance (Fig. 2).

About two months after the 0403 Hualien earthquake, researchers from the NCREE collaborated with four scholars from the Earthquake Engineering Research Institute (EERI) in the USA and seven scholars from the New Zealand Society for Earthquake Engineering (NZSEE) from May 27 to June 1, 2024. They visited the Construction Department of Hualien County Government (Fig. 3) and inspected several buildings in the Hualien area to assess damage and the demolition progress of hazardous structures, as well as to observe follow-up disposal and post-disaster recovery effort. During this survey, the team examined a building retrofitted with buckling-restrained braces developed by the NCREE [Tsai et al., 2014] (Fig. 4) and conducted in-depth visits to many buildings in the Hualien area that either sustained no damage to their main structures, experienced only slight damage to structural components, or had partially damaged non-structural elements. This survey aimed to evaluate the effectiveness of seismic retrofitting and to review the repair and recovery plans for buildings damaged by the 0403 earthquake.

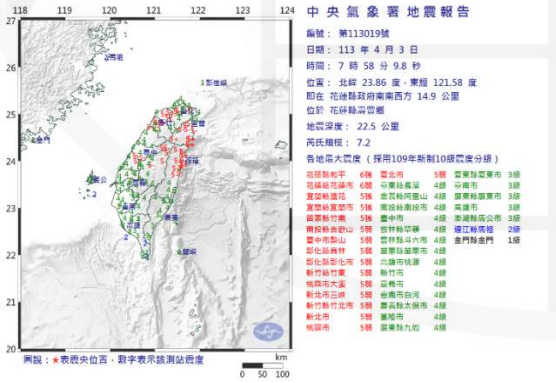

Fig. 1. 0403 Hualien Earthquake Information from the Central Weather Administration (CWA)

Fig. 2. Team S visited a retrofitted building

Fig. 3. NCREE-EERI-NZSEE team visited the Construction Department of Hualien County Government

Fig. 4. NCREE-EERI-NZSEE team visited a retrofitted building

Reconnaissance and Observations

As shown in Fig. 5, the survey included buildings with different functions, such as residential buildings, commercial establishments (e.g., hotels, restaurants), mixed residential and commercial buildings, school buildings, and hospitals. The subjects covered buildings with different damage conditions, such as undamaged, minor damage, and severe damage, as well as structures that remained intact but lost functionality due to damage to non-structural components. In addition, the survey highlighted several examples of buildings that successfully withstood seismic events after retrofitting, which demonstrate the effectiveness of the Taiwan government's policies in promoting the seismic performance evaluation, improvement, and retrofitting of old buildings. The survey also examined numerous buildings that incorporated new earthquake-resistant technologies, such as buildings with seismic control elements or seismic isolation systems, to understand their seismic effectiveness.

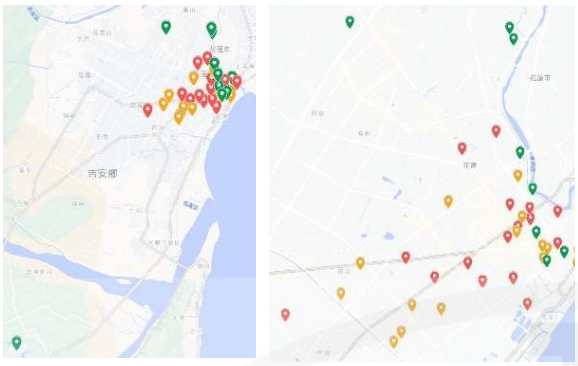

(a) Hualien area (b) Hualien City and Ji'an Township

Fig. 5. Survey and Location Distribution Diagram (Credit: Google map)

The collapsed buildings and most of the red-tagged buildings identified by the survey team were constructed before 1999 and were not retrofitted. Consequently, the reinforcement detailing of these buildings clearly does not meet the seismic requirements of the current code (e.g., transverse steel bar spacing, seismic hooks). In addition, the poor configuration of the building's structural system (e.g., high ceilings on the first floor, an insufficient number of columns and walls on the lower floors) makes them prone to weak ground floor formation, which can lead to severe earthquake damage or collapse.

A four-story reinforced concrete (RC) street building (Fig. 6) is a common "triangular configuration," which has the potential for seismic torsion due to its irregular structure. The first floor contains a storefront with large windows to accommodate business needs. After the 0403 Hualien earthquake, the building was initially assessed as yellow-tagged, but after a series of aftershocks, it was later classified as red-tagged on May 3. An inspection of the building's exterior (Fig. 6(a)) shows that the structural damage is concentrated on the first floor, with noticeable failure at the base of the column (Fig. 6(b)). However, the structure from the second to fourth floors appears quite intact, indicating that the building has an irregular design with a weak ground floor. In addition, the structural damage exposes certain blind spots in the quality of early construction (e.g., concrete quality control, rebar splicing), which are noteworthy factors to consider when assessing the seismic resistance of existing buildings from the early construction period.

(a) Exterior of the building (b) Cracking of concrete at the base of the column

Fig. 6. Red-tagged Four-story RC Building

In addition, it is worth noting that the buildings that collapsed or were severely damaged in the 0403 Hualien earthquake had all previously experienced the 0206 Hualien earthquake in 2018. This indicates that the structural system, construction method, dynamic characteristics, and seismic characteristics of these buildings are closely related to their seismic response. Therefore, the seismic resistance of older buildings should be properly assessed, and appropriate reinforcements should be implemented.

During the field inspection, the team visited several retrofitted buildings, five of which were private. Among these, three were general residential buildings, and two were commercial buildings. None of the main structures of the retrofitted buildings inspected by the team showed significant damage, and there were no red or yellow notices posted. This highlights the importance of proactive measures taken by building owners to improve the seismic performance of the structures and demonstrates the effectiveness of seismic retrofitting of buildings.

Conclusions

Researchers from NCREE, along with scholars from the Mexican Society of Earthquake Engineering, have jointly published a reconnaissance report on the 0403 Hualien earthquake [Lin et al., 2024] through the EERI website to share the observations from the field inspection. The main cause of the seismic damage to buildings during the 0403 Hualien earthquake remains the existing problems of poor structural systems and inadequate earthquake resistance. Consequently, related structural safety concerns require ongoing attention from the government. The NCREE research team mourns the victims of the 0403 Hualien earthquake and offers prayers for the missing, injured, and victims who were facing challenges related to housing reinforcement and reconstruction. At the same time, we look forward to the collaborative efforts of government authorities, professional organizations, and the public in developing a more comprehensive post-earthquake recovery plan to prepare for the challenges of future earthquakes.

References

Central Weather Administration (CWA)，(2024)，0403 Hualien Earthquake Report https://www.cwa.gov.tw/

Hualien County Government, (2024), Website of 0403 Hualien Earthquake Information https://www.hl.gov.tw/0403/News_Content.aspx?n=34577&s=159206 (retrieved on 2024/06/05)

Tsai, K.C., Wu, A.C., Wei, C.Y., Lin, P.C., Chuang, M.C., and Yu, Y.J., (2014), "Welded end-slot connection and debonding layers for buckling-restrained braces", Earthquake Engineering & Structural Dynamics, 43(12), 1785-1807.

Lin et al., (2024), EERI Earthquake Reconnaissance Report: ML 7.2 Earthquake of April 3, 2024 in Hualien, Taiwan – Prepared by the National Center for Research on Earthquake Engineering & the Mexican Society of Earthquake Engineering (https://learningfromearthquakes.org/earthquakes/hualien-city-taiwan/)

Infrasound Monitoring of the Tatun Volcano Group

Min-Hung Shih [1], Ya-Chuan Lai[2], Cheng-Horng Lin[3]

史旻弘[1]、賴雅娟[2]、林正洪[3]

Abstract

The Tatun Volcano Group, located north of the Taipei metropolitan area, has been identified as hosting active hydrothermal systems or deeper magmatic processes. Consequently, monitoring volcanic activity in this region is critical for safeguarding the Taipei metropolitan area. In this study, we established a high-density real-time infrasound monitoring system at two major fumaroles, Dayoukeng and Shiaoyoukeng. Each site was equipped with six stations configured in a circular network, enabling continuous recording of acoustic signals generated by fumarole activity by utilizing the low-frequency characteristics of infrasound waves. The monitoring system deployed in this project integrates high-precision sensors, specialized data loggers, custom-designed wind filters, and Band 20 communication frequency band, overcoming the challenges associated with equipment installation and data transmission. Approximately 11 kilometers of fiber-optic network were constructed to facilitate real-time data transmission back to the monitoring center. Furthermore, automatic signal recognition was implemented using the YOLOv9 deep learning model. The deployment of this dense infrasound monitoring system significantly enhances the ability to characterize fumarole activity at Shiaoyoukeng and Dayoukeng. It provides critical datasets for understanding infrasound signals and offers new perspectives for volcanic surveillance.

Keywords: Tatun Volcano Group, volcano monitoring, fumarole, infrasound

Introduction

The Tatun Volcano Group (TVG), located in northern Taiwan, lies adjacent to the densely populated Taipei urban area, encompassing approximately one-third of Taiwan's population as well as critical political and economic centers. Previous studies and ongoing monitoring efforts have revealed the existence of an active hydrothermal system beneath the TVG, and the presence of a magma reservoir has been inferred (Huang et al., 2021; Lin, 2016). These findings indicate that the possibility of future volcano activity cannot be excluded. In particular, the sudden phreatic eruption at Mount Ontake, Japan, in 2014, which caused significant casualties (Kaneko et al., 2016), underscored the urgent need for real-time monitoring of volcanic phreatic eruptions and highlighted the latent risk of similar events at the TVG.

In this study, a high-density real-time infrasound monitoring network at the two most active fumaroles within the TVG—Dayoukeng and Shiaoyoukeng is established. Infrasound, characterized by frequencies below 20 Hz and thus inaudible to the human ear, possess long propagation distances and strong penetrative capability, making them particularly suitable for environmental monitoring in volcanic areas. Various volcanic sources, including eruptions, pyroclastic flows, and lahars, can be effectively detected by infrasound sensors (Johnson & Ripepe, 2011). In steaming regions, vigorous gas emissions generate air vibrations that produce distinctive acoustic signals, allowing infrasound monitoring to capture the activity characteristics and intensity variations of gas emissions. This infrasound offers real-time, reliable data that enhances the comprehensive understanding of volcano activity and improves the effectiveness of eruption early warning systems.

By integrating high-precision sensors, stable transmission, and innovative artificial intelligence,

[1] Research Fellow, National Center for Research on Earthquake Engineering
[2] Assistant Researcher, National Center for Research on Earthquake Engineering
[3] Research Fellow, Inst. of Earth Sciences, Academia Sinica

this study aims to achieve automated, accurate recognition and classification of various volcanic activity signals. The establishment of this high-performance monitoring and early warning system will promote advancements and innovation in the field of volcano monitoring.

Infrasound Monitoring Network

To effectively capture the real-time activity of fumaroles within the TVG, the dense, ring-shaped infrasound monitoring networks are established individually at Shiaoyoukeng and Dayoukeng. Each network hosts six infrasound stations arranged to ensure comprehensive recording and monitoring capabilities from multiple directions. Station locations were selected based on spatial distribution, topographic and environmental conditions, and operational feasibility to ensure complete coverage of fumarole (Figure 1). This network configuration ensures signal integrity and enables precise spatial characterization of gas emissions, enhancing the capability to assess potential phreatic eruption hazards. The circular arrangement allows the research team to effectively capture infrasound signals from different directions, enabling real-time analysis of intensity of gas emissions, frequency of activity and spatial variations. These data complement seismic and geochemical observations, providing a more comprehensive volcanic monitoring system.

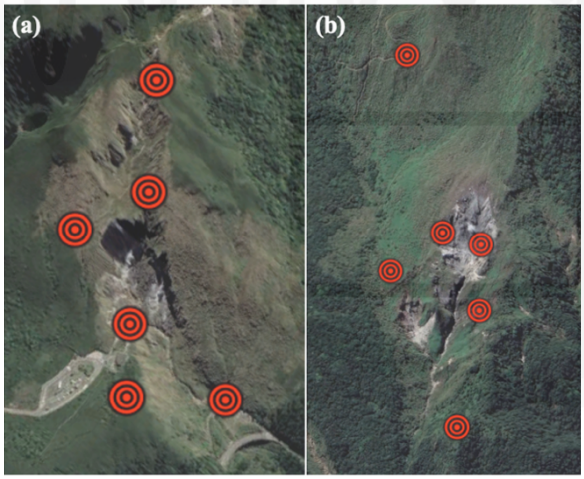

Fig. 1. Layout of the (a) Shiaoyoukeng and (b) Dayoukeng infrasound network

Each infrasound monitoring station integrates a Chaparral M60 sensor (0.03–240 Hz), a DATA-CUBE3ext recorder with GPS timing, and a Raspberry Pi 4 microcomputer for real-time data conversion into MiniSEED format. A redesigned circular PVC wind filter minimizes environmental noise. Data transmission is supported by Alfa Network Tube-E4G routers utilizing Band 20 technology, while solar-powered systems ensure stable operation in remote areas, enabling continuous, real-time volcanic monitoring.

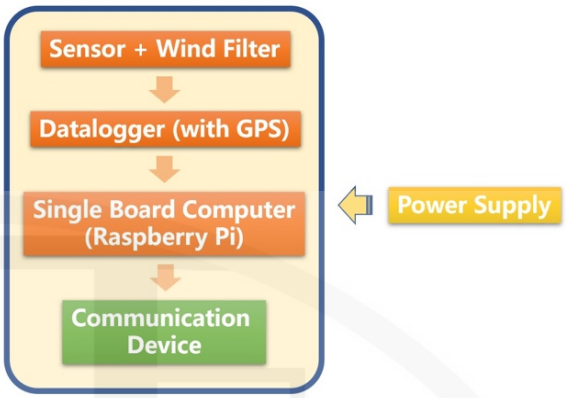

Fig. 2. Schematic diagram of the infrasound station

A major challenge in establishing the TVG monitoring system was securing stable, real-time, and secure data transmission. This project adopted a dual communication approach to address this challenge. In collaboration with the National Center for High-Performance Computing (NCHC), approximately 3 kilometers and 8 kilometers of fiber-optic backbone networks were installed for Shiaoyoukeng and Dayoukeng, respectively. Cables were surface-laid with environmental-friendly techniques and reinforced with steel rods to withstand weather changes and wildlife activities. The Dayoukeng section, from Qingtiangang to the vent, presented significant construction challenges due to steep terrain.

To address the coverage limitations of fiber-optic networks in areas with complex topography, this project also implemented the experimental communication frequency band, called Band 20, to bridge the connection between the fiber backbone and remote monitoring stations. Small cells of Band 20 were established at both the Dayoukeng and Shiaoyoukeng, enabling real-time data transmission through 4G communication systems to the nearby stations. The Band 20 frequency band provides a private and isolated network environment, enhancing data security by reducing the risk of signal interference or interception during transmission. By integrating fiber-optic and Band 20 transmission, a robust and reliable communication infrastructure was established for the infrasound monitoring networks at the two major fumaroles. This hybrid system significantly improves the real-time performance and reliability of volcanic activity monitoring.

Data Collection

Analysis of data collection across the 2024 monitoring period revealed notable differences between the two networks, reflecting distinct environmental and technical challenges. The

Shiaoyoukeng network achieved an average annual data acquisition rate exceeding 90%, with some stations reaching up to 98%, demonstrating the effectiveness of system design and equipment deployment. However, some stations exhibited seasonal outages during winter, likely due to reduced solar power efficiency and increased equipment moisture during the rainy season. Occasional equipment failures and maintenance demands further highlighted the importance of routine management in mountain areas. Band 20 communication stability was also found to be affected under bad weather conditions.

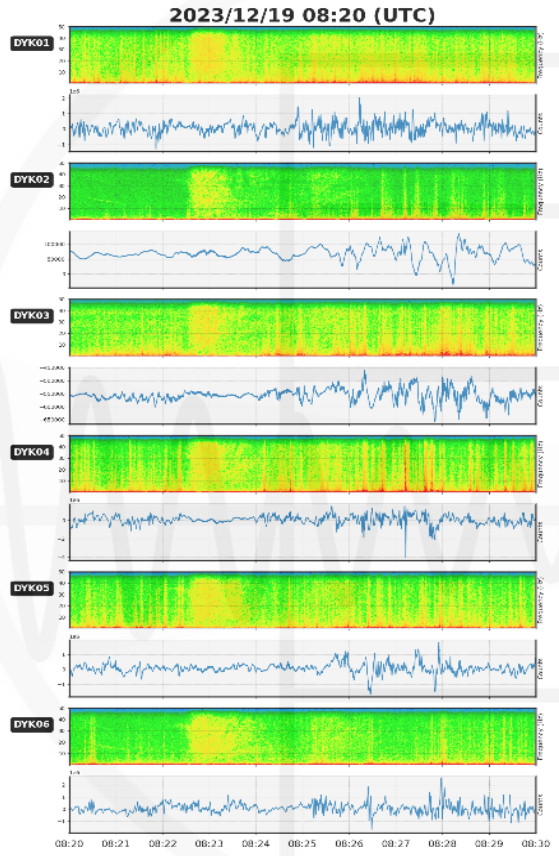

Fig. 3. Example of infrasound waveforms recorded at Dayoukeng and the corresponding spectrograms.

In contrast, the Dayoukeng network faced more severe challenges, achieving an overall data acquisition rate of approximately 87%. While some individual stations performed steadily (up to 95%), others suffered prolonged data interruptions caused by topographical relief, heavy rainfall, and dense fog, again likely exacerbated by reduced solar efficiency during winter time. Overall, future improvements should focus on enhancing transmission stability, reinforcing auxiliary power supply systems to mitigate seasonal environmental impacts, and strengthening routine maintenance efforts. These enhancements will ensure better data continuity and monitoring effectiveness, thereby advancing real-time volcanic monitoring and early warning capabilities.

Application of Artificial Intelligence

To enhance the efficiency of volcanic signal identification, this project applied artificial intelligence techniques to the analysis of infrasound data. The latest YOLOv9 deep learning model (Wang et al., 2024) was adopted to perform rapid, accurate real-time classification of infrasound events. Infrasound signals were converted into spectrograms and labeled into four categories, which are Bar, Wave, Curve, and Trapezoid, selected through manual experience. A standardized dataset containing 836 images and 1,153 labeled events was established for model training and validation.

Testing results showed that the YOLOv9 model achieved excellent performance, with an average precision of 0.967 for Bar-type signals and an overall precision of approximately 0.898 (Figure 4). The model processed each image within approximately 41.5 ms, achieving a throughput of about 24 images per second, sufficient for real-time monitoring applications. Compared with traditional methods, this AI model enables faster and more accurate identification of volcanic infrasound signals, providing powerful technical support for scientific research and disaster early warning systems.

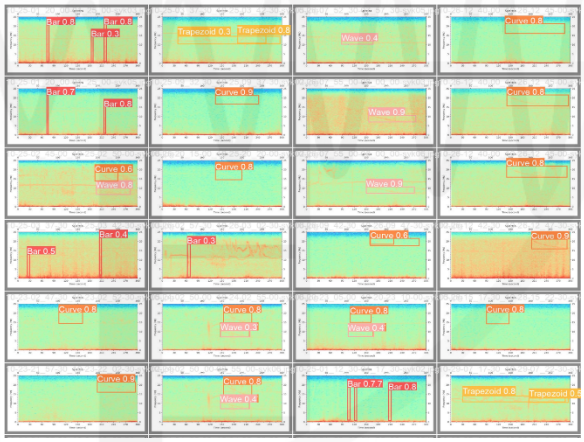

Fig. 4. Detection results of signal classification using the deep learning model

Outcomes and Future Prospects

Through the establishment of a high-density, real-time infrasound monitoring network, this project successfully conducted continuous observations at the most active fumaroles of the TVG and acquired a substantial volume of high-quality monitoring data. A standardized volcanic infrasound dataset, which is the first of its kind in Taiwan, was developed. The incorporation of AI-based analysis using the YOLOv9 deep learning model resulted in an automatic recognition system achieving 89.8% classification accuracy and processing 24 spectrograms per second, greatly enhancing volcanic activity monitoring

efficiency.

Moreover, the project overcame significant challenges related to communication and power supply in mountain regions, establishing a stable and efficient data transmission network through the integration of Band 20 systems and more than 11 kilometers of fiber-optic cabling. Innovative wind filter designs significantly improved data reliability by reducing environmental noise. Looking forward, this project provides valuable tools for research and enhances volcanic monitoring and hazard mitigation. The developed technologies and workflows can also be adapted to similar volcanic regions through international collaboration.

References

Huang, HH., Wu, ES., Lin, C.H., Ko, J. Y.-T., Shih M.H., Koulakov, I., (2021). Unveiling Tatun volcanic plumbing structure induced by post-collisional extension of Taiwan mountain belt. Scientific Reports, 11, 5286.

Kaneko, T., Maeno, F. & Nakada, S., (2016) . 2014 Mount Ontake eruption: characteristics of the phreatic eruption as inferred from aerial observations. Earth Planet Sp 68, 72.

Lin, C.H., (2016). Evidence for a magma reservoir beneath the Taipei metropolis of Taiwan from both S-wave shadows and P-wave delay, Scientific Reports, Vol. 6, 39500.

Wang, C.Y., Yeh, I.H., & Liao, H.Y.M., (2024). YOLOv9: Learning What You Want to Learn Using Programmable Gradient Information. arXiv preprint arXiv:2402.13616.

Application of Soil Gas Monitoring in the Tatun Volcano Group, Taiwan

Hsiao-fen Lee[1] and Jing-Sin Liu[2]

李曉芬[1]、劉進興[2]

Abstract

The Tatun Volcano Group (TVG) is an active volcanic system located approximately 15 km north of metropolitan Taipei. Two nuclear power plants are also situated a few kilometers northeast of the TVG, making careful monitoring of volcanic activity essential for residents in northern Taiwan. Over the past decade, fumarolic gas samples have been regularly collected to track variations in chemical compositions and helium isotope ratios. The results suggest that volcanic activity at the TVG has remained stable. However, following an M_L 4.2 earthquake on February 12, 2014, hydrogen chloride (HCl) concentrations increased significantly in gas emissions from several fumaroles in the study area. This distinctive response provides useful information for establishing a detailed model of the TVG's hydrothermal system. These data help fill a gap in the current understanding of the TVG and offer crucial insights for evaluating the tectonic settings of northern Taiwan.

Keywords: Tatun Volcanic Group, soil CO_2 flux.

1. Introduction

Taiwan is located at the complex convergent boundary between the Eurasian Plate and the Philippine Sea Plate, resulting in a highly active and structurally complex geological setting. The Tatun Volcano Group (TVG), situated in northern Taiwan and covering approximately 250 km², has long been a focus of discussion regarding its volcanic activity. Multiple lines of geophysical and geochemical evidence support the hypothesis that the TVG remains active. Helium isotope analyses of fumarolic gases reveal that over 60% of the helium originates from a mantle-derived source, suggesting the presence of a deep-seated magma reservoir beneath northern Taiwan. In addition, microseismicity in the region implies ongoing fluid or magmatic movement. Primary volcanic ash layers found in sediment cores from the Taipei Basin have been attributed to past eruptions of the TVG, with stratigraphic evidence pointing to an eruption less than 20,000 years ago. Fresh volcanic ash discovered on the slopes of Mt. Chihsing has further revised this estimate to approximately 6,000 years ago. Seismic tomography conducted by Lin (2016) also identified a possible magma reservoir at a depth of around 20 km beneath the northeastern sector of the volcanic group. Together, these findings provide compelling evidence that the TVG should be considered an active volcanic system.

Volcanic gases are critical indicators of subsurface magmatic processes, and long-term gas monitoring plays a key role in assessing volcanic activity and forecasting potential eruptions. In addition to direct sampling from fumaroles, volcanic gases also diffuse through the surrounding soil and are released into the atmosphere. These soil gas emissions reflect changes in subsurface stress and fluid migration, with concentrations of carbon dioxide and sulfur compounds typically increasing with elevated volcanic activity.

Compared to intermittent manual sampling, continuous soil gas monitoring provides stable, real-time data acquisition with improved operational safety. Commonly monitored gases include carbon dioxide (CO_2) and radon (Rn). CO_2 is primarily released from deep magmatic sources and can migrate efficiently through rock fractures and soil pores. Radon, a

[1] Associate Researcher, National Center for Research on Earthquake Engineering

[2] Project Research Assistant, National Center for Research on Earthquake Engineering

radioactive gas produced by the decay of radium, is highly sensitive to recent geodynamic changes due to its short half-life, and is frequently used in both fault and volcanic monitoring.

In this study, two automated soil gas monitoring stations were established in the TVG: one in the Ba-yan hydrothermal area (BY) and another in the Siao-you-keng hydrothermal area (SYK). The monitoring system employs the closed-chamber method to continuously measure CO_2 and Rn fluxes, alongside environmental sensors that record soil temperature, humidity, and rainfall. These supplementary data help distinguish volcanic signals from environmental noise, thereby enhancing the reliability and interpretability of long-term geochemical monitoring results.

2. Methods

For CO_2 monitoring, this study employed the closed-chamber method developed by Chiodini *et al.* (1998) to estimate soil CO_2 fluxes in volcanic areas. In this method, a sealed chamber is placed over the soil surface, and the rate at which CO_2 concentration increases inside the chamber is measured to calculate the gas flux emitted from the soil to the atmosphere over time.

The system consists of three main components:

(1) a closed-loop accumulation chamber,

(2) a CO_2 analyzer, and

(3) a data acquisition and control unit (computer or data logger).

The CO_2 analyzer (Edinburgh Instruments, UK) employs non-dispersive infrared (NDIR) spectroscopy to detect CO_2 concentrations with high sensitivity and stability. The chamber has an internal volume of approximately 6.2×10^{-3} m³ and is equipped with inlet and outlet ports that connect to the CO_2 analyzer, forming a closed gas circulation loop. A small fan inside the chamber ensures homogenous mixing of CO_2 and air, preventing stratification and improving measurement accuracy. To maintain pressure equilibrium between the inside and outside of the chamber, a capillary vent is installed on top. Additionally, desiccant is used in the inlet tubing to minimize moisture interference with the gas analyzer.

During operation, the monitoring system initiates a reset cycle at the start of each hour by activating an electric pump to flush the chamber and lower the internal CO_2 concentration. A new accumulation cycle then begins, with the system automatically recording the CO_2 concentration over time. The rate of increase (slope in parts per million per second) is used to calculate the hourly CO_2 flux.

The locations and internal configurations of the monitoring stations are shown in Figures 1 and 2.

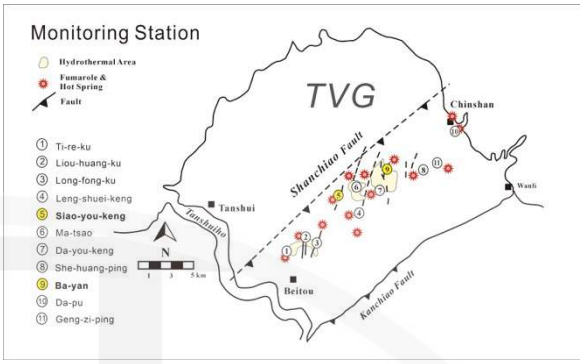

Fig. 1. Distribution of major hydrothermal areas and fumaroles in the TVG. Yellow circles indicate soil gas flux monitoring stations at SYK (5) and BY (9). Red asterisks mark fumaroles and hot springs, and pale yellow areas denote active hydrothermal zones. The dashed line indicates the trace of the Shanchiao Fault.

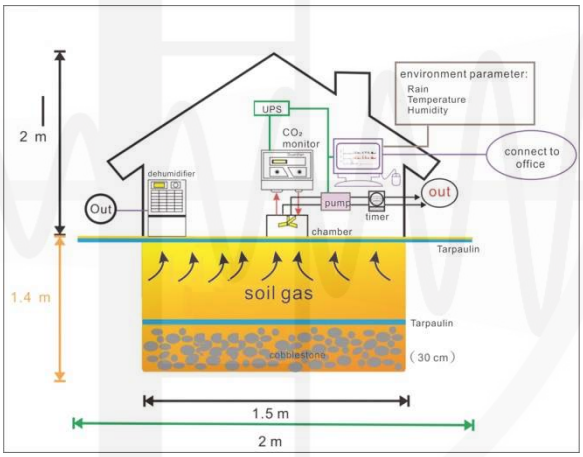

Fig. 2. Schematic diagram of the internal configuration of the continuous soil-gas monitoring station.

3. Results and Discussion

This study conducted long-term soil CO_2 flux monitoring at two sites in the TVG: BY and SYK. Statistical analysis of data from 2014 to 2025 reveals an overall stable trend, though several notable high-flux anomalies were identified. These anomalies warrant further investigation into their underlying mechanisms and spatiotemporal characteristics.

3.1 Ba-yan Area

Figure 3 shows the monthly time series of CO_2 flux at the BY monitoring station from 2014 onward, presented as box-and-whisker plots. A distinct high-flux plateau occurred from mid-to-late 2016, during

which monthly medians approached or exceeded the defined outlier threshold (990 g/m²/day), and the number of outliers increased significantly. This anomaly is likely related to the M_L 4.2 earthquake that struck the Shilin District of Taipei on February 12, 2014— the largest seismic event in the TVG area in the past decade. The earthquake may have induced shallow structural disturbances and fault weakening, creating upward migration pathways for deep CO_2 and resulting in significantly increased surface emissions after a delay of 1–2 years.

From 2017 to 2020, CO_2 flux at BY gradually returned to a stable, moderate-to-low level. Although short-term increases were observed in early 2021 and between March and April 2025 (*e.g.*, June 2021, and March–April 2025), most of these did not exceed the outlier threshold and are therefore presumed to be driven by localized environmental factors such as rainfall, temperature, or variations in surface heat flow.

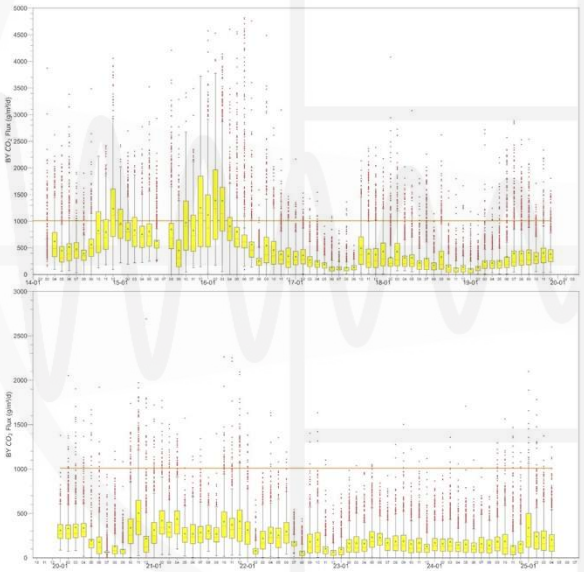

Fig. 3. Box-and-whisker plots of CO_2 fluxes (g/m²/d) at the BY station from 2014 to 2025. The upper panel shows data from 2014 to 2019; the lower panel shows data from 2020 to 2025. Each box represents the monthly distribution of flux values, including the median, interquartile range (IQR), and outliers. The orange horizontal line indicates the upper threshold for anomalies (990 g/m²/day). The anomalously high flux plateau in 2016 is prominent and likely linked to post-seismic deep fluid migration following the 2014 Shilin earthquake.

3.2 Siao-you-keng Area

Figure 4 presents the monthly soil CO_2 flux variations at the SYK monitoring station from 2014 to 2025. Similar to the BY site, SYK exhibited a significant increase in CO_2 flux from mid-2015 to early 2016, marked by elevated median values and a higher frequency of outliers, with several months exceeding the station's established threshold (129 g/m²/day). Although this anomaly occurred slightly later than at BY, it may reflect differences in local geothermal intensity, soil permeability, or subsurface gas pathways. Nonetheless, the data also support the hypothesis that the increase was triggered by deep fluid migration toward the surface following the 2014 earthquake.

Between 2020 and 2024, SYK experienced multiple short-term increases in CO_2 flux (*e.g.*, June–July 2020, May–June 2021, April 2022, March–May 2023, and March 2024), each accompanied by a significant rise in outlier frequency. Although these events did not form an extended high-flux plateau, they suggest intermittent volcanic gas release. These short-lived anomalies may reflect pulsed gas transport from depth or episodic activation of shallow gas conduits. Their seasonal clustering—mostly in spring and early summer—also suggests influence from surface environmental factors such as rainfall, groundwater variation, or shallow heat-flow dynamics.

Additional multi-parameter observations support this interpretation. Since 2018, fumarolic emissions have shown increased concentrations of hydrogen chloride (HCl) and helium (He), along with sharp rises in cation concentrations in nearby hot springs—indicators of enhanced magmatic-hydrothermal activity. Concurrently, the TVG has experienced intensified seismicity, including several earthquakes exceeding magnitude 3. In 2021, GNSS monitoring also recorded significant vertical displacement in the main geothermal area. Episodes of localized mud ejections have also been reported. These geochemical and geophysical anomalies partially overlap with the intermittent high CO_2 fluxes observed at SYK. While SYK has not experienced a sustained high-flux phase, the recurrence of outlier events and supporting multi-source data suggest it may have undergone phases of transient instability driven by subsurface pressure changes and fluctuating gas pathway dynamics.

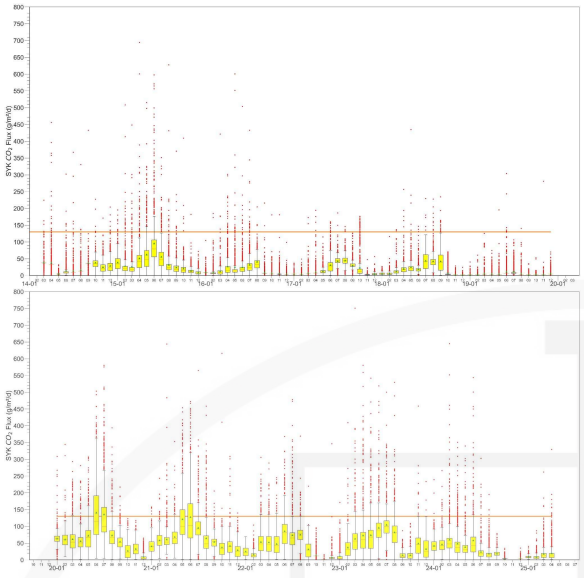

Fig. 4. Time series of soil CO_2 flux at SYK from 2014 to 2025. The upper panel shows data from 2014 to 2019; the lower panel shows data from 2020 to 2025. Each box-and-whisker plot represents the monthly distribution of flux values, including the median, IQR, and outliers. The orange horizontal line indicates the anomaly threshold defined by the IQR method (Q3 + 1.5 × IQR; threshold = 129 g/m²/day). Multiple high-flux events are observed during 2015–2016 and after 2020, with a notable increase in anomaly frequency in recent years, suggesting sustained changes in volcanic degassing activity.

4. Conclusions

This study conducted long-term soil CO_2 flux monitoring at two sites—BY and SYK—within the TVG from 2014 to 2025. While the overall trends remained relatively stable, several high-flux anomalies were identified, each displaying distinct temporal and spatial characteristics.

At the BY site, a pronounced high-flux plateau in 2016 may be linked to the M_L 4.2 Shilin earthquake in 2014, which likely enhanced deep fluid migration. In contrast, the SYK site exhibited a two-phase anomaly: one occurring around 2015–2016 and another after 2020, marked by recurrent short-term spikes, increased outlier frequencies, and intensified volatility. These flux anomalies partially coincided with multiple geophysical and geochemical indicators, including increases in HCl and helium concentrations in fumaroles, sharp cation rises in hot springs, elevated seismicity, localized mud ejections, and vertical displacement recorded by GNSS. Together, these observations suggest that the TVG may have experienced transient episodes of unrest, resulting in enhanced volcanic gas emissions.

In conclusion, soil CO_2 flux monitoring provides critical insight into shallow degassing processes in volcanic systems. Integrating such data with seismic, deformation, and isotopic observations will be essential for improving assessments of the TVG's activity and potential future hazards.

References

Lin, C.H. (2016) Evidence for a magma reservoir beneath the Taipei metropolis of Taiwan from both S-wave shadows and P-wave delays, Scientific Reports, 6, 39500.

Chiodini, G., Cioni, R., Guidi, M., Raco, B., & Marini, L. (1998). Soil CO_2 flux measurements in volcanic and geothermal areas. Applied Geochemistry, 13(5), 543–552.

A Real-time Monitoring Framework for Seismic Activity in the Chianan Region

Yu-Chih Huang[1], Strong Wen[2], Da-Yi Chen[3], Che-Min Lin[4], Wen-Tzong Liang[5], Chih-Wei Chang[6]

黃有志[1]、温士忠[2]、陳達毅[3]、林哲民[4]、梁文宗[5]、張志偉[6]

Abstract

The Chianan region is densely populated and has experienced numerous damaging shallow earthquakes, indicating a high potential for seismic hazards. The area is characterized by complex geological structures, including thrust faults, strike-slip faults, and blind faults potentially beneath the alluvial plains. Different fault types exhibit distinct surface ruptures and associated damage distributions, highlighting the need for detailed assessment of each fault's activity and their potential interactions. In recent years, seismic activity in the Chianan area has become more frequent, with several felt earthquake sequences in locations such as Xingang–Minxiong, Puzi–Taibao, Budai–Yizhu, Zhongpu, and Madou–Jiali. This suggests that while the Western Foothills remain a primary seismic hotspot, seismicity in the western plains is also increasing. To improve monitoring and understanding of seismogenic characteristics, a denser short-period seismic network has been deployed, equipped with real-time data transmission. This network integrates broadband seismic stations operated by Academia Sinica and National Chung Cheng University to enhance station coverage and lateral resolution. In collaboration with the Central Weather Administration, real-time data acquisition and earthquake location analyses are performed using SeisComP software to provide higher-resolution background seismicity. These efforts support detailed assessment of seismic potential and provide essential observation for earthquake damage evaluation and disaster mitigation in the Chianan region.

Keywords: Chianan region, seismic activity, short-period seismometer

Historical Earthquakes and Seismogenic Structures

Several destructive shallow earthquakes have occurred in southwestern Taiwan, causing significant casualties and damage. The 1906 Meishan earthquake, with a focal depth of ~6 km, produced ~13 km of surface rupture along the Meishan Fault, showing a maximum right-lateral offset of ~2.4 m and vertical displacement of ~1.8 m. West of Minxiong, the fault trace is inferred to be buried and extends for ~12 km. The 1941 Chungpu earthquake, at a depth of ~12 km, triggered a massive landslide in Caoling, forming a landslide-dammed lake in the Qingshui River. This event is likely related to activity along the Chukou Fault. The 1946 Xinhua earthquake (depth ~5 km) caused a 12-km-long right-lateral surface rupture along the Xinhua Fault. Notably, areas affected by soil liquefaction during this event also experienced similar phenomena during the 2016 Meinong earthquake. The 1964 Baihe earthquake caused a large fire in Chiayi City and ruptured the Chukou Fault over ~40 km. In addition, several moderate-sized damaging earthquakes have also occurred in the region, such as the 1998 Rueili earthquake, the 1999 Chiayi earthquake, and the 2010 Jiasian earthquake.

Based on the 2021 active fault map of Taiwan published by the Geological Survey and Mining Management Agency (https://fault.gsmma.gov.tw/), several active faults were identified in the Chianan area. Holocene active faults include the Meishan Fault, Tachienshan Fault, Chukou Fault, Liuchia Fault, and Xinhua Fault. Late Pleistocene active faults include the Chiuchiungkeng Fault, Mugiliao Fault, Kouhsiaoli Fault, Houjialih Fault, and Zuozhen Fault. The Meishan Fault, Tachienshan Fault, Liuchia Fault,

[1] Associate Researcher, National Center for Research on Earthquake Engineering
[2] Associate Professor, National Chung Cheng University
[3] Section Chief, Central Weather Administration
[4] Research Fellow, National Center for Research on Earthquake Engineering
[5] Senior Research Scientist, Academia Sinica
[6] Assistant Technologist, National Center for Research on Earthquake Engineering

Xinhua Fault, Chiuchiungkeng Fault, and Kouhsiaoli Fault have been designated geologically sensitive areas within a 300 m wide strip along their surface traces. Additionally, according to Chen et al. (2006), the Meishan and Xinhua Faults are characterized by right-lateral slip, while the Zuozhen Fault exhibits left-lateral slip. The width of the fault deformation zones can reach several hundred meters. These observations indicate that the Chianan area hosts a complex fault system, which includes not only thrust faults but also strike-slip faults, as well as blind faults that may lie beneath the alluvial plains (Figs. 1 and 2; Chen et al., 2006; Brown et al., 2022). Notably, these faults exhibit distinct surface rupture and associated damage patterns. Therefore, the activity and interrelationships among these faults must be further assessed.

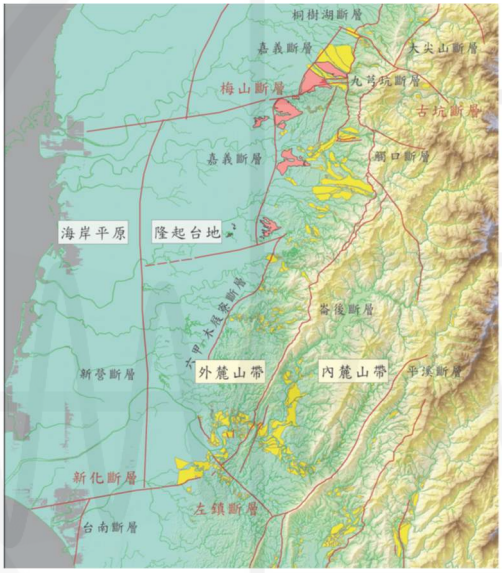

Fig. 1. Geomorphic subdivisions and active faults in the Chianan area (Chen et al., 2006).

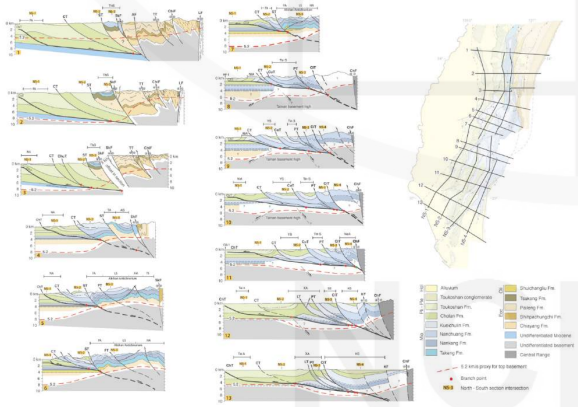

Fig. 2. Geological profile of the Western Foothills (Brown et al., 2022).

Short-period real-time Seismic Monitoring Network

The short-period seismometer is a compact, lightweight, low-power, highly sensitive, and easy-to-operate instrument that can be quickly deployed in the field (Lin, 2020). In addition, it is cost-effective, enabling the acquisition of a larger number of units, thereby facilitating intensive observations in study areas and significantly enhancing the spatial resolution of seismic monitoring. As a result, short-period seismometers have been widely applied for monitoring seismic activity near faults in recent years. These observations improve the understanding of the spatiotemporal distribution of seismic activity and provide crucial parameters for assessing fault activity (Su et al., 2019; Wen, 2021).

To improve the monitoring of seismic activity in the Chianan region, a short-period real-time seismic network was deployed based on seismic activity, fault distribution, and existing seismic stations. The network is equipped for real-time data transmission via mobile signals, powered by solar panels, with routine maintenance conducted seasonally (Fig. 3). In addition, real-time broadband seismic data from Academia Sinica and National Chung Cheng University have been integrated into the network (Fig. 4). Furthermore, in collaboration with the Central Weather Administration, SeisComP software (https://www.seiscomp.de/) is applied for real-time data acquisition and earthquake detection.

Fig. 3. Configuration of the short-period seismic stations.

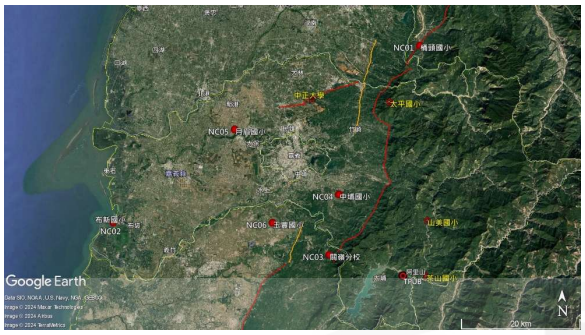

Fig. 4. Distribution of stations in the real-time seismic monitoring network in the Chianan region.

Seismicity in the Chianan Region

In recent years, the Chianan region has experienced frequent seismic activity, including several felt earthquake sequences. To monitor seismic events in real time, SeisComP software was applied for seismic data acquisition, integration, and detection of seismic events. Fig. 5 shows the distribution of seismicity detected using SeisComP between December 1, 2023, and December 31, 2024. The results indicate that most seismic events had magnitudes ranging from 1 to 4 and focal depths of less than 20 km. In addition, localized seismic clusters were observed in areas such as Alishan and Gukeng. Most seismic events occurred particularly on the hanging walls of the Tachienshan and Chukou Faults. However, seismicity in the Western Coastal Plain has also increased over the past two years.

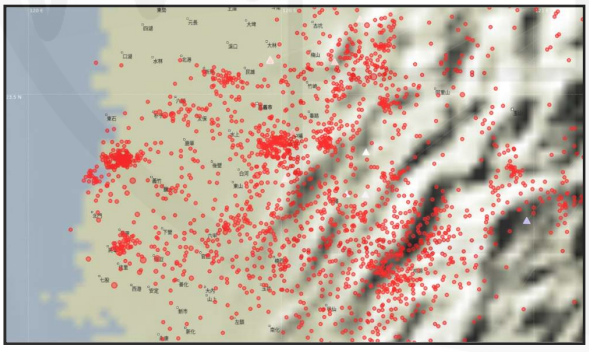

Fig. 5. Seismic activity detected by SeisComP from December 1, 2023 to December 31, 2024.

The Xingang–Minxiong seismic sequence was most active in August and September 2023, with several felt events. After the main seismic sequence, M < 4 events occurred along the western side of the Meishan Fault at depths of ~10 km (Fig. 6). The Puzi–Taibao sequence in February–March 2024 was characterized by events 113004 and 113009, as reported by the Central Weather Administration. This sequence included sparse aftershocks with focal depths between 5 and 15 km and predominantly thrust-type focal mechanisms (Fig. 7). The Budai–Yizhu sequence, which began on April 1, 2024, was more active, featuring several felt events, including 113017, 113018, 113198, and 113199. Numerous aftershocks occurred at depths of 6–10 km, with strike-slip and thrust focal mechanisms (Fig. 8).

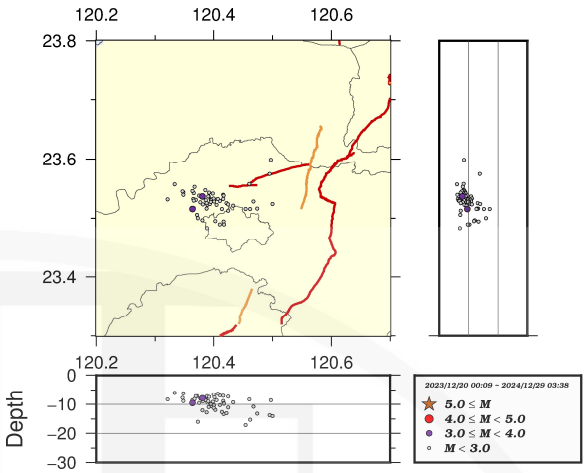

Fig. 6. Seismicity in the Xingang–Minxiong area in 2024.

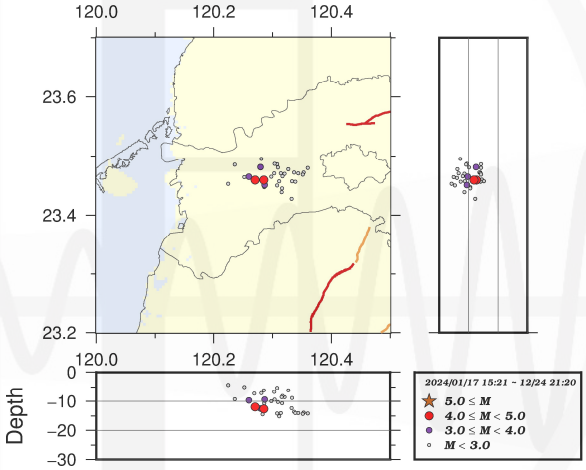

Fig. 7. Seismicity during the February–March 2024 Puzi–Taibao earthquake sequence.

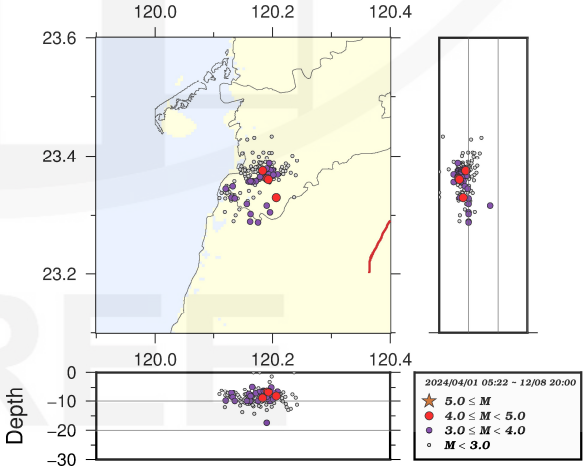

Fig. 8. Seismicity during the Budai–Yizhu earthquake sequence beginning on April 1, 2024.

Seismic activity has been continuously observed in the Zhongpu area, with a prominent sequence beginning on October 27, 2024, including events 113483, 113484, and 113485 (Fig. 9). Larger events were located at shallow depths of ~5 km, while smaller earthquakes were more widely distributed and

occurred at greater depths. The most recent sequence was observed in the Madou–Jiali area (Fig. 10), beginning on November 16, 2024, with event 113493. Event 113498 was the largest one with magnitude 5.5 that occurred on November 22. Events with magnitudes larger than 3 were distributed across a wider area, with focal depths concentrated between 10 and 15 km.

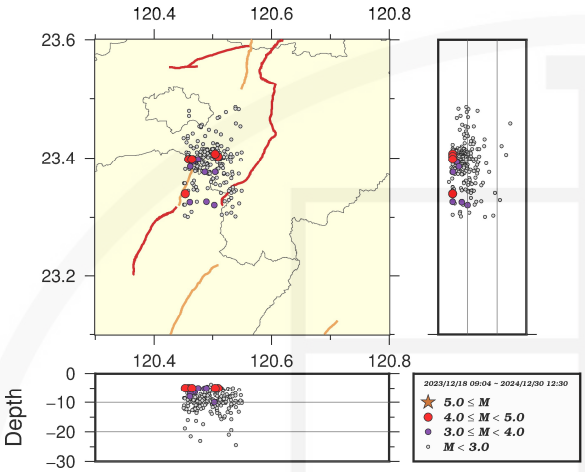

Fig. 9. Seismicity during the Zhongpu earthquake sequence.

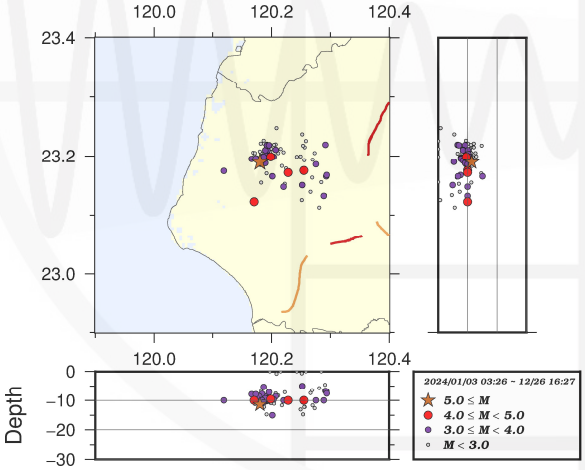

Fig. 10. Seismicity during the Madou–Jiali earthquake sequence beginning on November 16, 2024.

Summary

The establishment of a real-time seismic monitoring network requires continuous adjustments to station deployment to enhance spatial resolution. Applying machine learning techniques for automatic seismic phase picking and event detection can significantly improve processing efficiency and reduce manual workload. Through the analysis of seismic events with large datasets, the accuracy of earthquake location can be improved. The results can then be compared with known active faults and seismogenic structures to comprehensively assess the seismic potential in the Chianan region. Some findings from this study have been presented at academic conferences and in project reports of the National Science and Technology Council. These findings serve as essential references for seismic hazard assessment and future disaster mitigation, aiming to reduce the impact of potential future earthquakes.

References

Brown, D., Alvarez-Marron, J., Camanni, G., Biete, C., Kuo-Chen, H., and Wu, Y.-M. (2022), "Structure of the south-central Taiwan fold-and-thrust belt: Testing the viability of the model", *Earth Sci. Rev.* 231, 104094.

Chen, W. S., Yeh, M. G., Yang, C. C., Shih, R. C., Lin, C. W., and Hou, C. S. (2006), "Structural characteristics of the Meishan fault", *Bull. Central Geol. Survey, MOEA* 19, 135–151. (in Chinese with English abstract)

Lin, C. J. (2020), "The testing results of short-period instruments", *TEC Newsletter* 29, 1-3. (in Chinese)

Su, P. L., Chen, P. F. and Wang, C. Y. (2019), "High-resolution 3-D P wave velocity structures under NE Taiwan and their tectonic implications", *J. Geophys. Res.* 124, 11601-11614.

Wen, S. (2021), "Earth magnifier - high-resolution seismic array", *TEC Newsletter* 34, 5. (in Chinese)

Nonlinear Site Response Observed by the NDHU Downhole Array during the April 2, 2024, ML 7.2 Earthquake in Taiwan

Che-Min Lin[1], Hung-Hao Hsieh[2], Jyun-Yan Huang[3], Yun-Yu Wang[4], Kuei-Mei Lin[4], Hung-Ming Chen[5] and Chia-Han Chen[3]

林哲民[1]、謝宏灝[2]、黃雋彥[3]、王允佑[4]、林貴梅[4]、陳鴻明[5]、陳家漢[3]

Abstract

On April 2, 2024, an earthquake with a local magnitude (M_L) of 7.2 occurred in Hualien County, eastern Taiwan. As the strongest earthquake in Taiwan in a quarter century, it induced extremely strong ground motion with a maximum peak ground acceleration (PGA) of 1.5 g and a peak ground velocity (PGV) exceeding 80 cm/s in the nearfield. Within two months after the mainshock, thousands of aftershocks occurred in a northeast-striking linear region of approximately 70 km, including seven events above M_L 6.0. The National Dong Hwa University (NDHU) downhole array, which consists of four accelerometers installed at depths of 0, 20, 30, and 70 m and is located just 6 km from the epicenter, observed a PGA of 271 gal. This study analyzes numerous downhole records from the earthquake sequence to investigate the local nonlinear site response to ground motion. For weak ground motions with peak acceleration below 10 gal, the PGA observed at the ground surface was approximately 2.3 times greater than that at a depth of 70 m. Spectral ratios of surface to downhole horizontal accelerations indicate a predominant soil-amplification frequency of 1.9 Hz, which agrees with the theoretical transfer function of the soil profile. The second and third soil-amplification modes also appear at approximately 5.3 Hz and 8 Hz, respectively. As input ground motion increased, both the amplification and the dominant frequencies decreased. During the mainshock, the surface PGA was only 1.5 times that of the 70 m input value (181 gal), and the predominant frequency shifted to 1.4 Hz. These results demonstrate that nonlinear site response at the NDHU downhole array reduced both PGA and predominant frequency. The significant nonlinearity observed enables further research on soil behavior.

Keywords: 2024 Hualien earthquake, strong motion, nonlinear site response, downhole seismometer

Introduction

A strong earthquake with a local magnitude (M_L) of 7.2 struck Shoufeng Township, Hualien County, eastern Taiwan, at 7:58 AM (UTC) on April 2, 2024. The U.S. Geological Survey (USGS) reported a moment magnitude (M_W) of 7.4. This was the strongest earthquake in Taiwan since the 1999 Chi-Chi event. According to the Central Weather Administration, the earthquake had a focal depth of 19.7 km, and a maximum intensity of 6+ was recorded in Heping, Xiulin Township, Hualien County. This corresponds to a maximum peak ground velocity (PGV) exceeding 80 cm/s and a maximum peak ground acceleration (PGA) of 1.5 g observed in Taroko. In addition, the intensities in the counties in northern Taiwan all reached intensity 5−, while intensity 3 was recorded in the south. Based on data from several organizations, the focal mechanism of the April 2 Hualien earthquake was a northeast-southwest trending thrust fault, consistent with the main tectonic stress pattern caused by plate collision in eastern

[1] Research Fellow, National Center for Research on Earthquake Engineering
[2] Assistant Researcher, National Center for Research on Earthquake Engineering
[3] Associate Researcher, National Center for Research on Earthquake Engineering
[4] Research Assistant, National Center for Research on Earthquake Engineering
[5] Assistant Technologist, National Center for Research on Earthquake Engineering

Taiwan. In the month after the mainshock, approximately 1,800 aftershocks with a magnitude of 3 or higher had occurred, with epicenters distributed in a northeast-southwest trending linear zone over 70 km along the eastern coast of Hualien. Seven of these aftershocks exceeded magnitude 6 and the large aftershocks also generated strong ground motions in the area.

Site effects are one of the essential factors affecting the intensity of ground motion. However, soils can exhibit nonlinear behavior under strong ground motion, with reduced stiffness and increased damping, causing the site's resonance frequency to shift to lower values and suppressing high-frequency seismic wave energy. Given the importance of nonlinear site effects under strong ground motion in both seismic motion research and disaster mitigation, this study investigates the nonlinear site response near the epicenter of the 2024 Hualien earthquake. A large amount of mainshock and aftershock data recorded by a downhole seismometer array was analyzed to examine these effects in detail.

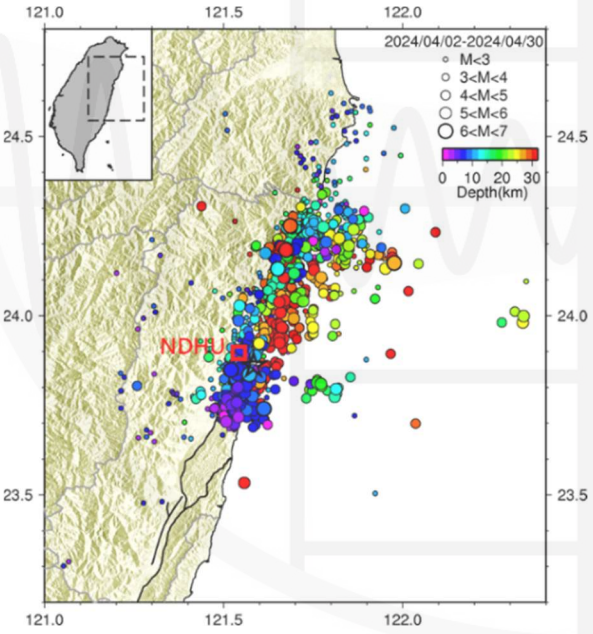

Fig. 1. Locations of the NDHU downhole array and the epicenter of the 2024 Hualien earthquake sequence

NDHU Downhole Seismometer Array

The National Center for Research on Earthquake Engineering (NCREE) installed a downhole seismometer array on the National Dong Hwa University (NDHU) campus in June 2015. The array comprises four accelerometers, one at the surface and three at depths of 20, 30, and 70 m. The array has observed more than 3,000 seismic motion records over the years. Historical data show that the average PGA amplification within the top 70 m of soil at this site is approximately 2.7 times, indicating significant site amplification. Located just 6 km from the epicenter of the 2024 Hualien mainshock, the NDHU downhole array observed a surface PGA of 271 gal. It also recorded nearly 1,000 aftershock records, including strong ground motions from several large events near the epicenter. However, due to equipment issues, most of the available data were recorded only at the surface and at a depth of 70 m. Therefore, this study focuses on the nonlinear site response of the complete stratum between the surface and a depth of 70 m at the NDHU array.

All seismic data were manually inspected to ensure quality and to identify P-wave and S-wave arrival times. The data were then grouped based on the horizontal PGA (RotD50) observed at a depth of 70 m. Considering the large number of seismic data with PGA less than 50 gal, these were divided into four groups based on PGA magnitude. The PGA distribution, quantity, and average PGA for each group are shown in Table 1. The following analysis uses the average values of these four weak-motion groups to facilitate discussion and obtain representative site responses under different levels of ground motion. Only four seismic records had horizontal PGAs greater than 50 gal, all with epicentral distances within 8 km of the NDHU array, and input PGAs at a depth of 70 m ranging from 65 to 181 gal. These events are presented in Table 2. To supplement the strong-motion dataset, the study also includes strong-motion records from two historical M_L 6.3 earthquakes observed by the NDHU array on February 6, 2018, and April 18, 2019. Their details are also listed in Table 2.

Tab. 1. Summary of four of weak-motion groups

PGA range of Horizontal RotD50 (gal)	Event Number	Geomean PGA (gal)
$1 \geqq PGA > 10$	329	2.4
$10 \geqq PGA > 20$	28	12.4
$20 \geqq PGA > 30$	9	23.3
$30 \geqq PGA > 50$	7	36.8

Tab. 2. Six strong-motion events from the 2024 Hualien earthquake sequence and two historical strong-motion events

Origin Time	Magnitude (M_L)	Depth (km)	Epicentral Distance (km)	PGA of Horizontal RotD50 (gal)
2024-04-02 23:58	7.2	22.52	5.95	181.5
2024-04-23 00:04	6.1	11.68	7.63	107.9
2024-04-22 18:32	6.2	7.74	6.00	100.4
2024-04-23 02:21	5.5	8.86	4.39	65.1

Origin Time	Magnitude (M_L)	Depth (km)	Epicentral Distance (km)	PGA of Horizontal RotD50 (gal)
2018-02-06 15:50	6.3	6.31	29.40	102.9
2019-04-18 05:01	6.3	20.33	17.32	136.9

Nonlinear Site Response Analysis

In this study, the seismic time history observed by the downhole seismometer at a depth of 70 m is considered as the input signal. After passing through the 70-m soil column, the seismic waveforms recorded at the surface are treated as the output signals. Therefore, by dividing the surface signal by the downhole signal, the actual site amplification factor of the 70-m stratum can be directly observed. Figure 2 shows the relationship between the surface-to-downhole PGA ratio and the downhole PGA. For weak motions with input PGA below 10 gal, the average PGA amplification is 2.31 times. As the input PGA increases, the amplification gradually decreases, reaching an average of 1.77 times for PGAs between 30 and 50 gal. For the four strong-motion events with higher PGA, the amplification drops further to between 1.39 and 1.53 times. This reduction in PGA amplification indicates significant nonlinear site response at the NDHU array.

Fourier spectra of the three-component acceleration time histories were calculated to obtain the spectral ratios between the surface and downhole recordings. Figure 3 shows the spectral ratios for all three components across the four weak-motion groups and six strong-motion events, representing the observed transfer functions of the 70-m soil column. The transfer functions of the two horizontal components for weak motions indicate that the first and most significant spectral peak occurs at approximately 1.9 Hz, with a ratio of 3.5. This peak can be considered the predominant frequency of the stratum. As input ground-motion PGA increases, the first peak frequency gradually decreases, reaching 1.4 Hz during the mainshock with the highest PGA. The peak spectral ratio gradually increases with rising PGA, reaching values above 6, although reversals and decreases are observed in some components for specific earthquake events. In addition, the transfer functions show second and third spectral ratio peaks at higher frequencies—between 4 and 5.3 Hz and between 6 and 9 Hz, respectively—whose peak frequencies and ratios also change with input PGA. For the vertical component, the first spectral peak appears at approximately 7 Hz. Although the peak spectral ratio increases with increasing input PGA, the corresponding peak frequency shows no significant change.

To objectively evaluate the nonlinear response of the observed transfer functions during the April 2 Hualien earthquake sequence, this study referenced the degree of nonlinearity (DNL) proposed by Noguchi and Sasatani (2011). Using the transfer functions from weak-motion events with PGA below 10 gal as a reference baseline, the three-component DNL values were calculated for the remaining three weak-motion groups and six strong-motion events and summarized in Figure 4. As shown, the variation in DNL values indicates that as he input ground motion increases, the degree of nonlinear response in the stratum also increases, reaching a maximum at approximately 100 gal and showing no further significant increase thereafter. Notable differences in DNL values are also observed between different events and components.

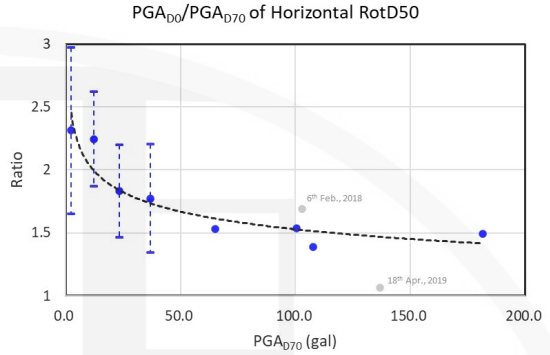

Fig. 2. Site amplification of horizontal PGA with nonlinear behavior observed at the NDHU array

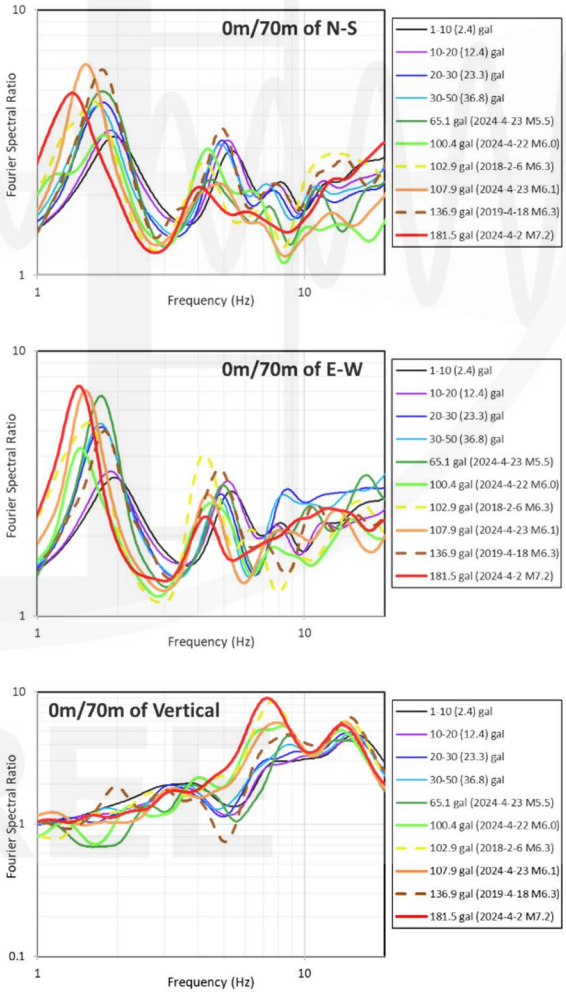

Fig. 3. Three-component spectral ratios between the surface and downhole data for various input motions

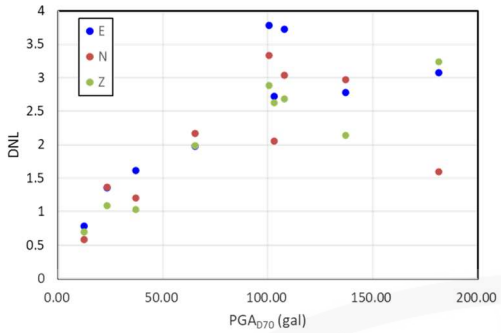

Fig. 4. Three-component DNL values for various input motions

Theoretical Analysis

Based on the soil test data and downhole velocity profile from the NDHU downhole array, and following the soil stratigraphy and parameters established by Wang (2019), the observed horizontal acceleration time histories at a depth of 70 m were used as input to calculate the theoretical transfer functions (Figure 5). These calculations were performed for the six strong-motion events using STRATA, a program for equivalent linear site-response analysis (Kottke and Rathje, 2009). The theoretical transfer functions exhibit three peaks that are similar to those observed in downhole data. A comparison of the peak frequencies and peak spectral ratios derived from the observed and theoretical transfer functions is presented in Figure 6. The results show that while the observed peak frequencies follow a trend similar to the theoretical ones, the theoretical peak frequencies are overestimated by approximately 20%. In terms of peak amplitude, the overestimation is even more pronounced, with theoretical values reaching up to 170% of the observed values.

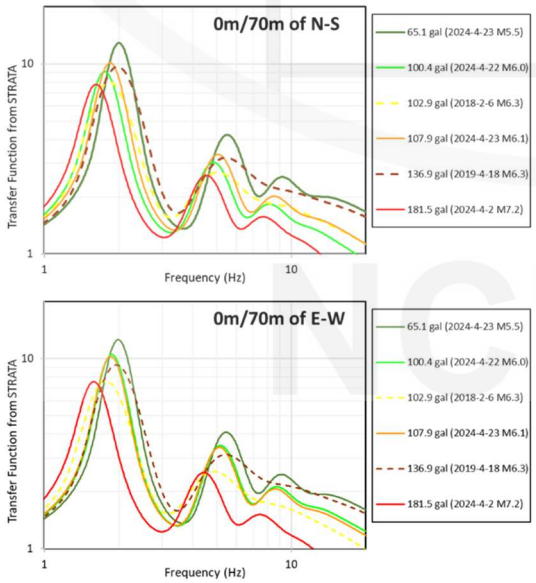

Fig. 5. Theoretical transfer functions of six strong motion events calculated using downhole time histories as input

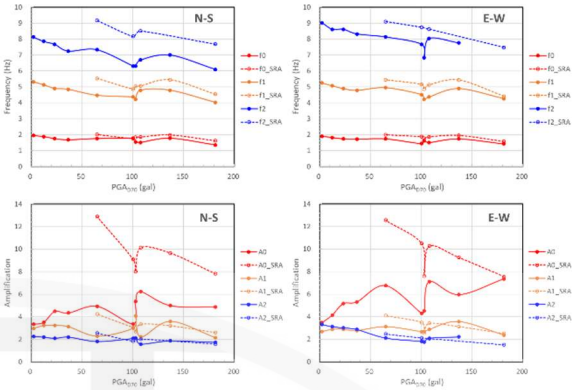

Fig. 6. Comparison of the three peak frequencies (upper two figures) and peak amplitudes (lower two figures) of the observed and theoretical horizontal transfer functions

Conclusions

In summary, analysis of the 2024 Hualien earthquake sequence data collected by the NDHU downhole seismometer array revealed significant nonlinear site effects within the upper 70 m of soil. As the intensity of input ground motion increased, PGA amplification was suppressed, and the predominant frequency of the observed transfer function gradually decreased—both characteristic of nonlinear site response. The significant nonlinearity observed provides a valuable basis for further research on soil behavior.

References

Kottke, A. R., and Rathje, E. M. (2009). “Technical manual for Strata”, Berkeley, Calif.: Pacific Earthquake Engineering Research Center.

Noguchi, S, and Sasatani, T. (2011). “Nonlinear soil response and its effects on strong ground motions during the 2003 Miyagi-Oki intraslab earthquake”, Earthquake, 63(2), 165-87 (in Japanese).

Wang, Y.-Y. (2019). ″Utility Comparison Between Application-Specific Differentially Private Models and General Purpose Differentially Private Synthetic Dataset″, Master's Theses, Department of Earth Sciences, National Central University.

Shaking Table Test of Scaled Reinforced Concrete Containment Vessel

Chang-Ching Chang[1], Chiun-Lin Wu[2], Yi-Lung Mo[3], Thomas T.C. Hsu[4]

張長菁[1] 吳俊霖[2] 莫詒隆[3] 徐增全[4]

Abstract

The containment structure is crucial for the safety mechanisms in nuclear power plants, serving as the first barrier to prevent the release of radioactive materials. Its structural integrity is vital to the overall safety of nuclear power plants. To investigate its seismic performance, this study used the containment structure of the Advanced Boiling Water Reactor (ABWR) as a prototype and designed a 1:20 scale model. Shaking table tests were conducted using a long-stroke, high-speed seismic simulation shaking table at the Tainan Laboratory of the National Center for Research on Earthquake Engineering (NCREE). This report presents the planning and execution of these tests on the scaled containment model, including specimen design, experimental setup, measurement systems, input ground motions, data analysis, and observations of failure mechanisms. The results enhance our understanding of the global structural behavior of containment structures under seismic loading and serve as a foundation for validating the Cyclic Softened Membrane Model (CSMM) theory proposed by a professor at the University of Houston, Texas. By capturing the seismic mechanical behavior of the containment structure, this research aims to clarify its overall structural characteristics and the mechanisms of failure.

Keywords: containment vessel, scaled model, shaking table test, seismic responses, NPP, CSMM

Introduction

The seismic safety of nuclear facilities has been a vital concern in the operation of nuclear power plants for many years. On March 11, 2011, the Great East Japan Earthquake caused a serious accident at the Fukushima Daiichi Nuclear Power Plant. This event resulted in damage to the primary containment vessel, leading to a radioactive leak. The incident once again brought global attention to the issue of nuclear safety.

The containment structure serves as the first barrier against the release of radioactive materials, making it a vital component of nuclear safety systems. Its seismic performance significantly impacts the overall safety of nuclear facilities. Typically, containment vessels are constructed as reinforced concrete composite shell structures, which exhibit complex mechanical behavior that is challenging to model accurately using existing methods (Hsu and Wu, 2016). Moreover, research specifically focused on their seismic performance remains relatively limited. To date, most experimental efforts have concentrated on assessing static internal pressure resistance, with relatively few investigations dedicated to dynamic external loading scenarios.

Hirama et al. (2005, 2007) conducted a series of studies and shaking table tests on containment structures, primarily focusing on validating their design strength and safety. However, these studies provided limited insight into the underlying failure mechanisms. Although many researchers have proposed simulation-based analytical methods for evaluating containment structures (Liu et al., 2016; Liu et al., 2020; Luu et al., 2017; Luu et al., 2019; Wu et al., 2019), the lack of sufficient experimental data, especially under dynamic loading conditions, has hindered the comprehensive validation of these

[1] Associate Researcher, National Center for Research on Earthquake Engineering
[2] Research Fellow, National Center for Research on Earthquake Engineering
[3] Professor, University of Houston, Houston, Texas, USA
[4] Professor, University of Houston, Houston, Texas, USA

models.

Therefore, the National Center for Research on Earthquake Engineering (NCREE) and the University of Houston jointly initiated a series of experimental and analytical studies. These efforts aim to enhance the understanding of the seismic response of containment structures. The results of this research not only establish a foundation for validating theoretical models but also provide valuable insights into the seismic design and assessment of other essential civil infrastructure.

Experimental Specimen Design and Setup

The scaled model used in this study was designed based on the containment structure of the Advanced Boiling Water Reactor (ABWR). The prototype structure features an outer diameter of 33 m, an inner diameter of 29 m, and a height of 29.5 m. These dimensions are illustrated in Figure 1 (USNRC, 1997)

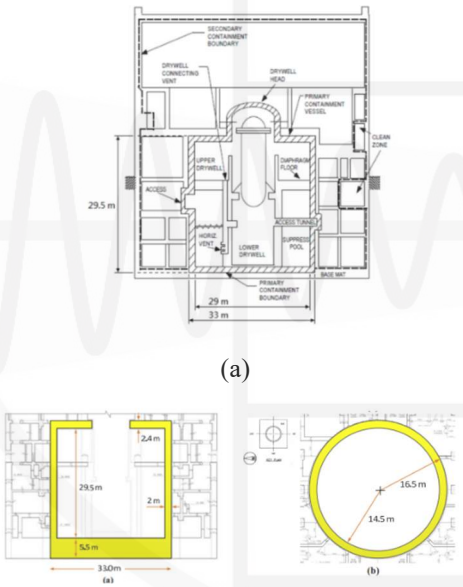

(a) (b) (c)

Fig. 1. ABWR Building

Shaking table tests were conducted at the Tainan Laboratory of the NCREE, utilizing a long-stroke, high-speed seismic simulation shaking table. The tests employed a uniaxial shaking configuration. Considering the load capacity of the shaking table and the anticipated failure strength of the specimen, the containment structure was designed at a 1:20 scale. The detailed dimensions of the scaled model are listed in Table 1.

For reinforcement, both horizontal and vertical bars were arranged in double layers. The reinforcement ratios were 1.1% for horizontal bars and 2.3% for vertical bars.

To accurately simulate the boundary conditions of the actual containment structure and replicate its failure mechanisms, the foundation at the base and the floor slab at the top of the specimen were constructed according to the prototype design. Along with the top slab, a reinforced concrete mass block was added to replicate the payload from the upper structure. This ensured that the loading conditions of the scaled model closely matched those of the actual containment vessel. The top slab was designed in a rectangular shape to fit the dimensions of the mass block.

The test specimen consisted of three main components: the top slab, the primary containment vessel, and the bottom foundation. The configuration of these components is illustrated in Figure 2, while the completed specimen is shown in Figure 3.

Table 1. Dimensions of the RCCV specimen

Name	Dimensions
$\boldsymbol{D}_o$ (Inner diameter, mm)	1050
D_i (Outer diameter, mm)	850
t (Thickness, mm)	100
H (Height, mm)	1280
D_{Vb} (Vertical rebars diameter, mm)	9.53 (#3)
ρ_v (Vertical reinforcement ratio, %)	2.30 %
D_{Hb} (Horizontal diameter, mm)	6.35 (#2)
ρ_h (Horizontal reinforcement ratio, %)	1.09%

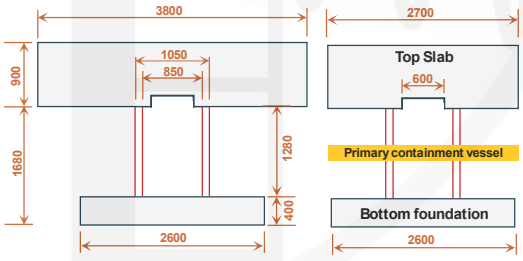

(a) (b)

Fig. 2. Dimensions of the 1/20 scale containment

Fig. 3. Constructed specimen.

Experimental Procedure and Instrumentation

The specimen was firmly anchored to the table to ensure a secure connection between the specimen's foundation and the shaking table and to prevent issues such as translational movement, rotation, uplift, or rocking during seismic testing, high-strength prestressed bolts. This setup ensured the stability and integrity of the test throughout the shaking process.

The experiment was conducted in two phases, with the configurations for each phase illustrated in Figures 4 and 5. The payload distributions and the installation of mass blocks are detailed in Table 2.

Fig. 4. Test setup with mass blocks for Phase I

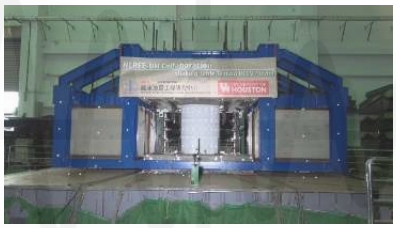

Fig. 5. Test setup with mass blocks for Phase I

Table 2. Payload setup for Phase I and Phase II

	Phase I	Phase II
Mass block	305.76 kN	203.84 kN
Top slab	220.5 kN	220.5 kN
Steel frame	-	196 kN
Axial load	526.26N	600.74 kN
Bottom foundation	64 kN	64 kN
Primary containment vessel	9 kN	9 kN

Phase I focused on low-intensity seismic inputs to observe the elastic response of the specimen. Phase II involved higher-intensity seismic inputs and was divided into two parts. 1) The first part extended the elastic response into the nonlinear regime. To ensure the specimen began in an elastic state, the shaking direction was rotated 90° from Phase I, and the specimen was reoriented accordingly. 2) The second part was conducted after the specimen had reached a damaged state. Due to the output limitations of the shaking table, the time scaling factor of the input ground motion was adjusted from $1/\sqrt{20}$ to $1/\sqrt{2}$, facilitating the progression of the specimen toward ultimate failure and collapse.

Instrumentation installed for this experiment included the following: 1) triaxial accelerometers - to record the dynamic acceleration responses of the specimen; 2) displacement transducers - to measure lateral displacements; 3) strain gauges - to monitor variations in the strain field during seismic loading; 4) optical dynamic measurement system - to capture the overall seismic response of the specimen.

The collected acceleration and displacement data were used to analyze hysteresis behavior, providing insights into the nonlinear dynamic characteristics of the containment structure.

The East–West (90°) component of the September 21, 1999 Chi-Chi earthquake, recorded at the Sun-Moon-Lake station (TCU084) in Yuchi Township, Nantou County (peak ground acceleration, PGA = 0.989 g; epicentral distance = 9.23 km; intensity VII) was selected. Because of the scaled nature of the specimen, the duration of the seismic wave was also scaled, as illustrated in Figure 6. The specific seismic wave inputs used in the tests are listed in Tables 3 and 4.

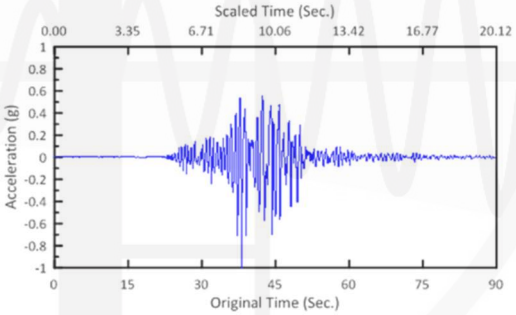

Fig. 6. Time histories of the seismic excitation input

Table 3. Seismic loading level for Phase I

Time scaling factor : $1/\sqrt{20}$	
Test case	Seismic loading level
Run 0-1	0.28 g
Run 0-2	0.54 g
Run 0-3	0.81 g
Run 0-4	1.07 g

Table 4. Seismic loading level for Phase II

Time scaling factor: $1/\sqrt{20}$		Time scaling factor: $1/\sqrt{2}$	
Test case	Seismic loading level	Test case	Seismic loading level
Run 1-1	1.73 g	Run 2-1	0.52 g
Run 1-2	1.84 g	Run 2-2	1.0 g
Run 1-3	2.18 g	Run 2-3	1.4 g
		Run 2-4	1.6 g
		Run 2-5	1.8 g

Final Failure Condition

During Phase I, the specimen was subjected to low-intensity seismic excitation, which resulted in minor cracks. This indicated that the structural response remained within the elastic range. This phase effectively captured elastic seismic behavior and the mechanical characteristics of the containment structure.

In Phase II, the specimen ultimately experienced shear failure, resulting in its collapse. The final failure condition is shown in Figure 7.

Fig. 7. Final failure condition

Conclusions

This study successfully conducted scaled shaking table tests on a 1:20 model of the ABWR containment structure to examine its seismic behavior under dynamic loading. The investigation followed a two-phase experimental program that systematically observed and analyzed both the elastic and nonlinear responses of the specimen. The experimental results provide valuable insights into the overall seismic response and failure mechanisms of reinforced concrete shell-type containment structures. The collected data support further analysis of hysteresis behavior and nonlinear dynamic characteristics. These findings contribute to the validation of advanced theoretical models, such as the CSMM framework, and provide a robust foundation for future simulation and analytical studies.

Acknowledgments

This research was supported by the NCREE and the University of Houston. The authors thank all the technical staff who contributed to the experiment and data processing.

References

Hsu, T.T.C., Wu, C.L. (2016). Cyclic Tests of Cylindrical Concrete Containment Structures and Their 3-D Finite Element Predictions. *16th US-Japan-NZ Workshop on the Improvement of Structural Engineering and Resiliency*, Nara, Japan; 2016.

Hirama, T., Goto, M., Hasegawa, T., Kanechika, M., Kei, T., Mieda, T., Abe, H., Takiguchi, K., & Akiyama, H. (2005). Seismic proof test of a reinforced concrete containment vessel (RCCV): Part 1: Test model and pressure test. *Nuclear Engineering and Design*, 235(13), 1335–1348. https://doi.org/10.1016/j.nucengdes.2005.01.002

Hirama, T., Goto, M., Kumagai, H., Naito, Y., Suzuki, A., Abe, H., Takiguchi, K., & Akiyama, H. (2007). Seismic proof test of a reinforced concrete containment vessel (RCCV). Part 3. Evaluation of seismic safety margin. *Nuclear Engineering and Design*, 237(11), 1128–1139.

Liu, J., Kong, J., Kong, X. (2016). Shaking table model tests of concrete containment vessel (CCV) for CPR1000 nuclear power plant. *Nuclear Energy*, 93, 186-204. https://doi.org/10.1016/j.pnucene.2016.08.016.

Liu, C., Yang, Y., Wang, J. J., Fan, J. S., Tao, M. X., & Mo, Y. L. (2020). Biaxial reinforced concrete constitutive models for implicit and explicit solvers with reduced mesh sensitivity. *Engineering Structures*, 219. https://doi.org/10.1016/j.engstruct.2020.110880

Luu, C. H., Mo, Y. L., & Hsu, T. T. C. (2017). Development of CSMM-based shell element for reinforced concrete structures. Engineering Structures, 132, 778–790. https://doi.org/10.1016/j.engstruct.2016.11.064

Luu, H. C., Mo, Y. L., Hsu, T. T. C., & Wu, C. L. (2019). FE simulation of cylindrical RC containment structures under reserved cyclic loading. *Engineering Structures*, 179, 255–267. https://doi.org/10.1016/j.engstruct.2018.10.050

Wu, C. L., Hsu, T. T. C., Chang, C. Y., Lu, H. J., Yang, H. C., Chang, C. C., Chen, Y. C., & Yang, Y. Sen. (2019). Reversed cyclic tests of 1/13 scale cylindrical concrete containment structures. *Concrete Structures in Earthquake* (pp. 131–150). Springer. https://doi.org/10.1007/978-981-13-3278-4_9

United States Nuclear Regulatory Commission (USNRC). (1997). Issued design certification - advanced boiling-water reactor (ABWR). http://www.nrc.gov/reactors/new-reactors/design-cert/abwr.html

Development of Suspension Seismic-Isolation Devices and Verification using Scaled Specimen Tests

Chung-Han Yu[1], Shiang-Jung Wang

游忠翰[1]　汪向榮[2]

Abstract

This study develops a suspension-type seismic-isolation device in order to address the lack of effective isolation measures for suspended equipment, such as surgical lights, X-ray machines, overhead conveyors, and large display boards. Conventional isolators are designed to operate under compression and cannot function effectively under tensile conditions. Building upon the well-established sloped rolling-type isolation technology developed in previous studies, the proposed tension-based design retains the advantage of a constant maximum transmitted acceleration regardless of external excitations. Shaking table tests were conducted on a scaled specimen fabricated using 3D printing and installed within a rigid frame. Experimental results demonstrate that the device significantly reduces input acceleration and are in strong agreement with theoretical predictions. Minor unexpected responses were observed, however, indicating potential for further design refinements. Overall, this study confirms the feasibility of suspension seismic isolation and provides a foundation for future development and validation of full-scale prototypes in practical applications.

Keywords: Suspended equipment, suspension seismic-isolation technology, shaking table test, equations of motion, 3D-printed specimen.

Introduction

In recent years, post-earthquake reconnaissance conducted worldwide has shown that advances in seismic design and construction materials have generally enabled buildings to achieve the design objectives of having no damage under minor earthquakes, repairable damage under moderate earthquakes, and no collapses under major earthquakes. In other words, properly designed and constructed buildings are unlikely to collapse within their service life. However, these reconnaissance findings highlight a critical issue: even when structures remain intact, earthquakes often cause the loss of building functionality, resulting in broader social and economic impacts. For instance, damage to communication equipment may paralyze the emergency response system, the failure of precision instruments in high-technology facilities or hospitals may significantly disrupt industrial operations and threaten human lives, and the destruction of collections in museums or research institutes may lead to irretrievable cultural losses. Furthermore, many studies have indicated that critical systems in hospitals, such as power supplies, air conditioning, and suspended medical equipment, are particularly vulnerable to excessive vibration. These observations underscore the importance of ensuring that performance-based seismic design not only addresses structural safety but also maintains the functionality of essential equipment during strong ground shaking in order to truly achieve resilience objectives.

Among the strategies for equipment protection, directly applying seismic-isolation technology to equipment is considered practical and effective. Simply anchoring cabinets or equipment to floors may prevent overturning but cannot protect delicate internal components from excessive acceleration. In contrast, equipment isolation can significantly reduce transmitted acceleration, thereby safeguarding both external stability and internal functionality. Commonly used rubber bearings, though effective for buildings, are often too stiff for sensitive equipment requiring low acceleration responses. Friction pendulum bearings, on the other hand, suffer from

[1] Associate Researcher, National Center for Research on Earthquake Engineering

[2] Professor, National Taiwan University of Science and Technology

unstable activation due to static friction and are unfavorable for devices sensitive to high frequencies. As a result, rolling-based bearings have emerged as a promising solution for equipment isolation. They offer extremely low friction, allow precise control of transmitted acceleration when combined with damping mechanisms, and can be integrated into raised isolation flooring systems, offering both economic and maintenance advantages.

In particular, sloped rolling-type isolators are considered well-suited for equipment isolation thanks to their mechanical characteristics [1]. Their main advantages include the absence of a fixed horizontal natural frequency thereby avoiding resonance, stable control of horizontal acceleration, reliable self-centering capability, inherent frictional damping to suppress excessive displacements, and flexible design that allows precise adjustment of damping through spring modules. Previous studies have confirmed that, within a reasonable range of slope angles, such systems can consistently provide stable low-acceleration responses independent of input ground motion characteristics. Further theoretical analyses [2] have shown that the transmitted acceleration is closely related to the slope angle and frictional damping and that it can be effectively described using a simplified flag-shaped hysteresis model.

Design Concept of the Suspension Seismic-Isolation Device

The design concept of the suspension-type seismic-isolation device is illustrated in Figure 1. Similar to the sloped rolling-type isolator, the device consists of three sloped plates (upper, middle, and lower) and two sets of rollers placed between the upper–middle and middle–lower plates. At the central junction of each sloped plate, a circular arc with fixed curvature is designed to prevent collisions during roller movement. Each roller set consists of two rollers arranged in parallel to prevent out-of-plane torsional behavior during motion while providing a certain level of torsional resistance. The roller ends are connected to side plates; therefore, the device includes four side plates in total. Two upper side plates connect the rollers between the upper and middle plates, while two lower side plates connect the rollers between the middle and lower plates. The upper plate is anchored to the structural ceiling, and the lower plate is attached to the protected equipment. Since the two sets of rollers move orthogonally, the isolator can provide seismic protection in any horizontal direction.

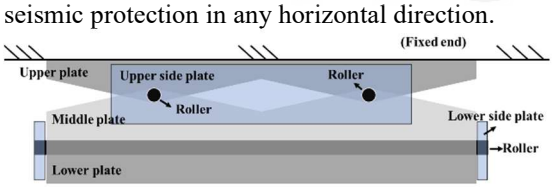

Fig. 1. Schematic diagram of the suspension seismic-isolation device.

The equations of motion for the suspension isolator can be derived from the free-body equilibrium diagram shown in Figure 2. For simplicity, the conceptual model in Figure 1 is reduced to a single roller in a single direction since the mechanical behavior is symmetric. In Figure 2, the upper structural floor is assumed to accelerate to the left, while the roller moves to the right along the slope. Here, M, m_1, and m_2 represent the masses of the equipment, the upper plate, and the roller, respectively; θ_1 and θ_2 are the slope angles; r is the roller radius; g is gravitational acceleration; and $\ddot{x}_g$ ($\ddot{z}_g$) denotes the horizontal (vertical) ground-acceleration input. The displacement, velocity, and acceleration responses of the equipment and lower plate relative to point O are represented by $x_1(z_1)$, $\dot{x}_1(\dot{z}_1)$, and $\ddot{x}_1(\ddot{z}_1)$, while those of the roller relative to point O are denoted as $x_2(z_2)$, $\dot{x}_2(\dot{z}_2)$, and $\ddot{x}_2(\ddot{z}_2)$. The roller's moment of inertia is denoted by I, and α is its angular acceleration, while f_1 and f_2 represent rolling friction forces acting between the upper plate and roller and between the roller and lower plate, respectively. Finally, N_1 and N_2 are the corresponding normal forces. The internal sliding friction damping force (F_D) is modeled using Coulomb's law.

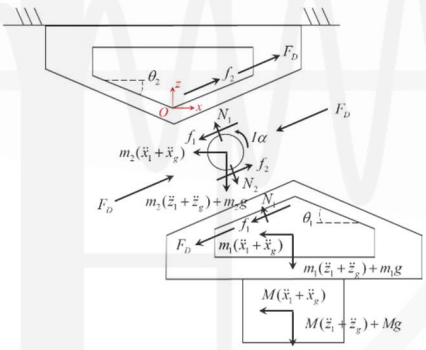

Fig. 2. Free-body diagram of the suspension seismic-isolation device.

By considering force equilibrium, rotational equilibrium, and compatibility conditions, and assuming that: (1) the roller mass is negligible compared with the combined mass of the upper plate and equipment; (2) within a reasonable design range of slope angles (generally less than 12°), no sliding occurs along the slope; (3) the rolling friction between the roller and slope is negligible compared with the internal sliding friction damping force; (4) slope angles θ_1 and θ_2 are sufficiently small that higher-order terms of their trigonometric functions can be ignored; and (5) no vertical ground motion is applied, a simplified generalized solution for the horizontal and vertical transmitted acceleration responses of the lower plate when the roller moving on the slope surface (beyond the curved section with fixed radius) can be obtained as:

$$\ddot{x}_1 = \frac{-(\cos\theta_1 + \cos\theta_2)}{4(M+m_1)}\left[2F_D \operatorname{sgn}(\dot{x}_1) + (M+m_1)g(\sin\theta_1 + \sin\theta_2)\operatorname{sgn}(x_1)\right] - \ddot{x}_g \quad (1)$$

and:

$$\ddot{z}_1 = \frac{-(\sin\theta_1 + \sin\theta_2)\operatorname{sgn}(x_1)}{4(M+m_1)}\left[2F_D \operatorname{sgn}(\dot{x}_1) + (M+m_1)\ddot{x}_g(\cos\theta_1 + \cos\theta_2)\right] . \quad (2)$$

Verification Using a Scaled Specimen Test

To preliminarily verify the theoretical accuracy of the proposed suspension isolation device, a small-scale, single-direction specimen was designed. To simplify the isolation behavior and avoid complex dynamic responses, side plates and other damping mechanisms were omitted. The initial scaled specimen is shown in Figure 3. The specimen was 250 mm in length, 95 mm in width, and 112 mm in height. The contact surface between the lower plate and rollers was initially flat (roller upper side) but was later modified to a 6° slope when manufacturing the specimen. The upper plate–roller contact surface (roller lower side) was also a 6° slope, and the transition region between slopes was designed as a circular arc with a 100 mm radius of curvature. The roller diameter was 21 mm, and the maximum isolation displacement was approximately 80 mm. Because of the small size and complex geometry, the upper and lower plates were fabricated using 3D printing with Nylon12 material (density: 1.01 g/cm³; ultimate tensile strength: 50 MPa; Young's modulus: 1.85 GPa; elongation at break: 11%).

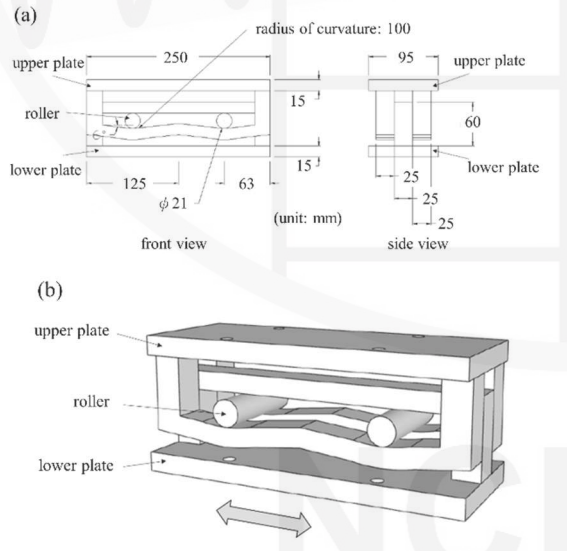

Fig. 3. Design of the scaled suspension-type isolation specimen: (a) design drawing and (b) 3D schematic diagram.

In addition, a one-story rigid frame was constructed to perform shaking table tests under different sinusoidal excitations with various frequencies and maximum acceleration levels. The suspension seismic-isolation device was installed at the ceiling (second floor), with several loading blocks attached to the lower plate to simulate equipment weight. A photograph of the installed specimen is shown in Figure 4. The tests were conducted using the small-scale uniaxial long-stroke shaking table at the National Center for Research on Earthquake Engineering (NCREE) (Figure 5). The table has a maximum acceleration capacity of 1 g, a maximum velocity of 400 mm/s, a stroke of ±250 mm, and a maximum payload of 50 kg.

Fig. 4. Installed specimen and frame.

Fig. 5. The small-scale uniaxial long-stroke shaking table.

Representative test results are shown in Figures 6(a) to (d), where the input accelerations (blue curves) measured at the frame top and output accelerations from the lower plate of the isolation device (red curves) are compared. Due to the small degree of flexibility in the frame, the input accelerations differed slightly from ideal input sinusoidal waves. The transmitted accelerations were significantly lower than the inputs, so the results clearly demonstrate the superior performance of the isolation device. According to Eq. (1), when neglecting the friction force (as noted above, a damping mechanism was not included in the specimen design), the maximum design acceleration of specimens with both 460 N and 736 N loading was 102 gal, which is consistent with results at 2Hz in Figures 6(a) and (c). However, at a higher excitation frequency (3 Hz, Figures 6(b) and (d)), the rollers continued to move within the curved section, resulting in non-constant maximum acceleration values that were smaller than those observed in the sloped region. This result indicates that the suspension device performs even better under high-frequency excitation.

To further verify the theoretical formulation, the acceleration and displacement responses of the specimen with 736 N loading under a maximum acceleration of 250 gal and 2 Hz frequency sinusoidal excitation were compared with analytical predictions, as shown in Figure 7. The theoretical responses were calculated from Eqs. (1) and (2) using input accelerations measured at the top of the frame. The comparison reveals strong agreement in terms of maximum acceleration and displacement. However, during roller movement along the curved surface, measured accelerations were slightly higher than

theoretical values. A preliminary explanation is that the Young's modulus of Nylon12 is significantly lower than that of metal, leading to larger elastic deformation when the roller was located in the unsupported central region of the slope. As the roller moved to the sloped segments supported on both ends, the deformation decreased. This cyclic increase and decrease in deformation irregularly altered the effective curvature, in turn slightly increasing accelerations. Nevertheless, this effect did not significantly influence the overall maximum responses and may be addressed for improvement in future designs.

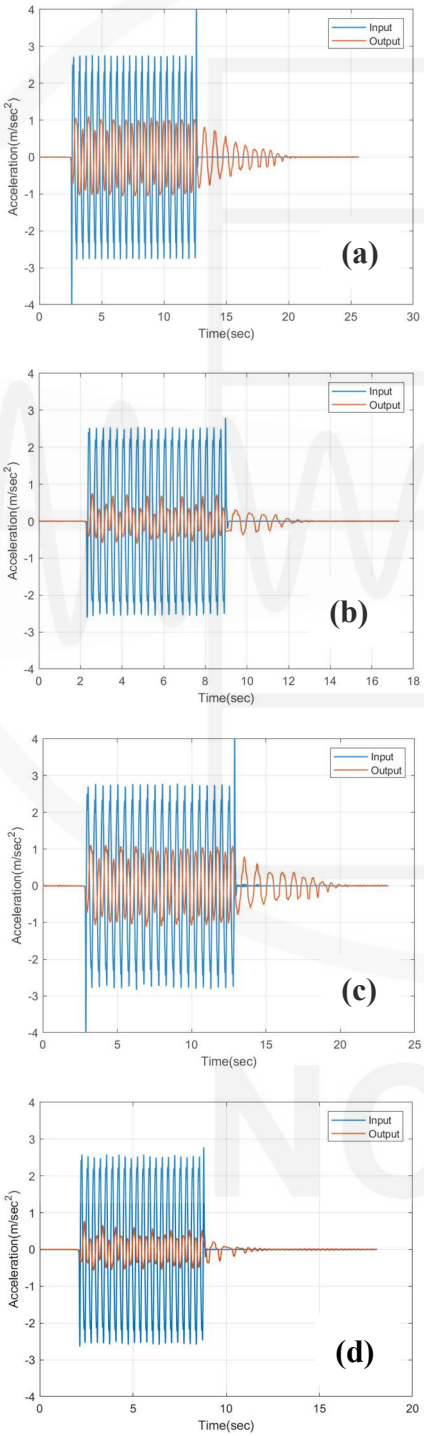

Fig. 6. Acceleration response histories from shaking table tests: (a) 450 N, 250 gal, 2 Hz; (b) 450 N, 250 gal, 3 Hz; (c) 736 N, 250 gal, 2 Hz; and (d) 736 N, 250 gal, 3 Hz.

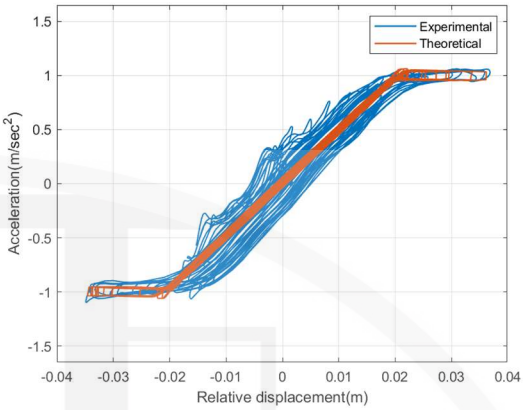

Fig. 7. Comparison of analytical and experimental responses for a specimen with 736 N loading under maximum acceleration of 250 gal and 2 Hz frequency sinusoidal excitation.

Summary

This study addressed the problem of loss of functionality of suspended equipment during earthquakes by proposing and validating a suspension-type seismic-isolation device. Both theoretical derivations and scaled model experiments confirmed that the device can effectively reduce transmitted acceleration, demonstrating excellent isolation performance, particularly under high-frequency excitations. The experimental data showed overall good agreement with theoretical predictions, verifying the feasibility of the design concept. Although minor discrepancies were observed due to material properties, these did not affect the overall performance. Future work will focus on improving material selection and optimizing structural configuration to further enhance isolation efficiency.

References

1. S. J. Wang, C. H. Yu, W. C. Lin, J. S. Hwang, & K.C. Chang. (2017). A generalized analytical model for sloped rolling-type seismic isolators. Engineering Structures, 138, 434-446.
2. S. J. Wang, C. H. Yu, C. Y. Cho, & J. S. Hwang. (2019). Effects of design and seismic parameters on horizontal displacement responses of sloped rolling-type seismic isolators. Structural Control and Health Monitoring, 26(5), e2342.

NCREE

NCREE

NATIONAL INSTITUTES OF APPLIED RESEARCH

National Center for Research on Earthquake Engineering

No. 200, Sec. 3, Xinhai Rd., Taipei 106219, Taiwan(R.O.C.)
Tel: +886-2-6630-0888 Fax: +886-2-6630-0858
https://www.ncree.niar.org.tw